# Topological phases in Luttinger materials

**Dissertation zur Erlangung des**
**naturwissenschaftlichen Doktorgrades**
**der Julius-Maximilians-Universität Würzburg**

15 83

vorgelegt von

Julian Benedikt Mayer

aus Werneck

Würzburg, 2023

Eingereicht am ..........................................................................................
bei der Fakultät für Physik und Astronomie

1. Gutachter: Prof. Dr. Ewelina Hankiewicz

2. Gutachter: Prof. Dr. Giorgio Sangiovanni

3. Gutachter: ..........................................................................................

der Dissertation

Vorsitzende(r): ..........................................................................................

1. Prüfer: Prof. Dr. Ewelina Hankiewicz

2. Prüfer: Prof. Dr. Giorgio Sangiovanni

3. Prüfer: ..........................................................................................

im Promotionskolloquium

Tag des Promotionskolloqiums: ..........................................................................

Doktorurkunde ausgehändigt am: ......................................................................

# Zusammenfassung

Die Suche nach topologischen Materialien ist ein beherrschendes Thema der aktuellen Forschung im Bereich der kondensierten Materie. In dieser Arbeit wird das 4-Band Luttinger-Modell untersucht, welches die $j = 3/2$ Zustände vieler Halbleiter beschreibt. Dieses Modell beschreibt eine Vielzahl von topologischen Zuständen und ermöglicht die analytische Betrachtung der zugehörigen topologischen Oberflächenzustände. Die Existenz dieser Oberflächenzustände ist überaus erstrebenswert, da sie auf Grund ihrer topologischen Natur besonders gegen kleine Störungen geschützt sind.

Im ersten Teil dieser Arbeit wird die Existenz von einem oder zwei Oberflächenzuständen in Abhängigkeit des Verhältnisses der effektive Massen in der quadratischen Luttinger-Halbmetallphase vorhergesagt. Diese Zustände mit topologischen Ursprung können mit den invertierten $s$- und $p$-Orbitalen aus der Bandstruktur und der angenäherten chiralen Symmetrie des Kreuzungspunktes in Verbindung gebracht werden. Daher sind die Resultate dieser Arbeit relevant für eine Vielzahl an Materialien, wie HgTe, $\alpha$-Sn und Iridium-Verbindungen. Diese Materialien werden häufig mit Hilfe von Deformation bearbeitet, indem der Kristall auf einem Substrat mit unterschiedlicher Gitterkonstanten gewachsen wird. Dies führt zu Deformationspotentialen, welche auf die Elektronen wirken. Während Dehnungen häufig verwendet werden, um einen topologisch isolierenden Zustand mit einer Bandlücke zu erzeugen, wird in dieser Arbeit Kompression betrachtet, um eine topologische Halbmetallphase herbeizuführen. Hierbei unterscheidet man zwischen Dirac- und Weyl-Halbmetallen, in Abhängigkeit von der gleichzeitigen Präsenz von Inversions- und Zeitumkehrsymmetrie. Ein Hauptteil dieser Arbeit ist die theoretische Untersuchung der Oberflächenzustände in Luttinger-Halbmetallen beim Übergang in diese topologischen Halbmetallphasen.

Die relative Stärke des Kompressionspotentials im Vergleich zu Termen, welche mithilfe gängiger Inversionssymmetrie berechnet wurden, erlaubt die Definition einer Symmetriehierarche für das System. Hierbei bildet das Luttinger-Modell mit kubischer Symmetrie das Ursprungsmodell für kleine Energien mit der höchsten Symmetrie. Da die Inversionssymmetrie brechenden Terme in der Weyl-Halbmetallphase schwach in vielen Materialien sind, lässt sich ein kleiner Energie- und Impulsbereich finden, in dem die Oberflächenzustände Fermi-Bögen zwischen zwei Weyl-Punkten mit unterschiedlicher Chiralität ausbilden. Als Konsequenz existieren zweidimensionale (2D) Impulsebenen zwischen den Weyl-Punkten, die als effektive 2D Chern-Isolatoren mit chiralen Randzuständen in der Bandlücke angesehen werden können. Außerhalb des Bereichs der Inversion brechenden Terme dominieren die Kompressionspotentiale und das System ist ein

effektives Dirac-Halbmetall mit zwei doppelt entarteten Dirac-Punkten in der Bandstruktur. Im Energiebereich außerhalb der Kompressionsstärke dominieren die quadratischen Terme des Luttinger-Modells und das Energiespektrum lässt sich nicht von einem ungestörten Luttinger-Halbmetall unterscheiden. Um die Symmetriehierarchie abzuschließen, werden die Grenzen des Luttinger-Modells untersucht, bei dem die entfernten $j = 1/2$ Zustände einen signifikanten Effekt auf die $j = 3/2$ Zustände aufweisen. Hier verliert das Luttinger-Modell seine Gültigkeit und kompliziertere Modelle, wie das 6-Band Kane-Modell, müssen in Betracht gezogen werden.

Im zweiten Teil dieser Arbeit werden theoretisch zwei verschiedene Systeme für $s$-wellenartige, supraleitende $j = 3/2$ Teilchen in Luttinger-Materialien unter dem Einfluss eines Magnetfeldes analysiert. Zuerst wird der Fokus auf eine eindimensionale Kette gelegt, bei der die intrinsische Spin-Orbit-Kopplung von inversionsassymetrischen Kristallen eine topologische Bandlücke öffnet. Im Gegensatz zu Atomketten, die mit einer herkömmlichen quadratischen Dispersion mit Rashba- oder Dresselhaus-Spin-Orbit Kopplung modelliert werden, bilden sich zwei topologische Phasenübergänge wegen des unterschiedlichen Effekts des Magnetfeldes auf die $|j_z| = 3/2$ und $|j_z| = 1/2$ Zustände. Darüber hinaus wird ein 2D Josephson-Kontakt mit lokalisierten Andreev-Zuständen innerhalb der supraleitenden Bandlücke diskutiert. Hierbei is die intrinsische Spin-Orbit-Kopplung des Luttinger-Modells ausreichend, um eine topologische Bandlücke zu öffnen, selbst mit intakter Inversionssymmetrie. Dies resultiert aus der Hybridisierung der $|j_z| = 1/2$ und $|j_z| = 3/2$ Zustände in Kombination mit der supraleitenden Kopplung.

Konsequenterweise können beide Systeme Majorana-Randzustände bilden. Diese sind höchst relevant für die wissenschaftliche Forschung wegen ihrer nichtabelschen Austauschstatistik und ihrer Stabilität gegen Dekoherenz, was sie prädestiniert für die Realisierung topologischer Quantencomputer macht. Diese Majorana-Randzustände haben eine flache Energiedispersion und werden von der topologischen Bandlücke geschützt. Interessanterweise lassen sich die Resultate dieser Arbeit für die topologisch supraleitende Phase im Luttinger-Modell sowohl auf das Halbmetall- als auch auf das Metallregime anwenden. Dies induziert eine Relevanz für metallische Systeme, wie zum Beispiel p-dotiertem GaAs. Hierduch werden neue Möglichkeiten für die Realisierung topologischer Supraleitung eröffnet.

# Abstract

The hunt for topological materials is one of the main topics of recent research in condensed matter physics. We analyze the 4-band Luttinger model, which considers the total angular momentum $j = 3/2$ hole states of many semiconductors. Our analysis shows that this model hosts a wide array of topological phases and allows analytical calculations of the related topological surface states. The existence of these surface states is highly desired due to their strong protection against perturbations.

In the first part of the thesis, we predict the existence of either one or two two-dimensional (2D) surface states of topological origin in the three-dimensional (3D) quadratic-node semimetal phase of the Luttinger model, called the Luttinger semimetal phase. We associate the origin of these states with the inverted order of $s$ and $p$-orbital states in the band structure and approximate chiral symmetry around the node. Hence, our findings are essential for many materials, including HgTe, $\alpha$-Sn, and iridate compounds. Such materials are often modified with strain engineering by growing the crystal on a substrate with a different lattice constant, which adds a deformation potential to the electrons. While tensile strain is often used to drive such materials into a gapped topological insulator regime, we apply compressive strain to induce a topological semimetal regime. Here, we differentiate between Dirac and Weyl semimetals based on inversion and time-reversal symmetry being simultaneously present or not. One major part of this thesis is the theoretical study of the evolution of the Luttinger semimetal surface states in these topological semimetal phases.

The relative strength of the compressive strain and typical bulk inversion asymmetry (BIA) terms allow the definition of a symmetry hierarchy in the system. The cubic symmetric $\mathbf{O}_h$ Luttinger model is the highest symmetry low-energy parent model. Since the BIA terms in the Weyl semimetal phase are small in most materials, we find a narrow energy and momentum range around the Weyl points where the surface states form Fermi arcs between two Weyl nodes with opposite chirality. Consequently, we see 2D momentum planes between the Weyl points, which can be considered as effective 2D Chern insulators with chiral edge states connecting the valence and conduction band in the bulk gap. Exceeding the range of the BIA terms, the compressive strain becomes dominating, and the system behaves like a Dirac semimetal with two doubly degenerate linear Dirac nodes in the band structure. For energies larger than the compressive strain strength, the quadratic terms in the Luttinger model dominate and surface band structure is indistinguishable from an unperturbed Luttinger semimetal. To conclude this symmetry hierarchy, we analyze the limit of the Luttinger model when the remote $j = 1/2$

electron states show a considerable hybridization with the $j = 3/2$ hole states around the Fermi level. Here, the Luttinger model is not valid anymore and one needs to consider more complicated models, like the 6-band Kane Hamiltonian.

In the second part of this thesis, we analyze theoretically two different setups for $s$-wave superconductivity proximitized $j = 3/2$ particles in Luttinger materials under a magnetic field. First, we explore a one-dimensional wire setup, where the intrinsic BIA of inversion asymmetric crystals opens a topological gap in the bulk states. In contrast to wires, modeled by a quadratic dispersion with Rashba or Dresselhaus spin-orbit coupling, we find two topological phase transitions due to the different effects of magnetic fields to $|j_z| = 3/2$ heavy-hole (HH) and $|j_z| = 1/2$ light-hole (LH) states. Second, we discuss a two-dimensional Josephson junction setup, where we find Andreev-bound states inside the superconducting gap. Here, the intrinsic spin-orbit coupling of the Luttinger model is sufficient to open a topological gap even in the presence of inversion symmetry. This originates from the hybridization of the light and heavy-hole bands in combination with the superconducting pairing.

Consequently, both setups can form Majorana-bound states at the boundaries of the system. The existence of these states are highly relevant in the scientific community due to their non-abelian braiding statistics and stability against decoherence, making them a prime candidate for the realization of topological quantum computation. Majorana-bound states form at zero energy and are protected by the topological gap. We predict that our findings of the topological superconductor phase of the Luttinger model are valid for both semimetal and metal phases. Hence, our study is additionally relevant for metallic systems, like p-doped GaAs. This opens a new avenue for the search for topological superconductivity.

“The most important tool of the theoretical physicist is his wastebasket.“

Albert Einstein

# Contents

# Acronyms

Following acronyms are used throughout this Thesis. Each of them is defined at its first occurrence.

| Acronym: | Description and page of first occurrence: |
|---|---|
| 1D | One-dimensional 3 |
| 2D | Two-dimensional 7 |
| 2DEG | Two-dimensional Electron Gas 3 |
| 3D | Three-dimensional 7 |
| ABS | Andreev Bound State 3 |
| BDG | Bogoliubov-de Gennes 3 |
| BIA | Bulk Inversion Asymmetry 7 |
| DSM | Dirac Semimetal 2 |
| HH | Heavy-hole 8 |
| LH | Light-hole 8 |
| LSM | Luttinger Semimetal 107 |
| MBS | Majorana Bound State 2 |
| PHS | Particle-hole Symmetry 6 |
| SC | Superconductor 2 |
| SOC | Spin-orbit Coupling 2 |
| TI | Topological Insulator 9 |
| TRS | Time-reversal Symmetry 2 |
| WSM | Weyl Semimetal 2 |

# 1 Introduction

What are the consequences of the most fundamental geometric properties of a system? This question gave rise to the mathematical discipline of topology in the later part of the 19th century. It concerns stable characteristics under continuous deformations, like stretching, twisting, or bending. Consequently, a topologist considers a coffe mug and a donut equivalent objects since both have a single hole. While you can put your finger through the handle of a coffe mug, you cannot put your finger through a potato.One can only transform both objects into each other by adding or removing a hole, making them members of different topological classes.

Many believed that topology is just an abstract mathematical concept like number theory, which would never find concrete applications. However, solid states physicists found the potential of topology with the prediction of the topological insulator almost a century later [1, 2, 3, 4, 5]. This initiated the hunt for topological materials, whose robustness under perturbations makes them attractive for commercial use in technology.

Many models have been established to identify and analyze topological materials. For instance, the density functional theory models a many-body system numerically by considering an effective potential acting on the electrons [6]. This potential is built from a sum of external potentials given by the elemental composition of the lattice and an effective potential representing the interactions between the electrons. While it was successfully used to predict the overall band structure of many materials, it is known to be computationally demanding for systems with strong spin-orbit interactions and does not allow a deep analytical understanding of a problem.

A rather opposite approach is the so-called BHZ model, developed by Bernevig, Hughes, and Zhang in 2006 [7]. It focuses solely on the two lowest two-dimensional

(2D) energy subbands around the Fermi level with the additional spin degree of freedom. The resulting Hamiltonian is a $4 \times 4$ matrix, which can easily be diagonalized analytically. It was famously used to discuss the electronic properties of a 2D topological insulator with its metallic edge states in the bulk gap [5].

In this thesis, we consider the three-dimensional (3D) 4-band Luttinger model, derived by J. M. Luttinger in 1956 [8]. It describes the $j = 3/2$ HH and LH states in semiconductors. We show that it allows the analytical study of materials with zinc-blende structure, like HgTe, $\alpha$-Sn, or iridate compounds.

These materials are of particular interest for their rich potential for topological phases. By themselves, they host a strong intrinsic spin-orbit coupling (SOC) and an inverted band structure, which makes them a quadratic-node semimetal. Confining the crystal in a quantum-well setup leads to the formation of subbands in the dispersion, giving an insulating phase. If the thickness of the quantum-well exceeds a critical value, the conduction and valence bands invert, and the system is a 2D topological insulator [7, 5, 9]. If the crystal is grown on a substrate with a different lattice constant, the lattice is strained, and deformation potentials act on the electrons. Here, tensile strain opens a gap between the $j = 3/2$ states and induces a 3D topological insulator phase with 2D Dirac surface states [10].

During our study, we apply compressive strain to the lattice, which splits the quadratic node of the dispersion into multiple linear nodes. These are characteristic of a topological semimetal phase, classified in two different categories. If the system preserves both time-reversal symmetry (TRS) and inversion symmetry, we find a Dirac semimetal (DSM) phase with double degenerate Dirac nodes [11, 12, 13]. The breaking of at least one of these symmetries splits the Dirac nodes into sets of Weyl nodes, indicating a Weyl semimetal (WSM) phase. The Weyl nodes have a finite chirality and act as sources and sinks of Berry curvature [14, 15]. This gives rise to exciting physics, like negative magnetoresistance, the existence of Fermi arcs on the surface, or the chiral anomaly [16, 17, 18, 19].

Another topological phase considered in this thesis is the topological superconductor (SC). This phase is highly desired for forming Majorana bound states (MBSs), manifesting as zero-energy modes at the boundaries of the system [20, 21]. Their non-abelian statistics and protection against decoherence make them the ideal candidate for realizing topological quantum computation [22]. The $j = 3/2$ states of the Luttinger model allow the formation of higher-order $d$ or $f$-wave Cooper pairs in addition to the $s$ and $p$-wave states of ordinary $j = 1/2$ models.

It was discussed that combining a magnetic field and SOC for a semiconducting one-dimensional (1D) nanowire with $s$-wave proximitized superconductivity can lead to a topological phase with MBSs at its ends [21]. Similarly, a 2D Josephson junction, modeled by an ordinary two-dimensional electron gas (2DEG), can host MBSs at the boundaries [23, 24, 25]. Here, the Zeeman field splits the double degenerate Andreev bound states (ABSs), creating a topological regime between two crossings, where an additional SOC opens a topological gap that protects the MBSs against perturbations. We predict that the intrinsic SOC of Luttinger materials allows the formation of a topological SC phase without the need for artificial SOC.

This thesis is structured as follows: In Ch. 2, we introduce physical concepts necessary for the findings of this work. Here, we discuss the idea of topological classes and invariants determined by the fundamental symmetries of the system. Afterward, we show the most relevant features of 3D topological semimetals, categorized in Weyl and Dirac semimetals. Considering topological superconductivity, we introduce the Bogoliubov-de Gennes (BdG) formalism and discuss the significance of ABSs and MBSs.

In Ch. 3, we analyze the formation and evolution of 2D topological surface states in the semimetallic phases of the 3D Luttinger model. For this, we begin with the 3D quadratic-node Luttinger semimetal phase and link the existence of 2D topological surface states in this gapless regime to the inverted band structure of the 6-band Kane model and approximate chiral symmetry, discussed in Ref. [26]. Then, we study the evolution of the 2D surface states in the DSM phase under compressive strain as perturbations. We explain the effect of inversion symmetry in two steps. First, we focus only on linear-momentum bulk inversion asymmetry (BIA) terms, which introduces a line-node semimetal phase. Afterward, we add the cubic BIA terms, which drive the system in a 3D WSM phase with the formation of 2D Fermi arcs and 2D momentum planes with non-trivial Chern numbers between the Weyl nodes [19]. The additional publication of the analysis of Ch. 3 is submitted to PRB [27].

In Ch. 4, we apply proximitized $s$-wave superconductivity to the Luttinger model in its metal and semimetal phases. First, we consider a 1D wire setup with a Zeeman field, where SOC of inversion symmetry breaking crystals is sufficient to open a topological gap that protects MBSs at the ends. We show that the coexistence of $|j_z| = 1/2$ and $|j_z| = 3/2$ states which act differently in a magnetic field, leads to two topological phase transitions, limiting the magnetic field range of the MBSs. Next, we consider a 2D Josephson junction setup, where the intrinsic SOC of Luttinger materials is sufficient to form topological regimes even if the lattice conserves inversion symmetry. Also, we show that the interplay of $|j_z| = 1/2$ and $|j_z| = 3/2$ states give rise to exciting features in the Josephson junction setup. The findings of Ch. 4, considering the semimetal phase, are also published in Ref. [28].

Finally, we conclude our findings and give an outlook on potential future continuations of this study in Ch. 5.

# 2 Introduction to topological semimetals and superconductors

## Contents

## 2.1 Classification of topological matter in different symmetry classes

This thesis will study different topological phases in the Luttinger model [8]. To do so, we will introduce the topological invariant $\mathcal{Q}$, which indicates whether a system is a topologically trivial or non-trivial regime. The existence of a topological invariant depends on discrete symmetries and the dimensionality of the system [29, 30, 31, 32, 33].

It is convenient to separate solid-state systems into ten unique classes, dedicated by their relation to three discrete symmetries time-reversal symmetry (TRS), particle-hole symmetry (PHS), and chiral symmetry [34]. Each discrete symmetry is associated with the symmetry operators $\hat{\mathcal{T}}$, $\hat{\mathcal{C}}$, and $\hat{\mathcal{S}}$.

A system has TRS if it is invariant under the reversion of time. The reversal of time leads to a change in the propagation direction and rotation of a particle, which affects the momentum $\mathbf{p}$ and spin $\sigma$. Therefore, the TRS operator acts as

$$\hat{\mathcal{T}} : (\mathbf{r}, t) \mapsto (\mathbf{r}, -t) \quad \text{and} \quad \hat{\mathcal{T}} : (\mathbf{p}, \sigma) \mapsto (-\mathbf{p}, -\sigma). \tag{2.1}$$

The anti-unitarity of the TRS operator means that it can be written as

$$\hat{\mathcal{T}} = \hat{U}_{\mathcal{T}} \mathcal{K}, \tag{2.2}$$

where $\hat{U}_{\mathcal{T}}$ is a unitary matrix and $\mathcal{K}$ is the complex conjugation operator. A system preserves TRS if the single-particle Hamiltonian commutes with $\hat{\mathcal{T}}$ leading to

$$\hat{\mathcal{T}} \hat{H}(\mathbf{p}) \hat{\mathcal{T}}^{-1} = \hat{H}(-\mathbf{p}). \tag{2.3}$$

Consequently, the conservation of TRS indicates the constriction to the dependence on momentum and spin of the eigenenergy and, therefore, in the band structure, i.e.,

$$\epsilon(\mathbf{p}, \sigma) =_{\mathcal{T}} \epsilon(-\mathbf{p}, -\sigma). \tag{2.4}$$

Here, we add a subscript to the equal sign $=_{\mathcal{T}}$ to indicate the consquences of the

TRS. This notation is used frequently in this section. One finds that the TRS operator's square depends on the system's spin. It distinguishes between bosonic particles with integer spin and fermionic particles with half-integer spin as

$$\hat{\mathcal{T}}^2 = \begin{cases} +1 & \text{bosons,} \\ -1 & \text{fermions,} \end{cases} \tag{2.5}$$

indicated by the '±' entry in Tab. 2.1. In the absence of TRS, where the Hamiltonian does not commute with $\hat{\mathcal{T}}$, due to, i.e., a magnetic field, is indicated by '0'.

The second discrete symmetry is the PHS. As the name suggests, it relates electrons with holes, which corresponds to an interchange of creation and annihilation operators in second quantization. If the single-particle Hamiltonian anti-commutes with the PHS operator $\hat{\mathcal{C}}$, the system is particle-hole symmetric. This leads to

$$\hat{\mathcal{C}}\hat{H}(\mathbf{p})\hat{\mathcal{C}}^{-1} = -\hat{H}(-\mathbf{p}), \tag{2.6}$$

which indicates a relation between positive and negative energy states with opposite momentum

$$\epsilon(\mathbf{p}, \sigma) =_{\mathcal{C}} -\epsilon(-\mathbf{p}, \sigma). \tag{2.7}$$

The PHS operator squares to

$$\hat{\mathcal{C}}^2 = \pm 1, \tag{2.8}$$

indicated by the '±' entry in Tab. 2.1. For superconducting systems, PHS is essential due to the shape of the Bogoliubov-de Gennes (BdG) equation (see Sec. 2.3). Due to the relation of Bogoliubov quasi-particles, one finds the condition $\hat{\mathcal{T}}^2 = -\hat{\mathcal{C}}^2$ [29, 35], which means that the symmetry classes BDI and CII are only relevant in fine-tuned Hamiltonians.

The third discrete symmetry is chiral symmetry, a combination of TRS and PHS ($\hat{\mathcal{S}} = \hat{\mathcal{T}} \cdot \hat{\mathcal{C}}$). Hence, a system with both TRS and PHS preserves always chiral symmetry, while only one of these symmetries leads to chiral asymmetry. Interestingly, systems with both broken TRS and PHS can either have chiral symmetry or not. This corresponds to the symmetry classes A and AIII, which are called complex classes [32]. The chiral symmetry operator is unitary, which must anti-commute with the single-particle Hamiltonian. One gets the condition

$$\hat{\mathcal{S}}\hat{H}(\mathbf{p})\hat{\mathcal{S}}^{-1} = -\hat{H}(\mathbf{p}), \tag{2.9}$$

which relates positive with negative energy states without the inverted sign of the momentum

$$\epsilon(\mathbf{p},\sigma) =_{\mathcal{S}} -\epsilon(\mathbf{p},\sigma), \tag{2.10}$$

in contrast to the PHS. The chiral symmetry operator only comes in one flavor,

$$\hat{\mathcal{S}}^2 = +1. \tag{2.11}$$

An additional symmetry that is important to the systems discussed in this thesis is the inversion symmetry, also known as parity [10]. While it does not contribute to the periodic table from Tab. 2.1, it has a significant impact on the Hamiltonian and band structure of the system. An inversion symmetric system is equivalent to its mirror image in three dimensions. Similar to the TRS operator, inversion in space also inverts the propagation direction, meaning the momentum. On the other hand, it does not affect the spin. In summary, the inversion symmetry operator $\hat{\mathcal{P}}$ acts as

$$\hat{\mathcal{P}}:(\mathbf{r},t)\mapsto(-\mathbf{r},t) \quad \text{and} \quad \hat{\mathcal{P}}:(\mathbf{p},\sigma)\mapsto(-\mathbf{p},\sigma). \tag{2.12}$$

A single-particle Hamiltonian conserves inversion symmetry if

$$\hat{\mathcal{P}}\hat{H}(\mathbf{p})\hat{\mathcal{P}}^{-1} = \hat{H}(-\mathbf{p}) \tag{2.13}$$

is satisfied. One finds the inversion symmetry relation to the energy dispersion

$$\epsilon(\mathbf{p},\sigma) =_{\mathcal{P}} \epsilon(-\mathbf{p},\sigma). \tag{2.14}$$

Kramers' degeneracy is a relevant consequence of the coexistence of TRS and inversion symmetry. Combining Eqs. (2.4) and (2.14), one can immediately show that

$$\epsilon(\mathbf{p},\sigma) =_{\mathcal{T},\mathcal{P}} \epsilon(\mathbf{p},-\sigma), \tag{2.15}$$

meaning that every state has a degenerate Kramers' partner state with the same energy and momentum, but opposite spin.

Even though it is not discussed in this thesis, we like to point out that parity in a 2D quantum system gives rise to interesting consequences. A mirror operation on both spatial components would be equivalent to a rotation in two dimensions. Hence, parity in 2D is defined by inverting only one spatial component with

$$\hat{\mathcal{P}}_x : (x,y,t) \mapsto (-x,y,t), \quad \text{and} \quad \hat{\mathcal{P}}_y : (x,y,t) \mapsto (x,-y,t). \tag{2.16}$$

An odd number of massless 2D Dirac fermions conserves parity symmetry on a classical level, which cannot be maintained on the quantum level [36, 37]. This contradiction is called the parity anomaly, which has major consequences for the Dirac surface states of a 3D topological insulator [38, 39, 40, 41]. This includes a re-entrant quantum Hall effect in a single topological surface state of the tensile strained 3D topological insulator (Hg,Mn)Te, which we discuss in detail in Ref. [42], which is in preparation.

In summary, one finds ten different symmetry classes, which are presented in Tab. 2.1 [34]. Schnyder et al. [29] showed that any system of a specific symmetry class could be linked to one of four different types of topological invariants in $d$ dimensions: (1) A $\mathbb{Z}$ topological invariant can take any integer value ($\mathcal{Q} \in \{0, \pm 1, \pm 2, \ldots\}$) and is called the Chern number [43, 44, 40]. Prominent examples of these phases are the quantum Hall and quantum anomalous Hall effect with chiral states at the system's boundary. (2) The $2\mathbb{Z}$ invariant can only take even integer values ($\mathcal{Q} \in \{0, \pm 2, \pm 4, \ldots\}$). This is related to a topological phase, where the symmetry of the system demands a doubling of the degrees of freedom. (3) A $\mathbb{Z}_2$ invariant can only have one of two values ($\mathcal{Q} = \pm 1$ or $\mathcal{Q} \in \{0, 1\}$). A possible relation is the existence of an even or odd number of Majorana bound states (MBSs) in topological superconductors (SCs) (see Sec. 4.2) or topological insulators (TIs) in $d = \{2, 3\}$ [2, 3, 4, 7, 5, 33, 45]. (4) The '0' entries in Tab. 2.1 correspond to systems without a topological phase.

| class | $\mathcal{T}$ | $\mathcal{C}$ | $\mathcal{S}$ | $d=0$ | $d=1$ | $d=2$ | $d=3$ |
|---|---|---|---|---|---|---|---|
| A | 0 | 0 | 0 | $\mathbb{Z}$ | 0 | $\mathbb{Z}$ | 0 |
| AIII | 0 | 0 | $+$ | 0 | $\mathbb{Z}$ | 0 | $\mathbb{Z}$ |
| AI | $+$ | 0 | 0 | $\mathbb{Z}$ | 0 | 0 | 0 |
| BDI | $+$ | $+$ | $+$ | $\mathbb{Z}_2$ | $\mathbb{Z}$ | 0 | 0 |
| D | 0 | $+$ | 0 | $\mathbb{Z}_2$ | $\mathbb{Z}_2$ | $\mathbb{Z}$ | 0 |
| DIII | $-$ | $+$ | $+$ | 0 | $\mathbb{Z}_2$ | $\mathbb{Z}_2$ | $\mathbb{Z}$ |
| AII | $-$ | 0 | 0 | $2\mathbb{Z}$ | 0 | $\mathbb{Z}_2$ | $\mathbb{Z}_2$ |
| CII | $-$ | $-$ | $+$ | 0 | $2\mathbb{Z}$ | 0 | $\mathbb{Z}_2$ |
| C | 0 | $-$ | 0 | 0 | 0 | $2\mathbb{Z}$ | 0 |
| CI | $+$ | $-$ | $+$ | 0 | 0 | 0 | $2\mathbb{Z}$ |

Table 2.1: Periodic table of gapped topological materials with their topological invariant up to three dimensions $d$ [29, 30, 31, 32]. The systems are classified by their discrete symmetries [34], time-reversal $\mathcal{T}$, particle-hole $\mathcal{C}$, and chiral or sublattice $\mathcal{S}$ symmetry. The entry '0' indicates the absence of symmetry or a topological invariant. The '±' listings indicate whether the symmetry operator squares to $\pm 1$. A $\mathbb{Z}$ topological invariant can take all integer values, a $2\mathbb{Z}$ only even numbers, and a $\mathbb{Z}_2$ only two discrete values.

A unique feature of a $d$-dimensional topological system is the existence of a $(d-1)$-dimensional state at the boundary. We can understand this by imagining a junction of a topological and trivial insulator. A topological phase transition is associated with the inversion of the bulk bands in the band structure. Hence, a critical gap closing point must arise at the boundary of the junction. This leads to the gapless boundary state, characteristic to the topological materials [46, 29, 47, 48, 49, 50]. Throughout this work, we are interested in the behavior of such edge ($d = 1$) and surface ($d = 2$) states forming as a consequence of this bulk-boundary correspondence.

## 2.2 Topological Semimetals

The majority of study in the field of topological materials lies in systems with a gapped band structure, like TIs. This section is dedicated to their gapless relatives, called topological semimetals [15]. In contrast to the well-known two-dimensional (2D) gapless states, like the linear Dirac nodes in graphene [51, 52] or the surface states of a three-dimensional (3D) TI [33, 45], the line nodes of topological semimetal are 3D themselves.

One can differentiate them into two classes, the Weyl semimetal (WSM) and the Dirac semimetal (DSM). We can study both types of topological semimetals in the context of the Luttinger model. Following, we will introduce the physical properties of both WSMs and DSMs.

### 2.2.1 Weyl semimetals

The defining feature of a WSM is the existence of non-degenerate linear crossing points in the 3D bulk band structure, called Weyl points. It is convenient to write the simplest 3D low-energy Hamiltonian of a Weyl point as

$$\hat{H}_{\mathrm{WP}}(\mathbf{p}) = v\mathbf{p} \cdot \hat{\boldsymbol{\sigma}} = v(p_x\hat{\sigma}_x + p_y\hat{\sigma}_y + p_z\hat{\sigma}_z), \tag{2.17}$$

where $\mathbf{p} = (p_x, p_y, p_z)^T$ is the momentum, $v$ is the Fermi velocity, and $\hat{\boldsymbol{\sigma}} = (\hat{\sigma}_x, \hat{\sigma}_y, \hat{\sigma}_z)^T$ are the $2 \times 2$ Pauli matrices, representing a certain degree of freedom in the system, like spin. This Hamiltonian is well known from high-energy physics and describes Weyl fermions. Hermann Weyl first considered it to describe massless particles in the Dirac equation [53, 14]. The Weyl point has the dispersion

$$\epsilon^{\pm}_{\mathrm{WP}}(\mathbf{p}) = \pm|v\mathbf{p}|, \tag{2.18}$$

which shows a linear crossing at $\mathbf{p} = 0$. Since all three Pauli matrices in $\hat{H}_{\mathrm{WP}}(\mathbf{p})$ have a momentum-dependent term, one cannot destroy the Weyl point by small perturbations. One can consider, i.e., a magnetic field $\mathbf{B}$ which changes the Hamiltonian to

$$\hat{H}_{\mathrm{WP}}(\mathbf{p}) + \hat{H}_Z = (v\mathbf{p} + \mathbf{B}) \cdot \hat{\boldsymbol{\sigma}}. \tag{2.19}$$

One can immediately see that the magnetic field only shifts the Weyl point in momentum space without lifting the crossing. This demonstrates the topological protection of a single Weyl point.

Since the band structure of a WSM is gapless, one needs to define the topological invariant by the winding number around the Weyl point [29]. It can be determined by calculating the Berry curvature $\mathcal{F}_n(\mathbf{p})$ of $\hat{H}_{\mathrm{WP}}(\mathbf{p})$, given by [54]

$$\mathcal{F}_n(\mathbf{p}) = \nabla_{\mathbf{p}} \times \mathcal{A}_n(\mathbf{p}) = -\operatorname{Im}\left[\sum_{n' \neq n} \langle \nabla_{\mathbf{p}} n | n' \rangle \times \langle n' | \nabla_{\mathbf{p}} n \rangle\right], \tag{2.20}$$

where $\mathcal{A}_n(\mathbf{p}) = i \langle n | \nabla_{\mathbf{p}} | n \rangle$ is the Berry potential of a filled energy state $|n\rangle$. Applying the Nabla operator to the Schrödinger equation, one can find the identity

$$\langle n' | \nabla_{\mathbf{p}} \left[\hat{H} \,|n\rangle\right] = \langle n' | \nabla_{\mathbf{p}} [\epsilon_n \,|n\rangle] \tag{2.21}$$

$$\Rightarrow \langle n' | \nabla_{\mathbf{p}} \hat{H} | n \rangle + \langle n' | \hat{H} | \nabla_{\mathbf{p}} n \rangle = \epsilon_n \langle n' | \nabla_{\mathbf{p}} n \rangle \tag{2.22}$$

$$\Rightarrow \langle n' | \nabla_{\mathbf{p}} n \rangle = \frac{\langle n' | \nabla_{\mathbf{p}} \hat{H} | n \rangle}{\epsilon_n - \epsilon_{n'}}. \tag{2.23}$$

Combining Eqs. (2.20) and (2.23), one gets

$$\mathcal{F}_n(\mathbf{p}) = -\operatorname{Im}\left[\sum_{n' \neq n} \frac{\langle n | \nabla_{\mathbf{p}} \hat{H} | n' \rangle \times \langle n' | \nabla_{\mathbf{p}} \hat{H} | n \rangle}{(\epsilon_n - \epsilon_{n'})^2}\right]. \tag{2.24}$$

Therefore, the Weyl point, described by $\hat{H}_{\mathrm{WP}}(\mathbf{p})$, has the berry curvature

$$\mathcal{F}_{\mathrm{WP}}(\mathbf{p}) = v \frac{\mathbf{p}}{2|v\mathbf{p}|^3}. \tag{2.25}$$

By integrating around the Weyl point in the Brillouin zone, we find the chirality of the Weyl point

$$c = \operatorname{sgn}(v), \tag{2.26}$$

which can be either $+1$ or $-1$. Notice that it acts as a monopole charge of Berry flux. It is possible, that the projection on the surface leads to two distinct Weyl points at the same position in the surface Brillouin zone. This way, one can find a Weyl point with an effective chirality of $c = 0$ or $c = \pm 2$. In general, a Weyl point can only be destroyed by hybridization with another Weyl point of opposite chirality [15].

The Nielsen-Ninomiya theorem states that the sum of all Weyl point chiralities in a system must be zero [55, 56]. So, every Weyl point has a partner Weyl point with opposite chirality. The minimal number of Weyl points in a system is related to the system's symmetry. As discussed in Sec. 2.1, the band structure of a system with both TRS and inversion symmetry is double degenerate everywhere due to Kramers' theorem. Since Weyl points cannot be degenerate, a WSM can only exist if either TRS or inversion symmetry or both is broken.

While TRS and inversion symmetry cannot be present simultaneously, a WSM can conserve one of them. In this case, every Weyl point at $\mathbf{p}^W$ must have a symmetry partner Weyl point at $-\mathbf{p}^W$. From Eq. (2.12), we find that $\hat{H}_{\mathrm{WP}} =_{\mathcal{P}} -\hat{H}_{\mathrm{WP}}$ due to the sign flip in momentum but not in the spin. This means that inversion symmetry partner Weyl points have opposite chirality [16]. Therefore, an inversion symmetric WSM has a minimum of two Weyl points in the bulk. For TRS, Eq. (2.1) indicates that $\hat{H}_{\mathrm{WP}} =_{\mathcal{T}} \hat{H}_{\mathrm{WP}}$ due to a sign flip in both momentum and spin, which cancels in the low-energy Hamiltonian. Consequently, a Weyl point and its TRS partner always have the same chirality [57]. Since the sum of the chirality of all Weyl points needs to vanish, a WSM with TRS must have a minimum of four Weyl points in the bulk.

Let us consider a 3D bulk Brillouin zone as a series of effective 2D cuts. If the cut does not intersect one or more Weyl points, the 2D spectrum is gapped, which allows the association with a topological invariant. We illustrate this by taking the Weyl point Hamiltonian at a constant $p_z$ value

$$\hat{H}_{\mathrm{Ch}}(p_x, p_y, p_z = \frac{m}{v}) = v(p_x\hat{\sigma}_x + p_y\hat{\sigma}_y) + m\hat{\sigma}_z, \tag{2.27}$$

which resembles the Hamiltonian of a 2D Chern insulator [58, 59, 60]. Here it is well-known that the system is topologically non-trivial for $m < 0$. In a WSM, $m$ has different sign for 2D cuts on opposite sites of the Weyl point. This indicates a topological phase transition and the existence of topological surface states. So, the related quantum anomalous Hall effect is an essential feature of a WSM. The integral of a 2D cut with a single fixed momentum component $p$ is the Chern number, given by the integral over the Berry curvature [15]

$$C(p) = \int \frac{\mathrm{d}^2\mathbf{p}}{2\pi}\mathcal{F}(\mathbf{p}). \tag{2.28}$$

Consequently, one finds that the difference of the Chern numbers of two parallel 2D cuts is given by the sum of all chiralities of Weyl points in between

$$C(p_2) - C(p_1) = \sum_{p_1 < p_i < p_2} c(p_i). \tag{2.29}$$

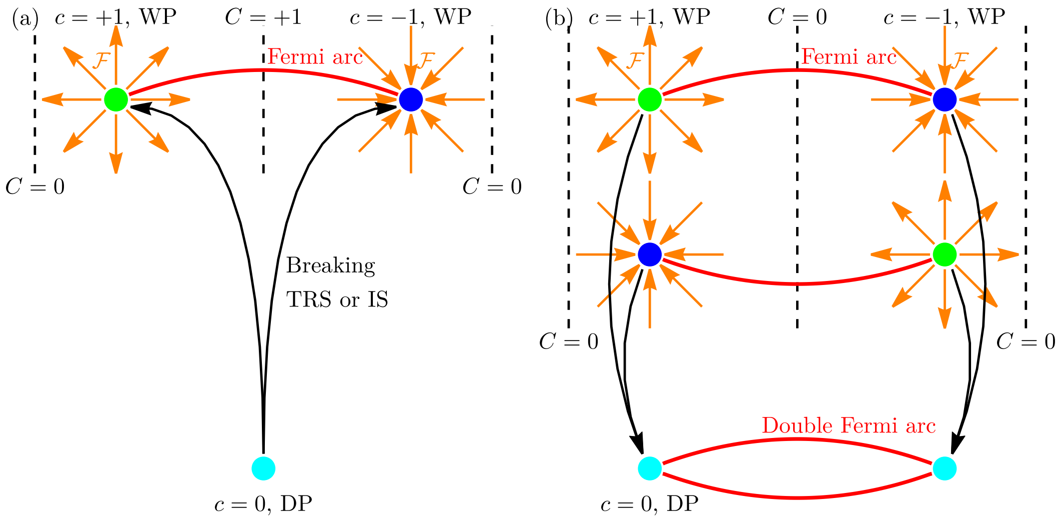

Figure 2.1: Conceptional illustration of a Dirac point (cyan), with chirality $c = 0$, splitting into two Weyl points (green, blue) with $c = \pm 1$. The chirality of the Weyl points is the monopole charge of Berry curvature $\mathcal{F}$ (orange arrows). The Chern numbers $C$ of the 2D cuts (dashed lines) in the Brillouin zone changes at a Weyl point by its chirality [see Eq. (2.29)]. The $C \neq 0$ in between two Weyl points with opposite $c$ indicates the existence of chiral surface states, which form a Fermi arc (red) connecting the Weyl points in the projected surface Brillouin zone. (a) Case, where two partner Weyl points merge into a Dirac point, destroying the Fermi arc. (b) Case of two non-partner Weyl points merging into a Dirac point, keeping the Fermi arcs intact and forming a double Fermi arc.

Since Weyl points always come in pairs of opposite chirality, one can always find a non-trivial topological phase between them. The surface state in this region is always chiral, indicating a crossing with the Fermi energy. Consequently, the Fermi surface of the surface states forms a single curve connecting two Weyl points with opposite chirality. This is called Fermi arc [16], which originates from a $c = +1$ Weyl point as the source and terminates at a $c = -1$ Weyl point as the sink (see

Fig. 2.1).

The existence of Fermi arcs is a unique feature of WSMs. Another compelling property is the chiral anomaly [17, 18], which states that a single Weyl point coupled to an electromagnetic field breaks the conservation of electric charge. This anomaly can only be resolved with the existence of a second Weyl point with opposite chirality, where the charge is pumped through the Fermi arcs by parallel magnetic and electric fields [61]. A further feature of the WSM is the negative magnetoresistance [62] which can be already derived in semiclassical kinetics.

In this thesis, we discuss the existence and evolution of the WSM phase in the Luttinger model, induced by compressive strain and inversion symmetry breaking, motivated by Ref. [63]. Our findings helped to explain an experiment, discussed by Ref. [19], on compressive strained HgTe with an inversion asymmetric lattice structure.

### 2.2.2 Dirac semimetals

The second kind of topological semimetals is the DSM, characterized by spin-degenerate gapless linear bulk nodes called Dirac points [11, 12, 13]. One can consider a Dirac point as the superposition of two Weyl points with opposite chirality. The most general low-energy Hamiltonian can be written as

$$\hat{H}_{\mathrm{DP}}(\mathbf{p}) = \begin{pmatrix} \hat{H}_{\mathrm{WP}}(\mathbf{p}) & m\hat{1}_2 \\ m\hat{1}_2 & -\hat{H}_{\mathrm{WP}}(\mathbf{p}) \end{pmatrix}, \tag{2.30}$$

where $m$ is the hybridization of both Weyl points. For $m \neq 0$, the Weyl points couple and open a gap. $\hat{H}_{\mathrm{DP}}$ resembles a general low-energy Hamiltonian of a 3D insulator, which is topologically trivial for $m > 0$ and non-trivial for $m < 0$.

The topological transition point arises for $m = 0$, where the gap closes, and both Weyl points are degenerate, leading to zero chirality (see Fig. 2.1). This degeneracy requires both TRS and inversion symmetry due to Kramers' theory. Since the topological invariant is zero, Dirac points are not topologically protected. Therefore

Dirac points are not stable against perturbations like magnetic fields.

One way to form a DSM is to induce a band-inversion in a system with multiple double degenerate bands without breaking TRS or inversion symmetry. An anti-crossing usually prevents the resulting fourfold degenerate crossing point. A DSM requires this accidental crossing to lie on a high symmetry line in the Brillouin zone [15]. The mechanism discussed in this thesis is applying compressive strain to a quadratic nodal semimetal. This moves the valence (conduction) band up (down) in energy, leading to two Dirac points at the Fermi energy [64]. Alternatively, a DSM can form by exploiting additional spatial symmetries of the lattice, which is not discussed here [65, 11, 66, 67].

Since a Dirac point can be understood as a superposition of two opposite chirality Weyl points, Fermi arcs can often form also in DSMs [15]. Let's consider a system with four Weyl points that form two pairs connected by Fermi arcs. Introducing TRS and inversion symmetry to the system leads to one of three cases: (1) All four Weyl points collapse into a single Dirac point, and (2) the Weyl points merge with their partner, destroying the Fermi arcs [see Fig. 2.1(a)], or (3) the Weyl points merge with another Weyl point, which is not connected via a Fermi arc [see Fig. 2.1(b)]. In the last case, the two Fermi arcs survive, leading to a double Fermi arc system [12, 68, 69].

Since the Dirac points have a trivial topological invariant, the double Fermi arcs are not protected. They can only exist if additional spatial symmetries are present. Therefore, double Fermi arcs are fragile surface states which can easily be decoupled from the singularities and deformed to a single point in momentum space by perturbation [70, 71].

In Sec. 3.6, we study the DSM phase in compressive strained Luttinger semimetals, which preserve inversion symmetry. The analysis in the framework of the more realistic Luttinger model allows for a description beyond the effective models used for DSMs and WSMs. This makes $\alpha$-Sn a prime candidate for future experiments related to our study [72]. Additionally, recent ARPES measurements confirmed the existence of a DSM phase in materials like $Na_3Bi$ [73, 74] and $Cd_3As_2$ [75, 76, 77].

## 2.3 Topological superconductivity

The mathematical field of topology proved itself to be valuable for solid-state physics. In this chapter, we discuss the concept of topological semimetals and hinted at interesting features of TIs. A third relevant application of topology are SCs, discussed in this work.

The concept of non-trivial topological SCs was first discussed by Read and Green [78] in 2D systems and Kitaev [79] in 1D wires. Since superconductivity demands the existence of PHS, the symmetry classes D and DIII (see Tab. 2.1) are most relevant to half-integer spin SCs. Both classes can be in a non-trivial topological phase in 1D and 2D. This is related to the non-abelian Majorana fermions, which form due to bulk-boundary correspondence.

In this section, we introduce the concept of superconductivity in the Bogoliubov-de Gennes (BdG) equation [80] and discuss the physical features of their characteristic states.

### 2.3.1 Superconducting pairing potential and the Bogoliubov-de Gennes equation

For a general introduction, we use the single-band effective Hamiltonian for a SC in second quantization [81, 35]

$$\mathcal{H} = \mathcal{H}_0 + \frac{1}{2} \sum_{\boldsymbol{p},\boldsymbol{p}',s_1,s_2,s_3,s_4} V_{s_1,s_2,s_3,s_4}(\boldsymbol{p},\boldsymbol{p}') c^\dagger_{-\boldsymbol{p},s_1} c^\dagger_{\boldsymbol{p},s_2} c_{\boldsymbol{p}',s_3} c_{-\boldsymbol{p}',s_4}, \tag{2.31}$$

$$\text{with} \quad \mathcal{H}_0 = \sum_{\boldsymbol{p},s_1,s_2} \mathcal{H}_{s_1,s_2}(\boldsymbol{p}) c^\dagger_{\boldsymbol{p},s_1} c_{\boldsymbol{p},s_2}. \tag{2.32}$$

Here $c_{\boldsymbol{p},s}$ ($c^\dagger_{\boldsymbol{p},s}$) is the annihilation (creation) operator of an electron with momentum $\boldsymbol{p}$ and spin $s =\uparrow,\downarrow$, following the fermionic anticommutation relations $\{c_n, c_m\} = \{c^\dagger_n, c^\dagger_m\} = 0$ and $\{c_n, c^\dagger_m\} = \delta_{nm}$. The term $\mathcal{H}_{s_1,s_2}(\boldsymbol{p})$ is the normal non-interacting Hamiltonian of the system, and $V_{s_1,s_2,s_3,s_4}(\boldsymbol{p},\boldsymbol{p}')$ is the pairing interaction of the particles. In a SC, Cooper pairs form from particles with opposite momentum [82], which leads to the two body operator $c_{\boldsymbol{p},s}c_{-\boldsymbol{p},s'}$ having a non-zero expectation value. Therefore, one can define the pair potential

$$\Delta_{s,s'}(\boldsymbol{p}) = -\sum_{\boldsymbol{p}',s_3,s_4} V_{s',s,s_3,s_4}(\boldsymbol{p},\boldsymbol{p}')\left\langle c_{\boldsymbol{p}',s_3}c_{-\boldsymbol{p}',s_4}\right\rangle. \tag{2.33}$$

Using the mean-field approximation [35], the Hamiltonian (2.31) simplifies to

$$\mathcal{H} = \mathcal{H}_0 + \frac{1}{2}\sum_{\boldsymbol{p},s_1,s_2}\Big[\Delta_{s_1,s_2}(\boldsymbol{p})c^\dagger_{\boldsymbol{p},s_1}c^\dagger_{-\boldsymbol{p},s_2} + \text{h.c.}\Big]. \tag{2.34}$$

It is convenient to rewrite the first term to only sum over positive momenta. Using the fermionic anticommutation relation, we get

$$\mathcal{H}_0 = \sum_{\boldsymbol{p}>0,s_1,s_2}\Big[\mathcal{H}_{s_1,s_2}(\boldsymbol{p})c^\dagger_{\boldsymbol{p},s_1}c_{\boldsymbol{p},s_2} - \mathcal{H}^*_{s_1,s_2}(-\boldsymbol{p})c_{-\boldsymbol{p},s_2}c^\dagger_{-\boldsymbol{p},s_1} + \mathcal{H}_{s_1,s_2}(-\boldsymbol{p})\Big], \tag{2.35}$$

where the constant last term is only an energy shift, which will be neglected. The complex conjugation in the second term comes from the interchange of the operators and the Hamiltonian's hermicity. One can rewrite the total Hamiltonian into a matrix form

$$\mathcal{H} = \frac{1}{2}\sum_{\boldsymbol{p},s_1,s_2}\begin{pmatrix}c^\dagger_{\boldsymbol{p},s_1}, c_{-\boldsymbol{p},s_1}\end{pmatrix}\hat{H}_0(\boldsymbol{p})\begin{pmatrix}c_{\boldsymbol{p},s_2}\\ c^\dagger_{-\boldsymbol{p},s_2}\end{pmatrix} \tag{2.36}$$

$$\text{with}\quad \hat{H}_0(\boldsymbol{p}) = \begin{pmatrix}\mathcal{H}_{s_1,s_2}(\boldsymbol{p}) & \Delta_{s_1,s_2}(\boldsymbol{p})\\ \Delta^\dagger_{s_1,s_2}(\boldsymbol{p}) & -\mathcal{H}^*_{s_1,s_2}(-\boldsymbol{p})\end{pmatrix}. \tag{2.37}$$

The Hilbert space is now effectively doubled, which means that $\hat{H}_0(\boldsymbol{p})$ acts on wave functions whose first half is composed of annihilation operators of electrons. The second half is built from creation operators of the same electron. Therefore, $\hat{H}_0(\boldsymbol{p})$ automatically has PHS, which exchanges electrons and holes. Here, the PHS operator is given by $\hat{\mathcal{C}} = \hat{\tau}_x\mathcal{K}$, where the Pauli matrix $\hat{\tau}_x$ acts on the particle and hole blocks and $\mathcal{K}$ is the complex conjugation operator. The PHS relation indicates that for a given state with energy

$$\hat{H}_0(\boldsymbol{p})\begin{pmatrix}u_s(\boldsymbol{p})\\ v^*_s(-\boldsymbol{p})\end{pmatrix} = E(\boldsymbol{p})\begin{pmatrix}u_s(\boldsymbol{p})\\ v^*_s(-\boldsymbol{p})\end{pmatrix}, \tag{2.38}$$

a particle-hole symmetric partner state exists with negative energy

$$\hat{\mathcal{C}}\hat{H}_0(\boldsymbol{p})\hat{\mathcal{C}}^{-1}\hat{\mathcal{C}}\begin{pmatrix} u_s(\boldsymbol{p}) \\ v_s^*(-\boldsymbol{p}) \end{pmatrix} = -\hat{H}_0(-\boldsymbol{p})\begin{pmatrix} v_s(-\boldsymbol{p}) \\ u_s^*(\boldsymbol{p}) \end{pmatrix} = -E(-\boldsymbol{p})\begin{pmatrix} v_s(-\boldsymbol{p}) \\ u_s^*(\boldsymbol{p}) \end{pmatrix}. \tag{2.39}$$

Taking the basis of the eigenvectors, one can diagonalize the Hamiltonian via

$$\hat{U}^\dagger(\boldsymbol{p})\hat{H}_0(\boldsymbol{p})\hat{U}(\boldsymbol{p}) = \mathrm{diag}[E_1(\boldsymbol{p}), E_2(\boldsymbol{p}), -E_1(-\boldsymbol{p}), -E_2(-\boldsymbol{p})], \tag{2.40}$$

$$\text{with} \quad \hat{U}(\boldsymbol{p}) = \begin{pmatrix} u_s^{(i)}(\boldsymbol{p}) & v_s^{(i)}(\boldsymbol{p}) \\ v_s^{(i)*}(-\boldsymbol{p}) & u_s^{(i)*}(-\boldsymbol{p}) \end{pmatrix}, \tag{2.41}$$

$i \in \{1, 2\}$, and $E_i(\boldsymbol{p}) \geq 0$. Taking Eq. (2.40), we can write the total Hamiltonian in the diagonal form

$$\mathcal{H} = \sum_{\boldsymbol{p},i} E_i(\boldsymbol{p})\alpha^\dagger_{\boldsymbol{p},i}\alpha_{\boldsymbol{p},i}, \tag{2.42}$$

$$\text{where} \quad \alpha_{\boldsymbol{p},i} = \sum_s \left[u_s^*(\boldsymbol{p})c_{\boldsymbol{p},s} + v_s(-\boldsymbol{p})c^\dagger_{-\boldsymbol{p},s}\right] \tag{2.43}$$

is the operator for the so-called Bogoliubov quasi-particles, which satisfy the fermionic anticommutation relations. The excitation energy $E_i(\boldsymbol{p})$ separates the Cooper pair into a quasi-electron and a quasi-hole.

It is important to note that each element of $\hat{H}_0(\boldsymbol{p})$ is a $2N \times 2N$ matrix, where $N$ is the number of orbitals in the system, which have a spin $(=\uparrow, \downarrow)$ degree of freedom. Therefore, the basis vector $(c^\dagger_{\boldsymbol{p},s_1}, c_{-\boldsymbol{p},s_1})$ is a $4N$ component vector $(c^\dagger_{\boldsymbol{p},1}, \dots, c^\dagger_{\boldsymbol{p},2N}, c_{-\boldsymbol{p},1}, \dots, c_{-\boldsymbol{p},2N})$. The general Hamiltonian can finally be written with the BdG Hamiltonian [80]

$$\mathcal{H} = \frac{1}{2}\sum_{\boldsymbol{p},n_1,n_2} \left(c^\dagger_{\boldsymbol{p},n_1}, c_{-\boldsymbol{p},n_1}\right)\hat{H}_{\mathrm{BdG}}(\boldsymbol{p})\begin{pmatrix} c_{\boldsymbol{p},n_2} \\ c^\dagger_{-\boldsymbol{p},n_2} \end{pmatrix}, \tag{2.44}$$

$$\text{with} \quad \hat{H}_{\mathrm{BdG}}(\boldsymbol{p}) = \begin{pmatrix} \hat{H}_{n_1,n_2}(\boldsymbol{p}) & \Delta_{n_1,n_2}(\boldsymbol{p}) \\ \Delta^\dagger_{n_1,n_2}(\boldsymbol{p}) & -\hat{H}^*_{n_1,n_2}(-\boldsymbol{p}) \end{pmatrix}, \tag{2.45}$$

$n_{1,2} = 1, \dots, 2N$, and $\hat{H}_{n_1,n_2}(\boldsymbol{p})$ is the usual Bloch Hamiltonian taken relative to the chemical potential. Using the BdG Hamiltonian, we can now describe superconducting states in any material, either a SC by itself or one with induced superconductivity by the proximity effect [83, 84].

In general, Cooper pairs are formed by pairs of half-spin particles. Therefore, the total angular momentum $l$ of a Cooper pair is an integer, which can either be even ($l \in \{0, 2, 4, \ldots\}$) or odd ($l \in \{1, 3, 5, \ldots\}$). Consequently, the corresponding pairing potentials need to have either even or odd parity to conserve inversion symmetry in the system. In analogy to atomic orbitals, the Cooper pairs are labeled as $s$-wave ($l = 0$), $p$-wave ($l = 1$), $d$-wave ($l = 2$), and so on. This work focuses on $s$-wave superconductivity, where the Cooper pairs are formed only between between particles with opposite spins.

When there is only $s$-wave superconducting coupling, it is often convenient to introduce a basis transformation using the TRS operator $\hat{\mathcal{T}} = \hat{U}_{\mathcal{T}}\mathcal{K}$. Applying the unitary part of the operator $\hat{U}_{\mathcal{T}}$ to the quasi-holes allows us to rewrite the Hamiltonian as

$$\mathcal{H} = \frac{1}{2} \sum_{\boldsymbol{p}, n_1, n_2} \left( c^\dagger_{\boldsymbol{p}, n_1}, c_{-\boldsymbol{p}, n_1} \hat{U}^\dagger_{\mathcal{T}} \right) \begin{pmatrix} \hat{H}_{n_1, n_2}(\boldsymbol{p}) & \Delta_{n_1, n_2}(\boldsymbol{p}) \hat{U}^\dagger_{\mathcal{T}} \\ \hat{U}_{\mathcal{T}} \Delta^\dagger_{n_1, n_2}(\boldsymbol{p}) & -\hat{\mathcal{T}} \hat{H}_{n_1, n_2}(-\boldsymbol{p}) \hat{\mathcal{T}}^{-1} \end{pmatrix} \begin{pmatrix} c_{\boldsymbol{p}, n_2} \\ \hat{U}_{\mathcal{T}} c^\dagger_{-\boldsymbol{p}, n_2} \end{pmatrix}. \tag{2.46}$$

This new basis has a couple of benefits: First, an $s$-wave superconducting coupling term $\Delta(\boldsymbol{p})$ is now proportional to the unit matrix. Also, every TRS conserving term is proportional to $\hat{\tau}_z$ and every TRS breaking term to $\hat{\tau}_0$. As a drawback, the PHS and TRS operators change in the new basis to be $\hat{\mathcal{C}} = -i\hat{\tau}_y \hat{U}_{\mathcal{T}} \mathcal{K}$ and $\hat{\mathcal{T}} = \hat{\tau}_y \hat{1} \mathcal{K}$.

### 2.3.2 Majorana bound states and non-abelian statistics

One of the most characteristic features of topological SCs is the existence of MBSs. Its concept first appeared when Majorana found in 1937 [20] that the Dirac equation has a solution that describes a particle identical to its antiparticle. The Dirac equation describes the relativistic motion of particles and reads [85]

$$i\frac{\hbar}{c}\partial_t \Psi(\boldsymbol{r}, t) = \left[ -i\hbar \hat{\boldsymbol{\alpha}} \cdot \boldsymbol{\partial}_{\boldsymbol{r}} + \hat{\beta} mc \right] \Psi(\boldsymbol{r}, t). \tag{2.47}$$

Here, $m$ is the mass of a particle, and $c$ is the speed of light. The $4 \times 4$ matrices $\hat{\boldsymbol{\alpha}} = (\hat{\alpha}_1, \hat{\alpha}_2, \hat{\alpha}_3)^T$ and $\hat{\beta}$ can be chosen freely, as long as the relations

$$\{\hat{\alpha}_i, \hat{\alpha}_j\} = 2\delta_{ij}, \quad \left\{\hat{\alpha}_i, \hat{\beta}\right\} = 0, \quad \hat{\beta}^2 = \hat{1}_4, \tag{2.48}$$

with $\{A, B\} = AB + BA$ being the anti-commutator, are satisfied. Therefore, we can take

$$\hat{\alpha}_1 = \hat{\nu}_x \hat{\sigma}_x, \quad \hat{\alpha}_2 = \hat{\nu}_x \hat{\sigma}_z, \quad \hat{\alpha}_3 = \hat{\nu}_z \hat{\sigma}_0, \text{ and } \quad \hat{\beta} = \hat{\nu}_x \hat{\sigma}_y, \tag{2.49}$$

which are tensor products of two sets of Pauli matrices $\hat{\nu}_i$ and $\hat{\sigma}_i$. This basis satisfies all conditions of Eq. (2.48) and gives purely real $\hat{\boldsymbol{\alpha}}^* = \hat{\boldsymbol{\alpha}}$ and an imaginary $\hat{\beta}^* = -\hat{\beta}$ [35]. It follows that the complex conjugate of the Dirac equation (2.47) takes the shape

$$i\frac{\hbar}{c}\partial_t \Psi^*(\boldsymbol{r}, t) = \left[-i\hbar\hat{\boldsymbol{\alpha}} \cdot \boldsymbol{\partial_r} + \hat{\beta} mc\right]\Psi^*(\boldsymbol{r}, t), \tag{2.50}$$

which means that the particle $\Psi$ and the antiparticle $\Psi^*$ satisfy the same Dirac equation. The resulting real field $\Psi$, which describes its own antiparticle, is today called Majorana fermion ($\gamma = \gamma^\dagger$). In general, Majorana fermions appear in high-energy particle physics, but recently topological SCs have been considered to host them as well [86]. One case discussed in this thesis is the formation of MBSs as zero energy solutions of the BdG-equation at the ends of topologically SC wires (see Sec. 2.3.4).

Majorana fermions give rise to exciting features, like its non-abelian statistics or the prospect of topological quantum computation. Let us consider a solution for a Majorana fermion with

$$\gamma_1 = c^\dagger + c \quad \text{and} \quad \gamma_2 = i\left(c^\dagger - c\right), \tag{2.51}$$

where $c^{(\dagger)}$ denotes annihilation (creation) operators of an electron with the reciprocal relations

$$c = \frac{1}{2}(\gamma_1 + i\gamma_2) \quad \text{and} \quad c^\dagger = \frac{1}{2}(\gamma_1 - i\gamma_2). \tag{2.52}$$

The fermionic operators satisfy the relations

$$\{c_i, c_j\} = \left\{c_i^\dagger, c_j^\dagger\right\} = 0, \quad \left\{c_i, c_j^\dagger\right\} = \delta_{ij}, \quad \text{and} \quad \{\gamma_i, \gamma_j\} = 2\delta_{ij}. \tag{2.53}$$

The $c$ operator rotates with a shift of superconducting phase $\phi$ by $\phi/2$: $c \to e^{i\phi/2}c$ and $c^\dagger \to e^{-i\phi/2}c^\dagger$. Therefore, the Majorana fermion transforms accordingly with $\gamma \to e^{-i\phi/2}c^\dagger + e^{i\phi/2}c$. From this, one can see that an entire evolution of $\phi \to \phi + 2\pi$ leads to a sign change in the Majorana zero mode $\gamma \to -\gamma$ [87, 88].

This sign change has unique consequences under the braiding of multiple Majorana modes. Having a system of $2N$ Majorana fermions, one can define an exchange operation for neighboring particles. The braid operation $T_i$ interchanges the Majoranas $\gamma_i$ and $\gamma_{i+1}$ ($i = 1, \dots, 2N-1$) leading to

$$T_i\colon \quad \begin{cases} \gamma_i \to \gamma_{i+1} \\ \gamma_{i+1} \to -\gamma_i \\ \gamma_j \to \gamma_j \end{cases} \qquad \text{for} \quad j \neq i \text{ and } j \neq i+1. \tag{2.54}$$

A series of braid operations form a braid group $\mathbf{B}_{2N}$ [89]. The basic operations in this group can always be reduced to the sequential application of two braid operations, which satisfy the relations

$$T_i T_j = T_j T_i, \quad \text{for} \quad |i-j| > 1, \tag{2.55}$$

$$T_i T_j T_i = T_j T_i T_j, \quad \text{for} \quad |i-j| = 1. \tag{2.56}$$

One finds the representation for the braid operator [87, 90]

$$\hat{B}_{i+1,i} = \frac{1}{\sqrt{2}}(1 + \gamma_{i+1}\gamma_i), \tag{2.57}$$

where $\gamma_j \to \hat{B}_{i+1,i}\gamma_j\hat{B}^\dagger_{i+1,i}$ with $j \in \{i, i+1\}$ describes the clockwise exchange of two neighboring Majoranas. This exchange operation results in $\gamma_i \to \gamma_{i+1}$ and $\gamma_{i+1} \to -\gamma_i$. Two Majorana modes form a Majorana fermion, which acts on the fermionic number state as ladder operators via

$$c\,|1\rangle = \frac{\gamma_1 + i\gamma_2}{2}\,|1\rangle = |0\rangle \quad \text{and} \quad c^\dagger\,|0\rangle = \frac{\gamma_1 - i\gamma_2}{2}\,|0\rangle = |1\rangle\,. \tag{2.58}$$

We expect the braid operator to leave the eigenvalue of the number operator unchanged. It acts on the number states by multiplication with a phase

$$\hat{B}_{12}\,|0\rangle = \frac{1}{\sqrt{2}}(1+i)\,|0\rangle \quad \text{and} \quad \hat{B}_{12}\,|1\rangle = \frac{1}{\sqrt{2}}(1-i)\,|1\rangle\,. \tag{2.59}$$

To highlight the non-trivial features of the non-abelian statistics, we consider a system of at least four Majorana states, described by two number states $|n_1 n_2\rangle$. As expected, a braid operation with two Majorana states of the same fermion has a trivial effect

$$\hat{B}_{12}\,|0n_2\rangle = \frac{1}{\sqrt{2}}(1+i)\,|0n_2\rangle\,, \qquad \hat{B}_{12}\,|1n_2\rangle = \frac{1}{\sqrt{2}}(1-i)\,|1n_2\rangle\,, \tag{2.60}$$

$$\hat{B}_{34}\,|n_1 0\rangle = \frac{1}{\sqrt{2}}(1+i)\,|n_1 0\rangle\,, \qquad \hat{B}_{34}\,|n_1 1\rangle = \frac{1}{\sqrt{2}}(1-i)\,|n_1 1\rangle\,. \tag{2.61}$$

This can easily be understood because one fermion is not affected by the exchange of two states in a different fermion. More interesting is the braid operation of two Majorana states of separate fermions. One finds [90]

$$\hat{B}_{23}\,|00\rangle = \frac{1}{\sqrt{2}}(|00\rangle + i\,|11\rangle), \qquad \hat{B}_{23}\,|11\rangle = \frac{1}{\sqrt{2}}(|11\rangle - i\,|00\rangle), \tag{2.62}$$

$$\hat{B}_{23}\,|01\rangle = \frac{1}{\sqrt{2}}(|01\rangle + i\,|10\rangle), \qquad \hat{B}_{23}\,|10\rangle = \frac{1}{\sqrt{2}}(|10\rangle - i\,|01\rangle), \tag{2.63}$$

which conserves the total parity of the system since $n_1 + n_2$ stays either even or odd. This indicates that the Majorana fermions can considerably impact the realization of fault-tolerant quantum computation [22]. Here one can, i.e., consider the states $|00\rangle$ and $|11\rangle$ as two levels of a qubit. Exchanging two states of different fermions $\hat{B}_{23}$ entangles the two configurations of the qubit and acts as a Hadamard gate, essential to quantum computation.

The non-abelian nature of the Majorana fermions comes from the commutator relations of the braid operators. As expected, two operators commute if different fermions are involved ($[\hat{B}_{i-1,i}, \hat{B}_{i+2,i+1}] = 0$). Although, if the same Majorana fermion is involved, one gets the non-abelian statistics

$$\left[\hat{B}_{i-1,i}, \hat{B}_{i,i+1}\right] = \gamma_{i-1}\gamma_{i+1}. \tag{2.64}$$

In general, the clockwise exchange of two Majorana vertices can not be performed in 1D. Hence, the non-abelian representation of the braid group $\mathbf{B}_{2N}$ can only exist in 2D [91]. Different devices are exploited to achieve non-trivial braiding in 1D systems, like topological superconducting wires. Here, one can consider sequences of T-shaped junctions to allow a step-wise exchange of Majorana modes at the ends of the wires [92, 90, 93, 94, 95].

### 2.3.3 Andreev bound states in Josephson junctions

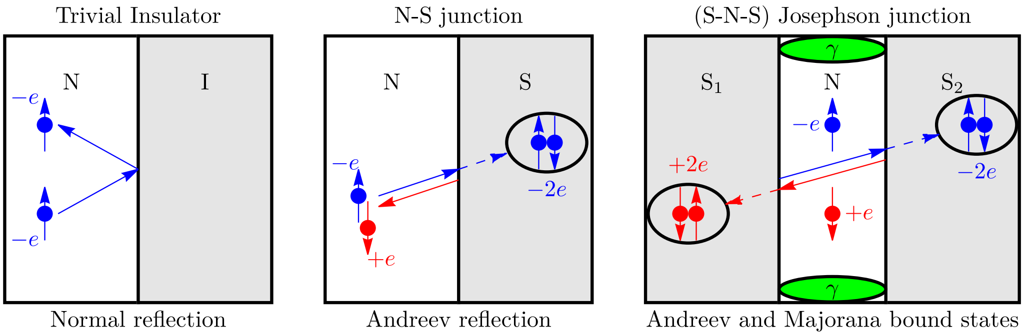

Figure 2.2: Schematic presentation of the concept of Andreev reflection and the formation of Andreev and Majorana bound states. (left) Usual junction of a normal conductor (N) and a trivial insulator (I), where an incoming electron (blue) with charge $-e$ is normally reflected at the interface. After reflection, the electron is preserving its charge and spin (indicated by the arrows). (middle) Junction of a normal conductor with an $s$-wave superconductor (S), termed N-S junction. At the interface, an incoming electron with charge $-e$ is Andreev reflected and becomes a hole (red) with charge $+e$ and opposite spin. Consequently, a cooper pair with charge $-2e$ is formed in the S region by two electrons with opposite spins. (right) The sandwich structure of two $s$-wave superconductors ($S_1$ and $S_2$) with a normal conductor as a barrier is termed Josephson junction. Here, Andreev reflection occurs at both N-S interfaces, which leads to the formation of a confined state in the N region, called Andreev bound state. In this setup, the Andreev bound states act as a quasi-1D superconducting state, which can host Majorana bound states $\gamma$ at the boundaries (green region) in a non-trivial topological phase [96, 25].

To understand the concept of ABSs, let us first consider a trivial reflection of an electron in a normal lead (N in Fig. 2.2) at an interface with a trivial insulator (I in Fig. 2.2) or vacuum. The initial trajectory is described with the velocity vector $\boldsymbol{v} = (v_x, v_y)^T$ and the electron has the charge $-e$ and spin $\sigma$. After the reflection, the velocity parallel to the interface $v_y$ is conserved, and the perpendicular component

$v_x$ is inverted $\boldsymbol{v} \to \hat{\boldsymbol{v}} = (-v_x, v_y)^T$. During the reflection, the electron's charge and spin stay unchanged.

In contrast, if the electron scatters at an interface with an $s$-wave SC (S in Fig. 2.2), the overall reflection process changes drastically. An incoming electron with spin $\sigma$ can couple with another electron with opposite spin $-\sigma$ and form a cooper pair in the S region. The Cooper pair has a combined charge of $-2e$ and moves through the SC. To preserve total charge, spin, and momentum, a hole with charge $+e$ and spin $-\sigma$ is emitted with the trajectory $-\boldsymbol{v}$. One can consider this as a single reflection process, called Andreev reflection [97], at the superconducting gap, where an incoming electron is reflected as an outgoing hole with an opposite spin. In a realistic system, Andreev reflection and normal reflection can occur simultaneously if the chemical potential is not much larger than the superconducting potential ($\mu \not\gg \Delta$).

Throughout this work, we consider a Josephson junction setup, which is a finite N region sandwiched between two SCs (see right panel of Fig. 2.2). Here, one has two N-S interfaces, where Andreev reflection can happen. This way, a right-moving electron with spin $\sigma$ gets Andreev reflected at the right N-S interface, which results in a left-moving hole with spin $-\sigma$. This hole gets Andreev reflected on the left N-S interface, giving a right-moving electron with spin $\sigma$. This sequence repeats indefinitely, which results in a bound state in the N region of the junction. This localized state is called ABS.

Usually, the N region of a Josephson junction is narrow. Therefore, one can consider the ABSs as the bulk states of a quasi-1D wire of a perpendicular orientation. It was found that these states can host a topological phase, where MBSs form at the ends of the N region (see green areas in Fig. 2.2) [23, 24, 25]. In Sec. 4.6, we discuss these states in a Luttinger Josephson junction in 2D.

### 2.3.4 Majorana bound states in a superconducting Rashba wire

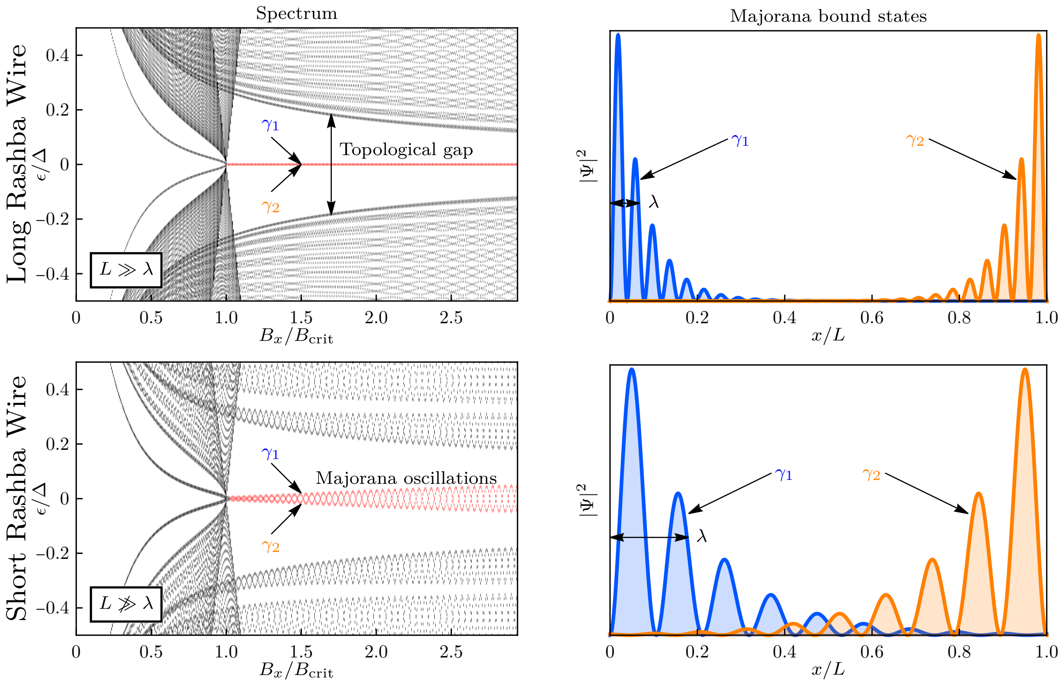

Figure 2.3: band structure of a 1D superconducting Rashba wire with finite length $L$, described by the Hamiltonian of Eq. (2.65). Beyond the critical magnetic field $B_{\text{crit}} = \sqrt{\Delta^2 + \mu^2}$ [Eq. (2.69)], the system is in a non-trivial topological phase with a topological gap opening due to the Rashba spin-orbit coupling ($\boldsymbol{n}_{\text{Rashba}} \perp \boldsymbol{n}_Z$). Majorana bound states ($\gamma_1$ and $\gamma_2$) form around zero energy, indicated in red. We compare the difference between a long wire, where $L$ is much larger than the localization length of the Majorana bound state $\lambda$, and a short wire, where the wavefunctions of the states overlap in the middle. The right column shows a schematic sketch of the localized wavefunctions of both bound states, indicating the finite overlap, which leads to hybridization and the so-called Majorana oscillations in the spectrum [98]. We used parameters characteristic of HgTe quantum wells $m = 0.038 m_0/\hbar^2$, $\alpha = 16$meVnm, $\mu = 5$meV, and $\Delta = 1$meV [25].

The realization of topological superconductors is a highly desired goal due to the rich physical properties of MBSs (see Sec. 2.3.2). Since the discussion of $p$-wave superconducting Kitaev chains [79], different systems have been considered. Intuitively, driving non-trivial topological materials into a superconducting phase is a promising approach. Hence, the behavior of Cooper pairs in TIs [99, 100, 101, 102, 103], WSMs [104, 105, 106], and DSMs [107, 108] are of wide interest in recent studies. Sato et al. showed in 2009 [21] that even ordinary electrons with a quadratic energy dispersion can achieve topological superconductivity under a specific combination of a Zeeman and Rashba SOC field. This section shows the formation of MBSs in 1D superconducting Rashba wires.

Using the Nambu basis $(c_\uparrow, c_\downarrow, c_\downarrow^\dagger, -c_\uparrow^\dagger)$, the BdG Hamiltonian is given by [21, 109, 110]

$$\hat{H}_{\mathrm{R,W}}(\boldsymbol{p}) = \hat{\tau}_z \left[ \frac{p_x^2}{2m} \hat{1}_2 + \alpha p_x \hat{\sigma}_y - \mu \right] + \hat{\tau}_x \Delta_s + B_x \hat{\sigma}_x. \tag{2.65}$$

Here, $m$ is the effective mass, $\alpha$ is the strength of the Rashba SOC, $\mu$ is the chemical potential, $\Delta_s$ is the proximitized $s$-wave pairing potential, and $B_x$ is an applied Zeeman field in $x$-direction parallel to the wire. Without superconductivity ($\Delta_s = 0$), the dispersion of the quasi-electrons in the Rashba wire has the form

$$\varepsilon_\pm^{\mathrm{R,W}}(p_x) = \frac{p_x^2}{2m} - \mu \pm \sqrt{B_x^2 + \alpha^2 p_x^2}. \tag{2.66}$$

From this, one can see that the Rashba SOC term without magnetic field ($B_x = 0$) lifts the spin degeneracy of the parabolic band. This leads to two parabolas, which are shifted in momentum by $\pm p_{\mathrm{SO}} = \pm \alpha m$ and in energy by $\epsilon_{\mathrm{SO}} = -m\alpha^2/2$. Without mixing the spins, the two parabolas cross at $p = 0$, giving a spin degeneracy at this point. A finite magnetic field introduces such spin mixing, removing the degeneracy and opening a gap of size $2B_x$.

Therefore a small chemical potential ($|\mu| < |B_x|$) will only leave the $\varepsilon_-^{\mathrm{R,W}}$ states around the Fermi energy since the $\varepsilon_+^{\mathrm{R,W}}$ are moved up by the Zeeman field. This way, the proximitized $s$-wave coupling leads to the formations of Cooper pairs, which are effectively spinless. Projecting the Hamiltonian from Eq. (2.65) onto the low energy states $c_-$ gives the effective Hamiltonian

$$\mathcal{H}_p = \sum_{p_x} \left[ \varepsilon_-^{\mathrm{R,W}}(p_x) c_-^\dagger(p_x) c_-(p_x) + \Delta_p(p_x) c_-^\dagger(p_x) c_-^\dagger(-p_x) + \mathrm{H.c.} \right], \tag{2.67}$$

where $\Delta_p(p_x) = i\alpha p_x \Delta_s / \sqrt{B_x^2 + \alpha^2 p_x^2}$ is a superconducting coupling term with $p$-wave symmetry $[\Delta_p(p_x) = -\Delta_p(-p_x)]$ [109, 98]. This effective Hamiltonian resembles the $p$-wave Kitaev chain, which was predicted to host MBSs in the topologically non-trivial regime [79].

The existence of topologically protected states at the ends of the wire demands a non-trivial topological invariant. Hence, one can look for a topological transition given by a band inversion in the bulk states. We take the Hamiltonian $\hat{H}^{\mathrm{R,W}}$ at $p_x = 0$ and find the energy

$$\varepsilon_\pm^{\mathrm{R,W}}(p_x = 0) = \tau \left[ \sqrt{\Delta^2 + \mu^2} \pm B_x \right], \tag{2.68}$$

where $\tau = \pm 1$ refers to the quasi-particle and hole states. We see a critical magnetic field, where the bands cross at zero energy, and the gap is inverted. This critical field is given by

$$B_{\mathrm{crit}}^2 = \Delta^2 + \mu^2. \tag{2.69}$$

We find that the gap inversion at $B_{\mathrm{crit}}$ is related to a topological phase transition, with a non-trivial topological invariant ($\mathcal{Q} = -1$) for $B_x > B_{\mathrm{crit}}$ (see Sec. 4.2 for details).

According to the bulk boundary correspondence, a non-trivial topology induces the existence of localized states at the boundary of the system. We calculate the spectrum of $\hat{H}^{\mathrm{R,W}}(p_x \to -i\partial_x)$ [Eq. (2.65)], discretized on a finite chain depicted in Fig. 2.3. We notice that the bulk states undergo a gap inversion at $B_x = B_{\mathrm{crit}}$, and a localized state forms at each end of the wire in the topological gap for $B_x > B_{\mathrm{crit}}$. We identify this state as the MBS ($\gamma_1$ and $\gamma_2$), which has a finite localization length $\lambda$ proportional to the inverse of the topological gap.

The right column of Fig. 2.3 illustrates a schematic sketch of the wavefunctions of the MBSs. In long Rashba wires with $L \gg \lambda$, the wavefunction of $\gamma_1$ has no overlap with $\gamma_2$, leading to no hybridization between the two end states. Consequently, the MBSs are degenerate at zero energy. If the wire is short ($L \not\gg \lambda$), the boundary states overlap, giving a finite hybridization between $\gamma_1$ and $\gamma_2$. This lifts the states' degeneracy, which shift to finite energies, which oscillate around $\epsilon = 0$ with the magnetic field. This behavior is called Majorana oscillations [98].

### 2.3.5 Majorana bound states in 2DEG Josephson junctions

Realizing a 1D chain of atoms is a challenging task for experimental groups due to their susceptibility to defects. Hence, considering a 2D setup is more appealing to realize in the laboratory. Here, we take the Josephson junction setup, where a normal conducting barrier separates two SCs. It is named after Brian David Josephson, who received the Nobel prize for the prediction of superconducting Cooper pair tunneling through a barrier [111].

In this section, we briefly introduce the latest research in planar Josephson junctions modeled by a 2DEG with Rashba and Dresselhaus SOC, discussed in Refs. [23, 24, 25]. For this discussion, we focus on Rashba SOC only, described by the Hamiltonian

$$\begin{aligned}\hat{H}^{\mathrm{R,JJ}}(x,p_y) = \hat{\tau}_z &\left[\frac{\hat{p}_x^2 + p_y^2}{2m} + \alpha(\hat{p}_x\hat{\sigma}_y - p_y\hat{\sigma}_x) + \frac{1}{2}m\alpha^2 - \mu\right] \\ &+ [V_0\hat{\tau}_z - B_x\hat{\sigma}_x - B_y\hat{\sigma}_y]h(x) + \Delta(x)[\hat{\tau}_x\cos\phi(x) - \hat{\tau}_y\sin\phi(x)], \quad (2.70)\end{aligned}$$

where $\hat{p}_x = -i\partial_x$ is the momentum operator, $m$ is the effective mass, $\alpha$ is the strength of the Rashba SOC, $\mu$ is the chemical potential, $V_0$ is the chemical potential mismatch between the N and S regions, $(B_x, B_y)$ is the magnetic field in the $(x, y)$-direction, and $\Delta(x) = \Delta\Theta(|x| - W/2)$ is the $s$-wave superconducting potential with a given phase $\phi(x) = \mathrm{sgn}(x)\phi/2$ [see Fig. 4.1(b)]. Here, $\hat{\tau}$ and $\hat{\sigma}$ are two sets of Pauli matrices, where $\hat{\tau}$ acts on the partice-hole degree of freedom and $\hat{\sigma}$ acts on the spin.

As mentioned in Sec. 2.3.3 one can find subgap ($|\epsilon| < |\Delta|$) ABS, confined to the N region of the junction. For a Josephson junction with infinite length $L$ perpendicular to the supercurrent [see Fig. 4.1(b)], $p_y$ is a good quantum number, giving the ABS a dispersion. It was found that a combination of perpendicular magnetic and SOC fields leads to a topological gap for all $p_y$ in the ABS spectrum.

Following Sec. 2.1, one can associate a topological invariant to this regime, which can either be trivial or non-trivial. Illustrating the topological gap as a function of $B_y$ and $\phi$ shows a diamond-shaped structure where the gap is closed [see Fig. 2.4(a)]. This is a critical phase transition, which inverts the gap and converts the system from trivial to topological. If the magnetic field deviates from the perpendicular direction to the SOC field ($B_x \neq 0$), the topological gap decreases or vanishes [25]. In the Luttinger Josephson junctions analyzed in Sec. 4.6, we use $B_x$ instead of $B_y$ due to the different nature of the SOC.

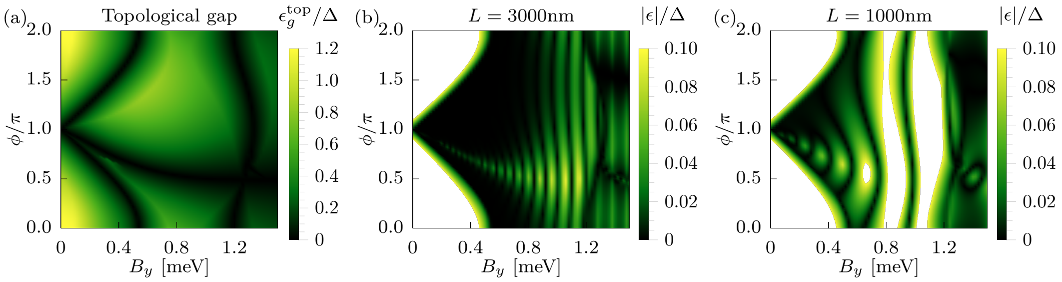

Figure 2.4: Josephson junction setup of a 2D Rashba model [Eq. (2.70)]. (a) Topological gap $E_g^{\text{top}} = \min_{p_y} E_g(p_y)$ of the Andreev bound states for a junction with infinite length ($L \to \infty$). (b, c) Absolute value of the lowest energy state in the junction with finite $L$, where the black regions correspond to the existence of zero energy Majorana bound states. Due to the finite localization length of the boundary states, Majorana oscillation increases with smaller $L$. The white regions correspond to energies exceeding the scale ($|E| > 0.1\Delta$). We use the parameters from Ref. [25], $m = 0.038 m_0/\hbar^2$, $W = 100$nm, $W_S = 450$nm, $\alpha = 16$meVnm, $\mu = 1$meV, $V_0 = 0.3$meV, $\Delta = 0.25$meV.

From the bulk-boundary correspondence, we expect the existence of topologically protected boundary states inside the diamond. Solving the BdG equation for a Josephson junction with finite $L$ shows the formation of MBSs at the ends of the N region [see Fig. 2.2(c)]. The lowest energy states as a function of $B_y$ and $\phi$ are shown in Figs. 2.4(b,c). The black regions correspond to zero-energy MBSs in the topological region with a finite localization length in the $y$-direction. Similar to the

1D superconducting Rashba wires, we find Majorana oscillations in the Josephson junction. These are related to the overlap of the MBS wavefunctions at opposite ends of the junction. We show that this effect is enhanced by decreasing $L$ since the localization length is proportional to the inverse of the topological gap and, therefore, constant.

Recent studies suggest that MBSs can also form in different Josephson junction setups, using $s$-wave SCs and 3D TIs [99, 112]. Here, it was shown that the proximitized $s$-wave superconductivity in the Dirac-like surface states of the TI induces effective $p$-wave correlations. This can be seen in the pair correlation of the Green's function, which hosts a $s$-wave and $p$-wave pairing compoment, due to the helicity of the surface states. Even without a magnetic field, this leads to a non-trivial topological phase with helical ABSs. In this case, the bound states' zero-energy crossing at $\phi = \pi$ is protected from perturbations, like a potential barrier in the junction. This zero-energy state can be identified as an MBS. In contrast to the 2DEG Rashba Josephson junction, where the MBS is effectively 1D, localized at the edge of the N region near the vacuum [see Fig. 2.2(c)], the MBS in the TI Josephson junction is bound to the entire 2D normal conducting surface of the 3D TI.

# 3 Evolution of topological surface states of the Luttinger semimetal

## Contents

---

Recently, materials with a zinc-blende structure, like HgTe and $\alpha$-Sn, are highly used in the scientific community for hosting a wide range of different topological phases [7, 5, 113, 114, 63, 26, 64, 72, 19]. Confining these crystals lead to an effective 2D insulator state, which is topological or trivial depending on its thickness [115]. Applying tensile strain to the lattice opens a gap in the band structure, leading to a 3D topological insulator phase.

Throughout this work, we focus on the 3D semimetal phases of these materials, which can also be tuned using strain engineering. Here, the valence and conduction bands around the Fermi energy consist of the $j = 3/2$ states, which can be described by the 4-band Luttinger model [8]. The bands host a quadratic node, forming a so-called Luttinger semimetal. Compressive strain shifts the bands in energy, leading to linear crossings and a topological semimetal phase, already introduced in Sec. 2.2.

Along this chapter, we use the Luttinger model to discuss the evolution of the surface states in the different semimetal phases. We take the quadratic-node Luttinger semimetal as a starting point, which evolves into a Dirac semimetal (DSM) under compressive strain, and a Weyl semimetal (WSM) if inversion symmetry is broken. Our findings are published in Ref. [27].

## 3.1 Semimetal phases in the Luttinger model

### 3.1.1 The 4-band Luttinger model

In this section, we derive the 4-band Luttinger model from the method of invariant [116]. The Luttinger model describes the $j = 3/2$ states of a solid. These states are generally sixfold degenerate at the $\Gamma$ point, consisting of the $|X\rangle$, $|Y\rangle$, and $|Z\rangle$ spherical harmonics of the $p$-orbital ($l = 1$) plus spin $|\uparrow, \downarrow\rangle$. With spin-orbit coupling (SOC), the split-off band separates itself from the other states in energy, leaving a fourfold degenerate state at the $\Gamma$ point. These four states are described by the wavefunction

$$|\Psi_L(\mathbf{r})\rangle = \begin{pmatrix} \left|\frac{3}{2},+\frac{3}{2}\right\rangle \\ \left|\frac{3}{2},+\frac{1}{2}\right\rangle \\ \left|\frac{3}{2},-\frac{1}{2}\right\rangle \\ \left|\frac{3}{2},-\frac{3}{2}\right\rangle \end{pmatrix}, \tag{3.1}$$

where the elements have the form $|j, j_z\rangle$. The $|j_z| = 3/2$ states are often referred to as HH states, and the $|j_z| = 1/2$ states are called LH states. The elements of the wavefunction can be written in the basis of spherical harmonics and spin by [116]

$$\left|\frac{3}{2},+\frac{3}{2}\right\rangle = -\frac{1}{\sqrt{2}}\,|X+iY\rangle \otimes |\uparrow\rangle\,, \tag{3.2}$$

$$\left|\frac{3}{2},+\frac{1}{2}\right\rangle = \frac{1}{\sqrt{6}}[2\,|Z\rangle \otimes |\uparrow\rangle - |X+iY\rangle \otimes |\downarrow\rangle], \tag{3.3}$$

$$\left|\frac{3}{2},-\frac{1}{2}\right\rangle = \frac{1}{\sqrt{6}}[|X-iY\rangle \otimes |\uparrow\rangle + 2\,|Z\rangle \otimes |\downarrow\rangle], \tag{3.4}$$

$$\left|\frac{3}{2},-\frac{3}{2}\right\rangle = \frac{1}{\sqrt{2}}\,|X-iY\rangle \otimes |\downarrow\rangle\,. \tag{3.5}$$

Notice that the Luttinger model is a $k \cdot p$ model, which preserves time-reversal symmetry (TRS) [see Sec. 2.1] with $\hat{\mathcal{T}}^2 = -1$ due to the half-integer spin. The additional conservation of particle-hole symmetry (PHS) and chiral symmetry is not demanded, while possible under the given circumstances discussed below. Its most general form has full spherical symmetry $\mathbf{O}(3)$, where inversion symmetry is also conserved. Depending on the lattice structure of the crystal, additional terms that lower the symmetry to cubic $\mathbf{O}_h$ and tetrahedral $\mathbf{T}_d$ are allowed. These three symmetry groups form a hierarchy chain of subgroups

$$\mathbf{O}(3) \supset \mathbf{O}_h \supset \mathbf{T}_d. \tag{3.6}$$

Following Eq. (3.6), we can separate the Luttinger model by the corresponding symmetry subgroups. Hence, the symmetry of the Hamiltonian can be lowered by adding specific terms. Taking $\mathbf{O}(3)$ as a starting point, the $\mathbf{O}_h$ symmetric model is given by

$$\hat{H}^{L}(\hat{\mathbf{p}}) \equiv \hat{H}^{\mathbf{O}_h}(\hat{\mathbf{p}}) = \hat{H}^{\mathbf{O}(3)}(\hat{\mathbf{p}}) + \hat{H}_{\square}(\hat{\mathbf{p}}), \tag{3.7}$$

where $\hat{\mathbf{p}} = (\hat{p}_x, \hat{p}_y, \hat{p}_z)^T = -i(\partial_x, \partial_y, \partial_z)^T$ is the momentum operator, and $\hat{H}_{\square}(\hat{\mathbf{p}})$ is the linear combination of all symmetry invariants of the $\mathbf{O}_h$ group. This Hamiltonian is original form of the Luttinger Hamiltonian, also labeled $\hat{H}^{L}(\hat{\mathbf{p}})$ [8]. To lower the system's symmetry to $\mathbf{T}_d$, one must break inversion symmetry, giving the Hamiltonian

$$\hat{H}^{\mathbf{T}_d}(\hat{\mathbf{p}}) = \hat{H}^{\mathbf{O}_h}(\hat{\mathbf{p}}) + \hat{H}_{\mathrm{BIA}}(\hat{\mathbf{p}}). \tag{3.8}$$

Here, $\hat{H}_{\mathrm{BIA}}(\hat{\mathbf{p}})$ is the bulk inversion asymmetry (BIA). For most materials, the symmetry-breaking terms are small and dominated by the next-higher element in the symmetry hierarchy from Eq. (3.6). We will show that this relation leads to momentum ranges, where the specific symmetry terms give the physical properties.

| Reps. | Symmetrized matrices | Irreducible tensor components |
|---|---|---|
| $\Gamma_1$ | $\hat{1}_4$; $\hat{\boldsymbol{J}}^2$ | 1; $\mathbf{p}^2$ |
| $\Gamma_2$ | $\hat{J}_x\hat{J}_y\hat{J}_z + \hat{J}_z\hat{J}_y\hat{J}_x$ | |
| $\Gamma_3$ | $\frac{1}{\sqrt{3}}\left(2\hat{J}_z^2 - \hat{J}_x^2 - \hat{J}_y^2\right)$, $\hat{J}_x^2 - \hat{J}_y^2$ | $\frac{1}{\sqrt{3}}\left(2p_z^2 - p_x^2 - p_y^2\right)$, $p_x^2 - p_y^2$ |
| $\Gamma_4$ | $\hat{J}_x$, $\hat{J}_y$, $\hat{J}_z$; $\hat{J}_x^3$, $\hat{J}_y^3$, $\hat{J}_z^3$ | $p_x\left(p_y^2 - p_z^2\right)$, c.p.; $B_x$, $B_y$, $B_z$ |
| $\Gamma_5$ | $\left\{\hat{J}_y, \hat{J}_z\right\}$, c.p.; $\left\{\hat{J}_x, \hat{J}_y^2 - \hat{J}_z^2\right\}$, c.p. | $p_x, p_y, p_z$; $p_y p_z$, c.p.;<br>$p_x\left(p_y^2 + p_z^2\right)$, c.p.; $p_x^3, p_y^3, p_z^3$ |

Table 3.1: Symmetrized matrices and irreducible tensor components for the $\Gamma_8 \otimes \Gamma_8^* = \Gamma_1 + \Gamma_2 + \Gamma_3 + 2\Gamma_4 + 2\Gamma_5$ block of the tetrahedral symmetry point group $\mathbf{T}_d$ (see App. A.3 for details). This corresponds to the $j = 3/2$ states in the Luttinger model. The tensor components are listed up to cubic order in momentum in addition to the constant magnetic fields. The $\hat{J}$ matrices are the $4 \times 4$ spin 3/2 matrices, defined in App. A.1. Here, c.p. is the cyclic permutation concerning $(x, y, z)$ [117, 116, 118].

The highest symmetry Hamiltonian can be derived by the method of symmetry invariants [116]. The Hamiltonian consists of the $\Gamma_1$ irreducible representations, presented in Tab. 3.1. We get the most general Hamiltonian with $\mathbf{O}(3)$ symmetry

$$\hat{H}^{\mathbf{O}(3)}(\mathbf{p}) = \alpha_0 \mathbf{p}^2 \hat{1}_4 + \alpha_z \hat{M}_z(\mathbf{p}). \tag{3.9}$$

The parameters $\alpha_0$ and $\alpha_z$ are material specific and related to the invariants of the $\mathbf{O}(3)$ group $\mathbf{p}^2\hat{1}_4$ and

$$\hat{M}_z(\mathbf{p}) = \frac{5}{2}\mathbf{p}^2\hat{1}_4 - 2\Big(\mathbf{p}\cdot\hat{\mathbf{J}}\Big)^2. \tag{3.10}$$

Here, $\hat{1}_4$ is the $4\times 4$ unit matrix, and $\hat{\mathbf{J}} = (\hat{J}_x, \hat{J}_y, \hat{J}_z)^T$ are the $j = 3/2$ spin matrices presented in App. A.1. Throughout this thesis, we take the convention $\alpha_z > 0$. From the orbital structure of the basis (3.1), we can see that all states are odd under the inversion symmetry. Therefore, odd powers of momentum are forbidden in the Hamiltonian.

A cubic symmetric crystal includes the $\mathbf{O}_h$ invariants in the Hamiltonian. Since inversion symmetry is still preserved, odd momentum terms are forbidden. Hence, the invariants consist of the remaining quadratic momentum terms in Tab. 3.1. They are part of the $\Gamma_3$ and $\Gamma_5$ irreducible representations and have the form

$$\frac{1}{3}\Big(2\hat{J}_z^2 - \hat{J}_\perp^2\Big)\big(2p_z^2 - p_\perp^2\big), \quad \Big(\hat{J}_x^2 - \hat{J}_y^2\Big)\big(p_x^2 - p_y^2\big), \quad \Big\{\hat{J}_y, \hat{J}_z\Big\}p_y p_z + \text{c.p.}, \tag{3.11}$$

where $\hat{J}_\perp^2 = \hat{J}_x^2 + \hat{J}_y^2$, $p_\perp^2 = p_x^2 + p_y^2$, and c.p. is the cyclic permutation. We can find a linear combination of these invariants to get

$$\hat{H}_\square(\mathbf{p}) = \alpha_\square \hat{M}_\square(\mathbf{p}) \tag{3.12}$$

with

$$\hat{M}_\square(\mathbf{p}) = p_x^2\hat{J}_x^2 + p_y^2\hat{J}_y^2 + p_z^2\hat{J}_z^2 - \frac{2}{5}\Big(\mathbf{p}\cdot\hat{\boldsymbol{J}}\Big)^2 - \frac{1}{5}\mathbf{p}^2\hat{\boldsymbol{J}}^2. \tag{3.13}$$

Here, $\alpha_\square$ is the cubic anisotropy. The Hamiltonian $\hat{H}^{\mathbf{O}_h}(\mathbf{p})$ [Eq. (3.7)] was first considered by Luttinger in 1956 [8], giving the name Luttinger model.

If inversion symmetry is broken, odd powers of momentum are allowed. Taking the remaining invariants of the $\mathbf{T}_d$, we find one linear term in the $\Gamma_5$ irreducible representation and four cubic terms in $\Gamma_4$ and $\Gamma_5$

$$\hat{H}_{\mathrm{BIA}}(\mathbf{p}) = \beta_1\hat{M}_1(\mathbf{p}) + \sum_{i=1}^{4}\beta_{3i}\hat{M}_{3i}(\mathbf{p}). \tag{3.14}$$

The material-specific $\beta$ parameters determine the strength of the BIA terms. The linear part has the form

$$\hat{M}_1(\mathbf{p}) = p_x\Big\{\hat{J}_x, \hat{J}_y^2 - \hat{J}_z^2\Big\} + \text{c.p.}, \tag{3.15}$$

and the cubic ones

$$\hat{M}_{31}(\mathbf{p}) = p_x\big(p_y^2 - p_z^2\big)\hat{J}_x + \text{c.p.}, \tag{3.16}$$

$$\hat{M}_{32}(\mathbf{p}) = p_x\big(p_y^2 - p_z^2\big)\hat{J}_x^3 + \text{c.p.}, \tag{3.17}$$

$$\hat{M}_{33}(\mathbf{p}) = p_x\big(p_y^2 + p_z^2\big)\Big\{\hat{J}_x, \hat{J}_y^2 - \hat{J}_z^2\Big\} + \text{c.p.}, \tag{3.18}$$

$$\hat{M}_{34}(\mathbf{p}) = p_x^3\Big\{\hat{J}_x, \hat{J}_y^2 - \hat{J}_z^2\Big\} + \text{c.p.}. \tag{3.19}$$

We conclude that $\hat{H}^{\mathbf{T}_d}(\mathbf{p})$ [Eq. (3.8)] contains all terms allowed by $\mathbf{T}_d$ and TRS up to cubic order in momentum. Therefore, the Luttinger model is considered the most general low-energy model for many materials, where the Fermi level resides in the $j = 3/2$ states.

It was shown that many quadratic nodal semimetals host interesting topological phases under strain [63]. The sample is grown on a substrate with a different lattice constant in actual experimental setups. The lattice mismatch leads to deformation since the sample must match the lattice constant of the substrate. Pikus and Bir showed [119, 120] that one could write the strain potential by substituting the momentum terms in the Hamiltonian with

$$p_i p_j \to u_{ij}, \tag{3.20}$$

where $u_{ij}$ is the strength of the potential along the direction of $p_i p_j$. Throughout this thesis, we apply strain in the $z$-direction. Hence, we use the substitution $p_z^2 \to u_{zz} \equiv u$ and get the strain Hamiltonian

$$\hat{H}_u = -u\bigg(\hat{J}_z^2 - \frac{5}{4}\hat{1}_4\bigg), \tag{3.21}$$

which has $\mathbf{D}_{\infty h}$ spatial symmetry. The sign of $u$ determines if the lattice is stretched (tensile strain) for $u > 0$ or compressed (compressive strain) for $u < 0$.

Adding strain to the quadratic nodal Luttinger semimetal drives the system into a different topological state. Tensile strain opens a gap between the HH and LH states, creating a class AI topological insulator (Tab. 2.1). Compressive strain splits the quadratic node into two linear nodes, inducing a DSM phase, described by the Dirac Hamiltonian

$$\hat{H}^{D}(\mathbf{p}) = \hat{H}^{\mathbf{O}_h}(\mathbf{p}) + \hat{H}_u. \tag{3.22}$$

We discuss the effect of strain on the bulk band structure in more detail in Sec. 3.1.2. The strain lowers the symmetry of the Hamiltonian to

$$\mathbf{D}_{4h} = \mathbf{O}_h \cap \mathbf{D}_{\infty h}. \tag{3.23}$$

Since TRS and inversion symmetry are still preserved, we expect the band structure to be double degenerate due to Kramers' theorem. Therefore, any linear crossings in the dispersion are Dirac points, as discussed in Sec. 2.2.2.

A WSM phase arises if either TRS or inversion symmetry is broken in a DSM. So, one expects the dispersion to form Weyl points if the BIA terms are added to the Hamiltonian. Interestingly, we find that the linear term of $\hat{H}_{\mathrm{BIA}}(\mathbf{p})$ is insufficient to drive the system into a WSM phase. Instead, it leads to an intermediate phase, where the Dirac points split into circular line nodes (see Secs. 3.1.2 and 3.1.3 for details). We call this phase line-node semimetal described by the Hamiltonian

$$\hat{H}^{LN}(\mathbf{p}) = \hat{H}^{D}(\mathbf{p}) + \beta_1 \hat{M}_1(\mathbf{p}), \tag{3.24}$$

with the symmetry

$$\mathbf{D}_{2d} = \mathbf{T}_d \cap \mathbf{D}_{\infty h}. \tag{3.25}$$

Taking the cubic BIA terms into account leads to the formation of eight separated linear Weyl points along the high symmetry lines $p_x = 0$ and $p_y = 0$. In this way, the Weyl Hamiltonian aquires the form

$$\hat{H}^{W}(\mathbf{p}) = \hat{H}^{\mathbf{T}_d}(\mathbf{p}) + \hat{H}_u. \tag{3.26}$$

We illustrate the evolution of the Luttinger semimetal phase under the effect of compressive strain, linear, and cubic BIA terms in Fig. 3.1.

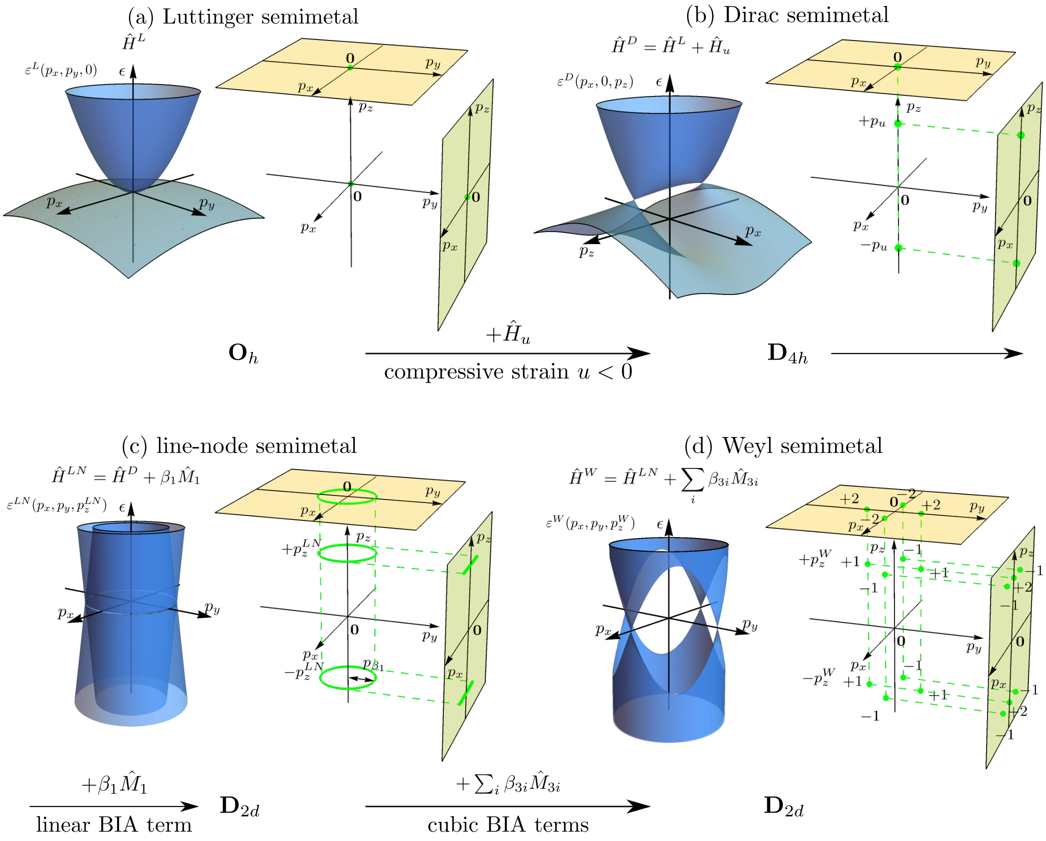

Figure 3.1: Evolution of the bulk band structure of the (a) Luttinger model $\hat{H}^L(\mathbf{p})$ [Eq. 3.7)] under symmetry lowering perturbations. (b) The quadratic node of the Luttinger semimetal phase splits into two linear Dirac nodes under compressive strain $\hat{H}_u$ [Eq. (3.21)] with $u<0$. (c) The Dirac points split into circular line-nodes with linear bulk-inversion-asymmetry terms $\beta_1\hat{M}_1(\mathbf{p})$ [Eq. (3.15)]. (d) The cubic bulk-inversion-asymmetry terms $\beta_3\hat{M}_3(\mathbf{p})$ form Eqs. (3.16)-(3.19) lift the line-node degeneracy for $p_xp_y \neq 0$ and give a Weyl semimetal phase. The position of the bulk crossings in the 3D Brillouin zone and the projected 2D surface Brillouin zones for a $y=0$ and $z=0$ boundary is illustrated next to the corresponding bulk dispersion.

In Chapter 4, we discuss superconducting systems described by the Luttinger model in a magnetic field, which breaks TRS. We consider the effect of the magnetic field by a Zeeman term, which comes from the constant momentum term in the $\Gamma_4$ irreducible representation in Tab. 3.1

$$\hat{H}_Z = \mathbf{B} \cdot \hat{\mathbf{J}}, \tag{3.27}$$

where $\mathbf{B} = (B_x, B_y, B_z)^T$ is the magnetic field vector with absorbed $g$ factor.

### 3.1.2 Evolution of the bulk band structure under symmetry breaking

In this section, we show the evolution of the bulk dispersion in the different semimetal phases of the Luttinger model introduced above. We start with the highest symmetry phase $\hat{H}^{\mathbf{O}(3)}(\mathbf{p})$ [Eq. (3.9)] with full rotational symmetry. Here, we find the double degenerate bulk eigenvalues

$$\varepsilon^{\mathbf{O}(3)}_{|j_z|=\frac{3}{2}}(\mathbf{p}) = \alpha_- \mathbf{p}^2, \qquad \varepsilon^{\mathbf{O}(3)}_{|j_z|=\frac{1}{2}}(\mathbf{p}) = \alpha_+ \mathbf{p}^2, \tag{3.28}$$

which is fourfold degenerate at the $\Gamma$ point ($\mathbf{p} = 0$) and invariant under any rotation in space. The modified parameters $\alpha_\pm = \alpha_0 \pm 2\alpha_z$ determine the effective masses of the HH ($\alpha_-$) and LH ($\alpha_+$) states. It is convenient to take $\alpha_z$ as an overall effective mass, which leaves $\hat{H}^{\mathbf{O}(3)}(\mathbf{p})$ with a single dimensionless parameter $\bar{\alpha}_0 \equiv \alpha_0/\alpha_z$.

Notice that Eq. (3.28) has two different phases. If $\tilde{\alpha}_+ > 0$ and $\tilde{\alpha}_- < 0$, the bands have opposite curvatures, and the system is a semimetal. In this case, the HH ($|j_z| = 3/2$) states have a hole-like character while the LH ($|j_z| = 1/2$) states are electron-like. We find the condition $|\bar{\alpha}_0| < 2$ for the semimetal phase, where one band is flat at $|\bar{\alpha}_0| = 2$, giving a critical phase transition point. For $|\bar{\alpha}_0| > 2$, both states have the same curvature indicating a metallic phase. In the absence of $\bar{\alpha}_0 = 0$, the effective masses of the HH and LH states are equal, giving PHS. Therefore, the Luttinger parameter $\alpha_0$ is the particle-hole asymmetry.

The cubic anisotropy $\alpha_\Box$ breaks the rotational symmetry and gives the energy dispersion

$$\varepsilon^L_\pm(\mathbf{p}) \equiv \varepsilon^{\mathbf{O}_h}_\pm(\mathbf{p}) = \alpha_0 \mathbf{p}^2 \pm \sqrt{4\tilde{\alpha}_z^2 \mathbf{p}^4 + 3\alpha_\Box\big(4\alpha_z - \tfrac{1}{5}\alpha_\Box\big)\big(p_x^2 p_y^2 + p_\perp^2 p_z^2\big)}, \tag{3.29}$$

with $p_\perp^2 = p_x^2 + p_y^2$ and $\tilde{\alpha}_z = \alpha_z - \frac{3}{10}\alpha_\square$. In a 1D wire, the last term vanishes, and $\alpha_\square$ only renormalizes the effective masses to $\tilde{\alpha}_\pm = \alpha_0 \pm 2\tilde{\alpha}_z$.

With strain, we can still find an analytical expression for the bulk dispersion

$$\varepsilon_\pm^D(\mathbf{p}) = \alpha_0\mathbf{p}^2 \pm \sqrt{4\tilde{\alpha}_z^2\mathbf{p}^4 + 3\alpha_\square\big(4\alpha_z - \tfrac{1}{5}\alpha_\square\big)\big(p_x^2p_y^2 + p_\perp^2p_z^2\big) + 2\tilde{\alpha}_z\big(2p_z^2 - p_\perp^2\big)u + u^2}. \tag{3.30}$$

It is instructive to consider the momentum $\mathbf{p} = (0, 0, p_z)^T$, where the bulk energy has the form

$$\varepsilon^D_{|j_z|=3/2}(0,0,p_z) = (\alpha_0 - 2\tilde{\alpha}_z)p_z^2 - u, \qquad \varepsilon^D_{|j_z|=1/2}(0,0,p_z) = (\alpha_0 + 2\tilde{\alpha}_z)p_z^2 + u. \tag{3.31}$$

At the Γ point, the quadratic node of the Luttinger semimetal splits, and a gap of $2|u|$ opens. For $u > 0$, the strain opens a topological gap for all $p_z$ and induces an insulator phase. From Tab. 2.1, we can identify this phase as a potential class AI insulator, which can be driven into a class A topological insulator phase under TRS breaking.

This work focuses on the compressive strain $u < 0$, which splits the quadratic node into two nodes along $p_z = \pm p_u$, with

$$p_u = \sqrt{\frac{|u|}{2\tilde{\alpha}_z}}, \tag{3.32}$$

and energy

$$\varepsilon_u = \alpha_0 p_u^2 = \frac{1}{2}\bar{\alpha}|u|. \tag{3.33}$$

Here, we use the dimensionless parameter renormalized by the cubic anisotropy

$$\bar{\alpha} = \frac{\alpha_0}{\tilde{\alpha}_z}. \tag{3.34}$$

Since the semimetal phase requires $|\bar{\alpha}| \leq 2$, we can find the restriction $|\varepsilon_u| < |u|$. Recall that the crossing points are double degenerate and linear, making them Dirac points in the DSM phase of the Luttinger model.

In order to make our study independent of the strength of the compressive strain, we introduce dimensionless parameters

$$\bar{p}_i = \frac{p_i}{p_{u0}}, \text{ with } \quad p_{u0} = \sqrt{\frac{|u|}{2\alpha_z}}, \tag{3.35}$$

$$\bar{\epsilon} = \frac{\epsilon}{|u|}, \tag{3.36}$$

which are going to be used throughout this chapter.

For the line-node phase of $\hat{H}^{LN}(\mathbf{p})$ [Eq. (3.24)], it is convenient to use cylindrical coordinates $\mathbf{p} = (p_\perp \cos(\varphi), p_\perp \sin(\varphi), p_z)^T$ and apply the unitary transformation $\tilde{H}^{LN}(\mathbf{p}) = \hat{U}_\varphi^\dagger \hat{H}^{LN}(\mathbf{p}) \hat{U}_\varphi$, with

$$\hat{U}_\varphi = \frac{1}{\sqrt{2}} \begin{pmatrix} 0 & -e^{-i\varphi} & 0 & -e^{-i\varphi} \\ 1 & 0 & 1 & 0 \\ e^{-i\varphi} & 0 & -e^{-i\varphi} & 0 \\ 0 & 1 & 0 & -1 \end{pmatrix}. \tag{3.37}$$

The transformed Hamiltonian has the block structure

$$\tilde{H}^{LN}(\mathbf{p}) = \begin{pmatrix} \tilde{h}^{+_m}(\mathbf{p}) & \tilde{h}_c(\mathbf{p}) \\ \tilde{h}_c^\dagger(\mathbf{p}) & \tilde{h}^{-_m}(\mathbf{p}) \end{pmatrix}, \tag{3.38}$$

where the diagonal blocks are given by

$$\tilde{h}^{\pm_m}(\mathbf{p}) = d_0^{\pm_m}(\mathbf{p}) \hat{1}_2 + \mathbf{d}^{\pm_m}(\mathbf{p}) \cdot \hat{\boldsymbol{\sigma}}, \tag{3.39}$$

with

$$d_0^{\pm_m}(\mathbf{p}) = \alpha_0 \mathbf{p}^2 \pm_m \frac{3}{2} \beta_1 p_\perp, \tag{3.40}$$

$$d_x^{\pm_m}(\mathbf{p}) = \left[ 2\sqrt{3}\sqrt{(}\alpha_z + \frac{1}{5}\alpha_\Box) p_\perp \mp_m \sqrt{3}\beta_1 \right] p_z, \tag{3.41}$$

$$d_y^{\pm_m}(\mathbf{p}) = \left[ \frac{\sqrt{3}}{2} \beta_1 \mp_m \sqrt{3} \left( \alpha_z + \frac{1}{5}\alpha_\Box \right) p_\perp p_u \right] p_\perp \sin(2\varphi), \tag{3.42}$$

$$d_z^{\pm_m}(\mathbf{p}) = \tilde{\alpha}_z \left[ 2\left(p_z^2 - p_u^2\right) - p_\perp^2 \right]. \tag{3.43}$$

The coupling between the two diagonal blocks has the shape

$$\tilde{h}_c(\mathbf{p}) = \left[\frac{m}{2p_u}\hat{\sigma}_x + \sqrt{3}i\tilde{\alpha}_z p_\perp \hat{\sigma}_y\right] p_\perp \cos(2\varphi). \tag{3.44}$$

At $\varphi = \pm\pi/4$, the Hamiltonian decouples into two blocks, and one can find the crossing of the bands at the momentum

$$p_{\perp 0}(\varphi = \pm\frac{\pi}{4}) = p_{\beta_1}, \quad p_{z0}^2(\varphi = \pm\frac{\pi}{4}) = p_u^2 + \frac{1}{2}p_{\beta_1}^2, \tag{3.45}$$

and energy

$$\varepsilon_0(\varphi = \pm\frac{\pi}{4}) = \varepsilon_u + \varepsilon_{\beta_1}, \tag{3.46}$$

with

$$\varepsilon_{\beta_1} = \frac{3}{2}\left(\alpha_0 + 2\alpha_z + \frac{2}{5}\alpha_\square\right), \tag{3.47}$$

$$p_{\beta_1} = \frac{|\beta_1|}{2\alpha_z + \frac{2}{5}\alpha_\square}. \tag{3.48}$$

For arbitrary $\varphi$, we cannot solve $\tilde{H}^{LN}(\mathbf{p})$ analytically. Nevertheless, we can confirm numerically the existence of two circular line nodes depicted in Fig. 3.1. Without $\alpha_\square$, the radius of the line node is constant $p_\perp(\varphi, \alpha_\square = 0) = p_{\beta_1}$, while $p_{z0}(\varphi)$ and the energy of the node $\varepsilon_0(\varphi)$ have a minimal angle dependency. The cubic anisotropy also introduces a small angle dependency to $p_\perp(\varphi)$.

We believe the line-node phase is accidental and not protected by a specific symmetry. It is also questionable if this phase can be realized in an actual material since the inversion symmetry has to be broken while the cubic BIA terms need to vanish. We include it in this thesis to distinguish between the effects of the linear and cubic BIA terms on the surface and bulk states.

To drive the system into a WSM phase, we need to add the cubic BIA terms from Eqs. (3.16)-(3.19). We apply the basis rotation from Eq. (3.37) and approximate the bulk energy for $\varphi = \pi/4$. Details are provided in Sec. A.4 of the Appendix. We find

$$\begin{aligned}\varepsilon_{\pm}^{W,\varphi=\frac{\pi}{4}}(q_\perp, q_z) &= \epsilon_0 + v_{0,\perp} q_\perp + v_{0,z} q_z \\ &\pm \sqrt{\left(v_{1,\perp} q_\perp + \epsilon_1\right)^2 + \epsilon_2^2 + \left(v_{z,\perp} q_\perp + v_{z,z} q_z + \epsilon_z\right)^2},\end{aligned} \tag{3.49}$$

with the shifted momentum coordinates $\mathbf{q} = (q_\perp, q_z) = (p_\perp - p_{\perp 0}, p_z - p_{z0})$ relative to the line-node coordinates from Eq. (3.45). The $v$ constants are related to the parameters of the line-node semimetal phase up to quadratic order in momentum. The cubic BIA terms give the $\epsilon_i$ constants. From the dispersion [Eq. (3.49)], we can see that $\epsilon_0$ shifts the energy, and $\epsilon_{1,z}$ moves the momentum of the line node without opening a gap along $\varphi = \pi/4$. The only term in the root that a shift in momentum cannot nullify is the constant $\epsilon_2$. Therefore, it opens a gap in the bulk states along $\varphi = \pi/4$ of the size $2|\epsilon_2|$, with

$$|\epsilon_2| = \sqrt{3}\left|\beta_{31} + \frac{7}{4}\beta_{32} + \beta_{33} - \beta_{34}\right| \frac{p_{\perp 0} p_{z0} p_u^2}{\sqrt{p_{\perp 0}^2 + 4p_{z0}^2}}, \tag{3.50}$$

leading to the destruction of the line node. Taking the perpendicular diagonal line $\varphi = -\pi/4$ only gives a relative change in sign of $\epsilon_2$. The shape of Eq. (3.50) suggests that each cubic BIA term $\beta_{3i}$ can equivalently open the gap. Since the magnitude of the cubic BIA terms is not discussed in the literature for most materials, we focus on $\beta_{31}$ in the discussion of the surface states.

### 3.1.3 Linearized model of the topological semimetal phase

Analytical calculations are impossible in the topological semimetal phases of the Luttinger model under compressive strain. We can use the linear nature of the Dirac nodes to perform an expansion around $(0, 0, \pm p_u)$. In this way, the wavefunction can be written as

$$|\psi(\boldsymbol{r})\rangle = e^{ip_u z}\left|\Psi^{+_u}(\boldsymbol{r})\right\rangle + e^{-ip_u z}\left|\Psi^{-_u}(\boldsymbol{r})\right\rangle, \tag{3.51}$$

where the labels $\pm_u$ indicate the linearization around the Dirac points at $p_z = \pm p_u$. Using the new momentum coordinates $\mathbf{k} = (k_x, k_y, k_z)^T = (p_x, p_y, p_z \mp_u p_u)^T$ and the basis $(|\Psi^{+_u}(\boldsymbol{r})\rangle\,, |\Psi^{-_u}(\boldsymbol{r})\rangle)^T$, we write the linearized Hamiltonian

$$\hat{\mathcal{H}}^D(\boldsymbol{k}) = \begin{pmatrix} \hat{\mathcal{H}}^{D,+_u}(\boldsymbol{k}) & 0 \\ 0 & \hat{\mathcal{H}}^{D,-_u}(\boldsymbol{k}) \end{pmatrix}. \tag{3.52}$$

The blocks of the distinct Dirac points have the shape

$$\hat{\mathcal{H}}^{D,\pm_u}(\boldsymbol{k}) = \varepsilon_u \hat{1}_4 \pm_u \begin{pmatrix} (v_0 - 2v_z)k_z & -v_\perp k_- & 0 & 0 \\ -v_\perp k_+ & (v_0 + 2v_z)k_z & 0 & 0 \\ 0 & 0 & (v_0 + 2v_z)k_z & v_\perp k_- \\ 0 & 0 & v_\perp k_+ & (v_0 - 2v_z)k_z \end{pmatrix}, \tag{3.53}$$

with $k_\pm = k_x \pm ik_y$. The energy of the Dirac point $\varepsilon_u$ from Eq. (3.33) acts only as a shift in energy. The $v$ parameters have the units of velocity and are given by

$$v_0 = 2\alpha_0 p_u, \qquad v_z = 2\tilde{\alpha}_z p_u, \qquad v_\perp = \sqrt{3}\left(2\alpha_z + \frac{2}{5}\alpha_\Box\right)p_u. \tag{3.54}$$

Taking the basis of the Luttinger model [Eq.(3.1)] into account, we see that the $j_z > 0$ and $j_z < 0$ are decoupled in Eq. (3.53) and form Kramers' partners. Using cylindrical coordinates $\mathbf{k} = (k_\perp \cos\varphi, k_\perp \sin\varphi, k_z)$, we find the dispersion around the Dirac points

$$\varepsilon_\pm^{\pm_u}(\boldsymbol{k}) = \varepsilon_u \pm_u v_0 k_z \pm \sqrt{v_\perp^2 k_\perp^2 + 4v_z^2 k_z^2}. \tag{3.55}$$

We can see that the spectrum in the vicinity of the Dirac points is rotational symmetric in the $p_x$-$p_y$ plane, even in the presence of cubic anisotropy. Neglecting the energy shift $\varepsilon_u$, we find that $\hat{\mathcal{H}}^D(\mathbf{k})$ has effective chiral symmetry due to

$$\hat{\mathcal{S}}^\dagger \hat{\mathcal{H}}^D(\mathbf{k})\hat{\mathcal{S}} = -\hat{\mathcal{H}}^D(\mathbf{k}), \quad \text{with} \quad \hat{\mathcal{S}} = \hat{\sigma}_x \otimes \hat{1}_4. \tag{3.56}$$

The consequence of this effective chiral symmetry is discussed in Sec. 3.6.2.

For the line-node semimetal phase, we linearize the linear BIA term around $p_z = \pm p_u$ and take the constant term. It has the shape

$$\beta_1 \hat{M}_1(0, 0, \pm_u p_u) = \pm_u m \begin{pmatrix} 0 & 0 & 1 & 0 \\ 0 & 0 & 0 & -1 \\ 1 & 0 & 0 & 0 \\ 0 & -1 & 0 & 0 \end{pmatrix}, \tag{3.57}$$

with $m = \sqrt{3}\beta_1 p_u$. We write the linearized Hamiltonian of the line-node semimetal phase as

$$\hat{\mathcal{H}}^{LN,\pm_u}(\boldsymbol{k}) = \hat{\mathcal{H}}^{D,\pm_u}(\boldsymbol{k}) + \beta_1 \hat{M}_1(0, 0, \pm_u p_u), \tag{3.58}$$

where $m$ couples the blocks for positive and negative $j_z$ states. It is convenient to apply the unitary transformation from Eq. (3.37), $\tilde{\mathcal{H}}^{LN,\pm_u}(\boldsymbol{k}) = \hat{U}_\varphi^\dagger \hat{\mathcal{H}}^{LN,\pm_u}(\boldsymbol{k}) \hat{U}_\varphi$ to get

$$\tilde{\mathcal{H}}^{LN,\pm_u}(\boldsymbol{k}) = \varepsilon_u \pm_u \begin{pmatrix} (v_0 + 2v_z)k_z & v_\perp k_\perp - m & 0 & 0 \\ v_\perp k_\perp - m & (v_0 - 2v_z)k_z & 0 & 0 \\ 0 & 0 & (v_0 + 2v_z)k_z & v_\perp k_\perp + m \\ 0 & 0 & v_\perp k_\perp + m & (v_0 - 2v_z)k_z \end{pmatrix}. \tag{3.59}$$

The unitary transformation restores the Hamiltonian's block-diagonal structure, which still preserves the effective chiral symmetry from Eq. (3.56). Solving the Schrödinger equation, we get the bulk dispersion

$$\varepsilon_\pm^{LN,\pm_u,-m}(\boldsymbol{k}) = \varepsilon_u \pm_u v_0 k_z \pm \sqrt{(v_\perp k_\perp - m)^2 + 4v_z^2 k_z^2}, \tag{3.60}$$

$$\varepsilon_\pm^{LN,\pm_u,+m}(\boldsymbol{k}) = \varepsilon_u \pm_u v_0 k_z \pm \sqrt{(v_\perp k_\perp + m)^2 + 4v_z^2 k_z^2}. \tag{3.61}$$

The energy spectrum is independent of the angle $\varphi$, which shows that the constant part of the BIA terms does not break the rotational symmetry of the linearized DSM Hamiltonian. By setting each term under the root to zero, we find that the Dirac points split into a ring-shaped line node. Its center lies at $\mathbf{p} = (0, 0, \pm p_u)^T$ with the radius

$$p_{\perp 0} = \frac{|m|}{v_\perp} = p_{\beta_1}, \tag{3.62}$$

with $p_{\beta_1}$ defined in Eq. (3.48). The independence of Eq.(3.62) on the angle $\varphi$ shows that the line node in the linearized model is a perfect circle. The radius corresponds to the solution of the full model at $\varphi = \pm\pi/4$.

## 3.2 Luttinger model as the low-energy limit of the Kane model

The band structure of crystalline solids is formed by a wide array of states given by the orbitals of the atoms [116]. Around the Fermi energy, the bands consist of $s$-orbitals with angular momentum $l = 0$ and $p$-orbitals with $l = 1$. The $s$-states form a double degenerate state, with spin $|\uparrow\rangle$ and $|\downarrow\rangle$ at the $\Gamma$ point, while the $p$-states are sixfold degenerate due to a combination of the three spherical harmonics $|X\rangle$, $|Y\rangle$, and $|Z\rangle$ with spin. With SOC, the sixfold degeneracy of the $p$-orbitals is lifted and splits into a fourfold degenerate point with a double degenerate split-off band.

In general, one can use the density functional theory to analyze the band structure in a solid [6]. Alternatively, one can apply a $k \cdot p$ approach to write a 14-band Hamiltonian, which describes the interactions between all possible $s$ and $p$-states, called the extended Kane model [121, 122, 123, 116]. On one hand, it accurately predicts experiments with semiconductors. On the other hand, it is not analytically solvable, which demands numerical calculations. Therefore, reducing the extended Kane model to the bands of the highest interest is often convenient. The resulting 8-band or 6-band Kane models are widely used in literature and allow analytical explanations of many experiments [114, 19, 124, 125]. The 4-band Luttinger model is the most general reduction of the extended Kane model and describes only the fourfold degenerate $j = 3/2$ states at the Fermi level. It enables analytical calculations while missing the explicit consideration of the fundamental gap between the $s$ and $p$-states.

In this section, we discuss the relation of the Luttinger model to the 6-band Kane model, which additionally considers the $j = 1/2$ states. Here, we demonstrate how the hybridization of the $j = 1/2$ and $j = 3/2$ states renormalize the Luttinger parameters and induce a quadratic-node semimetal phase.

### 3.2.1 The 6-band Kane model

In this section we introduce the 6-band Kane model, which describes $j = 1/2$ and $j = 3/2$ states in the basis

$$|\Psi_K(\mathbf{r})\rangle = \begin{pmatrix} \left|\Psi_{\frac{1}{2}}(\mathbf{r})\right\rangle \\ \left|\Psi_{\frac{3}{2}}(\mathbf{r})\right\rangle \end{pmatrix}, \quad \left|\Psi_{\frac{1}{2}}(\mathbf{r})\right\rangle = \begin{pmatrix} \left|\frac{1}{2}, +\frac{1}{2}\right\rangle \\ \left|\frac{1}{2}, -\frac{1}{2}\right\rangle \end{pmatrix}, \quad \left|\Psi_{\frac{3}{2}}(\mathbf{r})\right\rangle = \begin{pmatrix} \left|\frac{3}{2}, +\frac{3}{2}\right\rangle \\ \left|\frac{3}{2}, +\frac{1}{2}\right\rangle \\ \left|\frac{3}{2}, -\frac{1}{2}\right\rangle \\ \left|\frac{3}{2}, -\frac{3}{2}\right\rangle \end{pmatrix}, \tag{3.63}$$

where the components indicate the $|j, j_z\rangle$ quantum numbers. The basis states of $\left|\Psi_{\frac{3}{2}}(\mathbf{r})\right\rangle$ are given by Eqs. (3.2)-(3.5) and the $\left|\Psi_{\frac{1}{2}}(\mathbf{r})\right\rangle$ states are built from the spherical harmonics of the $s$-orbital [116]

$$\left|\frac{1}{2}, +\frac{1}{2}\right\rangle = |S\rangle \otimes |\uparrow\rangle\,, \quad \left|\frac{1}{2}, -\frac{1}{2}\right\rangle = |S\rangle \otimes |\downarrow\rangle\,, \tag{3.64}$$

which are even under inversion.

| Block | Reps. | Symmetrized matrices |
|---|---|---|
| $\Gamma_6 \otimes \Gamma_6^* = \Gamma_1 + \Gamma_4$ | $\Gamma_1$ | $\hat{1}_2$ |
| | $\Gamma_4$ | $\hat{\sigma}_x$, $\hat{\sigma}_y$, $\hat{\sigma}_z$ |
| $\Gamma_6 \otimes \Gamma_8^* = \Gamma_3 + \Gamma_4 + \Gamma_5$ | $\Gamma_3$ | $\hat{T}_{xx} - \hat{T}_{yy}$, $-\sqrt{3}\hat{T}_{zz}$ |
| | $\Gamma_4$ | $\hat{T}_{yz}$, $\hat{T}_{zx}$, $\hat{T}_{xy}$ |
| | $\Gamma_5$ | $\hat{T}_x$, $\hat{T}_y$, $\hat{T}_z$ |

Table 3.2: Symmetrized matrices for the additional blocks of the Kane model from Eq. (3.65). The $\Gamma_6 \otimes \Gamma_6^*$ block contains the $2\times 2$ Pauli matrices $(\hat{\sigma}_x, \hat{\sigma}_y, \hat{\sigma}_z)$ and the unit matrix $\hat{1}_2$. The coupling block $\Gamma_6 \otimes \Gamma_8^*$ is built from the $4\times 2$ $\hat{T}$ matrices, defined in App. A.1 [117, 116, 118].

The 6-band Kane Hamiltonian has the block-like structure

$$\hat{H}^K(\mathbf{p}) = \begin{pmatrix} \hat{H}_{\frac{1}{2}\frac{1}{2}}(\mathbf{p}) & \hat{H}_{\frac{1}{2}\frac{3}{2}}(\mathbf{p}) \\ \hat{H}_{\frac{3}{2}\frac{1}{2}}(\mathbf{p}) & \hat{H}_{\frac{3}{2}\frac{3}{2}}(\mathbf{p}) \end{pmatrix}, \quad \text{with} \quad \hat{H}_{\frac{1}{2}\frac{3}{2}}(\mathbf{p}) = \hat{H}^{\dagger}_{\frac{3}{2}\frac{1}{2}}(\mathbf{p}). \tag{3.65}$$

The blocks are given by

$$\hat{H}_{\frac{1}{2}\frac{1}{2}}(\mathbf{p}) = \Big(E_g + \gamma_{\frac{1}{2}}\mathbf{p}^2\Big)\hat{1}_2, \tag{3.66}$$

$$\hat{H}_{\frac{3}{2}\frac{3}{2}}(\mathbf{p}) = \gamma_0\mathbf{p}^2\hat{1}_4 + \gamma_z\hat{M}_z(\mathbf{p}) + \gamma_\square\hat{M}_\square(\mathbf{p}) + \beta_1^K\hat{M}_1(\mathbf{p}) + \sum_{i=1}^{4}\beta_{3i}^K\hat{M}_{3i}(\mathbf{p}), \tag{3.67}$$

$$\hat{H}_{\frac{1}{2}\frac{3}{2}}(\mathbf{p}) = v\hat{U}(\mathbf{p}) + B_-\hat{U}_-(\mathbf{p}) + B_+\hat{U}_+(\mathbf{p}). \tag{3.68}$$

The $j = 1/2$ block $\hat{H}_{\frac{1}{2}\frac{1}{2}}(\mathbf{p})$ is built from the $\Gamma_1$ symmetry invariant of the $\mathbf{T}_d$ group (see Tabs. 3.1 and 3.2). In addition, the $j = 1/2$ states are separated from the $j = 3/2$ states by an energy gap $E_g$. The $j = 3/2$ block $\hat{H}_{\frac{3}{2}\frac{3}{2}}(\mathbf{p})$ contains the same invariants as the Luttinger model, discussed in Sec. 3.1.1. The coupling terms between the $j = 1/2$ and $j = 3/2$ states are given by

$$\hat{U}(\mathbf{p}) = \frac{3}{\sqrt{2}}\Big(\hat{\boldsymbol{T}} \cdot \mathbf{p}\Big), \tag{3.69}$$

$$\hat{U}_-(\mathbf{p}) = -\frac{1}{2\sqrt{3}}\Big(\hat{T}_{xx} - \hat{T}_{yy}\Big)\big(2p_z^2 - p_x^2 - p_y^2\big) + \frac{\sqrt{3}}{2}\hat{T}_{zz}\big(p_x^2 - p_y^2\big), \tag{3.70}$$

$$\hat{U}_+(\mathbf{p}) = \sqrt{3}i\Big(\hat{T}_x p_y p_z + \text{c.p.}\Big), \tag{3.71}$$

where the $4 \times 2$ $\hat{T}$ matrices are presented in Sec. A.1 of the Appendix.

The Kane model shows the same symmetry hierarchy chain of the subgroups of the tetrahedral group $\mathbf{O}(3) \supset \mathbf{O}_h \supset \mathbf{T}_d$ [Eq. (3.6)]. The highest symmetry elements from the full spherical group $\mathbf{O}(3)$ are the $\gamma_{\frac{1}{2}}$, $\gamma_0$, $\gamma_z$, and $v$ terms. The linear momentum terms in $\hat{U}(\mathbf{p})$ are allowed since the $j = 1/2$ states are even and the $j = 3/2$ states are odd under the inversion operation. Combined with the cubic anisotropy $\gamma_\square$, they describe a lower cubic symmetric system. The linear $\beta_1^K$, the quadratic $B_\pm$, and the cubic momentum $\beta_{3i}^K$ terms are the BIA terms, which lower the symmetry to $\mathbf{T}_d$ and break inversion symmetry.

### 3.2.2 Hybridization effect between $j = 1/2$ and $j = 3/2$ states

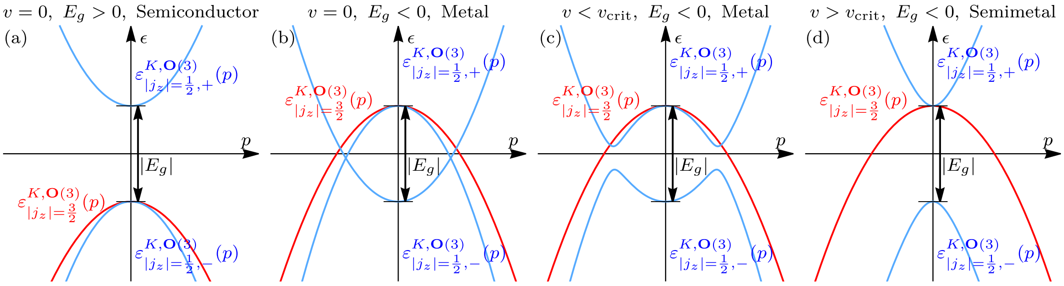

Figure 3.2: Schematic visualization of the effect of the hybridization $v$ between the $j = 1/2$ and $j = 3/2$ states in the $\mathbf{O}(3)$ symmetric Kane model [Eq. (3.65)], assuming $\gamma_{\frac{1}{2}} > 0$ and $\gamma_{\pm} < 0$. The dispersions of the Kane model are calculated with spherical symmetry, where the $|j_z| = 3/2$ heavy-hole states [Eq. (3.74)] decouple from the $|j_z| = 1/2$ electron and light-hole states [Eq. (3.73)]. (a) Usual band structure of a semiconductor, where the $s$-orbital states are above the $p$-orbital states in energy at $\mathbf{p} = 0$. This resembles the dispersion of materials, like GaAs. (b) Metal regime with a negative gap ($E_g < 0$), where the $s$ and $p$-orbital states are inverted at $\mathbf{p} = 0$. Without hybridization ($v = 0$), a crossing between the $|j_z| = 1/2$ states can be found. (c) With small hybridization [$v < v_{\mathrm{crit}}$ Eq. (3.77)], the crossing becomes an anti-crossing due to the coupling of the $|j_z| = 1/2$ states. (d) If the hybridization exceeds the critical value ($v > v_{\mathrm{crit}}$), the light-hole and electron state change character. Here, the light-hole state is electron-like and forms the conduction band, while the electron state becomes hole-like and gives an additional valence band inside the heavy-hole states. This chapter focuses on the quadratic-node semimetal phase (d), which can be found in materials like HgTe and $\alpha$-Sn.

This section shows the effect of the hybridization $v$ between the $j = 1/2$ and $j = 3/2$ states for full rotational symmetry $\mathbf{O}(3)$. We find that the Kane Hamiltonian $\hat{H}^K(\mathbf{p})$ from Eq. (3.65) decouples at $p_x = p_y = 0$ into two blocks corresponding to the sign of $j_z$. In the basis $(\left|\frac{1}{2};\pm\frac{1}{2}\right\rangle, \left|\frac{3}{2};\pm\frac{1}{2}\right\rangle, \left|\frac{3}{2};\pm\frac{3}{2}\right\rangle)^T$, the blocks have the form

$$\hat{H}^{K,\mathbf{O}(3)}(p_z) = \begin{pmatrix} E_g + \gamma_{\frac{1}{2}} p_z^2 & v p_z & 0 \\ v p_z & (\gamma_0 + 2\gamma_z) p_z^2 & 0 \\ 0 & 0 & (\gamma_0 - 2\gamma_z) p_z^2 \end{pmatrix}. \tag{3.72}$$

Here, one can see that the $|j_z| = 3/2$ HH state are fully decoupled from the $|j_z| = 1/2$ LH and electron states. Since we assume $\mathbf{O}(3)$ symmetry, we can replace the momentum $p_z$ with the general length of the momentum vector ($p_z \to p \equiv |\mathbf{p}|$). The block-like structure of Eq. (3.72) allows for easy diagonalization, which gives the overall double degenerate energy dispersion

$$\varepsilon^{K,\mathbf{O}(3)}_{|j_z|=\frac{1}{2},\pm}(p) = \frac{E_g + \left(\gamma_{\frac{1}{2}} + \gamma_+\right)p^2}{2} \pm \sqrt{v^2 p^2 + \left[\frac{E_g + \left(\gamma_{\frac{1}{2}} - \gamma_+\right)p^2}{2}\right]^2}, \tag{3.73}$$

$$\varepsilon^{K,\mathbf{O}(3)}_{|j_z|=\frac{3}{2}}(p) = \gamma_- p^2, \tag{3.74}$$

shown in Fig. 3.2. Here, we use $\gamma_\pm = \gamma_0 \pm 2\gamma_z$. For most materials with zinc-blende structure, the parameters of the Kane model have the constrictions $\gamma_{\frac{1}{2}} > 0$ and $\gamma_\pm < 0$.

To study the effect of the hybridization $v$, we expand Eq. (3.73) up to quadratic order in momentum

$$\varepsilon^{K,\mathbf{O}(3)}_{j=\frac{1}{2},|j_z|=\frac{1}{2}}(p) = E_g + \left(\gamma_{\frac{1}{2}} + \frac{v^2}{E_g}\right)p^2 + \mathcal{O}(p^4), \tag{3.75}$$

$$\varepsilon^{K,\mathbf{O}(3)}_{j=\frac{3}{2},|j_z|=\frac{1}{2}}(p) = \left(\gamma_+ - \frac{v^2}{E_g}\right)p^2 + \mathcal{O}(p^4). \tag{3.76}$$

The solution for the HH band [Eq. (3.74)] is already exact to second order in $p$.

The band structure of a typical semiconductor with a positive gap ($E_g > 0$), like GaAs, is shown in Fig. 3.2(a). Here, the HH and LH states for $j = 3/2$ form the valence band, while the electron $j = 1/2$ states give the conduction band. In this phase, the hybridization $v$ decreases the magnitude of the effective masses. The overall signs of the masses cannot be changed since $\gamma_{\frac{1}{2}} E_g > 0$ and $\gamma_+ E_g < 0$.

For materials with an inverted gap ($E_g < 0$), like HgTe or $\alpha$-Sn, the effect of the hybridization on the band structure is more significant. At $\mathbf{p} = 0$, the electron states are below the HH and LH states. Without hybridization ($v = 0$), the $|j_z| = 1/2$ states are not coupled, leading to a crossing at finite $p$ [see Fig. 3.2(b)]. This crossing is lifted under finite $v$, reopening a non-trivial gap between the $|j_z| = 1/2$ states [Fig. 3.2(c)]. From Eq. (3.76), one finds a critical hybridization

$$v_{\text{crit}}^2 = E_g \gamma_+, \tag{3.77}$$

where the LH states have a positive effective mass, giving an electron-like character, while the electron states become hole-like. The system is a quadratic-node semimetal for hybridizations that exceed the critical value, as shown in Fig. 3.2(d). Here, a fourfold degenerate node forms at the Fermi level, where the LH states are the conduction band and the HH states are the valence band. The $j = 1/2$ states form a remote band, separated by the gap $E_g$ inside of the HH continuum.

### 3.2.3 Derivation of Luttinger model from Kane model via a folding procedure

In this section, we show the effect of the $j = 1/2$ band on the parameters in the Luttinger model. Hence, we apply an effective folding procedure, called Löwdin partition theory [126, 119], to the 6-band Kane model from Eq. (3.65). This results in an effective 4-band model for the $j = 3/2$ states, including the effect of the hybridization to the $j = 1/2$ as a perturbation. Our derivation of the Luttinger parameters up to $\mathbf{O}_h$ symmetry is already discussed in Ref. [26]. Here, we show the effective BIA parameters additionally.

First, we write the Schrödinger equation for the 6-band Kane model $\hat{H}_K(\mathbf{p}) |\Psi_K\rangle = \epsilon |\Psi_K\rangle$ and exclude the $\left|\Psi_{\frac{1}{2}}\right\rangle$ states to get the effective folding equation for the $j = 3/2$ states

$$\left[\hat{H}_{\frac{3}{2}\frac{3}{2}}(\mathbf{p}) + \hat{H}_{\frac{3}{2}\frac{1}{2}}(\mathbf{p}) \frac{1}{\epsilon \hat{1}_2 - \hat{H}_{\frac{1}{2}\frac{1}{2}}(\mathbf{p})} \hat{H}_{\frac{1}{2}\frac{3}{2}}(\mathbf{p})\right] \left|\Psi_{\frac{3}{2}}\right\rangle = \epsilon \left|\Psi_{\frac{3}{2}}\right\rangle . \tag{3.78}$$

This equation acts as a Schrödinger equation for the original $j = 3/2$ states, modified by a correction term from the hybridization between the $j = 1/2$ and $j = 3/2$ states. We expand the correction term around the fourfold degenerate point of the $j = 3/2$

states $[(\epsilon, \mathbf{p}) = (0, 0)]$ to get the effective Schrödinger equation of the $j = 3/2$ states

$$\left[\hat{H}_{\frac{3}{2}\frac{3}{2}}(\mathbf{p}) + \hat{H}_{\frac{3}{2}\frac{1}{2}}(\mathbf{p})\frac{1}{0\hat{1}_2 - \hat{H}_{\frac{1}{2}\frac{1}{2}}(0)}\hat{H}_{\frac{1}{2}\frac{3}{2}}(\mathbf{p})\right]\left|\Psi_{\frac{3}{2}}\right\rangle = \epsilon\left|\Psi_{\frac{3}{2}}\right\rangle. \tag{3.79}$$

This expansion demands that the inverse in Eq. (3.79) is a small correction term. Hence, the validity condition of the folding procedure gives that the energy is far away from the $j = 1/2$ states $|\epsilon| \ll |E_g|$. Up to cubic order in momentum, this resembles the full Luttinger model, using

$$\left|\Psi_{\frac{3}{2}}\right\rangle \leftarrow |\Psi_L\rangle, \tag{3.80}$$

$$\hat{H}_{\frac{3}{2}\frac{3}{2}}(\mathbf{p}) + \hat{H}_{\frac{3}{2}\frac{1}{2}}(\mathbf{p})\frac{1}{0\hat{1}_2 - \hat{H}_{\frac{1}{2}\frac{1}{2}}(0)}\hat{H}_{\frac{1}{2}\frac{3}{2}}(\mathbf{p}) \leftarrow \hat{H}^{\mathbf{T}_d}(\mathbf{p}) + \mathcal{O}(\mathbf{p}^4), \tag{3.81}$$

where $\hat{H}^{\mathbf{T}_d}(\mathbf{p})$ is the full Luttinger Hamiltonian from Eq. (3.8) in the basis of $|\Psi_L\rangle$ from Eq. (3.1). By comparison, we can find the effective parameters of the Luttinger model

$$\alpha_0 = \gamma_0 - \frac{v^2}{2E_g}, \quad \alpha_z = \gamma_z - \frac{v^2}{4E_g}, \quad \alpha_\square = \gamma_\square. \tag{3.82}$$

From this, one can see that the coupling to the $j = 1/2$ states only changes the LH states to the lowest order since

$$\alpha_+ = \gamma_+ - v^2/E_g \quad \text{and} \quad \alpha_- = \gamma_-. \tag{3.83}$$

If the hybridization exceeds the critical value $v_{\text{crit}}$ [Eq. (3.77)] in a system with inverted band structure ($E_g < 0$), the LH states become electron-like ($\alpha_+ > 0$), even though the unhybridized state has hole-like nature ($\gamma_+ < 0$).

It is often discussed in the literature that materials like HgTe have topological surface states due to the inverted gap between the $j = 1/2$ and $j = 3/2$ states ($E_g < 0$) [7, 5]. The question arises of how the 4-band Luttinger model can host topological surface states when the $j = 1/2$ states are absent. Eq. (3.83) shows that the quadratic-node semimetal phase is only possible if $E_g < 0$. Hence, we argue that the topological nature of the inverted band structure is encoded in the $\alpha$ parameters of the Luttinger semimetal. Without an inverted band structure ($E_g > 0$), the Luttinger model is always in a metallic regime, which does not host surface states (see Sec. 3.5).

The folding procedure leads to a renormalization of the bare parameters of $\hat{H}_{\frac{3}{2}\frac{3}{2}}(\mathbf{p})$ by the hybridization. The shape of the renormalization term in Eq. (3.81) suggests that the lowest order term in $\hat{H}_{\frac{1}{2}\frac{3}{2}}(\mathbf{p})$, the linear momentum term $v$, can only appear as a correction term of quadratic order or higher. Therefore, the linear BIA term in the folded model is unchanged

$$\beta_1 = \beta_1^K. \tag{3.84}$$

The cubic BIA terms are affected by a combination of the quadratic BIA terms $B_\pm$ in one hybridization block and the linear $v$ term in the other. We find the renormalized cubic BIA terms of the Luttinger model

$$\beta_{31} = \beta_{31}^K + \frac{v\left(2B_+ - \frac{9}{2}B_-\right)}{\sqrt{6}E_g}, \qquad \beta_{32} = \beta_{32}^K + \frac{2vB_-}{\sqrt{6}E_g}, \tag{3.85}$$

$$\beta_{33} = \beta_{33}^K + \frac{vB_-}{3\sqrt{6}E_g}, \qquad \beta_{34} = \beta_{34}^K - \frac{2vB_-}{3\sqrt{6}E_g}. \tag{3.86}$$

We present the material-specific parameters of the Kane model and the resulting folded parameters of the Luttinger model for HgTe, $\alpha$-Sn, and GaAs in App. A.2. In this chapter, we use the $\mathbf{T}_d$ symmetric HgTe as an example to study the surface states in a WSM. Here, the bare quadratic and cubic BIA terms $B_\pm$ and $\beta_{3i}^K$ could not be found in the literature. Therefore, we consider $\beta_{3i}^K = 0$ and focus on $B_\pm$.

In Sec. 3.1.2, we showed that the gap around the Weyl points in the WSM phase of the Luttinger model is proportional to a linear combination of the cubic BIA terms. Now, using Eq. (3.50) we get

$$|\epsilon_2| \propto \left|\beta_{31} + \frac{7}{4}\beta_{32} + \beta_{33} - \beta_{34}\right| = \left|\frac{vB_+}{\sqrt{6}E_g}\right|. \tag{3.87}$$

Interestingly, $B_-$ cancels out, which suggests that $B_+$ is the most dominant higher-order BIA term. Hence, we set $B_- = 0$ and fit only the $B_+$ parameter to DFT band structure calculations (see Tab. A.1). Consequently, we agree with the approximation of Ref. [63] to only consider the $\beta_{31}$ parameter in the WSM calculations of the Luttinger model.

One often considers the well-known hard-wall boundary conditions to calculate surface states in the Kane model. For a sample occupying the $z > 0$ half-space, they read

$$|\Psi_K(x, y, z = 0)\rangle = 0. \tag{3.88}$$

This assumes that the system terminates at a usual insulator ($E_g > 0$), where the wavefunction needs to decay for $z \to -\infty$. At an interface with the vacuum ($E_g \to +\infty$), all components of $|\Psi_K(\mathbf{r})\rangle$ have to vanish already at the boundary $z = 0$. The Luttinger model does not include a gap, which makes the question for the boundary conditions of $|\Psi_L(\mathbf{r})\rangle$ non-trivial. Here, we only show the effective folded boundary conditions derived in Ref. [26]

$$|\Psi_L(x, y, z = 0)\rangle = 0. \tag{3.89}$$

While the physical interpretation is different in the absence of a gap, the effective boundary conditions have the same form as Eq. (3.88). Hence, we refer to them as hard-wall boundary conditions throughout this thesis.

## 3.3 Energy and momentum scales of the different phases in the Luttinger model

In the previous sections, we have introduced all possible topological semimetal phases of the Luttinger model and identified it as a low-energy model of the higher 6-band Kane model from Eq. (3.65). Each of the different phases has a characteristic parameter, which dominates the physical properties due to a specific gap opening in the spectrum.

To proceed with, we consider the 6-band Kane model as the highest order $k \cdot p$ model. As discussed in Sec. 3.2.1, it originates from a full 14-band Hamiltonian, which describes all possible interactions between $s$ and $p$-orbital states. Therefore, the Kane model is only valid up to a critical energy and momentum $(\epsilon_K^*, p_K^*)$ where the effect of the remote bands becomes relevant. The folding procedure explained in Sec. 3.2.3 restricts the validity of the 4-band Luttinger model to energies far away from the $j = 1/2$ states with a gap $E_g$. The DSM phase under compressive strain introduces a new gap opening around the $\Gamma$ point, given by the strength of the gap $2|u|$. The Dirac point splits into a ring-shaped line node under the linear BIA term. In the center of the line node, the energy bands are separated by $2|m| = 2\sqrt{3}|\beta_1|p_u$. In the WSM phase, the line node is lifted away from the high-symmetry planes $p_{x,y} = 0$ with a gap of the size $\varepsilon_{\beta_3}$, which we approximated by $|\epsilon_2|$ from Eq. (3.50) proportional to the cubic BIA $\beta_{3i}$ terms.

In HgTe, the relevant parameters for the different phases form a hierarchy

$$\varepsilon_{\beta_3} \ll |m| \lesssim |u| \ll |E_g| \ll \epsilon_K^*. \tag{3.90}$$

Each critical energy can be related to a critical momentum, which follows the same hierarchy

$$p_{\beta_3} \ll p_{\beta_1} \lesssim p_u \ll p_{E_g} \ll p_K^*, \tag{3.91}$$

with $p_{\beta_1}$ given in Eq. (3.48) and $p_u$ from Eq. (3.32). This suggests that the specific physical properties of a given semimetal phase are most relevant in the related energy and momentum range. So, e.g., in the WSM phase of the Luttinger model, the Weyl physics is most prominent in the energy range $|\epsilon - \varepsilon_W| \ll |m|$ around the Weyl point energy $\varepsilon_W$. After exceeding this range, the observed features will be dominated by the line-node physics in the regime $|\epsilon - \varepsilon_0] \ll |u|$ [see Eq. (3.46)]. For energies in the order of the strain, the features of the DSM dominate the WSM even without inversion symmetry. The BIA terms are often neglected in this regime.

This way, we can define an upper limit of each phase's energy and momentum regimes. Starting with the cut-off of the Kane model $(\epsilon_K^*, p_K^*)$, we can define the boundary of the Luttinger model

$$(\epsilon_L^*, p_L^*) = (|E_g|, p_{E_g}), \tag{3.92}$$

which demands that the energy must be far away from the $j = 1/2$ states.

The expansion to linear order in the DSM phase $\hat{\mathcal{H}}^D(\mathbf{k})$ from Eq. (3.52) is most precise in the vicinity of the Dirac points at $(\varepsilon_u, \mathbf{p}_u)$. Hence, we can find the critical energy and momentum where $\hat{\mathcal{H}}^D(\mathbf{k})$ is only valid for

$$|\epsilon - \varepsilon_u| \ll |u| \quad \text{and} \quad |\mathbf{p} \mp \mathbf{p}_u| \ll p_u. \tag{3.93}$$

The strength of the strain is a special parameter in this discussion. While the gap to the $j = 1/2$ states and the BIA terms are fixed for a given material, one can engineer the magnitude of $u$ by growing the sample on a different substrate. In this work, we assume that the strain is a continuous parameter. Considering that $|m| \propto p_u$, we find the relation

$$\frac{|m|}{|u|} \propto \sqrt{\frac{\beta_1^2}{\tilde{\alpha}_z |u|}}. \tag{3.94}$$

Therefore, the magnitude of the strain needs to be tuned to satisfy the hierarchy of Eq. (3.90) with $|m|/|u| \lesssim 1$.

It was discussed by Ruan et al. [63] that a significant small strain ($|m|/|u| > 1$) leads to a band structure with line-nodes in addition to the eight Weyl points, giving a type-II WSM phase, not discussed in this thesis. For a significant strong compressive strain $|u| \lesssim |E_g|$, the $j = 3/2$ states are close to the $j = 1/2$ states. Notice that this would violate the validity condition for the 4-band Luttinger model. We compare the Luttinger and Kane model in the WSM phase under different $u$ in Sec. 3.8.

## 3.4 Surface states in a semi-infinite system

The main results of this thesis regard the calculation and analysis of surface states in topological systems. A simple solution of the Schrödinger equation, where all momentum components are good quantum numbers, assumes an infinite extended sample. Here, we can only calculate the bulk states' dispersion. To compute the surface state dispersion, we use two different methods throughout this thesis. Chapter 4 considers systems of finite dimensionality, where two parallel boundaries exist along each spatial direction. We implement a tight-binding approach that discretizes the finite sample on a lattice structure, called the finite-difference method (see Sec. 4.3

for details).

This chapter analyzes surface states in semi-infinite samples with infinite length and only one boundary. While the method is applicable for any semi-infinite half-space, we demonstrate it on a 3D system occupying the $z > 0$ half-space with a surface at $z = 0$. Since translational symmetry in $x$ and $y$-direction is conserved, the in-plane momentum $(p_x, p_y)$ is a good quantum number and acts as a simple parameter. We take the ansatz of a plane-wave form of the surface state

$$|\Psi(x, y, z)\rangle = |\Psi(p_x, p_y, z)\rangle\, e^{i(p_x x + p_y y)}, \tag{3.95}$$

where the wavefunction $\hat{\Psi}(p_x, p_y, z)$ must be a solution to the Schrödinger equation

$$\hat{H}(p_x, p_y, \hat{p}_z)\, |\Psi(p_x, p_y, z)\rangle = \epsilon\, |\Psi(p_x, p_y, z)\rangle\,, \tag{3.96}$$

where $\hat{p}_z = -i\partial_z$ is the momentum operator and $\epsilon$ is the energy. The surface state needs to be localized at the system's surface, meaning that the wavefunction needs to decay into the bulk. Additionally, $|\Psi(p_x, p_y, z)\rangle$ needs to vanish at the interface to satisfy the continuity condition. Therefore, we get two general boundary conditions,

$$|\Psi(p_x, p_y, z \to +\infty)\rangle = 0, \tag{3.97}$$

$$|\Psi(p_x, p_y, z = 0)\rangle = 0. \tag{3.98}$$

We assume that the Hamiltonian of the system does not vary in $z$. Hence, we can solve Eq. (3.96) with the ansatz

$$|\Psi(p_x, p_y, z)\rangle = |\psi(\mathbf{p})\rangle\, e^{ip_z z}, \tag{3.99}$$

where $\mathbf{p} = (p_x, p_y, p_z)$ is the 3D momentum. The $z$-independent spinor $|\psi(\mathbf{p})\rangle$ satisfies the Schrödinger equation

$$\hat{H}(\mathbf{p})\, |\psi(\mathbf{p})\rangle = \epsilon\, |\psi(\mathbf{p})\rangle\,. \tag{3.100}$$

From Eq. (3.100), we get the characteristic equation

$$\det\left[\hat{H}(\mathbf{p}) - \epsilon\hat{1}\right] = 0, \tag{3.101}$$

with the unit matrix $\hat{1}$. To satisfy the boundary condition (3.97), we need to solve Eq. (3.101) for $p_z$ with a positive imaginary part.

In general, one can only find complex $p_z$ solutions in the gap of the projected surface bulk band structure

$$E_{-_b}(p_x, p_y) < \epsilon < E_{+_b}(p_x, p_y), \tag{3.102}$$

where $E_{\pm_b}(p_x, p_y)$ are the boundaries of the projected bulk states. They are given by the maximum and minimum values of the 3D bulk states relative to $p_z$,

$$E_{-_b}(p_x, p_y) = \max_{p_z} \epsilon_{-_b}(\mathbf{p}), \quad \text{and} \quad E_{+_b}(p_x, p_y) = \min_{p_z} \epsilon_{+_b}(\mathbf{p}). \tag{3.103}$$

In the gap, one finds $N_{p_z} \times N_H$ complex momentum $p_{zj}(p_x, p_y, \epsilon)$ solutions, where $N_{p_z}$ is the highest order of $p_z$ in the Hamiltonian and $N_H = 4$ is the size of the Hilbert space. Without the cubic BIA term $\hat{M}_{34}(\mathbf{p})$ [$\beta_{34} = 0$ in Eq. (3.14)], the Luttinger Hamiltonian is quadratic in $p_z$ ($N_{p_z} = 2$). We find $N_{p_z} \cdot N_H = 8$ complex momentum solutions, of which four have positive and four negative imaginary parts. For the considered system with $z > 0$, only the $\operatorname{Im} p_{zj}(p_x, p_y, \epsilon) > 0$ ($j \in \{1, 2, 3, 4\}$) solutions lead to a decaying wavefunction into the bulk.

In conclusion, the general solution for the surface-state wavefunction at given energy $\epsilon$ reads

$$|\Psi(p_x, p_y, z, \epsilon)\rangle = \sum_{j=1}^{4} c_j \, |\psi_j(p_x, p_y, \epsilon)\rangle \, e^{ip_{zj}(p_x, p_y, \epsilon)z}, \tag{3.104}$$

with the arbitrary coefficients $c_j$. We combine Eqs. (3.104) and (3.98) to get the effective matrix equation

$$\hat{\chi}(p_x, p_y, \epsilon)\boldsymbol{c} = 0, \tag{3.105}$$

with

$$\hat{\chi}(p_x, p_y, \epsilon) = \Big( |\psi_1(p_x, p_y, \epsilon)\rangle \quad \dots \quad |\psi_4(p_x, p_y, \epsilon)\rangle \Big) \quad \text{and} \quad \boldsymbol{c} = \begin{pmatrix} c_1 \\ c_2 \\ c_3 \\ c_4 \end{pmatrix}. \tag{3.106}$$

We can find the non-trivial solutions of Eq. (3.105) by solving

$$\det \hat{\chi}(p_x, p_y, \epsilon) = 0. \tag{3.107}$$

The solutions to this characteristic equation give the surface-state dispersion $\epsilon = \mathcal{E}(p_x, p_y)$.

Including the $\hat{M}_{34}(\mathbf{p})$ cubic BIA term increases the highest order of $p_z$ to cubic in the Hamiltonian. Following the discussion above, this leads to 12 complex momentum solutions, from which six satisfy BC (3.97). A significant problem arises if the gap in the projected bulk states remains: $\hat{\chi}(p_x, p_y, \epsilon)$ is now a $6 \times 4$ non-square matrix, where the determinant is not defined.

To resolve this problem, we make use of the momentum scales of the specific terms in the Hamiltonian, as discussed in Sec. 3.3. In the scale of the cubic BIA terms ($p \sim \alpha_z/\beta_3$), we can differentiate the momentum solutions $p_{zj}(p_x, p_y, \epsilon)$ into two groups. The first group consists of the typical eight complex momenta, also present without cubic BIA terms. The second group is built from the additional momenta, which are of a much larger magnitude due to $\alpha_z \gg \beta_3$. Since the momentum solutions of the second group exceed the validity range of the Luttinger model, we can discard them and proceed with the calculation only with group one. This resolves $\hat{\chi}(p_x, p_y, \epsilon)$ into a square matrix, where the determinant is well defined.

## 3.5 Quadratic node Luttinger semimetal phase

### 3.5.1 Chiral symmetric nodal model as the parent model

Another point that we discuss throughout this thesis, is the evolution of the topological features of the Luttinger model under symmetry lowering perturbations. While it can be considered as a low-energy approximation model of a full $k \cdot p$ model, it is instructive to look at it from a different perspective. The quadratic-node Luttinger semimetal phase is gapless, which does not allow associating a topological invariant. For this reason, we take a general chiral-symmetric nodal semimetal model in 2D and analyze the properties of the topological edge states. The discussion is presented in detail in Ref. [26]. We summarize the results relevant to the full Luttinger model in this section.

We consider the Hamiltonian of a chiral-symmetric nodal semimetal in the two-state basis $\hat{\psi}(x, y) = (\psi_a(x, y), \psi_b(x, y))^T$

$$\hat{H}_N(\mathbf{p}) = \begin{pmatrix} 0 & p_-^N \\ p_+^N & 0 \end{pmatrix}, \tag{3.108}$$

with $p_\pm = p_x \pm i p_y$ and the integer $N \in \mathbb{N}$ giving the momentum order of the node. Following the method of Ref. [127], we find that the winding number of the node is given by $N$, indicating a non-trivial topological behavior.

Assuming a semi-infinite system that occupies the $y > 0$ half-plane, $p_x$ is still a good quantum number, while $p_y$ needs to be replaced with the momentum operator $\hat{p}_y = -i\partial_y$. We take the Schrödinger equation

$$\hat{H}_N(p_x, \hat{p}_y)\hat{\psi}(x, y) = \epsilon\hat{\psi}(x, y), \tag{3.109}$$

with a plane-wave ansatz

$$\hat{\psi}(x, y) = \hat{\psi}(p_x, y)e^{ip_x x}. \tag{3.110}$$

Using the method described in Sec. 3.4, we can show that only flat edge states exist with

$$\mathcal{E}_N = 0. \tag{3.111}$$

Therefore, the Schrödinger equation gives two equations for the edge states

$$(p_x + \partial_y)^N \psi_a(p_x, y) = 0, \qquad (p_x - \partial_y)^N \psi_b(p_x, y) = 0, \tag{3.112}$$

which each have $N$ independent solution

$$\psi_{an}(p_x, y) = y^n e^{-p_x y}, \qquad \psi_{bn}(p_x, y) = y^n e^{p_x y}, \tag{3.113}$$

with $n = 0, \ldots, N-1$. Since the wavefunction needs to decay into the bulk $y \to \infty$, we find that $\psi_{an}(p_x, y)$ is only an edge-state solution for $p_x > 0$ and $\psi_{bn}(p_x, y)$ only for $p_x < 0$. To select the correct solutions, additional boundary conditions have to be applied.

In Ref. [26], we derived the asymptotic chiral-symmetric current-conserving boundary conditions for $\hat{H}_N(\mathbf{p})$. They come from the restriction that the probability current perpendicular to the boundary must vanish at the boundary $[j_y(x, y = 0) = 0]$. We can divide them into $N + 1$ groups $(N_a, N_b)$, with $N_{a,b} = 0, \ldots, N$ and $N_a + N_b = N$. The list of all possible boundary conditions is given by

$$\psi_a, \ldots, \partial_y^{N_a - 1}\psi_a, \psi_b, \ldots, \partial_y^{N_b - 1}\psi_b = 0. \tag{3.114}$$

Therefore, we get the general edge states for the group $(N_a, N_b)$

$$\hat{\psi}_n(p_x > 0, y) = \begin{pmatrix} 1 \\ 0 \end{pmatrix} y^n e^{-p_x y} \quad \text{with} \quad n = N_a, \ldots, N-1 \tag{3.115}$$

$$\hat{\psi}_n(p_x < 0, y) = \begin{pmatrix} 0 \\ 1 \end{pmatrix} y^n e^{p_x y} \quad \text{with} \quad n = N_b, \ldots, N-1. \tag{3.116}$$

We conclude that a chiral symmetric linear node ($N = 1$) has one flat edge state, while a quadratic node ($N = 2$) hosts two edge states. To show the relationship between the Luttinger model and $\hat{H}_{N=2}(\mathbf{p})$, we consider $\hat{H}^{\mathbf{O}(3)}(p_x, p_y, 0)$ [Eq. (3.9)] at $p_z = 0$. Here, the Hamiltonian decouples into two blocks of opposite chiralities. One block describes the $(\left|\frac{3}{2}, +\frac{3}{2}\right\rangle, \left|\frac{3}{2}, -\frac{1}{2}\right\rangle)$ states in the form of

$$\hat{h}^{\mathbf{O}(3)}_{+\frac{3}{2},-\frac{1}{2}}(p_x, p_y) = \begin{pmatrix} (\alpha_0 + \alpha_z)p_\perp^2 & -\sqrt{3}\alpha_z p_-^2 \\ -\sqrt{3}\alpha_z p_+^2 & (\alpha_0 - \alpha_z)p_\perp^2 \end{pmatrix}. \tag{3.117}$$

By comparison, we can see that one block of the Luttinger model at $p_z = 0$ resembles $\hat{H}_{N=2}(\mathbf{p})$ with additional chiral symmetry breaking terms on the diagonal. We show in Ref. [26] and the following section that the edge states of the Luttinger model correspond to the $(N_a, N_b) = (1, 1)$ class with one edge state on either side of the node. The chiral symmetry-breaking terms give a finite curvature to the edge states without destroying them entirely. Therefore, we can consider the quadratic chiral symmetric node with an $N = 2$ winding number as the parent model of the Luttinger Hamiltonian with non-trivial topology.

### 3.5.2 Surface states of the quadratic-node Luttinger semimetal

In this section, we calculate the surface states of the Luttinger model $\hat{H}^{\mathbf{O}(3)}(\mathbf{p})$ from Eq. (3.9). For full rotational symmetry, all surface orientations are equivalent. Here, we use $p_\perp$ as a notation for the general momentum perpendicular to the boundary.

First, we need to find the boundaries of the bulk spectrum. From Eq. (3.28), we find

$$E^L_{\pm_b}(p_\perp) = \alpha_z \bar{\alpha}_{\pm_b} p_\perp^2, \quad \text{with} \quad \bar{\alpha}_{\pm_b} = \bar{\alpha}_0 \pm 2. \tag{3.118}$$

The effective mass of the bulk boundary states is given by $\alpha_z$, modified by the dimensionless parameter $\bar{\alpha}_{\pm_b}$. The '+' ('−') subscript indicates the LH (HH) bands. At finite $p_\perp$, the projected LH states are consistently above the HH states ($E^L_{+_b}(p_\perp) > E^L_{-_b}(p_\perp)$) in the semimetal regime since $\alpha_z > 0$. A local gap

$$\left|E^L_{+_b}(p_\perp) - E^L_{-_b}(p_\perp)\right| = 4|\alpha_z|p_\perp^2 \tag{3.119}$$

separates them.

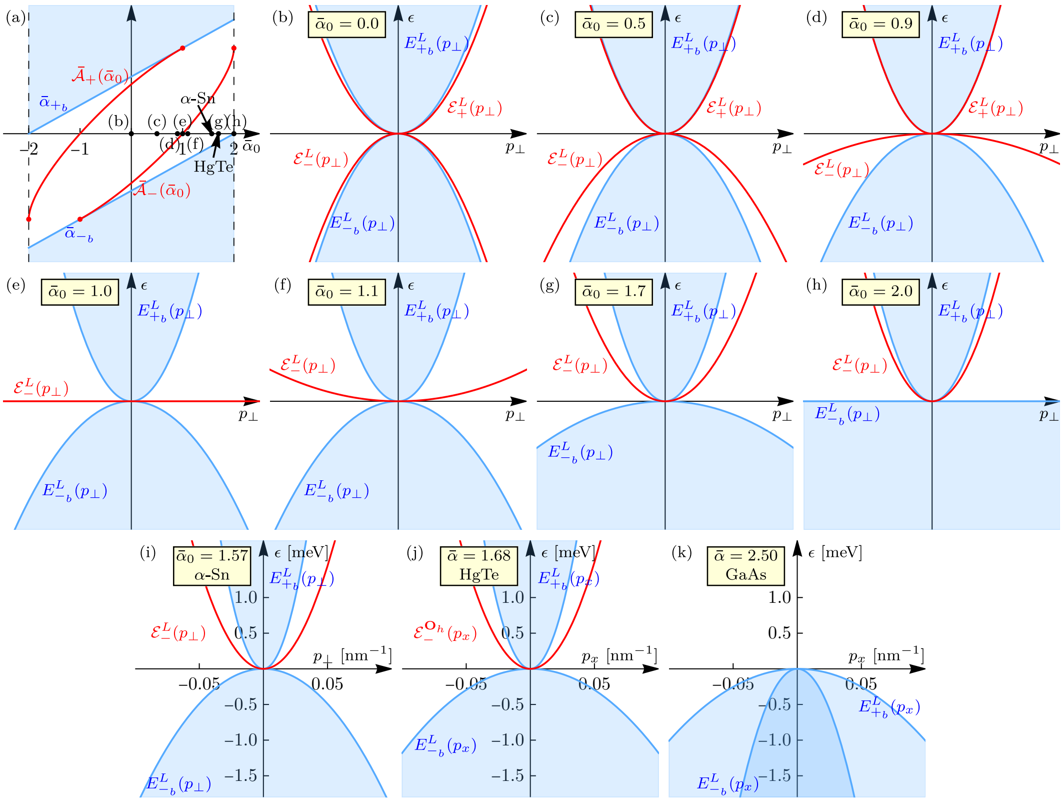

Figure 3.3: Surface band structure of the unperturbed Luttinger model (3.9) for a semi-infinite sample with arbitrary surface orientation due to symmetry. (a) Curvature of the projected bulk band boundaries $\alpha_{\pm_b}$ [Eq. (3.118)] (blue) and the surface states $\bar{\mathcal{A}}_\pm(\bar{\alpha}_0)$ [Eqs. (3.120) and (3.121)] (red) as a function of the effective mass ratio $\bar{\alpha}_0 = \alpha_0/\alpha_z$. The red points highlight the critical point, where a surface state disappears. The dashed lines give the boundaries of the semimetal phase of the Luttinger model ($|\bar{\alpha}_0| \leq 2$). (b-h) Surface dispersion of the projected bulk band boundaries $E^L_{\pm_b}(p_\perp)$ (blue) and the surface states $\mathcal{E}^L_\pm(p_\perp)$ (red). We show the evolution of the band structure for different mass ratios (b) $\bar{\alpha}_0 = 0$ with particle-hole symmetry, (c) $\bar{\alpha}_0 = 0.5$, (d) $\bar{\alpha}_0 = 0.9$, (e) $\bar{\alpha}_0 = 1.0$ where $\mathcal{E}^L_+(p_\perp)$ merges with the bulk and $\mathcal{E}^L_-(p_\perp)$ is flat, (f) $\bar{\alpha}_0 = 1.1$, (g) $\bar{\alpha}_0 = 1.7$, and (h) $\bar{\alpha}_0 = 2.0$ the limit of the semimetal phase with a flat valence band. (i-j) Surface band structure for realistic material parameters (Tab. A.2) with the cubic anisotropy ($\bar{\alpha} = \alpha_0/\tilde{\alpha}_z$, $\tilde{\alpha}_z = \alpha_z - \frac{3}{10}\alpha_\square$) [Eqs. (3.122) and (3.123)]. (i) α-Sn, (j) HgTe, and (k) GaAs in the metallic regime [128, 129].

Applying the method from Sec. 3.4, we find the surface states of the $\mathbf{O}(3)$ Luttinger model

$$\mathcal{E}^L_+(p_\perp) = \bar{\mathcal{A}}_+(\bar{\alpha}_0)\alpha_z p_\perp^2 \equiv \frac{1}{2}\left(3\bar{\alpha}_0 + \sqrt{3}\sqrt{4-\bar{\alpha}_0^2}\right)\alpha_z p_\perp^2 \quad \text{for} \quad -2 \leq \bar{\alpha}_0 < 1, \tag{3.120}$$

$$\mathcal{E}^L_-(p_\perp) = \bar{\mathcal{A}}_-(\bar{\alpha}_0)\alpha_z p_\perp^2 \equiv \frac{1}{2}\left(3\bar{\alpha}_0 - \sqrt{3}\sqrt{4-\bar{\alpha}_0^2}\right)\alpha_z p_\perp^2 \quad \text{for} \quad -1 < \bar{\alpha}_0 \leq 2. \tag{3.121}$$

One can see that it follows a quadratic behavior in momentum with the overall effective mass $\alpha_z$, which is modified by the dimensionless surface-state parameters $\bar{\mathcal{A}}_\pm(\bar{\alpha}_0)$. The evolution of the surface band structure under $\bar{\alpha}_0$ is shown in Fig. 3.3(a).

For $\bar{\alpha}_0 = 0$ [Fig. 3.3(b)], the bulk bands and the surface states are both particle-hole symmetric, with $\bar{\alpha}_{+_b} = -\bar{\alpha}_{-_b}$ and $\bar{\mathcal{A}}_+(\bar{\alpha}_0 = 0) = -\bar{\mathcal{A}}_-(\bar{\alpha}_0 = 0)$. The existence of two surface states is related to the chiral symmetric quadratic node $\hat{H}_{N=2}$ from Sec. 3.5.1. Considering the decoupled block $\hat{h}^{\mathbf{O}(3)}_{+\frac{3}{2},-\frac{1}{2}}(p_x, p_y)$ [Eq. (3.117)], we find that the $\mathcal{E}^L_\pm(p_\perp)$ surface states exist at $p_\perp \gtrless 0$, respectively, which corresponds to the $(N_a, N_b) = (1,1)$ boundary condition class. The diagonal terms of $\hat{h}^{\mathbf{O}(3)}_{+\frac{3}{2},-\frac{1}{2}}(p_x, p_y)$ give a finite curvature to the flat edge states of Eq. (3.111). Therefore, the surface states of the Luttinger semimetal are related to the well-defined $N = 2$ topological invariant without the requirement of explicit chiral symmetry. The Kramers' partner surface states at opposite momentum arise from the $(\left|\frac{3}{2}, +\frac{1}{2}\right\rangle, \left|\frac{3}{2}, -\frac{3}{2}\right\rangle)$ block.

A finite $\bar{\alpha}_0$ introduces a difference in the effective masses. For $0 < \bar{\alpha}_0 < 1$ [Figs. 3.3(c,d)], the $\mathcal{E}^L_+(p_\perp)$ surface state moves closer to the conduction band continuum, while the $\mathcal{E}^L_-(p_\perp)$ surface state becomes flatter. The critical point $\bar{\alpha}_0 = 1$ [Fig. 3.3(e)] gives a conceptional transition in the surface band structure. Here, the $\mathcal{E}^L_-(p_\perp)$ surface state is flat, since $\bar{A}_-(\bar{\alpha}_0 = 1) = 0$. Additionally, we find that $\bar{A}_+(\bar{\alpha}_0 = 1) = \bar{\alpha}_{+_b}$, meaning that the $\mathcal{E}^L_+(p_\perp)$ surface state merges with the bulk continuum and does not reappear for $\bar{\alpha}_0 > 1$.

In the $1 < \bar{\alpha}_0 \leq 2$ regime, the remaining $\mathcal{E}^L_-(p_\perp)$ surface state changes from hole-like to electron-like character $\operatorname{sgn}(\bar{\mathcal{A}}_-(0 \leq \bar{\alpha}_0 < 1)) \neq \operatorname{sgn}(\bar{\mathcal{A}}_-(1 < \bar{\alpha}_0 \leq 2))$. This can be seen in Figs. 3.3(f-h), the surface state bends closer to the conduction band. The case $\bar{\alpha}_0 = 1.7$ [Fig. 3.3(g)] is shown as a representation for both $\alpha$-Sn ($\bar{\alpha}_0 \approx 1.57$) and an $\mathbf{O}(3)$ symmetric approximation of HgTe ($\bar{\alpha}_0 \approx 1.77$). As discussed in Sec. 3.1.2, the valence band is flat at $\bar{\alpha}_0 = 2$, which gives the upper limit in $\bar{\alpha}_0$ for the semimetal regime of the Luttinger model. In the metallic regime ($|\bar{\alpha}_0| > 2$), the surface states disappear since $\mathcal{E}^L_\pm(p_\perp)$ becomes complex.

With the cubic anisotropy, we can only solve analytically for the surface states at $p_y = 0$. We find

$$\mathcal{E}^{\mathbf{O}_h}_+(p_x) = \frac{1}{2}\tilde{\alpha}_z p_x^2\left(3\bar{\alpha} + \sqrt{3}\sqrt{4-\bar{\alpha}^2}\right) \quad \text{for} \quad -2 \leq \bar{\alpha} < 1, \tag{3.122}$$

$$\mathcal{E}^{\mathbf{O}_h}_-(p_x) = \frac{1}{2}\tilde{\alpha}_z p_x^2\left(3\bar{\alpha} - \sqrt{3}\sqrt{4-\bar{\alpha}^2}\right) \quad \text{for} \quad -1 < \bar{\alpha} \leq 2, \tag{3.123}$$

with $\bar{\alpha} = \alpha_0/\tilde{\alpha}_z$ and $\tilde{\alpha}_z = \alpha_z - \frac{3}{10}\alpha_\square$. Lowering the symmetry from $\mathbf{O}(3) \to \mathbf{O}_h$, does not change the surface states significally. Along the high symmetry lines $p_{x,y} = 0$, the effective mass is only renormalized by the cubic anisotropy with the substitution $\bar{\alpha}_0 \to \bar{\alpha}$.

In Figs. 3.3(i-k), we present the surface band structure for realistic material parameters listed in Tab. A.2. The lattice of $\alpha$-Sn [Fig. 3.3(i)] is $\mathbf{O}(3)$ symmetric with $\bar{\alpha}_0 = 1.57$. Therefore, it hosts one electron-like surface state. HgTe shows a similar behavior with finite cubic anisotropy ($\bar{\alpha} \approx 1.68$). We neglect the BIA terms in Fig. 3.3(j), which we show to be reasonable in this momentum scale in Sec. 3.8. In Fig. 3.3(k), we show the band structure of the metallic regime in the Luttinger model, where we exemplarily pick p-doped GaAs. While the general Luttinger model does not host surface states, it has remarkable physical features in the superconducting phase, as discussed in Chapter 4.

### 3.5.3 Limits of the Luttinger model for large momentum

Throughout this chapter, we established the relation between the 4-band Luttinger model and the 6-band Kane model. As a low-energy approximation, the Luttinger model is only valid for energies far from the $j = 1/2$ states. In this section, we compare the surface band structure of both models in the quadratic-node semimetal regime to analyze this validity range.

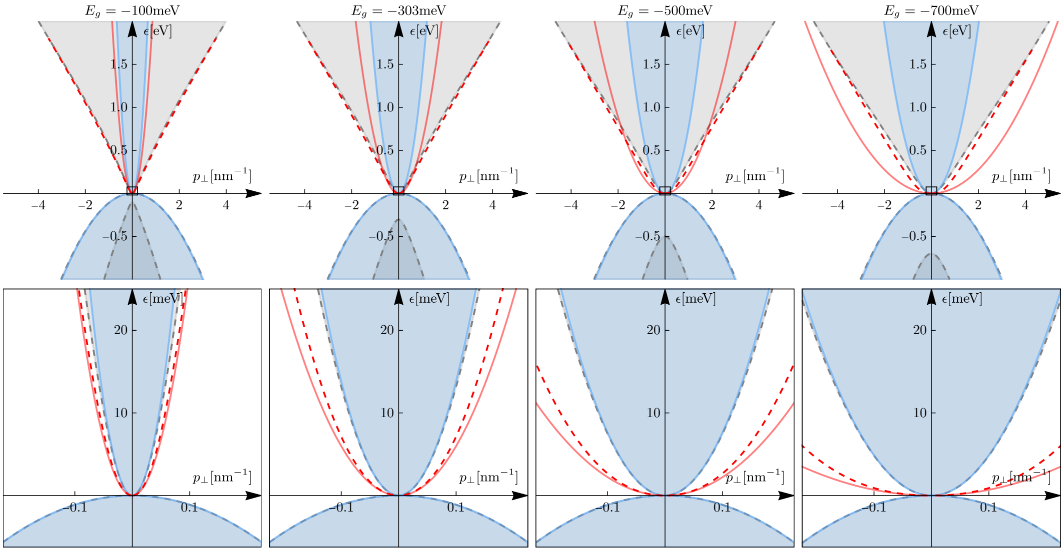

Figure 3.4: Comparison of the surface band structure of the quadratic-node semimetal phase of the Luttinger model $\hat{H}^{\mathbf{O}_h}(\mathbf{p})$ [Eq. (3.7)] and the Kane model [Eq. (3.65)]. The bulk continuum of the Luttinger (Kane) model is shown in blue (dashed gray), and the surface state is drawn in red (dashed orange). The columns correspond to different values of $E_g$, which is the gap between the $j = 1/2$ and $j = 3/2$ states. We use the effective masses of HgTe (see Tab. A.1) with artificial $E_g$ for the Kane model and the corresponding folded parameters from Eq. (3.82) in the Luttinger model. The framed plots in the second row show a zoom-in around the quadratic node, indicated by the framed inset in the top row.

In Fig. 3.4, we show the band structure calculations for the effective masses of HgTe [see Tab. A.1] with an artificially chosen energy gap $E_g$ between the $j = 1/2$ and $j = 3/2$ states. The effective $\alpha$-parameters of the Luttinger model are computed according to Eq. (3.82).

The large energy range in the top row of Fig. 3.4 reveals the conceptional difference between the two models far away from the $\Gamma$ point. Since the surface states and the bulk continuum of the Luttinger model are proportional to $p_\perp^2$, there is no critical momentum where both states merge. Hence, the Luttinger-surface-states exist in the entire surface Brillouin zone. The Kane-surface-states merge with the bulk continuum at considerable momentum when the linear terms of the $\hat{H}_{\frac{1}{2}\frac{3}{2}}(\mathbf{p})$ coupling block from Eq. (3.65) become dominant. This is related to the inverse gap between the $j = 1/2$ and $j = 3/2$ bands ($E_g < 0$), leading to topological surface states connecting the LH and $j = 1/2$ band. The method used in this chapter does not show any surface states inside the bulk continuum since the wavefunction gets oscillating components.

Larger magnitudes of $E_g$ lead to an increased validity range of the Luttinger model in momentum and energy. Here, the band structure of the Luttinger model is in good agreement with the Kane model, as shown in the framed plots of Fig. 3.4. This behavior is related to the folding procedure of Eq. (3.79), where the effect of the correction term decreases.

## 3.6 Dirac semimetal phase under compressive strain

In the previous section, we established that the quadratic-node Luttinger semimetal hosts either one or two surface states. This section discusses the behavior of these surface states under the application of compressive strain.

From the bulk dispersion calculations in Sec. 3.1.2, we know that compressive strain in the $z$-direction splits the quadratic node into two double-degenerate linear Dirac nodes at $\mathbf{p} = (0, 0, \pm p_u)$. The bulk dispersion and the Brillouin zone are shown in Fig. 3.1. While the surface orientation in the Luttinger semimetal phase is inconsequential, it is significant in the DSM phase. The separation of the Dirac points along the $p_z$-axis lead to two separate classes of surface Brillouin zones. On the $z = 0$ surface parallel to the strain, both Dirac points are projected onto each other. This section shows that this case is closely related to the chiral symmetric linear node $\hat{H}_{N=1}(\mathbf{p})$ from Eq. (3.108). Any different surface orientation has two separated Dirac points in the projected band structure. Even though the Dirac points have zero chirality, it is possible to find a double Fermi arc, as discussed in Sec. 2.2.2. In this thesis, we concentrate on a surface perpendicular to the strain, where the separation of the Dirac points is the largest. While any perpendicular surface orientation is physically equivalent, we use a boundary at $y = 0$ as an example in this section.

### 3.6.1 Surface perpendicular to the strain

We assume a sample that occupies the $y < 0$ half-space with a surface at $y = 0$. Here, the two Dirac points are separated in the projected surface Brillouin zone.

First, we consider the linearized Hamiltonian $\hat{\mathcal{H}}^{D,\pm_u}(\boldsymbol{k})$ from Eq. (3.53). The bulk boundaries with respect to $k_y$ are given by

$$E^{\pm_u}_{\pm_b}(k_x, k_z) = \varepsilon_u \pm_u v_0 k_z \pm \sqrt{v_\perp^2 k_x^2 + 4 v_z^2 k_z^2}. \tag{3.124}$$

To calculate the surface states, we need to establish the effective boundary conditions of the linearized model. Therefore, we compute the wavefunctions at the Dirac points

$[(p_x, p_z, \epsilon) = (0, \pm p_u, \varepsilon_u)]$ from the full Hamiltonian $\hat{H}^D(\mathbf{p})$ [Eq. (3.22)]

$$|\Psi_{+_u}(y)\rangle = \begin{pmatrix} \psi^{+_u}_{+\frac{3}{2}} \\ \psi^{+_u}_{+\frac{1}{2}} \\ \psi^{+_u}_{-\frac{1}{2}} \\ \psi^{+_u}_{-\frac{3}{2}} \end{pmatrix} + \left[ c_1^{+_u} \begin{pmatrix} \sqrt{4v_z^2 - v_0^2} \\ v_0 + v_z \\ 0 \\ -\sqrt{3}v_z \end{pmatrix} + c_2^{+_u} \begin{pmatrix} v_0 - v_z \\ -\sqrt{4v_z^2 - v_0^2} \\ -\sqrt{3}v_z \\ 0 \end{pmatrix} \right] e^{\kappa y}, \quad (3.125)$$

$$|\Psi_{-_u}(y)\rangle = \begin{pmatrix} \psi^{-_u}_{+\frac{3}{2}} \\ \psi^{-_u}_{+\frac{1}{2}} \\ \psi^{-_u}_{-\frac{1}{2}} \\ \psi^{-_u}_{-\frac{3}{2}} \end{pmatrix} + \left[ c_1^{-_u} \begin{pmatrix} -\sqrt{4v_z^2 - v_0^2} \\ v_0 + v_z \\ 0 \\ -\sqrt{3}v_z \end{pmatrix} + c_2^{-_u} \begin{pmatrix} v_0 - v_z \\ \sqrt{4v_z^2 - v_0^2} \\ -\sqrt{3}v_z \\ 0 \end{pmatrix} \right] e^{\kappa y}, \quad (3.126)$$

where $\kappa = 2p_u v_\perp / \sqrt{4v_z^2 - v_0^2}$, $\psi^{\pm_u}_{j_z}$ corresponds to the elements of the wavevector in the linearized model, and $c^{\pm_u}_{1,2}$ are constant coefficients. In general, the wavefunction of the surface states cannot grow into the sample $y \to -\infty$. We can apply the hard-wall boundary condition $|\Psi_{\pm_u}(y = 0)\rangle = 0$ to eliminate the $c^{\pm_u}_{1,2}$ constants and get the four effective boundary conditions for the linearized model

$$\sqrt{3}\psi^{+_u}_{+\frac{3}{2}} + (\bar{v}_0 - 1)\psi^{+_u}_{-\frac{1}{2}} + \sqrt{4 - \bar{v}_0^2}\psi^{+_u}_{-\frac{3}{2}} = 0, \quad (3.127)$$

$$\sqrt{3}\psi^{+_u}_{+\frac{1}{2}} + (\bar{v}_0 + 1)\psi^{+_u}_{-\frac{3}{2}} - \sqrt{4 - \bar{v}_0^2}\psi^{+_u}_{-\frac{1}{2}} = 0, \quad (3.128)$$

$$\sqrt{3}\psi^{-_u}_{+\frac{3}{2}} + (\bar{v}_0 - 1)\psi^{-_u}_{-\frac{1}{2}} - \sqrt{4 - \bar{v}_0^2}\psi^{-_u}_{-\frac{3}{2}} = 0, \quad (3.129)$$

$$\sqrt{3}\psi^{-_u}_{+\frac{1}{2}} + (\bar{v}_0 + 1)\psi^{-_u}_{-\frac{3}{2}} + \sqrt{4 - \bar{v}_0^2}\psi^{-_u}_{-\frac{1}{2}} = 0, \quad (3.130)$$

with $\bar{v}_0 = v_0/v_z$. While the $j_z > 0$ and $j_z < 0$ states are decoupled in the Hamiltonian, we find that the effective boundary conditions introduce a hybridization between the blocks. Additionally, we see that the $+_u$ and $-_u$ states are completely independent for the $y = 0$ surface orientation.

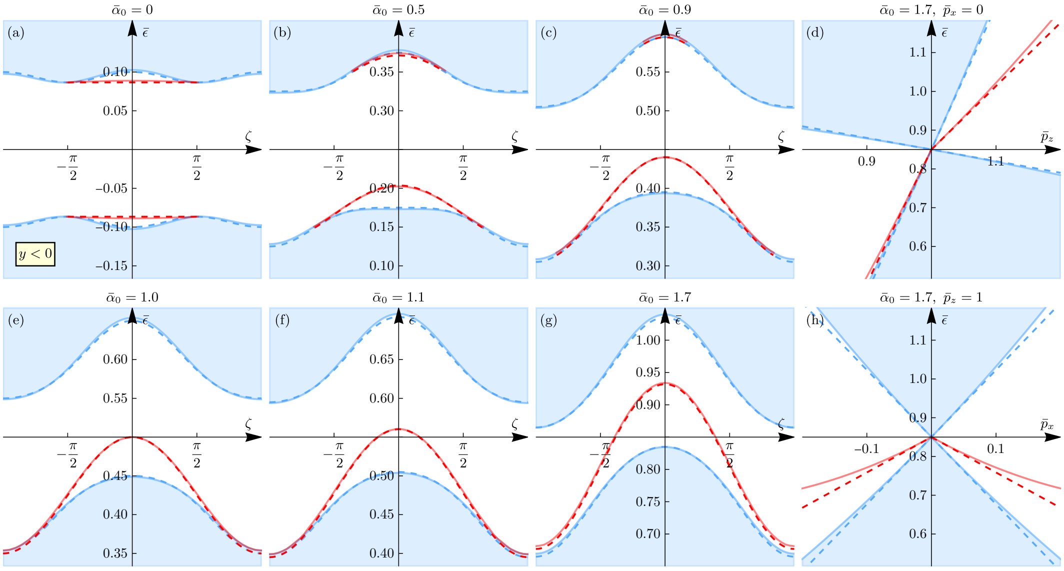

Figure 3.5: Comparison of the $y = 0$ surface band structure of the full quadratic Luttinger model with compressive strain $\hat{H}^D(\mathbf{p})$ [Eq. (3.22)] (solid lines) and the linearized model $\hat{\mathcal{H}}^D(\mathbf{k})$ [Eq. (3.52)] (dashed lines). The linearized model gives the projected bulk boundaries by $E^{\pm_u}_{\pm_b}(k_x, k_z)$ [Eq. (3.124)] (dashed blue) and the surface states by $\mathcal{E}^{\pm_u}_{\pm, y<0}(k_x, k_z)$ [Eq. (3.136)] (dashed red), while the states in the full model are calculated numerically. (a-c, e-g) Polar momentum coordinates, with $(\bar{p}_x, \bar{p}_z) = (\bar{p}_r \sin\zeta, 1 + \bar{p}_r \cos\zeta)$ and $(k_x, k_z) = \bar{p}_r p_u(\sin\zeta, \cos\zeta)$ for $\bar{p}_r = 0.05$. The evolution under the effective mass ratio is shown, with (a) $\bar{\alpha}_0 = 0$, (b) $\bar{\alpha}_0 = \alpha_0/\alpha_z = 0.5$, (c) $\bar{\alpha}_0 = 0.9$, (e) $\bar{\alpha}_0 = 1.0$, (f) $\bar{\alpha}_0 = 1.1$, and (g) $\bar{\alpha}_0 = 1.7$. (d,h) Dispersion for a constant momentum component (d) $\bar{p}_x = 0$ ($k_x = 0$) and (h) $\bar{p}_z = 1$ ($k_z = 0$) for $\bar{\alpha}_0 = 1.7$. We use the dimensionless units $\bar{\epsilon} = \epsilon/|u|$ [Eq. (3.36)] and $\bar{p}_i = p_i/p_{u0}$ [Eq. (3.35)].

Following the method of Sec. 3.4, one can calculate the surface states in the linearized model

$$\left|\Psi^{+_u}_{j_z>0}(y,\mathbf{k},\epsilon)\right\rangle = c^{+_u}_{j_z>0}\begin{pmatrix} v_\perp k_x - \sqrt{v_\perp^2 k_x^2 + 4v_z^2k_z^2 - (v_0k_z-\epsilon)^2} \\ (v_0 - 2v_z)k_z - \epsilon \end{pmatrix} e^{\kappa_{+_u} y}, \tag{3.131}$$

$$\left|\Psi^{+_u}_{j_z<0}(y,\mathbf{k},\epsilon)\right\rangle = c^{+_u}_{j_z<0}\begin{pmatrix} -v_\perp k_x + \sqrt{v_\perp^2 k_x^2 + 4v_z^2k_z^2 - (v_0k_z-\epsilon)^2} \\ (v_0 + 2v_z)k_z - \epsilon \end{pmatrix} e^{\kappa_{+_u} y}, \tag{3.132}$$

$$\left|\Psi^{-_u}_{j_z>0}(y,\mathbf{k},\epsilon)\right\rangle = c^{-_u}_{j_z>0}\begin{pmatrix} -v_\perp k_x + \sqrt{v_\perp^2 k_x^2 + 4v_z^2k_z^2 - (v_0k_z+\epsilon)^2} \\ -(v_0 - 2v_z)k_z - \epsilon \end{pmatrix} e^{\kappa_{-_u} y}, \tag{3.133}$$

$$\left|\Psi^{-_u}_{j_z<0}(y,\mathbf{k},\epsilon)\right\rangle = c^{-_u}_{j_z<0}\begin{pmatrix} v_\perp k_x - \sqrt{v_\perp^2 k_x^2 + 4v_z^2k_z^2 - (v_0k_z+\epsilon)^2} \\ -(v_0 + 2v_z)k_z - \epsilon \end{pmatrix} e^{\kappa_{-_u} y}, \tag{3.134}$$

with

$$\kappa_{+_u} = \sqrt{k_x^2 + \frac{4v_z^2k_z^2 - (v_0k_z-\epsilon)^2}{v_\perp^2}} \quad \text{and} \quad \kappa_{-_u} = \sqrt{k_x^2 + \frac{4v_z^2k_z^2 - (v_0k_z+\epsilon)^2}{v_\perp^2}}. \tag{3.135}$$

We can rewrite the boundary conditions from Eqs. (3.127)-(3.130) with these wavefunctions into a matrix equation to eliminate the constant coefficients $c^{\pm_u}_{j_z}$. From this, one finds the surface state dispersion

$$\mathcal{E}^{\pm_u}_{\pm,y<0}(k_x,k_z) = \pm_u \frac{1}{2} v_z\left(3\bar{v}_0 k_z \pm \sqrt{\left(4-\bar{v}_0^2\right)\left(\bar{v}_\perp^2 k_x^2 + 3k_z^2\right)}\right), \tag{3.136}$$

with $\bar{v}_\perp = v_\perp/v_z$. Similar to the Luttinger semimetal phase, the surface-state dispersion becomes complex for $|\bar{v}_0| > 2$. It is convenient to rewrite the surface state dispersion into polar coordinates with $(k_x,k_z) = k_\perp(\sin\zeta,\cos\zeta)$

$$\mathcal{E}^{\pm_u}_{\pm,y<0}(k_\perp,\zeta) = \pm_u \frac{1}{2} v_z k_\perp\left(3\bar{v}_0 \cos\zeta \pm \sqrt{\left(4-\bar{v}_0^2\right)\left(\bar{v}_\perp^2 \sin^2\zeta + 3\cos^2\zeta\right)}\right). \tag{3.137}$$

This highlights that the surface states around the Dirac points have axial symmetry, even in the presence of cubic anisotropy $\alpha_\square$. Comparing the surface states with the boundary of the bulk, one can find a critical condition for the merging of a single surface state

$$\bar{v}_0 = \pm \frac{2\cos\zeta}{\sqrt{4\cos^2\zeta + \bar{v}_\perp^2 \sin^2\zeta}}, \tag{3.138}$$

which can be rewritten to

$$\cos\zeta = \pm \frac{\bar{v}_0 \bar{v}_\perp}{\sqrt{4 + \bar{v}_0^2 (\bar{v}_\perp^2 - 4)}}. \tag{3.139}$$

We note that the merging condition is only dependent on the momentum angle and independent of the magnitude. Hence, the surface states form a circle segment in the Brillouin zone with the Dirac point in the center.

For $\alpha_\square = 0$, this simplifies to

$$\cos^2\zeta = \frac{3\bar{\alpha}_0^2}{4 - \bar{\alpha}_0^2}, \tag{3.140}$$

which only has a solution if $\bar{\alpha}_0^2 \leq 1$. From this, we find that for $|\bar{\alpha}_0| \leq 1$, two surface states exist, which merge with the bulk continuum at some critical angle. For $|\bar{\alpha}_0| > 1$, one surface state immerse into the bulk, leaving only the second surface state, which exists all around the Dirac points. This resembles the conditions for the number of surface states in the Luttinger semimetal phase.

We show the behavior of Eq. (3.137) with neglected cubic anisotropy under the evolution of $\bar{\alpha}_0$ as dashed lines in Fig. 3.5. Here, we show a circular path around the $p_z = +p_u$ Dirac point with a small radius of $k_\perp = 0.05 p_u$. As mentioned before, the system conserves PHS for $\bar{\alpha}_0 = 0$ [Fig. 3.5(a)]. The surface states merge with the bulk continuum at the critical angle $\zeta_{\text{crit}}(\bar{\alpha}_0 = 0) = \pm\pi/2$ given by Eq. (3.140). As consequence, the surface states along $k_x = 0$ only exist for $k_z > 0$, which corresponds to $\zeta = 0$. Along $k_z = 0$, the surface states follow the bulk continuum closely for both $k_x \gtrless 0$, which resembles the critical angles $\zeta = \pm\pi/2$.

Breaking PHS, we find that the magnitude of the merging angle for the $\mathcal{E}^{\pm_u}_{+,y<0}(k_\perp, \zeta)$ solution becomes smaller, while the merging angle of $\mathcal{E}^{\pm_u}_{-,y<0}(k_\perp, \zeta)$ grows towards $\pm\pi$. At the critical point $\bar{\alpha}_0 = 1$, the $\mathcal{E}^{\pm_u}_{+,y<0}(k_\perp, \zeta)$ solution has merged with the bulk continuum for all angles and disappears. The $\mathcal{E}^{\pm_u}_{-,y<0}(k_\perp, \zeta)$ state decouples

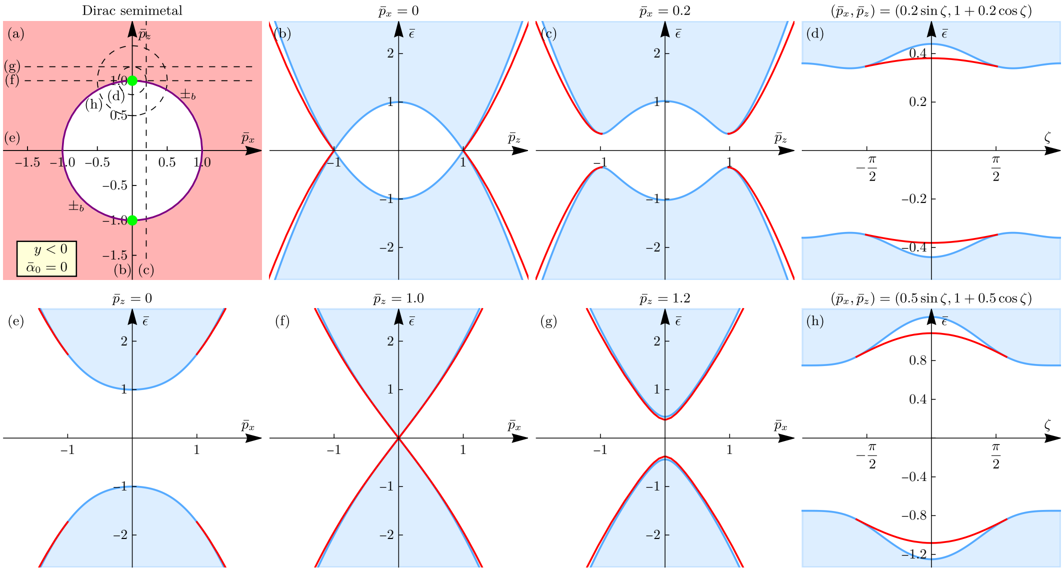

Figure 3.6: Surface band structure for a Dirac semimetal [$\hat{H}^D(\mathbf{p})$ from Eq. (3.22)] occupying the $y < 0$ half-space. Here, we neglect the cubic anisotropy ($\alpha_\square = 0$) and take the effective mass ratio $\bar{\alpha}_0 = \alpha_0/\alpha_z = 0$, corresponding to particle-hole symmetry. (a) Fermi contour at the energy of the Dirac points [$\epsilon = \varepsilon_u$, Eq. (3.33)] in the projected surface Brillouin zone, with dimensionless momenta $\bar{p}_{x,z} = p_{x,z}/p_{u0}$ [Eq. (3.35)]. The positions of the Dirac points are shown with green points and the merging contour of the surface states with the bulk continuum is projected in purple. The label $+_b$ ($-_b$) corresponds to a merging with the conduction (valence) band. The number of existing surface states at a given momentum is indicated by the red shading. The absence of surface states is shown in white, one surface state in light-red, and two surface states in dark-red. (b,c) Surface dispersion for constant $\bar{p}_x$, at (b) $\bar{p}_x = 0$ and (c) $\bar{p}_x = 0.2$. The energy is given in dimensionless units relative to the strain $\bar{\epsilon} = \epsilon/|u|$ [Eq. (3.36)]. The color code for the surface states and bulk boundaries corresponds to Fig. 3.3. (e-g) Surface dispersion for constant $\bar{p}_z$, at (e) $\bar{p}_z = 0$, (f) $\bar{p}_z = 1.0$, and (g) $\bar{p}_z = 1.2$. (d,h) Surface dispersion in polar coordinates $(\bar{p}_x, \bar{p}_z) = (\bar{p}_r \sin\zeta, 1 + \bar{p}_r \cos\zeta)$ around the upper Dirac point for (d) $\bar{p}_r = 0.2$ and (h) $\bar{p}_r = 0.5$.

linearized model $\hat{\mathcal{H}}^{D,\pm_u}(\mathbf{k})$ [Eq. (3.53)].

We show the evolution of the $y < 0$ surface band structure in Figs. 3.6-3.11. Here, we use the dimensionless parameters $\bar{\epsilon} = \epsilon/|u|$ and $\bar{p}_{x,z} = p_{x,z}/p_{u0}$ from Eqs. (3.36) and

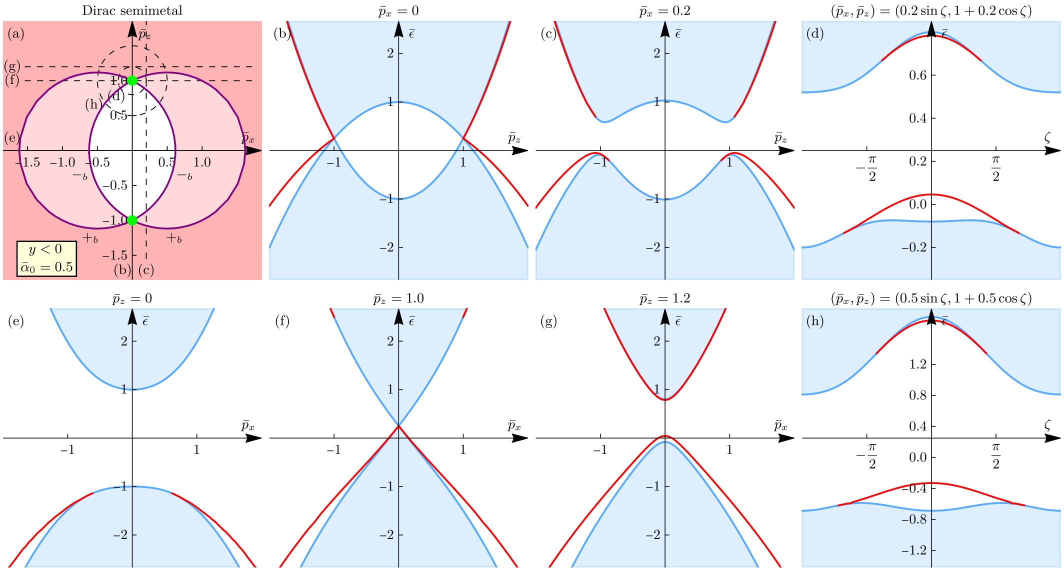

Figure 3.7: Surface band structure for a Dirac semimetal [$\hat{H}^D(\mathbf{p})$ from Eq. (3.22)] occupying the $y < 0$ half-space. The figure is analog to Fig. 3.6 for $\bar{\alpha}_0 = 0.5$. The color code in (a) gives the number of existing surface states at a given momentum, with either two (dark-red), one (light-red), or no surface states.

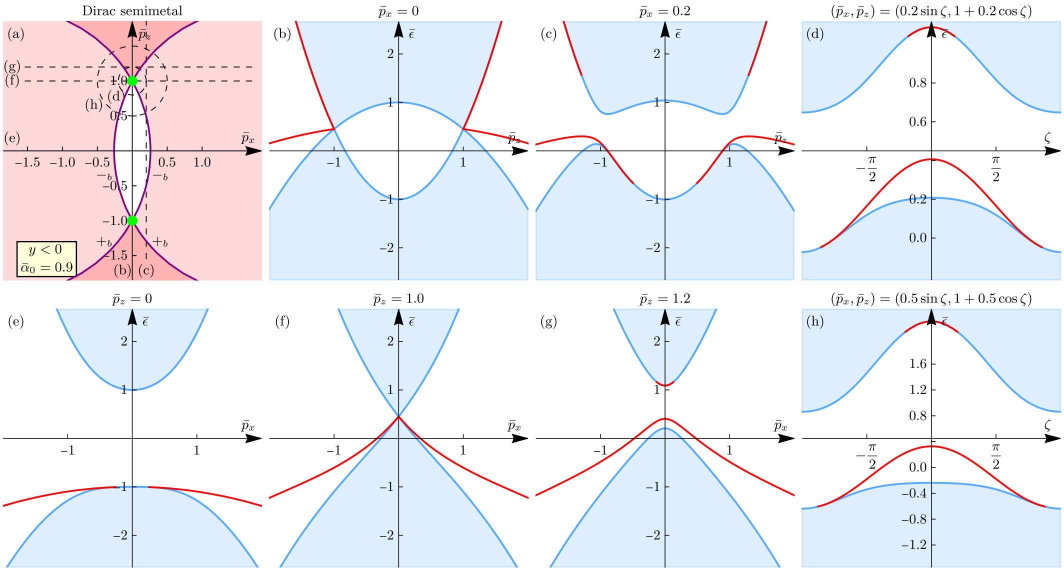

Figure 3.8: Surface band structure for a Dirac semimetal [$\hat{H}^D(\mathbf{p})$ from Eq. (3.22)] occupying the $y < 0$ half-space. The figure is analog to Fig. 3.6 for $\bar{\alpha}_0 = 0.9$.

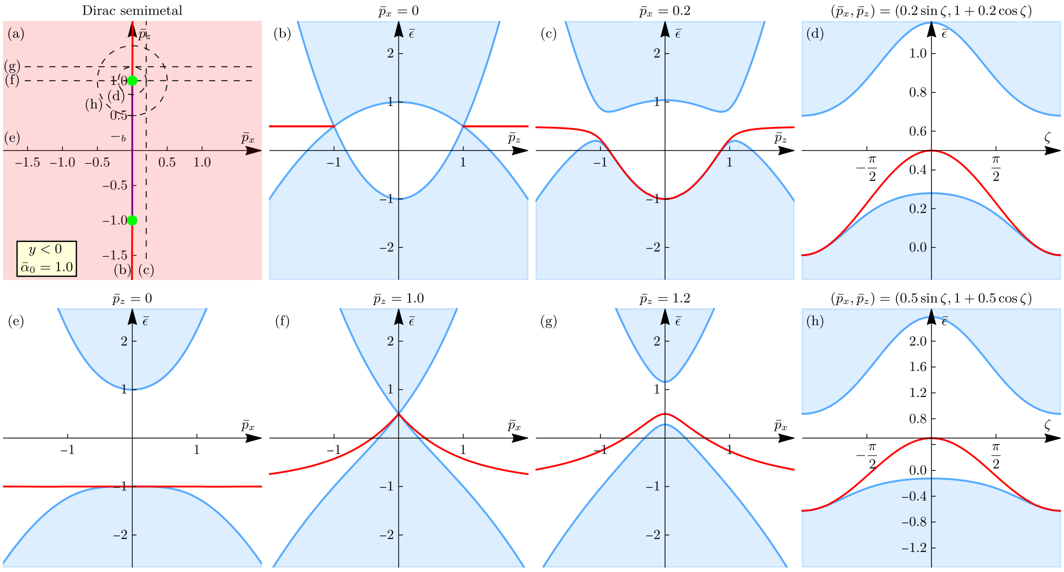

Figure 3.9: Surface band structure for a Dirac semimetal [$\hat{H}^D(\mathbf{p})$ from Eq. (3.22)] occupying the $y < 0$ half-space. The figure is analog to Fig. 3.6 for $\bar{\alpha}_0 = 1.0$, corresponding to the critical point where the upper surface state merges with the bulk continuum. In addition, (a) shows the Fermi contour of the surface state (red line) at $\epsilon = \varepsilon_u$ [Eq. (3.33)]. Here, one surface state exists in the entire surface Brillouin zone except for $\bar{p}_x = 0$ and $\bar{p}_z \in \{-1, 1\}$ (purple line).

(3.35) to give the most general results. Additionally, we neglect the cubic anisotropy $\alpha_\square = 0$. Fig. 3.6 shows the particle-hole symmetric case for $\bar{\alpha}_0 = 0$. Along the constant momentum paths $\bar{p}_x = 0$ [Fig. 3.6(b)] and $\bar{p}_z = 1$ [Fig. 3.6(f)], one can see the two Dirac points at $(\bar{p}_x, \bar{p}_z) = (0, \pm 1)$. From the linearized model, we know along which directions the surface states disperse from the Dirac points [see Eq. (3.140)]. These critical merging angles can also be seen in the circular momentum path around the crossing point with a radius of $0.2p_u$, depicted in Fig. 3.6(d). Leaving the vicinity of the Dirac point [Fig. 3.6(h)], we see that the merging angle deviates from the value from Eq. (3.140). This results in the merging contour, presented by the purple circle in Fig. 3.6(a), where the label $+_b$ corresponds to a merging point of the surface state with the conduction band and $-_b$ indicates a merging with the valence band. For $\bar{\alpha}_0 = 0$, the two contours are degenerate due to PHS. To conclude, two surface states exist outside of the circle (dark-red area), and none exist inside of it (white area).

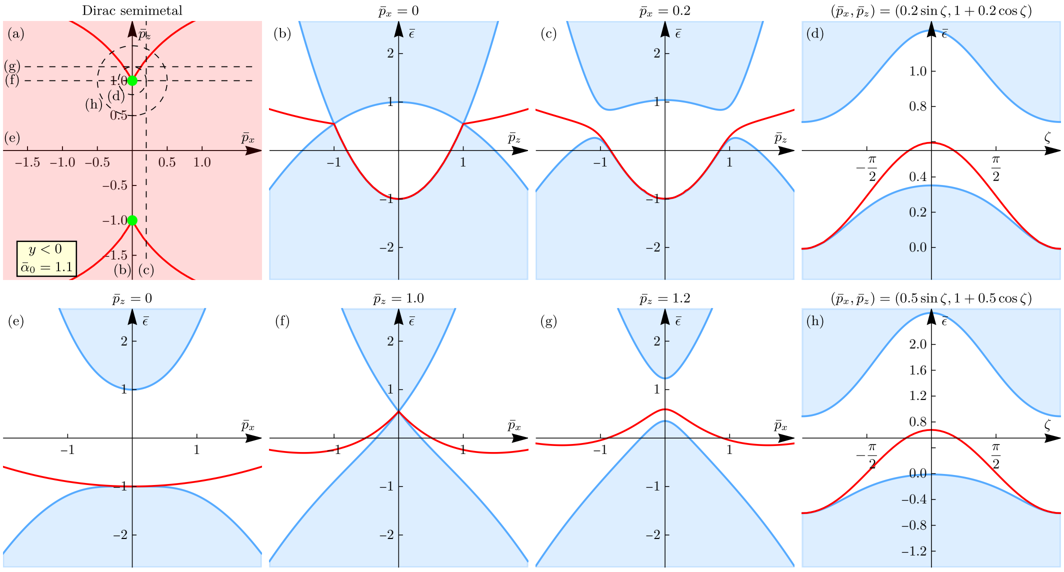

Figure 3.10: Surface band structure for a Dirac semimetal [$\hat{H}^D(\mathbf{p})$ from Eq. (3.22)] occupying the $y < 0$ half-space. The figure is analog to Fig. 3.9 for $\bar{\alpha}_0 = 1.1$. Here, the single surface state exists in the entire Brillouin zone, and the Fermi contour of the surface state forms a double Fermi arc.

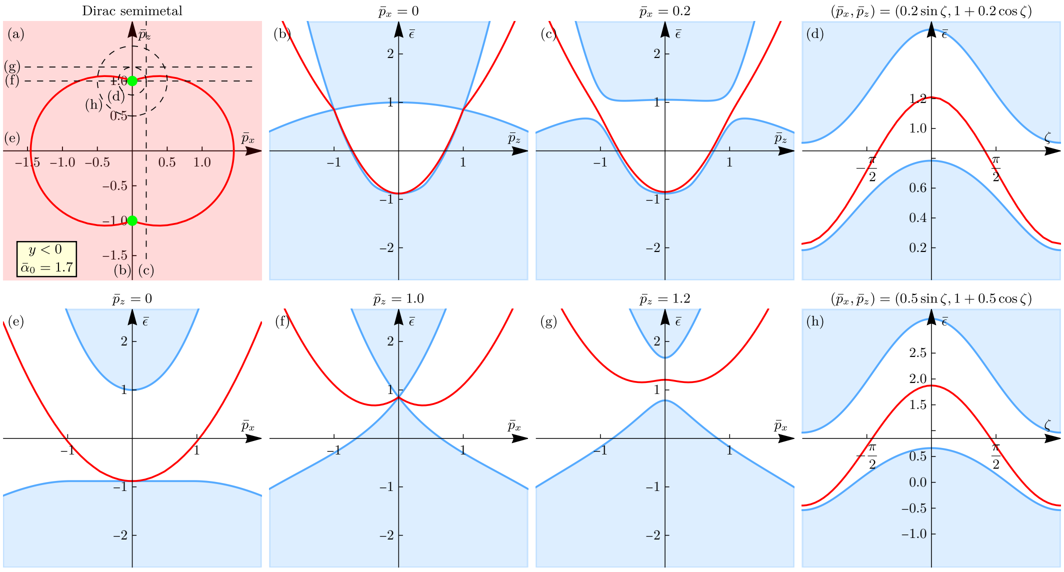

Figure 3.11: Surface band structure for a Dirac semimetal [$\hat{H}^D(\mathbf{p})$ from Eq. (3.22)] occupying the $y < 0$ half-space. The figure is analog to Fig. 3.10 for $\bar{\alpha}_0 = 1.7$, which is close to the material specific parameters of $\alpha$-Sn and HgTe [Tab. A.2].

Breaking PHS $0 < \bar{\alpha}_0 < 1$, we see that the surface states have a similar dependence on $\bar{\alpha}_0$ as in the Luttinger semimetal phase. In Figs. 3.7 and 3.8, we show the surface band structure for $\bar{\alpha}_0 = 0.5$ and $\bar{\alpha}_0 = 0.9$. Here, both surface states bend upwards in energy. The circular momentum paths show that the critical merging angle for the higher surface state decreases, and the lower state goes towards $\pm\pi$. This results in splitting the $+_b$ and $-_b$ merging contours in Figs. 3.7(a) and 3.8(a). Hence, a finite area in the surface Brillouin zone exists, where only one surface state exists (light-red area).

The critical point $\bar{\alpha}_0 = 1$ is presented in Fig. 3.9. Here, the upper surface state has completely merged with the conduction band, while the lower surface state becomes flat along the lines $\bar{p}_x = 0$ [Fig. 3.9(e)] and $\bar{p}_z = 0$ [Fig. 3.9(b)] for $|\bar{p}_z| > 1$. The critical merging angle can be calculated in the linearized model $\zeta_{\text{crit}} = \pm\pi$ [Eq. (3.140)]. Hence, the merging contour in Fig. 3.9(a) is reduced to a single line at $\bar{p}_x = 0$ for $|\bar{p}_z| < 1$ between the Dirac points. The rest of the surface Brillouin zone hosts a single surface state. The red line in Fig. 3.9(a) indicates the formation of a surface-state Fermi contour, where the surface state lies at the energy of the Dirac point $\epsilon = \varepsilon_u$ [Eq. (3.33)]. Since the surface state along $\bar{p}_x = 0$ is flat, the Fermi contour forms a line, which extends from $|\bar{p}_z| > 1$ to infinity, which is limited by the validity range of the Luttinger model.

The Figs. 3.10 and 3.11 illustrate the band structure for $\bar{\alpha}_0 = 1.1$ and $\bar{\alpha}_0 = 1.7$, where the critical point is exceeded. Here, we find that the single surface state exists in the entire surface Brillouin zone, giving the absence of a merging contour. For $1 < \bar{\alpha}_0 \leq 2$, the remaining surface state changed from a hole-like to an electron-like character. Interestingly, we find that the surface state has a negative velocity in the vicinity of the Dirac point along the constant momentum paths $\bar{p}_z = 1$ and $\bar{p}_z = 1.2$ [Figs. 3.10(f,g) and 3.11(f,g)]. Therefore, the linear surface-state Fermi surface evolves into a closed contour, connecting both Dirac points. We identify this contour as the double Fermi arcs discussed in Sec. 2.2.2.

The case $\bar{\alpha}_0 = 1.7$ from Fig. 3.11 is shown explicitly because it closely resembles the material-specific parameters for $\alpha$-Sn and HgTe, with neglected cubic anisotropy and BIA terms (see Tab. A.2). The following sections present the surface band structure along the same momentum paths in the equivalent momentum and energy ranges to show the effect of the linear and cubic BIA terms.

Each momentum path, which does not cross a Dirac point, has a finite gap between the valence and conduction band. As discussed in Sec. 2.2, we can consider these momentum planes as effective 2D insulators, which can be associated with a Chern number as a topological invariant. Due to the bulk-boundary correspondence, we see that the DSM phase of the Luttinger model only hosts trivial planes with zero Chern number. This agrees with the predictions due to the zero chirality of the Dirac points.

### 3.6.2 Surface parallel to the strain

In this section, we consider a system occupying the $z > 0$ half-space with the unique $z = 0$ surface orientation in the DSM phase, where both Dirac points are projected onto each other in the surface Brillouin zone (see Fig. 3.1). We first analyze the linearized model $\hat{\mathcal{H}}^D(\mathbf{k})$ from Eq. (3.52) for analytical calculations. We find the bulk boundaries with respect to $k_z$

$$E^{\pm_u}_{\pm_b}(k_x, k_y) = \varepsilon_u \pm \frac{1}{2} v_\perp k_\perp \sqrt{4 - \bar{v}_0^2}. \tag{3.141}$$

The bulk boundary becomes imaginary outside of the semimetal phase of the Luttinger model ($|\bar{v}_0| > 2$), showing that the linearized model is only well-defined if Dirac points are present.

To derive the effective boundary conditions for the $z = 0$ surface, we follow the method of the previous section and calculate the wavefunctions of the full Hamiltonian $\hat{H}^D(\mathbf{p})$ [Eq. (3.22)] at the Dirac points [$(p_x, p_y, \epsilon) = (0, 0, \varepsilon_u)$]

$$|\Psi(z)\rangle = \begin{pmatrix} \psi^{+_u}_{+\frac{3}{2}} \\ \psi^{+_u}_{+\frac{1}{2}} \\ \psi^{+_u}_{-\frac{1}{2}} \\ \psi^{+_u}_{-\frac{3}{2}} \end{pmatrix} e^{ip_u z} + \begin{pmatrix} \psi^{-_u}_{+\frac{3}{2}} \\ \psi^{-_u}_{+\frac{1}{2}} \\ \psi^{-_u}_{-\frac{1}{2}} \\ \psi^{-_u}_{-\frac{3}{2}} \end{pmatrix} e^{-ip_u z} \equiv \left|\psi^{+_u}(z)\right\rangle e^{ip_u z} + \left|\psi^{-_u}(z)\right\rangle e^{-ip_u z}. \tag{3.142}$$

Here, $|\psi^{\pm_u}(z)\rangle$ are the expanded four-component wavefunctions of the linearized Hamiltonian. We demand the wavefunction to vanish at the boundary and get the effective boundary conditions

$$\left|\psi^{+u}(z=0)\right\rangle + \left|\psi^{-u}(z=0)\right\rangle = 0. \tag{3.143}$$

With the established boundary condition, we can use the method from Sec. 3.4 to calculate the surface states of the sample. Using the wavefunction (3.51) of the linearized model, we make the ansatz for the surface state

$$\left|\psi^{+u}(z,k_\perp,\varphi,\epsilon)\right\rangle = \left(c_{+u1}\left|\psi_1^{+u}\right\rangle + c_{+u2}\left|\psi_2^{+u}\right\rangle\right)e^{ik_z^{+u}(k_\perp,\varphi,\epsilon)z}, \tag{3.144}$$

$$\left|\psi^{-u}(z,k_\perp,\varphi,\epsilon)\right\rangle = \left(c_{-u1}\left|\psi_1^{-u}\right\rangle + c_{-u2}\left|\psi_2^{-u}\right\rangle\right)e^{ik_z^{-u}(k_\perp,\varphi,\epsilon)z}, \tag{3.145}$$

which vanishes for $z \to \infty$. Here, $c_{\pm_u 1}$ and $c_{\pm_u 2}$ are arbitrary coefficients, $\left|\psi_{1,2}^{\pm_u}\right\rangle$ are the eigenvectors of the linearized Hamiltonian, and we use the polar coordinates $(k_x, k_y) = k_\perp(\cos\varphi, \sin\varphi)$. From the Schrödinger equation, we find the wavenumbers

$$k_z^{+u}(k_\perp,\varphi,\epsilon) = \frac{-\bar{v}_0(\epsilon-\varepsilon_u) + i\sqrt{v_\perp^2 k_\perp^2\left(4-\bar{v}_0^2\right) - 4(\epsilon-\varepsilon_u)^2}}{v_z\left(4-\bar{v}_0^2\right)}, \tag{3.146}$$

$$k_z^{-u}(k_\perp,\varphi,\epsilon) = \frac{\bar{v}_0(\epsilon-\varepsilon_u) + i\sqrt{v_\perp^2 k_\perp^2\left(4-\bar{v}_0^2\right) - 4(\epsilon-\varepsilon_u)^2}}{v_z\left(4-\bar{v}_0^2\right)}, \tag{3.147}$$

and the eigenvectors

$$\left|\psi_1^{+u}\right\rangle = \begin{pmatrix} -v_\perp k_\perp e^{-i\varphi} \\ \epsilon-\varepsilon_u-(v_0-2v_z)k_z^{+u} \\ 0 \\ 0 \end{pmatrix}, \quad \left|\psi_2^{+u}\right\rangle = \begin{pmatrix} 0 \\ 0 \\ v_\perp k_\perp e^{-i\varphi} \\ \epsilon-\varepsilon_u-(v_0+2v_z)k_z^{+u} \end{pmatrix}, \tag{3.148}$$

$$\left|\psi_1^{-u}\right\rangle = \begin{pmatrix} v_\perp k_\perp e^{-i\varphi} \\ \epsilon-\varepsilon_u+(v_0-2v_z)k_z^{-u} \\ 0 \\ 0 \end{pmatrix}, \quad \left|\psi_2^{-u}\right\rangle = \begin{pmatrix} 0 \\ 0 \\ -v_\perp k_\perp e^{-i\varphi} \\ \epsilon-\varepsilon_u+(v_0+2v_z)k_z^{-u} \end{pmatrix}. \tag{3.149}$$

Solving the boundary condition (3.143), we find flat surface-state solutions with the energy

$$\mathcal{E}_{z>0} = \varepsilon_u \tag{3.150}$$

and the wavefunctions

$$|\Psi_{j_z>0}(z)\rangle = v_\perp k_\perp \left[ \begin{pmatrix} -e^{-i\varphi} \\ i\sqrt{\frac{2-\bar{v}_0}{2+\bar{v}_0}} \\ 0 \\ 0 \end{pmatrix} e^{i(\kappa_z + p_u)z} + \begin{pmatrix} e^{-i\varphi} \\ -i\sqrt{\frac{2-\bar{v}_0}{2+\bar{v}_0}} \\ 0 \\ 0 \end{pmatrix} e^{i(\kappa_z - p_u)z} \right], \tag{3.151}$$

$$|\Psi_{j_z<0}(z)\rangle = v_\perp k_\perp \left[ \begin{pmatrix} 0 \\ 0 \\ e^{-i\varphi} \\ -i\sqrt{\frac{2+\bar{v}_0}{2-\bar{v}_0}} \end{pmatrix} e^{i(\kappa_z + p_u)z} + \begin{pmatrix} 0 \\ 0 \\ -e^{-i\varphi} \\ i\sqrt{\frac{2+\bar{v}_0}{2-\bar{v}_0}} \end{pmatrix} e^{i(\kappa_z - p_u)z} \right], \tag{3.152}$$

with

$$\kappa_z = i k_\perp \frac{\bar{v}_\perp}{\sqrt{4-\bar{v}_0^2}}. \tag{3.153}$$

The flat dispersion of the surface state shows the relation of the linearized DSM model with the linear chiral symmetric node $\hat{H}_{N=1}(\mathbf{p})$ from Eq. (3.108). We showed that the Hamiltonian $\hat{\mathcal{H}}^D(\mathbf{k})$ [Eq. (3.52)] inhabits effective chiral symmetry [see Eq. (3.56)] concerning the interchange of the $+_u$ and $-_u$ blocks.

The surface band structure for the $z > 0$ sample in the full Hamiltonian $\hat{H}^D(\mathbf{p})$ [Eq. (3.22)] with neglected cubic anisotropy is illustrated in Fig. 3.12. Here, we use the dimensionless quantities $\bar{\epsilon} = \epsilon/|u|$ and $\bar{p}_\perp = p_\perp/p_u$. Similar to the Luttinger semimetal phase, the system is PHS for $\bar{\alpha}_0 = 0$ [Fig. 3.12(a,b)]. Both surface states bend upwards in energy for increasing $\bar{\alpha}_0$. For the critical $\bar{\alpha}_0 = 1$ [Fig. 3.12(g,h)], one surface state is entirely flat and changes from a hole-like behavior to an electron-like one. In contrast to the Luttinger semimetal phase, the second surface state is still present for $1 \leq \bar{\alpha}_0 \leq 2$. It merges with the bulk dispersion for finite momentum [see Fig. 3.12(k)], where the merging point goes to zero for increasing $\bar{\alpha}_0$.

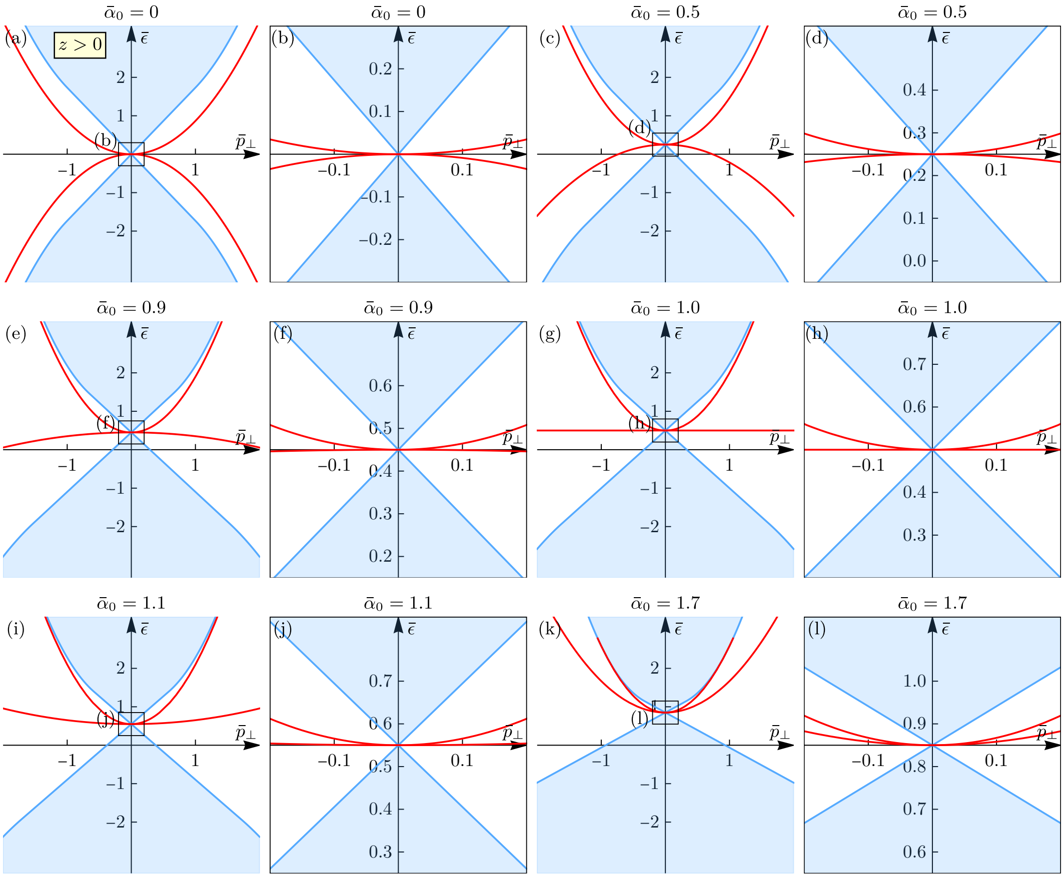

Figure 3.12: Surface band structure of the full quadratic Luttinger model with compressive strain $\hat{H}^D(\mathbf{p})$ [Eq. (3.22)] and neglected cubic anisotropy ($\alpha_\square = 0$) for a sample occupying the $z > 0$ half-space. We show the evolution under effective mass ratio for (a) $\bar{\alpha}_0 = \alpha_0/\alpha_z = 0$, (c) $\bar{\alpha}_0 = 0.5$, (e) $\bar{\alpha}_0 = 0.9$, (g) $\bar{\alpha}_0 = 1.0$, (i) $\bar{\alpha}_0 = 1.1$, and (k) $\bar{\alpha}_0 = 1.7$. The framed insets (b,d,f,h,j,l) show zooms around the projection of both Dirac points, emphasizing the linear regime. We use the dimensionless units $\bar{\epsilon} = \epsilon/|u|$ [Eq. (3.36)] and $\bar{p}_\perp = p_\perp/p_{u0}$ [Eq. (3.35)]. The projected bulk states are shown in blue, and the $z = 0$ surface states in red.

The framed plots in Fig. 3.12 present a small momentum range around the projected Dirac points. Here, one can see the linear behavior of the bulk continuum, which confirms the validity range of the linearized model $|\epsilon - \varepsilon_u| \ll |u|$ and $|\mathbf{p} \mp \mathbf{p}_u| \ll p_u$, discussed in Sec. 3.3. The surface states near the Dirac point are flat in the lowest order, which resembles the analytically calculated $\mathcal{E}_{z>0}$ from Eq. (3.150). Outside of the DSM range ($p \gg p_u$), the band structure of the DSM phase converges towards the quadratic-node Luttinger semimetal spectrum.

## 3.7 Nodal semimetal phase under inversion symmetry breaking

As discussed in Sec. 2.2, breaking inversion symmetry in a DSM leads to a WSM phase. It is educational to discuss an intermediate stage to understand the effect of the full BIA terms from Eq. (3.14) on the surface states. The application BIA terms up to linear order in momentum drives the system into a line-node semimetal phase, described by the Hamiltonian $\hat{H}^{LN}(\mathbf{p})$ from Eq. (3.24). This section analyzes the evolution of the surface states of the DSM phase in the line-node phase. We focus on the material-specific parameters of HgTe with neglected cubic BIA terms, shown in Tab. A.2.

### 3.7.1 Surface perpendicular to the strain

Here, we assume a system occupying the $y < 0$ half-space with a surface at $y = 0$. The projected surface Brillouin zone shows a line node connecting the momentum points $(p_x, p_z) = (-p_{\perp 0}, \sim p_{z0})$ and $(p_{\perp 0}, \sim p_{z0})$ [see Eq. (3.45)]. As discussed in Sec. 3.1.2, the exact $p_z$ coordinate has a minor dependency on $p_x$, which does not affect the discussion of this section.

Comparing Fig. 3.11 with Fig. 3.13 gives the effect of the linear BIA term on the surface band structure in the topological semimetal regime. The surface state is no longer mirror symmetric concerning the planes $p_x = 0$ or $p_z = 0$. Only the point-mirror symmetry for $(p_x, p_z) \to (-p_x, -p_z)$ is preserved due to the presence of TRS. The linear BIA term reintroduces merging contours, depicted by the purple lines in Figs. 3.13(a) and 3.14(a). Here, one can see a closed merging contour with the valence band $-_b$ around the Γ point. Additionally, two closed merging contours form at the edges of the line nodes.

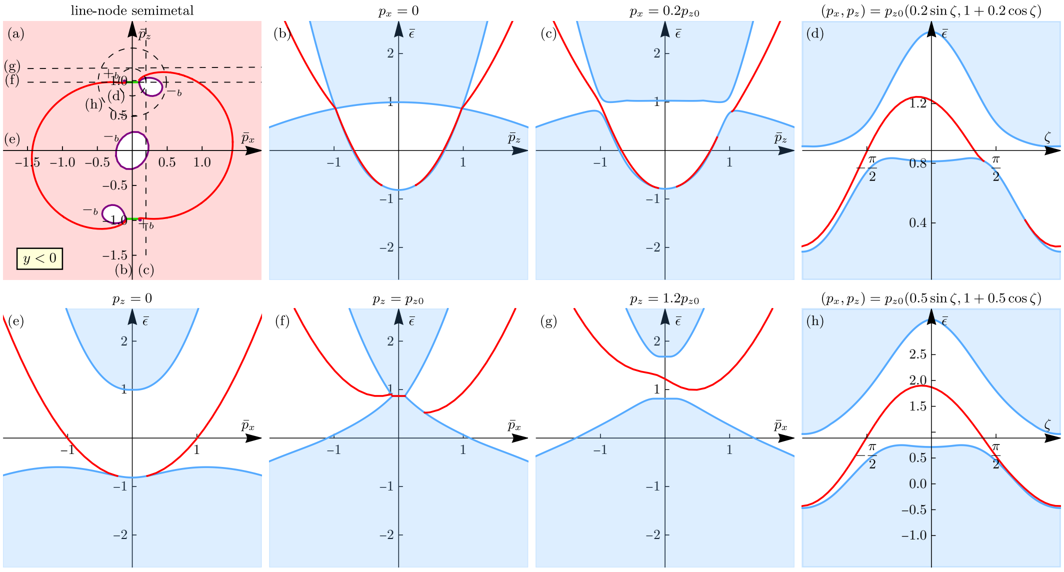

Figure 3.13: Surface band structure for a line-node semimetal [$\hat{H}^{LN}(\mathbf{p})$ from Eq. (3.24)] occupying the $y < 0$ half-space. We take the material-specific parameters for HgTe (see Tab. A.2) without cubic BIA terms. (a) Fermi contour at the energy of the line nodes [$\epsilon = \varepsilon_0$, Eq. (3.46)] in the projected surface Brillouin zone, with dimensionless momenta $\bar{p}_{x,z} = p_{x,z}/p_{u0}$ [Eq. (3.35)]. The positions of the line nodes are shown with green lines, and the merging contour of the surface states with the bulk continuum is projected in purple. The label $+_b$ ($-_b$) corresponds to a merging with the conduction (valence) band. The light-red shading indicates the existence of the surface state at a given momentum. The absence of surface states is shown in white. (b,c) Surface dispersion for constant $p_x$, at (b) $p_x = 0$ and (c) $p_x = 0.2p_{z0}$, where $p_{z0}$ is the $p_z$ coordinate of the line node from Eq. (3.45). The energy is given in dimensionless units relative to the strain $\bar{\epsilon} = \epsilon/|u|$ [Eq. (3.36)]. The color code for the surface states and bulk boundaries corresponds to Fig. 3.3. (e-g) Surface dispersion for constant $p_z$, at (e) $p_z = 0$, (f) $p_z = p_{z0}$, and (g) $p_z = 1.2p_{z0}$. (d,h) Surface dispersion in polar coordinates $(p_x, p_z) = p_{z0}(\bar{p}_r \sin\zeta, 1 + \bar{p}_r \cos\zeta)$ around the center of the upper line node for (d) $\bar{p}_r = 0.2$ and (h) $\bar{p}_r = 0.5$.

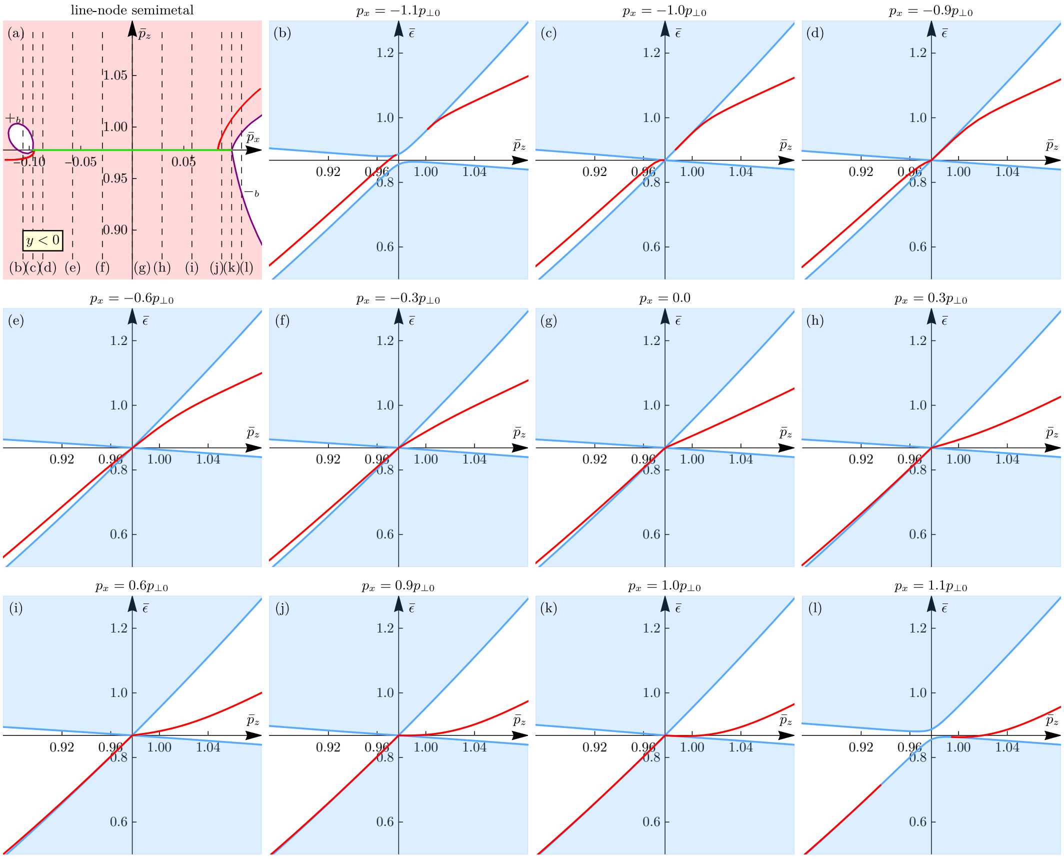

Figure 3.14: Surface band structure for a line-node semimetal [$\hat{H}^{LN}(\mathbf{p})$ from Eq. (3.24)] occupying the $y < 0$ half-space, analog to Fig. 3.13. (a) Fermi contour of the surface state at $\epsilon = \epsilon_0$ [Eq. (3.46)] (red line), where we checked that both contours terminate at the right edge of the line node around $(p_x, p_z) \approx (p_{\perp 0}, p_{z0})$ [Eq. 3.45)]. (b-l) Momentum planes for $p_x =$ const. in the vicinity of the line node, with (b) $p_x = -1.1p_{\perp 0}$, (c) $p_x = -1.0p_{\perp 0}$, (d) $p_x = -0.9p_{\perp 0}$, (e) $p_x = -0.6p_{\perp 0}$, (f) $p_x = -0.3p_{\perp 0}$, (g) $p_x = 0$, (h) $p_x = 0.3p_{\perp 0}$, (i) $p_x = 0.6p_{\perp 0}$, (j) $p_x = 0.9p_{\perp 0}$, (k) $p_x = 1.0p_{\perp 0}$, and (l) $p_x = 1.1p_{\perp 0}$.

In Fig. 3.14, we show momentum planes for $p_x =$ const. in the vicinity of the line node. Here, we see that the surface state merges with the conduction band for $p_x \leq -p_{\perp 0}$ and with the valence band for $p_x \geq p_{\perp 0}$ on both sides of the line node.

The bulk gap closes for $|p_x|p_{\perp 0}$, and the surface state originates from the line node towards both sides in $p_z$.

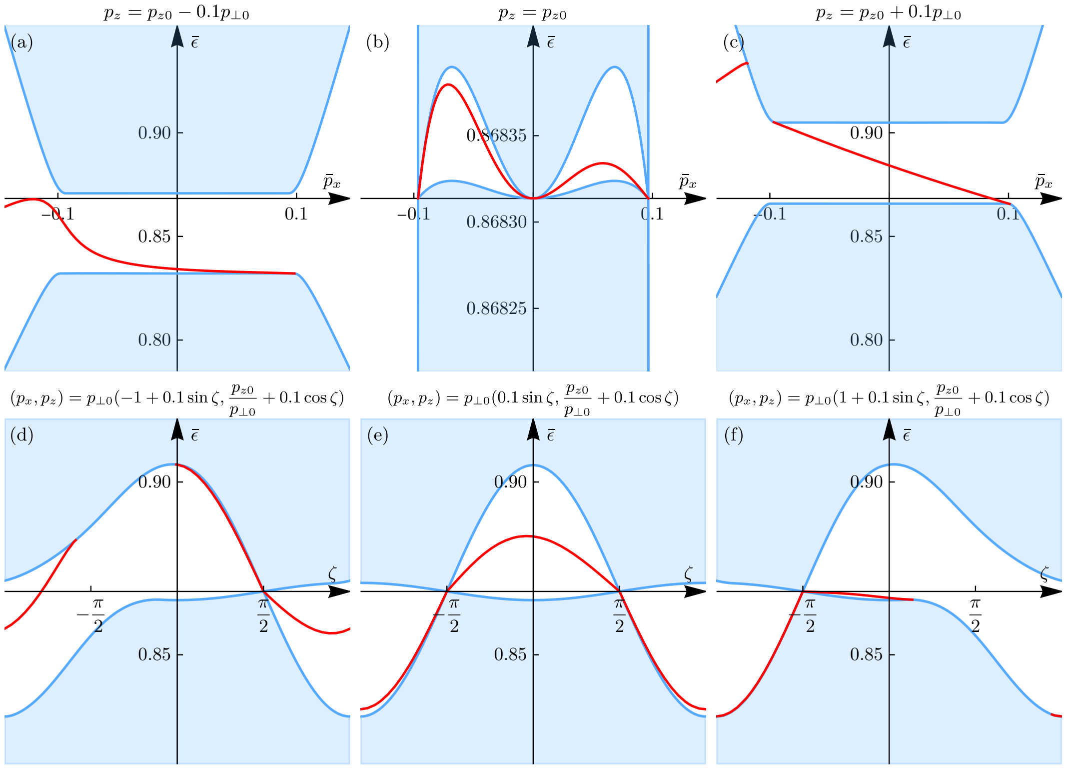

Figure 3.15: Surface band structure for a line-node semimetal [$\hat{H}^{LN}(\mathbf{p})$ from Eq. (3.24)] occupying the $y < 0$ half-space, analog to Fig. 3.13. (a-c) Momentum planes for $p_x = \text{const.}$ around the line node, with (a) $p_x = p_{z0} - 0.1p_{\perp 0}$ [Eq. (3.45)], (b) $p_z = p_{z0}$ directly at the line node, and (c) $p_x = p_{z0} + 0.1p_{\perp 0}$. (d-f) Circular momentum paths around (d) the left edge, (e) the center, and (f) the right edge of the line node, with the radius $0.1p_{\perp 0}$. The origin of the horizontal axes is always indicating the energy $\epsilon = \epsilon_0$ from Eq. (3.46).

In Fig. 3.15, one can see detailed zoom ins of the surface band structure around the line node. For $p_z = \text{const.}$ momentum planes [Figs. 3.15(a-c)], we see that the bulk continuum is almost flat in the vicinity of the line node. The surface state at $p_z = p_{z0} + 0.1p_{\perp 0}$ appears to be chiral for $|p_x| < p_{\perp 0}$ and connect the conduction and valence band through the gap. Nevertheless, the effective 2D Chern number of this momentum plane is still zero, due to a second surface state at $p_x \leq -p_{\perp 0}$ with the opposite chirality. The small gap at $p_z = p_{z0}$ and $|p_x| \leq p_{\perp 0}$ is due to the tiny fluctuations in the $p_z$ coordinate of the line node, as discussed in Sec. 3.1.2.

The Figs. 3.15(d-f) show the circular momentum paths around the left edge, right edge and center of the projected line node with a small radius $0.1 p_{\perp 0}$. Here, the projected line node is indicated by the gap closing at $\zeta \approx \pm\pi/2$, respectively. Since these momentum paths are not fully gapped, the effective Chern number is not defined. To conclude, the linear BIA term does not change the topological behavior of the surface states from the DSM phase.

### 3.7.2 Surface parallel to strain

For a line-node semimetal on the $z > 0$ half-space, we can see the full ring-shape of the node in the surface Brillouin zone [Fig. 3.16(a)]. Here, both line nodes at $p_z \approx p_{z0}$ are projected onto each other.

Taking a radial momentum direction along $\bar{p}_\perp$, with $(\bar{p}_x, \bar{p}_y) = \bar{p}_\perp(\cos\varphi, \sin\varphi)$, we see the effect of the linear BIA term by comparisson of Figs. 3.11(l) and 3.16(b-d). First, we note the gap opening at the $\Gamma$ point of the size $|2m|$, as showed in Sec. 3.1.2.

The two surface states cross at $p_\perp = 0$ and $\epsilon = \varepsilon_u$, due to Kramers' theorem. In general, the surface-state dispersion does not change significantly in the vicinity of the line node. This is related to the effective chiral symmetry of the linearized model $\tilde{\mathcal{H}}^{LN,\pm_u}(\mathbf{k})$ from Eq. (3.59), which is not broken by the linear BIA term. Therefore, the surface states can be approximated to be flat for small momenta, similar to the DSM phase.

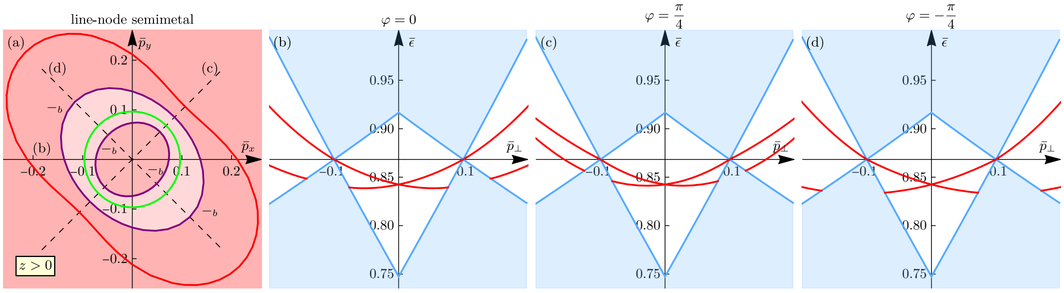

Figure 3.16: Surface band structure for a line-node semimetal [$\hat{H}^{LN}(\mathbf{p})$ from Eq. (3.24)] occupying the $z > 0$ half-space. (a) Fermi contour with the line node of the bulk states (green) and the surface states (red line) at $\epsilon = \varepsilon_0$ [Eq. 3.46]. Here, we use the unitless momentum $\bar{p}_{x,y} = p_{x,y}/p_{u0}$ from Eq. (3.35). The merging contours of the surface states with the bulk continuum with the valence band is shown by the purple lines with the label $-_b$. The number of existing surface states is indicated by the light-red shading with one state, and dark-red shading with two states. The dashed lines indicate the momentum cut of the corresponding band structure plots. (b-d) Surface band structure for the polar coordinates $(\bar{p}_x, \bar{p}_y) = \bar{p}_\perp(\cos\varphi, \sin\varphi)$, for (b) $\varphi = 0$, (c) $\varphi = \pi/4$, and (d) $\varphi = -\pi/4$. Here, we use the dimensionless energy $\bar{\epsilon} = \epsilon/|u|$ from Eq. (3.36).

The two bulk crossings along a radial momentum for $\varphi = \text{const.}$ are given by two blocks in the line-node semimetal Hamiltonian $\tilde{H}^{LN}(\mathbf{p})$ [Eq. (3.38)], which decouple completely at $\varphi = \pm\pi/4$. Hence, the surface state originating from one block appears to go unaffected through the bulk state of the other block. This results in the two merging contours, shown by the purple lines in Fig. 3.16(a).

Since both surface states have an electron-like character and $\varepsilon_u < \varepsilon_0$, we find a Fermi contour outside of the line node for $\epsilon = \varepsilon_0$. It forms a closed outline indicating a topologically trivial nature. We show in the next section, that this Fermi contour does not change conceptionally for increasing compressive strain in the Luttinger model, while it can shrink in the WSM phase of the Kane model.

## 3.8 Weyl semimetal phase under higher order inversion symmetry breaking

In this section, we analyze the surface states of the full WSM phase of the Luttinger model $\hat{H}^W(\mathbf{p})$ [Eq. (3.26)]. Particullarly, the effects of the cubic BIA terms are highlighted by comparisson with the line-node semimetal phase of the previous section.

Using the analysis of this chapter, we are able to explain surface transport measurements of compressive strained HgTe in Ref. [19]. Here, an additional surface potential generated Volkov-Pankratov states [1, 130], which coexisted with the surface states of the WSM.

### 3.8.1 Surface perpendicular to the strain

For a WSM sample, which occupies the $y < 0$ half-space, the eight Weyl points of the bulk project onto the surface to form six projected Weyl points (see Fig. 3.1). This leads to four single Weyl points at $(p_x, p_z) = (\pm p_\perp^W, \pm p_z^W)$ with a chirality of $c = -1$ and two double Weyl points at $(0, \pm p_z^W)$ with a chirality of $c = +2$.

First, we consider a large momentum and energy range shown in Figs. 3.17(a-h). We can see that the surface band structure in this scale is indistinguishable from the line-node semimetal phase, shown in Fig. 3.13. Even the momentum planes $p_z = p_z^W \pm p_\perp^W$ in Figs. 3.17(i,k) are identical to the line-node phase in Figs. 3.15(a,c). The $p_z = p_z^W$ momentum plane in the scale of the Weyl points changes conceptionally. In Fig. 3.17(j) we find the short Fermi arc, connecting the $c = +2$ Weyl point at $(0, +p_z^W)$ and the $c = -1$ Weyl point at $(+p_\perp^W, +p_z^W)$, which is also visible in the Fermi contour of Fig. 3.18(a).

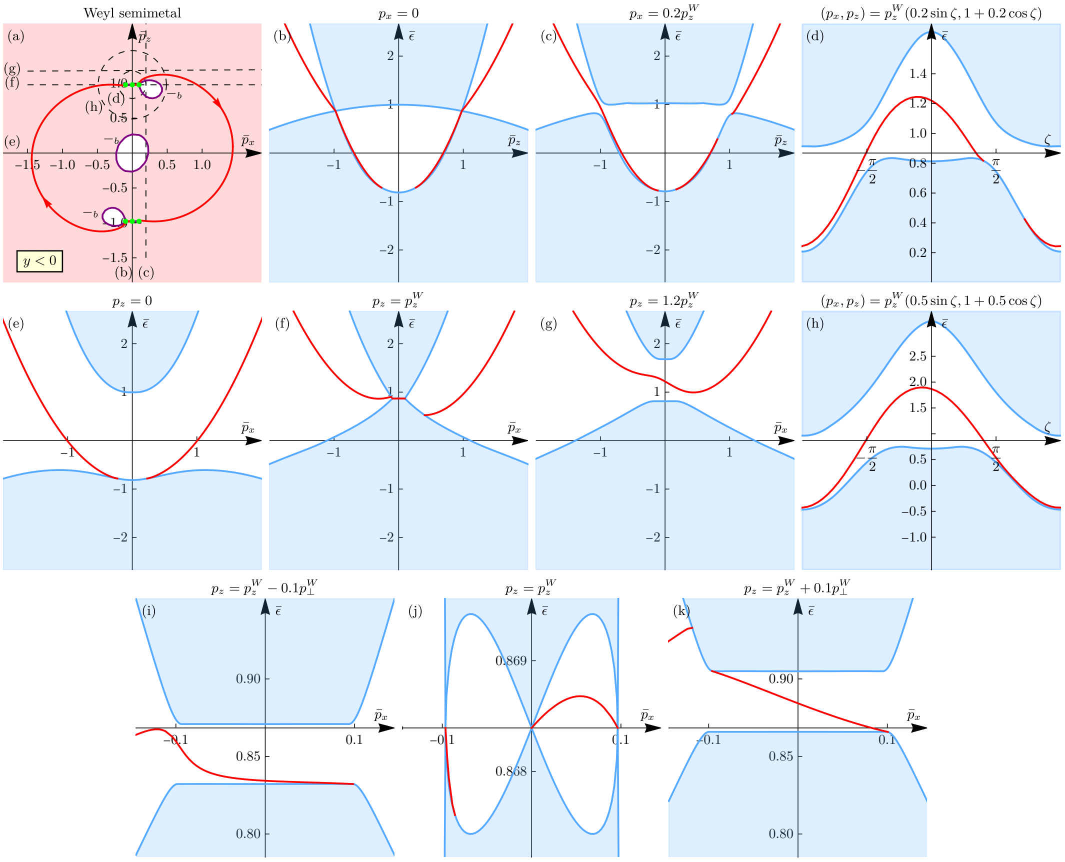

Figure 3.17: Surface band structure for a Weyl semimetal [$\hat{H}^W(\mathbf{p})$ from Eq. (3.26)] occupying the $y < 0$ half-space analog to Fig. 3.13. We take the material-specific parameters for HgTe (see Tab. A.2) where the cubic BIA terms were fitted to DFT calculations. (a) Fermi contour at the energy of the Weyl points ($\epsilon = \varepsilon_W$). The positions of the six projected Weyl points [$(p_x, p_z) = (\pm p_\perp^W, \pm p_z^W)$ and $(0, \pm p_z^W)$] are shown with green points, and the merging contour of the surface states with the bulk continuum is projected in purple. The label $+_b$ ($-_b$) corresponds to a merging with the conduction (valence) band. (b,c) Surface dispersion for constant $p_x$, at (b) $p_x = 0$ and (c) $p_x = 0.2p_z^W$. The energy is given in dimensionless units, relative to the strain $\bar{\epsilon} = \epsilon/|u|$ [Eq. (3.36)]. (e-g) Surface dispersion for constant $p_z$, at (e) $p_z = 0$, (f) $p_z = p_z^W$ with a zoom in around the Weyl points in (j), and (g) $p_z = 1.2p_z^W$. (d,h) Surface dispersion in polar coordinates $(p_x, p_z) = p_z^W(\bar{p}_r \sin\zeta, 1 + \bar{p}_r \cos\zeta)$ around the center between the upper Weyl points for (d) $\bar{p}_r = 0.2$ and (h) $\bar{p}_r = 0.5$. (i,k) Constant momentum plane for $p_z = p_z^W \mp 0.1p_\perp^W$.

The specific Weyl point setup of the projected $y = 0$ surface Brillouin zone lead to effective 2D momentum planes, with different topological behavior. Following the discussion from Sec. 2.2.1, we can consider distinct momentum planes and analyze effective 2D Chern numbers in the gapped regimes.

In the momentum planes, given by a constant $p_z$, the critical transitions of the 2D planes are located along $p_z = \pm p_z^W$. Since the sum of all Weyl point chiralities is zero along this plane, there is no phase transition and all $p_z = \text{const.}$ planes are effective 2D topologically trivial insulators. This can be seen through the bulk-boundary correspondence in Figs. 3.17(e) and (g).

On the other hand, the momentum planes given by a constant $p_x$ show a more interesting behavior. Here, we can find three critical planes $p_x = -p_\perp^W$, $p_x = 0$, and $p_x = +p_\perp^W$. In Fig. 3.18, we show the evolution of the surface states along different $p_x = \text{const.}$ planes around $p_z \sim +p_z^W$. Please note, that the surface states around $p_z \sim -p_z^W$ also contribute to the bulk-boundary correspondence and can be seen utilizing the TRS via $(p_x, p_z) \to (-p_x, -p_z)$. Away from the Weyl points [$|p_x| > p_\perp^W$, Fig. 3.18(b,l)], we find a zero Chern number. The chirality of Weyl points at $p_x = \pm p_\perp^W$ sum up to $c = -2$. Using Eq. (2.29), we expect an effective 2D Chern number of $C = +2$ in the $0 < p_x < p_\perp^W$ region [Fig. 3.18(h-k)]. Here, we find two surface states crossing the Fermi level with positive velocity around $p_z \sim +p_z^W$. Therefore, these momentum planes can be considered as effective 2D Chern insulators. It is worth to highlight that the chiralities of the Weyl points at $p_x = 0$ sum up to $c = +4$, leading to a topological transition from $C = +2 \to -2$ in the $-p_\perp^W < p_x < 0$ region.

Overall, the Fermi contour of the surface states forms Fermi arcs, which originate from the $c = +2$ Weyl points and terminate at the $c = -1$ Weyl points, as discussed in Sec. 2.2.1. In Fig. 3.18(a) and Fig: 3.17(a), we can see that two different Fermi arcs exist. A short Fermi arc, which connects the $(0, +p_z^W)$ with the $(+p_\perp^W, +p_z^W)$ Weyl point and a long arc between the $(0, -p_z^W)$ and $(-p_\perp^W, +p_z^W)$ Weyl point. Both arcs have a TRS partner at negative momentum. Driving the system into a DSM phase by reintroducing inversion symmetry, we find that the Weyl points merge into two Dirac points at $(0, \pm p_u)$. Here, the short Fermi arcs get annihilated, while the long arcs survive and form the double Fermi arcs, as depicted in Figs. 3.10(a) and 3.11(a).

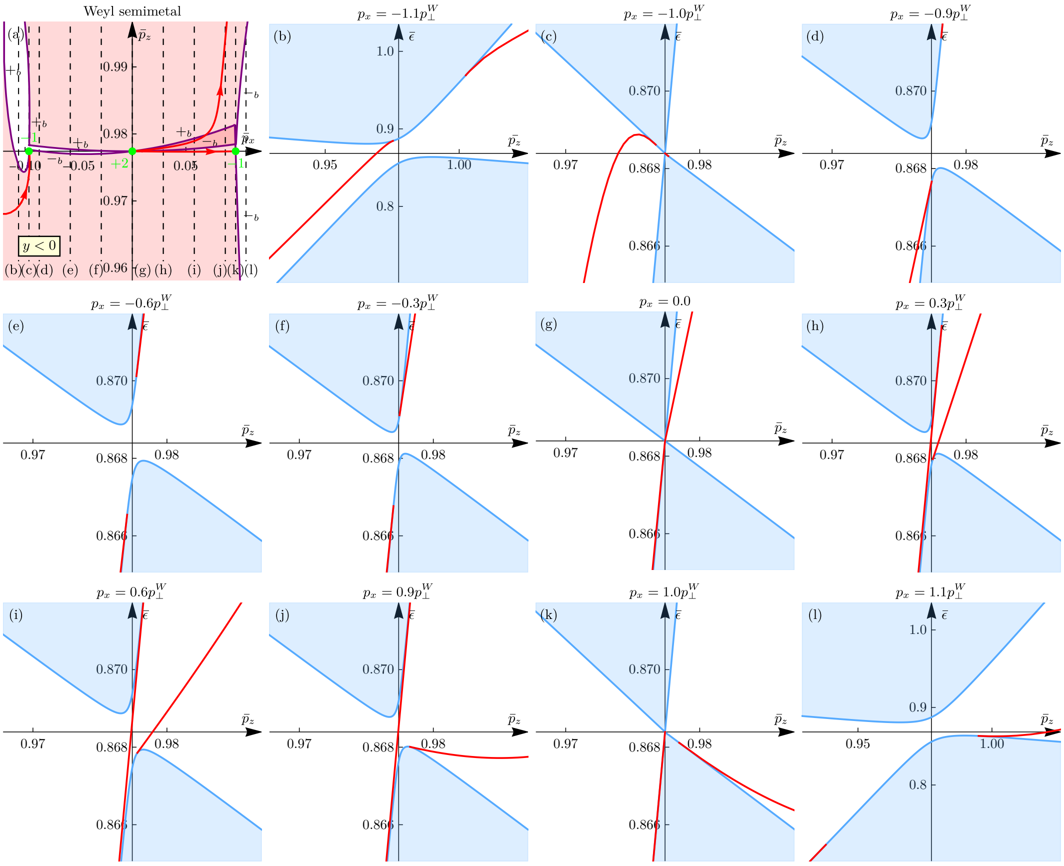

Figure 3.18: Surface band structure for a Weyl semimetal [$\hat{H}^W(\mathbf{p})$ from Eq. (3.26)] occupying the $y < 0$ half-space analog to Fig. 3.17. (a) Fermi contour at the energy of the projected Weyl points, indicated by the green points at $(p_x, p_z) = (\pm p_\perp^W, p_z^W)$ and $(0, p_z^W)$. The Fermi arcs of the surface states are shown in red and the arrows indicate the direction from a Weyl point with positive chirality to a Weyl point with negative chirality. The projected merging contours $\pm_b$ with the bulk continuum are shown in purple. The number of existing surface states at a given momentum is indicated by the red shading, where dark-red corresponds to two surface states, light-red for one surface state, and white for the absence of states. (b-l) Bulk (blue) and surface (red) dispersion for constant momentum $p_x =$ const. indicated by the plot label. We use the dimensionless units for the momentum $\bar{p}_i = p_i/p_{u0}$ [Eq. (3.35)] and energy $\bar{\epsilon} = \epsilon/|u|$ [Eq. (3.36)].

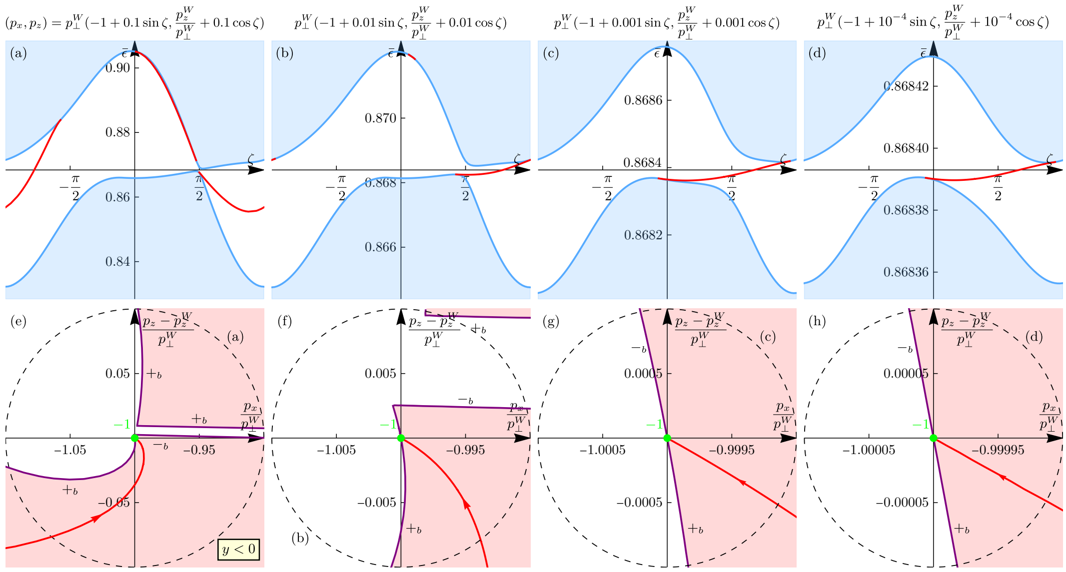

Figure 3.19: Surface band structure for a Weyl semimetal [$\hat{H}^W(\mathbf{p})$ from Eq. (3.26)] occupying the $y<0$ half-space analog to Fig. 3.17. (a-d) Circular momentum path around the Weyl point at $(p_x,p_z)=(-p_\perp^W,p_z^W)$ with $c=-1$ chirality for decreasing radii. The momentum path is given by $(p_x,p_z)=(-p_\perp^W+p_r\sin\zeta,p_z^W+p_r\cos\zeta)$, with (a) $p_r=0.1p_\perp^W$, (b) $p_r=0.01p_\perp^W$, (c) $p_r=0.001p_\perp^W$, and (d) $p_r=10^{-4}p_\perp^W$. (e-h) Fermi contour at the energy of the Weyl points ($\epsilon=\varepsilon_W$) analog to Fig. 3.18(a) in the momentum range of the corresponding band structure plot above, indicated by the dashed circles.

The monopole charge of the Weyl points can be better understood by analyzing the surface states in a circular momentum path around the node. Fig. 3.19 shows the circular momentum paths around the $c=-1$ Weyl point at $(-p_\perp^W,+p_z^W)$ with $(p_x,p_z)=(-p_\perp^W+p_r\sin\zeta,p_z^W+p_r\cos\zeta)$ for decreasing radius $p_r$ in addition to the Fermi and merging contours in the corresponding momentum range. We find a single chiral surface state in the range of $\zeta\in[-\pi,+\pi]$ which crosses the Fermi level with positive velocity. The Fermi contour in Fig. 3.19 becomes linear if the momentum radius is small. In this regime, the full Luttinger model in the WSM phase can be described by the well-known low-energy Hamiltonian for a single Weyl point $H_{WP}(\mathbf{p})$ from Eq. (2.17). A similar analysis can be performed for the Weyl point at $(+p_\perp^W, +p_z^W)$, shwon in Fig. 3.20.

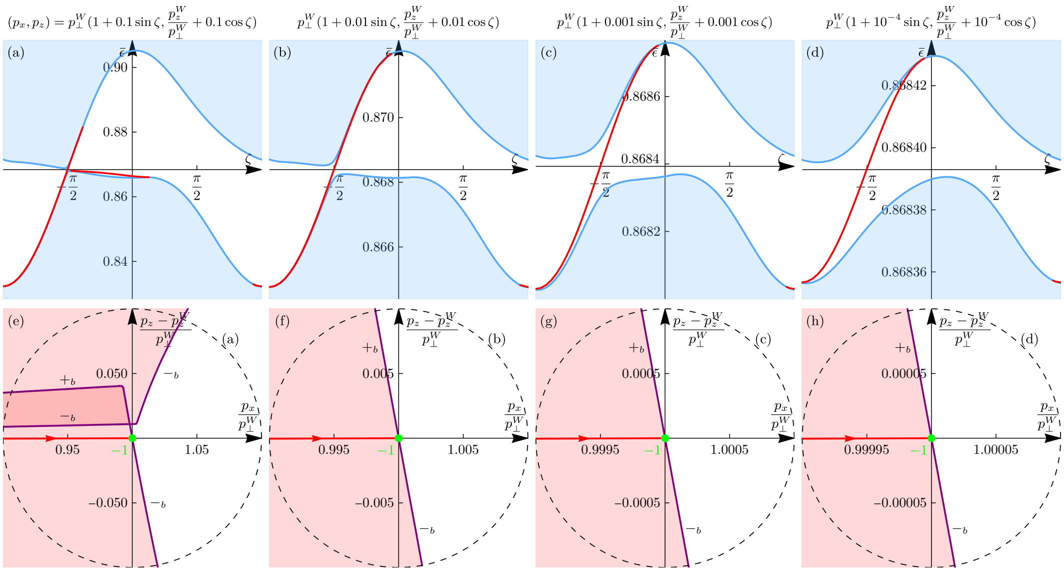

Figure 3.20: Surface band structure for a Weyl semimetal [$\hat{H}^W(\mathbf{p})$ from Eq. (3.26)] occupying the $y < 0$ half-space analog to Fig. 3.19. (a-d) Circular momentum path around the Weyl point at $(p_x, p_z) = (p_\perp^W, p_z^W)$ with $c = -1$ chirality for decreasing radii. The momentum path is given by $(p_x, p_z) = (p_\perp^W + p_r \sin\zeta, p_z^W + p_r \cos\zeta)$, with (a) $p_r = 0.1 p_\perp^W$, (b) $p_r = 0.01 p_\perp^W$, (c) $p_r = 0.001 p_\perp^W$, and (d) $p_r = 10^{-4} p_\perp^W$. (e-h) Fermi contour at the energy of the Weyl points ($\epsilon = \varepsilon_W$) analog to Fig. 3.18(a) in the momentum range of the corresponding band structure plot above, indicated by the dashed circles.

For the middle Weyl point at $(0, +p_z^W)$ (Fig. 3.21), we find two chiral surface states, which cross the Fermi level with negative velocity around $\zeta = +\pi/2$ [see Fig. 3.21(c)]. This confirms the superposition of two Weyl points in the projected surface Brillouin zone due to bulk-boundary correspondence. Interestingly, the momentum range of the linear regime is different for each Weyl point.

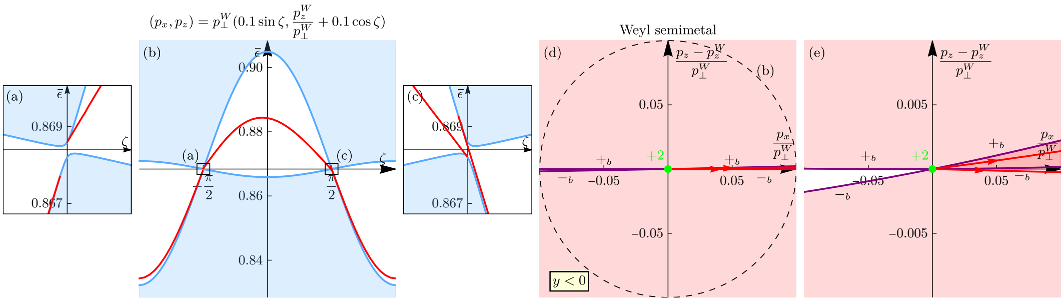

Figure 3.21: Surface band structure for a Weyl semimetal [$\hat{H}^W(\mathbf{p})$ from Eq. (3.26)] occupying the $y < 0$ half-space analog to Fig. 3.19. (a-c) Circular momentum path around the Weyl point at $(p_x, p_z) = (0, p_z^W)$ with $c = +2$ chirality. The momentum path is given by $(p_x, p_z) = (p_r \sin\zeta, p_z^W + p_r \cos\zeta)$, with $p_r = 0.1 p_\perp^W$. The framed insets (a,c) show a zoom around the regions with the smallest gap at $\zeta = \pm\pi/2$. (d) Fermi contour at the energy of the Weyl points ($\epsilon = \varepsilon_W$) analog to Fig. 3.18(a) in the momentum range of (b), indicated by the dashed circles. (e) Fermi contour analog to (d) with a smaller range in $p_z$ to show the seperation of the Fermi arcs and merging contours.

### 3.8.2 Surface parallel to the strain

The $z = 0$ surface leads to a projection of the Weyl points along the strain splitting in $p_z$. Here, the projected surface Brillouin zone hosts four double Weyl points, as shown in Fig. 3.1. The Weyl nodes are located at the momentum $(p_x, p_y) = (\pm p_\perp^W, 0)$ with $c = -2$ and $(0, \pm p_\perp^W)$ with $c = +2$. Hence, the physical properties of the WSM phase are most relevant in the range of the linear BIA term around the $\Gamma$ point.

The surface states of the $z > 0$ WSM system are shown in Fig. 3.22. The linear momentum paths for constant angles, using the polar coordinates $(p_x, p_y) = p_\perp(\cos\varphi, \sin\varphi)$ are given in Figs. 3.22(b,e,h). In the range of the linear BIA term we see no significant difference to the line-node semimetal phase in Fig. 3.16. The effect of the cubic BIA terms is clearly visible in the momentum range close to $p_\perp \sim p_{\beta_1}$ in Figs. 3.22(c,d,f,g,i,j). Similar to the previous section, we can analyze effective 2D momentum planes for the topological behavior. The diagonal momentum paths for $\varphi = \pm\pi/4$ have a zero effective 2D Chern number, since the chiralities of the Weyl points along a diagonal sum to zero. This is visualized by the bulk-boundary correspondence in the zoom-in plots of Figs. 3.22(f,g) for $\varphi = +\pi/4$ and (i,j) for $\varphi = -\pi/4$. Interestingly, the realization of the effective $C = 0$ 2D Chern number is different for the two diagonals. For $\varphi = +\pi/4$ [Figs. 3.22(f,g)], we see four crossings of the surface states with the Fermi level. Since two have positive and two negative velocity, they result in a zero Chern number. For $\varphi = -\pi/4$, no surface state crosses the Fermi level around $p_\perp \sim p_\perp^W$.

In summary, this results in two Fermi arcs, which connect the $c = +2$ Weyl point at $(0, +p_\perp^W)$ and the $c = -2$ Weyl point at $(+p_\perp^W, 0)$, and two time-reversal partner Fermi arcs at negative momentum. This is depicted in Fig. 3.22(a), where the additional trivial Fermi contour outside of the Weyl points is present, similar to the line-node semimetal phase in Fig. 3.16(a). The cubic BIA also introduces additional merging contours, which follow two close circular paths through the Weyl points, in between the Fermi arcs.

The Figs. 3.22(k-t) show the momentum region around the $c = -2$ Weyl point at $(p_x, p_y) = (+p_\perp^W, 0)$, using $(p_x, p_y) = (p_\perp^W + p_r \cos\zeta, p_r \sin\zeta)$. The circular momentum paths with the radius $p_r = 0.1 p_\perp^W$ is presented in Figs. 3.22(k-m) and the smaller radius $p_r = 0.01 p_\perp^W$ in Figs. 3.22(p-r). Here, we find the two chiral surface states, which cross the Fermi level with negative velocity around $\zeta \sim +\pi/2$. In Figs. 3.22(n,o,s,t), we show the Fermi contour around the considered Weyl point. The $p_x$ axis in Figs. 3.22(o,t) have a different range to highlight the critical momentum scale, where the Fermi arcs become linear. This gives the regime, where the full WSM Hamiltonian can be approximized by the linear low-energy Weyl node Hamiltonian $\hat{H}_{WP}(\mathbf{p})$ from Eq. (2.17).

For horizontal and vertical momentum planes, we find a topological transition of $\pm 2$ at $p_{x,y} = \pm p_\perp^W$ and $\pm 4$ at $p_{x,y} = 0$, respectively. Consequently, we find that the $0 < p_{x,y} < p_\perp^W$ momentum regions host an effective 2D Chern insulator phase with $C = +2$, while the $0 > p_{x,y} > -p_\perp^W$ momentum regions have $C = -2$.

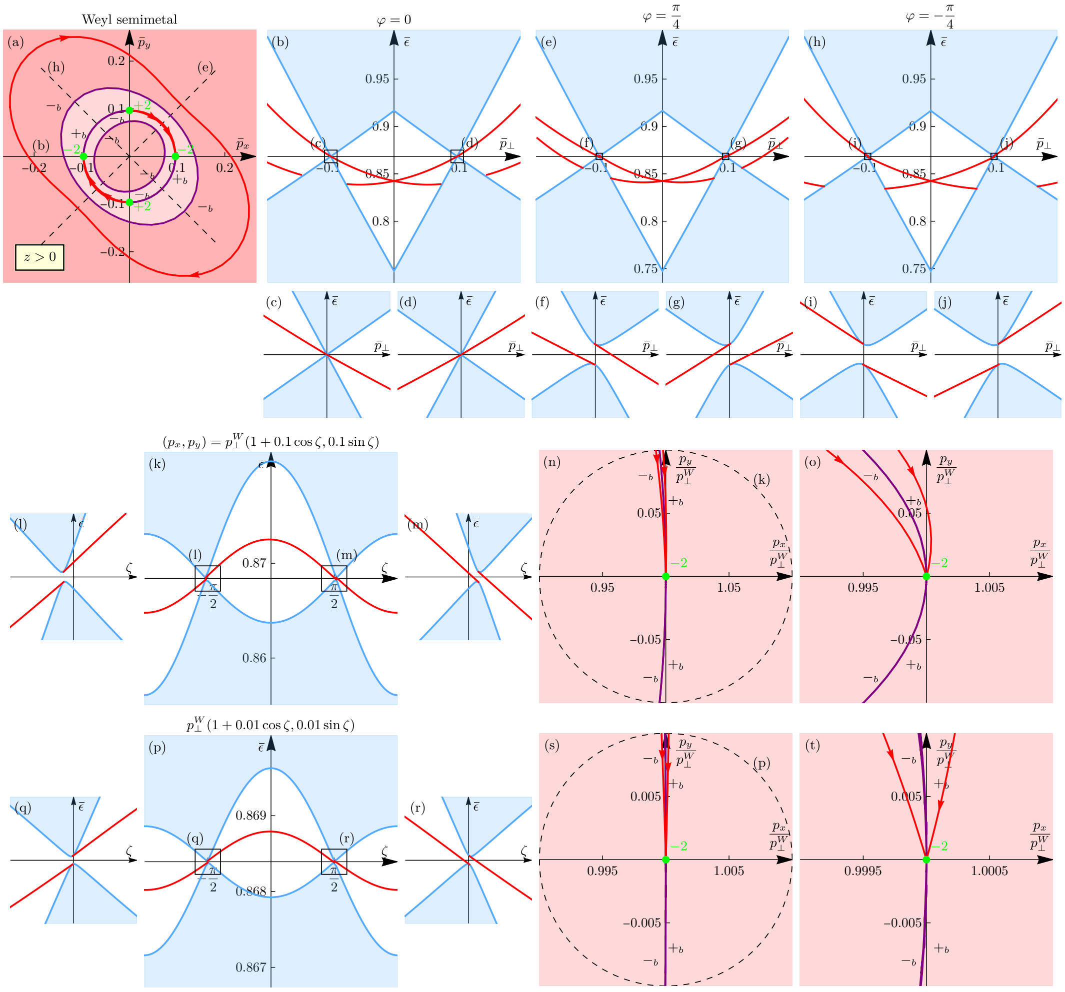

Figure 3.22: Surface band structure for a Weyl semimetal [$\hat{H}^W(\mathbf{p})$ from Eq. (3.26)] occupying the $z > 0$ half-space analog to Fig. 3.16. (a) Fermi contour at the energy of the Weyl points, which positions are indicated by the green points. The Fermi arcs of the surface states are shown by the red lines with arrows indicating the direction from positive to negative chirality. (b-j) Energy dispersion for a constant angle $\varphi$, with $(p_x, p_y) = p_\perp(\cos\varphi, \sin\varphi)$, as a function of $p_\perp$. The large momentum ranges are shown in (b,e,h) with zoom-ins around the gap minima in (c,d,f,g,i,j). (k-m, p-r) Circular momentum paths as a function of $\varphi$ around the Weyl point at $(p_x, p_y) = (+p_\perp^W, 0)$. (n,o,s,t) Zoom-in of the Fermi contour, analoge to (a), where (n,t) show enhanced $p_x$ axis, giving a non-square aspect ratio. We use the dimensionless variables with $|\epsilon| = \epsilon/|u|$ [Eq. 3.36)] and $\bar{p}_i = p_i/p_{u0}$ [Eq. 3.35)].

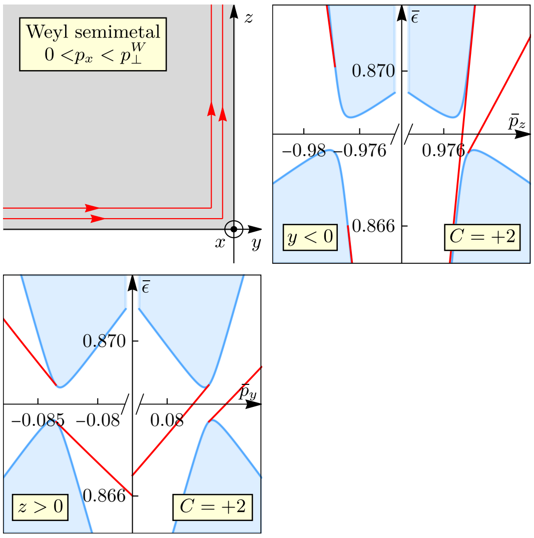

Figure 3.23: Chiral surface states (red arrows) in a Weyl semimetal with infinite length in the $x$-direction and two surfaces at $y = 0$ and $z = 0$. The framed plots show the surface band structure calculations in the momentum regime $0 < p_x < p_\perp^W$ for the semi-infite systems occupying the $y < 0$ and $z > 0$ half-spaces, respectively. In this momentum regime, the system is associated to an effective $C = +2$ Chern number, related to the surface states (red) which connect the valence and conductance bands of the bulk continuum (blue).

This behavior leads to physical consequences for a real WSM sample in 3D occupying both the $y < 0$ and $z > 0$ half-spaces. If the length of the system in the $x$-direction is infinite, we can consider a $p_x =$ const. momentum plane. For $p_x = p_\perp^W/2$, for instance, one can find two chiral states at the $z = 0$ surface with positive velocity. A second termination of the sample at $y = 0$ can be understood as a non straight continuation of the $z = 0$ surface plane. Hence, the bulk-boundary correspondence of the $z > 0$ surface states has to be continuous over the edge at $y = z = 0$. Therefore, it is possible to find two localized chiral states with positive velocity along the $y = 0$ surface. In total, the sample hosts two chiral surface states at the Fermi level, which move in a counter-clockwise direction around the edge, as presented in Fig. 3.23.

As discussed in Sec. 3.3, the Luttinger model is invalid if the compressive strain is too strong and the $j = 1/2$ states become relevant. This behavior is illustrated in Fig. 3.24, where we show the surface-state calculations for the Luttinger and Kane model for different strengths of strain. For minor strain with $u = -3$meV corresponding to a lattice mismatch of $\sim 1\%$, both models are in good agreement, where the Weyl points are connected pair-wise by the Fermi arcs and a trivial Fermi contour exists for $p_\perp > p_\perp^W$, as discussed above. While the surface states in the Luttinger model appear to be unaffected by increasing compressive strain, we find a significant evolution in the Kane model.

For $u = -10\text{meV}$, the crossing point of the surface states at $p_\perp = 0$ shifts up in energy in the Kane model. This leads to a separation of the Fermi arcs, which are still connecting the Weyl points pair-wise, and a decrease of the trivial Fermi contour, which now lies between the Weyl points ($p_\perp < p_\perp^W$). At $u = -14\text{meV}$ the Kane model undergoes a critical transition, where the crossing point of the surface states at $p_\perp = 0$ passes the Fermi level. Therefore, the trivial Fermi contour vanishes and reappears around $u = -16\text{meV}$, where the surface states at the $\Gamma$ point lies above the Fermi level. For $u = -17\text{meV}$, the trivial Fermi contour hybridizes with one set of Fermi arcs. This leads to a distinct change in the structure of the Fermi arcs, which are now connecting all four Weyl points in a circular shape. Here, both $\varphi = \pm\pi/4$ diagonals host surface states which cross the Fermi level around $p_\perp \sim p_\perp^W$, without diverging from the effective $C = 0$ 2D Chern number.

In conclusion, we find that the Luttinger model delivers a good description of the low-energy behavior of many topological semimetals. The most relevant condition is the absence of any additional bands close to the $j = 3/2$ states around the Fermi energy.

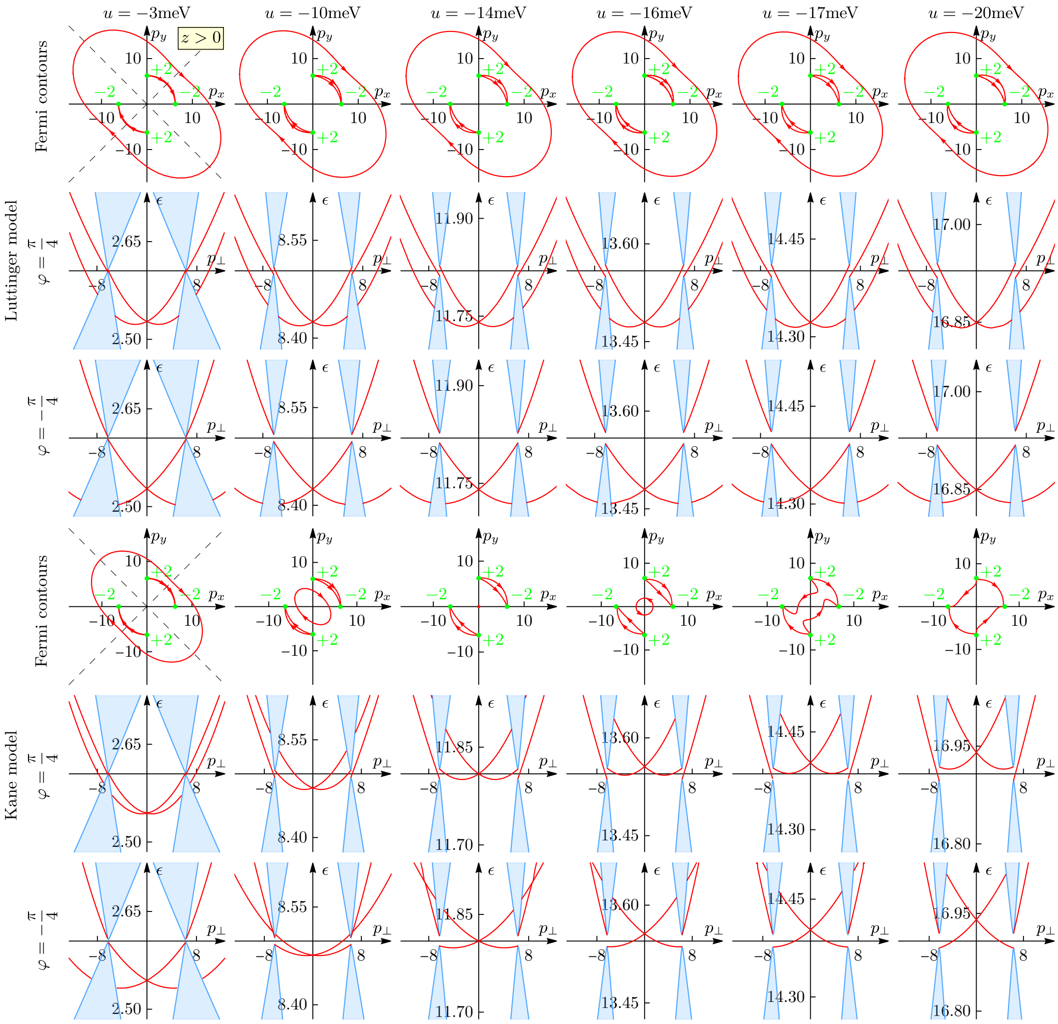

Figure 3.24: Comparison of the 4-band Luttinger model (three top rows) and 6-band Kane model (three bottom rows) in the Weyl semimetal phase with bulk-inversion-asymmetry and compressive strain $u$ occupying the $z > 0$ half-space. We show the Fermi contours with the Fermi arcs of the surface states in red and the positions of the projected Weyl points in green. The surface band structures are calculated along the diagonal momentum paths for $\varphi = \pm\pi/4$ with $(p_x, p_y) = p_\perp(\cos\varphi, \sin\varphi)$, analog to Figs. 3.22(e,h). The columns correspond to different strengths of compressive strain with increasing magnitude. The units of momentum is $\mu\mathrm{m}^{-1}$ and energy is meV and we take the material-specific parameters of HgTe from Tabs. A.2 and A.1.

# 4 Topological superconductivity within the Luttinger model

## Contents

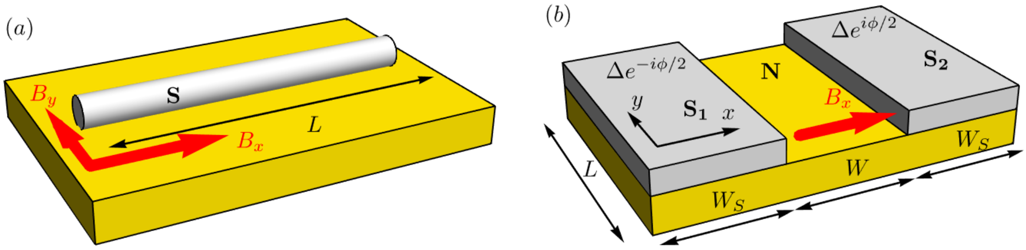

Figure 4.1: (a) Sketch of a 1D Luttinger wire of length $L$ in contact with a s-wave superconductor and in the presence of a Zeeman field $B_x$ or $B_y$. (b) Luttinger Josephson junction with a non-superconducting (N) region in between two superconductors ($S_1$, $S_2$) with a phase difference of $\phi$. The N and the $S_{1/2}$ regions have a width of $W$ and $W_S$ and the full junction has a length of $L$. A magnetic field in $x$ direction $B_x$ is applied only to the N region (red arrow).

Over the last decades, a tremendous interest in the formation of Majorana bound states (MBSs) has arisen [92, 93, 131, 132, 98]. These states were first predicted in high energy physics by Ettore Majorana in 1937 [20] as a fermion that is its antiparticle. It was later discovered that they also exist in condensed-matter systems as zero-energy modes, which appear at the boundaries of topological superconductors (SCs) [79, 90]. The topological protection of their nonlocal properties and non-abelian statistics make MBSs ideal candidates for topological quantum computation [22, 99, 133, 90, 132, 98]. Consequently, the interest in detecting signatures of MBSs in experiments is high [134, 131, 135, 136, 24].

It was predicted that MBSs emerge in semiconducting nanowires with proximitized $s$-wave superconductivity and spin-orbit coupling (SOC) [109, 110, 137, 138, 98, 139]. These systems go into a topological phase if a Zeeman field perpendicular to the SOC field inverts the SC gap in the bulk dispersion (see Fig. 2.3). A similar topological phase transition appears in 2D Josephson junction if the double degenerate Andreev bound states (ABSs) split at a finite Zeeman field (see Fig. 2.4). In these topological Josephson junctions, the MBSs form at the boundary between the normal region and the vacuum (see Fig. 2.2) and are protected by the topological gap in the ABS spectrum [140, 23, 136, 24, 25].

This chapter analyzes these two superconducting systems in the Luttinger model. This 4-band model provides a more realistic description of materials and their band structure in comparison to the 2-band model discussed before. Additionally, intrinsic spin-orbit interactions, especially bulk inversion asymmetry (BIA) terms, are already considered [116], leading to an inherent emergence of MBSs in the system without applying extra SOC.

As previously discussed, the Luttinger model hosts various topological phases with topological surface states, even without superconductivity. Furthermore, the description of $j = 3/2$ particles allows the existence of higher-order superconducting couplings beyond the usual *s*- and *p*-wave Cooper pairs [141, 142, 143, 144, 145, 146, 147]. This opens a new field of research that can analyze the combination of different superconducting effects, bulk states with intrinsic SOC, and topological surface states in the future. The findings of this chapter are also published in Ref. [28].

## 4.1 Superconducting pairing in j=3/2 carriers

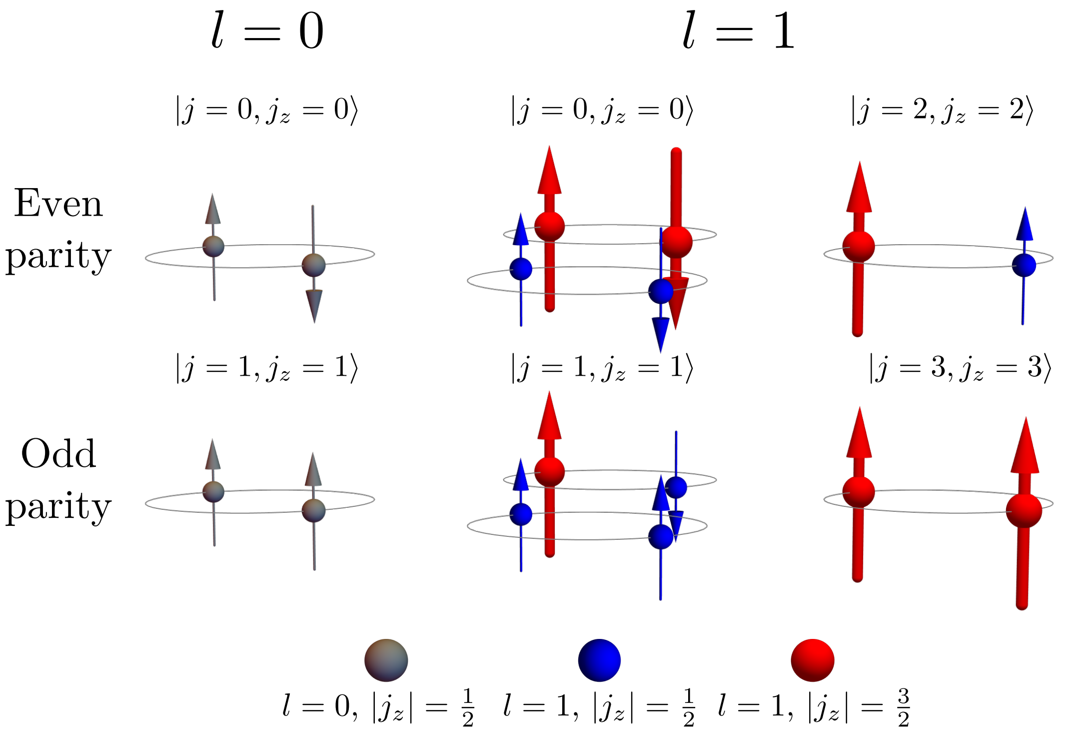

Figure 4.2: Schematic presentation of the possible Cooper pair states in $l = 0$ (gray) and $l = 1$ (red, blue) states.

Recently, a broad interest in the superconducting pairing in quadratic nodal semimetals, described by the Luttinger model, can be found in the scientific community [141, 148, 149, 150, 151, 142, 143, 145]. Due to the $j = 3/2$ character of the electrons forming the Cooper pairs, exotic spin pairings are possible. One can find the spin-singlet ($j = 0$) and spin-triplet ($j = 1$) pairings, which also arise in the traditional $j = 1/2$ SC with $l = 0$, but also spin-quintet ($j = 2$) and spin-septet ($j = 3$) pairings are realizable. We present a schematic overview of the different coupling possibilities in Fig. 4.2. The Clebsch-Gordon coefficients [152] in Tab. 4.1 correspond to all possible Cooper pair states [142, 145].

This thesis focuses on the singlet $s$-wave pairing state with $j = 0$. In the usual $l = 0$ states, only a combination of a $j_z = +1/2$ and $j_z = -1/2$ state can lead to an

$s$-wave superconducting pairing (see top left of Fig. 4.2). In Luttinger semimetals (LSMs) with $l = 1$, an $s$-wave state forms by a quantum mechanical superposition of a Cooper pair, consisting of a $j_z = +1/2$ and $j_z = -1/2$ state (blue in Fig. 4.2), and another Cooper pair, built from a $j_z = +3/2$ and $j_z = -3/2$ state (red in Fig. 4.2). In the basis $(\Psi_L, \Psi_L^*)^T$ [Eq. (3.1)], the $s$-wave pairing term in its most straightforward momentum independent form is given by [151, 142, 143, 145]

$$\hat{\Delta}_s = \Delta_s \hat{U}_{\mathcal{T}}, \quad \text{with} \quad \hat{U}_{\mathcal{T}} = e^{i\pi \hat{J}_y} = \begin{pmatrix} 0 & 0 & 0 & 1 \\ 0 & 0 & -1 & 0 \\ 0 & 1 & 0 & 0 \\ -1 & 0 & 0 & 0 \end{pmatrix}. \tag{4.1}$$

We want to briefly summarize the higher spin coupling terms discussed in the literature. The odd parity p-wave state ($j = 1$) usually consists of a combination of two spin-1/2 states with equal $j_z$ (see bottom left in Fig. 4.2). The LSM gives another possibility, leading to a superposition with an additional pairing between a $j_z = +3/2$ and $j_z = -1/2$ state (or vice versa). A possible momentum-dependent $p$-wave superconducting coupling term is discussed in Refs. [141, 145] and is given by

$$\hat{\Delta}_p(\boldsymbol{p}) = \Delta_p \begin{pmatrix} \frac{3}{4}p_- & \frac{\sqrt{3}}{2}p_z & \frac{\sqrt{3}}{4}p_+ & 0 \\ \frac{\sqrt{3}}{2}p_z & \frac{3}{4}p_+ & 0 & -\frac{\sqrt{3}}{4}p_- \\ \frac{\sqrt{3}}{4}p_+ & 0 & -\frac{3}{4}p_- & \frac{\sqrt{3}}{2}p_z \\ 0 & -\frac{\sqrt{3}}{4}p_- & \frac{\sqrt{3}}{4}p_z & -\frac{3}{4}p_+ \end{pmatrix}, \tag{4.2}$$

where $\Delta_p$ is a real constant.

A unique feature of superconducting pairing in LSMs is the higher spin $d$-wave ($j = 2$) and $f$-wave ($j = 3$) pairings. The $d$-wave Cooper pair arises from a combination of a $j_z = +3/2$ and $j_z = +1/2$ state, which is impossible without the existence of both heavy-hole (HH) and light-hole (LH) states. In general, the even parity $d$-wave state can be expanded by [151, 143]

$$\hat{\Delta}_d = \sum_i \Delta_{d,i} \hat{\Gamma}_i, \tag{4.3}$$

where the $\hat{\Gamma}_i$ matrices are given by

$$\hat{\Gamma}_{yz} = \frac{1}{\sqrt{3}}\Big(\hat{J}_y\hat{J}_z + \hat{J}_z\hat{J}_y\Big)\hat{U}_{\mathcal{T}}, \tag{4.4}$$

$$\hat{\Gamma}_{xz} = \frac{1}{\sqrt{3}}\Big(\hat{J}_z\hat{J}_x + \hat{J}_x\hat{J}_z\Big)\hat{U}_{\mathcal{T}}, \tag{4.5}$$

$$\hat{\Gamma}_{xy} = \frac{1}{\sqrt{3}}\Big(\hat{J}_x\hat{J}_y + \hat{J}_y\hat{J}_x\Big)\hat{U}_{\mathcal{T}}, \tag{4.6}$$

$$\hat{\Gamma}_{3z^2-r^2} = \frac{1}{3}\Big(2\hat{J}_z^2 - \hat{J}_x^2 - \hat{J}_y^2\Big)\hat{U}_{\mathcal{T}}, \tag{4.7}$$

$$\hat{\Gamma}_{x^2-y^2} = \frac{1}{\sqrt{3}}\Big(\hat{J}_x^2 - \hat{J}_y^2\Big)\hat{U}_{\mathcal{T}}. \tag{4.8}$$

Here, the subscripts are motivated by the corresponding spherical harmonics. All $\hat{\Gamma}_i$ matrices are generally even under time-reversal symmetry (TRS), which means that the pairing state preserves TRS if the amplitude $\Delta_{d,i}$ is real. A possible $d$-wave pairing term discussed by Refs. [148, 145] is given by

$$\tilde{\Delta}_d(\boldsymbol{p}) = \Delta_1 f(\boldsymbol{p})\eta_s + \Delta_0\Big(\hat{\Gamma}_{xz} + i\hat{\Gamma}_{yz}\Big), \tag{4.9}$$

with $\Delta_0$ and $\Delta_1$ being real constants, $\eta_s$ being a spin-singlet state with an isotropic form factor $f(\boldsymbol{p}) = p_z p_+$, which breaks TRS.

As discussed in Sec. 2.3, we use the convenient basis transformation from Eq. (2.46), which applies the unitary part of the TRS operator to the quasi-hole states

$$\Psi_N = \begin{pmatrix} \Psi_L \\ \hat{U}_{\mathcal{T}}\Psi_L^* \end{pmatrix}. \tag{4.10}$$

In this basis, the $s$-wave coupling term simplifies to be proportional to the unit matrix

$$\hat{\Delta}_s = \Delta_s \hat{1}_4, \tag{4.11}$$

which is used throughout the rest of the thesis.

| Pairing state | Cooper pair |
|---|---|
| Singlet ($j = 0$) | $\vert j=0, j_z=0\rangle = \frac{1}{2}\big(\vert\tfrac{3}{2},-\tfrac{3}{2}\rangle - \vert-\tfrac{3}{2},\tfrac{3}{2}\rangle - \vert\tfrac{1}{2},-\tfrac{1}{2}\rangle + \vert-\tfrac{1}{2},\tfrac{1}{2}\rangle\big)$ |
| Triplet ($j = 1$) | $\vert j=1, j_z=1\rangle = \frac{1}{\sqrt{10}}\big(\sqrt{3}\,\vert\tfrac{3}{2},-\tfrac{1}{2}\rangle - 2\,\vert\tfrac{1}{2},\tfrac{1}{2}\rangle + \sqrt{3}\,\vert-\tfrac{1}{2},\tfrac{3}{2}\rangle\big)$ |
| | $\vert j=1, j_z=0\rangle = \frac{1}{\sqrt{20}}\big(3\,\vert\tfrac{3}{2},-\tfrac{3}{2}\rangle - \vert\tfrac{1}{2},-\tfrac{1}{2}\rangle - \vert-\tfrac{1}{2},\tfrac{1}{2}\rangle + 3\,\vert-\tfrac{3}{2},\tfrac{3}{2}\rangle\big)$ |
| | $\vert j=1, j_z=-1\rangle = \frac{1}{\sqrt{10}}\big(\sqrt{3}\,\vert-\tfrac{3}{2},\tfrac{1}{2}\rangle - 2\,\vert-\tfrac{1}{2},-\tfrac{1}{2}\rangle + \sqrt{3}\,\vert\tfrac{1}{2},-\tfrac{3}{2}\rangle\big)$ |
| Quintet ($j = 2$) | $\vert j=2, j_z=2\rangle = \frac{1}{\sqrt{2}}\big(\vert\tfrac{3}{2},\tfrac{1}{2}\rangle - \vert\tfrac{1}{2},\tfrac{3}{2}\rangle\big)$ |
| | $\vert j=2, j_z=1\rangle = \frac{1}{\sqrt{2}}\big(\vert\tfrac{3}{2},-\tfrac{1}{2}\rangle - \vert-\tfrac{1}{2},\tfrac{3}{2}\rangle\big)$ |
| | $\vert j=2, j_z=0\rangle = \frac{1}{2}\big(\vert\tfrac{3}{2},-\tfrac{3}{2}\rangle + \vert\tfrac{1}{2},-\tfrac{1}{2}\rangle - \vert-\tfrac{1}{2},\tfrac{1}{2}\rangle - \vert-\tfrac{3}{2},\tfrac{3}{2}\rangle\big)$ |
| | $\vert j=2, j_z=-1\rangle = \frac{1}{\sqrt{2}}\big(\vert-\tfrac{3}{2},\tfrac{1}{2}\rangle - \vert\tfrac{1}{2},-\tfrac{3}{2}\rangle\big)$ |
| | $\vert j=2, j_z=-2\rangle = \frac{1}{\sqrt{2}}\big(\vert-\tfrac{3}{2},-\tfrac{1}{2}\rangle - \vert-\tfrac{1}{2},-\tfrac{3}{2}\rangle\big)$ |
| Septet ($j = 3$) | $\vert j=3, j_z=3\rangle = \vert\tfrac{3}{2},\tfrac{3}{2}\rangle$ |
| | $\vert j=3, j_z=2\rangle = \frac{1}{\sqrt{2}}\big(\vert\tfrac{3}{2},\tfrac{1}{2}\rangle + \vert\tfrac{1}{2},\tfrac{3}{2}\rangle\big)$ |
| | $\vert j=3, j_z=1\rangle = \frac{1}{\sqrt{5}}\big(\vert\tfrac{3}{2},-\tfrac{1}{2}\rangle + \sqrt{3}\,\vert\tfrac{1}{2},\tfrac{1}{2}\rangle + \vert-\tfrac{1}{2},\tfrac{3}{2}\rangle\big)$ |
| | $\vert j=3, j_z=0\rangle = \frac{1}{\sqrt{20}}\big(\vert\tfrac{3}{2},-\tfrac{3}{2}\rangle + 3\,\vert\tfrac{1}{2},-\tfrac{1}{2}\rangle + 3\,\vert-\tfrac{1}{2},\tfrac{1}{2}\rangle + \vert-\tfrac{3}{2},\tfrac{3}{2}\rangle\big)$ |
| | $\vert j=3, j_z=-1\rangle = \frac{1}{\sqrt{5}}\big(\vert-\tfrac{3}{2},\tfrac{1}{2}\rangle + \sqrt{3}\,\vert-\tfrac{1}{2},-\tfrac{1}{2}\rangle + \vert\tfrac{1}{2},-\tfrac{3}{2}\rangle\big)$ |
| | $\vert j=3, j_z=-2\rangle = \frac{1}{\sqrt{2}}\big(\vert-\tfrac{3}{2},-\tfrac{1}{2}\rangle + \vert-\tfrac{1}{2},-\tfrac{3}{2}\rangle\big)$ |
| | $\vert j=3, j_z=-3\rangle = \vert-\tfrac{3}{2},-\tfrac{3}{2}\rangle$ |

Table 4.1: Summary of all possible superconducting pairing states in the Luttinger model. We use the short notation $|j_{z,1}, j_{z,2}\rangle \equiv |j_1, j_2; j_{z,1}, j_{z,2}\rangle$, since $j_1 = j_2 = 3/2$. [142, 145]

## 4.2 Reflection matrix as topological invariant

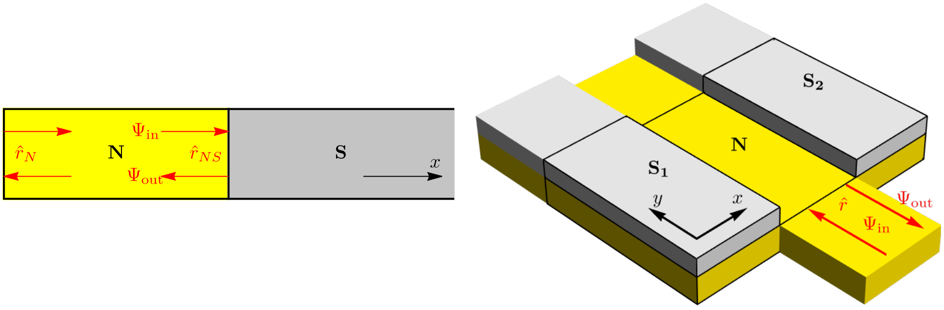

Figure 4.3: Schematic setup for determining of the topological invariant given by the reflection matrix. (left) 1D semi-infinite superconducting wire (S) connected to a normal conducting region (N). The red arrows indicate the scattering modes which reflect at the N-S interface $\hat{r}_{NS}$ and the left boundary of the N region $\hat{r}_N$. (right) Setup of the numerical calculation for the reflection matrix in a 2D Josephson junction (see Fig. 4.1). The black frame indicates the scattering region, where a single semi-infinite N lead is attached to one boundary of the finite N region between two superconductors ($\text{S}_1$ and $\text{S}_2$). The full Josephson junction becomes semi-infinite in $y \to \infty$ by a full S-N-S lead.

Throughout this work, we study superconducting systems under the effect of magnetic fields. These are members of the symmetry class D due to the conserved particle-hole symmetry (PHS) and broken TRS (see Sec. 2.1) [29, 30, 32]. In 1D, a $\mathbb{Z}_2$ invariant $\mathcal{Q}$ determines the topological classification, which gives the parity of the number of MBSs $\mathcal{N}$ at the system's boundary. If $\mathcal{N}$ is even, the system is topologically trivial with $\mathcal{Q} = +1$. The system is topologically non-trivial for odd $\mathcal{N}$ with $\mathcal{Q} = -1$.

Akhmerov et al. [153] showed that one can compute $\mathcal{Q}$ with the reflection matrix at the system boundary, where the MBSs form. Fulga et al. [154, 155] expanded this framework for general symmetry classes and higher dimensions. This section is dedicated to explaining the formalism and showing the concrete application for this work.

Only localized states contribute to the scattering in the system at zero energy. Therefore, one can describe the scattering problem of a 1D N-S interface (see Fig. 4.3) with the unitary $2M \times 2M$ reflection matrix $\hat{r}_{NS}$, where the number of modes $2M$ is even due to the PHS. The relation between the incoming and outgoing modes is given by

$$\hat{\Psi}_{\text{out}} = \hat{r}_{NS}\hat{\Psi}_{\text{in}}, \quad \text{with} \quad \hat{r}_{NS} = \begin{pmatrix} \hat{r}_{ee} & \hat{r}_{eh} \\ \hat{r}_{he} & \hat{r}_{hh} \end{pmatrix}. \tag{4.12}$$

Here, $\hat{r}_{ee}$ ($\hat{r}_{hh}$) is the normal reflection from electron to electron (hole to hole), and $\hat{r}_{eh}$ ($\hat{r}_{he}$) is the Andreev reflection from hole to electron (electron to hole). In a superconducting system, the reflection matrix should conserve PHS

$$\mathcal{C}^\dagger \hat{r}_{NS} \mathcal{C} = \hat{r}_{NS}, \tag{4.13}$$

which gives the symmetry relations

$$\hat{r}_{ee}^* = \hat{r}_{hh} \quad \text{and} \quad \hat{r}_{eh}^* = \hat{r}_{he}. \tag{4.14}$$

Using the unitary transformation, one can transform the reflection matrix into the so-called Majorana basis

$$\begin{aligned} \hat{r} &= \hat{\Omega}^\dagger \hat{r}_{NS} \hat{\Omega} \quad \text{with} \quad \hat{\Omega}^\dagger = \frac{1}{\sqrt{2}} \begin{pmatrix} 1 & 1 \\ -i & i \end{pmatrix} \\ &= \frac{1}{2} \begin{pmatrix} \hat{r}_{ee} + \hat{r}_{hh} + \hat{r}_{eh} + \hat{r}_{he} & i(\hat{r}_{ee} - \hat{r}_{hh} - \hat{r}_{eh} + \hat{r}_{he}) \\ -i(\hat{r}_{ee} - \hat{r}_{hh} + \hat{r}_{eh} - \hat{r}_{he}) & \hat{r}_{ee} + \hat{r}_{hh} - \hat{r}_{eh} - \hat{r}_{he} \end{pmatrix}. \end{aligned} \tag{4.15}$$

In this basis, the reflection matrix is purely real $\hat{r}^* = \hat{r}$ due to PHS. One can use the condition for a bound state in the 1D N-S junction [156]

$$\det\left(\hat{1} - \hat{r}_N \hat{r}_{NS}\right) = 0 \quad \text{with} \quad \hat{r}_N = \begin{pmatrix} \hat{U}_N & 0 \\ 0 & \hat{U}_N^* \end{pmatrix}, \tag{4.16}$$

where $\hat{r}_N$ is the reflection matrix from the terminated normal lead and $\hat{U}_N$ ($\hat{U}_N^*$) is an $M \times M$ unitary matrix of electron (hole) reflection amplitudes. Since a unitary transformation does not change the determinant of a matrix, we can rewrite the bound state condition

$$\det\left(\hat{1} + \hat{O}_N \hat{r}\right) = 0, \tag{4.17}$$

with the unitary and orthogonal matrix $\hat{O}_N = -\hat{\Omega}^\dagger \hat{r}_N \hat{\Omega}$. The shape of Eq. (4.17) implies that the number of eigenvalues $(-1)$ of $\hat{O}_N \hat{r}$ determines the number of bound states $\mathcal{N}$.

Using the properties of unitary matrices, one can easily show that

$$\det\left(\hat{O}_N\right) = \det(\hat{r}_N) = \det\left(\hat{U}_N\right)\det\left(\hat{U}_N^*\right) = 1. \tag{4.18}$$

Therefore, one can find the relation

$$\det\left(\hat{O}_N \hat{r}\right) = \det(\hat{r}) = \prod_{i=1}^{2M} \lambda_i = \pm 1, \tag{4.19}$$

where $\lambda_i$ are the eigenvalues of $\hat{r}$, which are either $+1$, $-1$ or come in conjugate pairs of $e^{\pm i\theta}$. This leads to the topological invariant

$$\mathcal{Q} = \det(\hat{r}) = (-1)^{\mathcal{N}}, \tag{4.20}$$

which determines if the number of bound states is even or odd.

It is essential to mention that the reflection matrix does not fully describe the scattering problem if a non-localized bulk state exists at zero energy due to a closed topological gap. Here, the transmission of the scattering matrix gives a finite contribution, making the reflection matrix non-unitary. The topological invariant is not defined without a gap, and we find $\det(r) = 0$.

Throughout this thesis, we calculate the reflection matrix of a system using the algorithms of the Kwant code [157]. For a 1D superconducting wire, we model the system by a semi-infinite normal conducting lead connected to a semi-infinite superconducting lead, as shown on the left of Fig. 4.3. For the 2D Josephson junction calculations, we apply a semi-infinite in $y \in ]-\infty, -L/2]$ direction normal lead on one side of the system at $-W/2 \leq x \leq W/2$. To counteract the effects of reflection with the opposite edge, we extend the entire Josephson junction with one normal and two superconducting leads for $y \in [L/2, \infty[$, as shown in the right of Fig. 4.3. This way, we can model the narrow N region of the Josephson junction as an effective 1D SC and get the topological invariant accordingly.

To verify this formalism, one can apply it to the 1D superconducting Rashba wire from Eq. (2.65). Here, we confirm numerically that the topological invariant is given by

$$\mathcal{Q}_{\text{Rashba wire}} = \begin{cases} +1 & \text{for} \quad B_x < \sqrt{\mu^2 + \Delta^2} \\ -1 & \text{for} \quad B_x > \sqrt{\mu^2 + \Delta^2} \end{cases} , \tag{4.21}$$

which agrees with the predictions of Refs. [109, 110]. Our numerical calculations in Sec. 2.3.4 show that MBSs form only in the magnetic field range, where $\mathcal{Q}_{\text{Rashba wire}} = -1$.

Additionally, we can calculate $\mathcal{Q}$ in the 2D Josephson junction setup, discussed in Sec. 2.3.5. We find $\mathcal{Q} = -1$ inside the boundaries of Fig. 2.4(a) and $\mathcal{Q} = +1$ outside of it. This confirms the validity of the method, which we use for the superconducting Luttinger systems throughout this chapter.

## 4.3 Finite-difference method

To study topological superconductivity in LSMs, we use two different setups. We can explore the bulk dispersion analytically in an infinite 1D wire ($L \to \infty$) since translation symmetry is preserved and $p_x$ is a good quantum number. The calculation of MBSs demands the existence of a boundary at the ends of the wire. We apply effective hard-wall boundary conditions given by:

$$\Psi\left(x = -\frac{L}{2}\right) = \Psi\left(x = \frac{L}{2}\right) = 0. \tag{4.22}$$

Consequently, this boundary condition breaks translation symmetry; therefore, $p_x$ is not a good quantum number.

Nevertheless, the junction between the normal and SC regions in the 2D Josephson junction setup [see Fig. 4.1(b)] already breaks translation symmetry in the $x$-direction. One must verify that the wavefunction is continuous at the interfaces in addition to the effective hard-wall boundary condition at the ends of the SCs

$$\Psi_{S_1}\left(x=-\frac{W}{2},y\right)=\Psi_N\left(x=-\frac{W}{2},y\right), \tag{4.23}$$

$$\Psi_{S_2}\left(x=\frac{W}{2},y\right)=\Psi_N\left(x=\frac{W}{2},y\right) \tag{4.24}$$

$$\Psi_{S_1}\left(x=-\frac{W}{2}-W_S,y\right)=\Psi_{S_2}\left(x=\frac{W}{2}+W_S,y\right)=0. \tag{4.25}$$

For a Josephson junction with infinite length in the $y$-direction ($L\to\infty$), we can analyze the ABSs with the good quantum number $p_y$, which act as effective bulk states in the subgap regime ($|\epsilon|<\Delta$) of the system. In parallel to the wire setup, one needs to introduce additional boundaries in the $y$-direction to calculate the MBSs, forming at the ends of the normal region (see Fig. 2.2). Therefore, we apply effective hard-wall boundary conditions in the $y$-direction via

$$\Psi\left(x,y=-\frac{L}{2}\right)=\Psi\left(x,y=\frac{L}{2}\right)=0. \tag{4.26}$$

In the case of broken translation symmetry, one must use the momentum operator $p_x\to-i\partial_x$. This leads to complicated differential equations, which we need to calculate numerically. Therefore, we map the continuum Hamiltonian in a given setup on a numerical grid, which can be interpreted as a finite lattice in real space with a lattice constant $a$, giving the distance between the lattice points. Using this mapping, one can approximate the derivative of the wavefunction with the finite-difference method

$$p_x\Psi(x)\to-i\partial_x\Psi(x)\approx-i\frac{\Psi(x+a)-\Psi(x-a)}{2a} \tag{4.27}$$

$$p_x^2\Psi(x)\to-\partial_x^2\Psi(x)\approx-\frac{\Psi(x+a)+\Psi(x-a)-2\Psi(x)}{a^2}. \tag{4.28}$$

Expanding the basis into the mapping of the real space lattice gives the new basis

$$\Psi(x) \to \begin{pmatrix} \Psi\big(x=-\frac{L}{2}\big) \\ \Psi\big(x=-\frac{L}{2}+a\big) \\ \Psi\big(x=-\frac{L}{2}+2a\big) \\ \cdots \\ \Psi\big(x=\frac{L}{2}\big) \end{pmatrix}, \tag{4.29}$$

which leads to a new $8N \times 8N$ Hamiltonian, where $N = L/a$ is the number of lattice points that are multiplied by the four spin states in the Luttinger model and particle-hole degree of freedom due to superconductivity. The finite-difference method is often referred to as the tight-binding method since the resulting Hamiltonian resembles a tight-binding Hamiltonian very closely.

In general, periodic boundary conditions $[\Psi(x) = \Psi(x+L)]$ allow simplifications to Eqs. (4.27) and (4.28). Using the identity $\Psi(x+a) = e^{ip_x a}\Psi(x)$, we get

$$-i\partial_x \Psi(x) \approx \frac{\sin(p_x a)}{a}\Psi(x) \tag{4.30}$$

$$-\partial_x^2 \Psi(x) \approx \frac{2}{a^2}[1-\cos(p_x a)]\Psi(x), \tag{4.31}$$

which also leads to a periodicity in momentum $[\hat{H}(p_x) = \hat{H}(p_x + 2\pi/a)]$.

Using the finite-difference method has both advantages and drawbacks. On the one hand, the eigenvalues of the resulting Hamiltonian contain any boundary states coming from the hard-wall boundary conditions. Additionally, the containment of the system to a finite size splits the bulk continuum into discrete subbands, which resembles the band structure in an experimental setup more realistically. On the other hand, one must choose a sufficiently small lattice constant $a$ for the numerical approximations in Eqs. (4.27) and (4.28) to be valid. Therefore, $N$ can proliferate until convergence is reached, leading to a huge Hamiltonian, where diagonalization is computationally demanding. Here, it is essential to exploit the sparseness of the Hamiltonian since only the coupling between adjacent lattice points is considered. Throughout this thesis, we use the Kwant package to conveniently generate and analyze such finite-difference Hamiltonians in Python [157].

## 4.4 Effective SOC field orientation in the isoparity basis

In the superconducting two-dimensional electron gas (2DEG) model with $j = 1/2$, the orientation of the SOC field relative to the magnetic field is essential for the topological behavior [109, 25, 98] (see Secs. 2.3.4 and 2.3.5). Here, the basis states are defined by the $z$-component of the spin $(\uparrow, \downarrow)$. Therefore, the Hamiltonian is a $2 \times 2$ matrix, which can be described by a linear combination of four basis matrices. It is convenient to use the Pauli matrices $\hat{\sigma}_i$ and write the specific terms of the Hamiltonian in the shape of $\boldsymbol{n} \cdot \hat{\boldsymbol{\sigma}}$, with $\hat{\boldsymbol{\sigma}} = (\hat{\sigma}_x, \hat{\sigma}_y, \hat{\sigma}_z)^T$. Since the spin orientation is proportional to $\hat{\boldsymbol{\sigma}}$, which allows to immediately read the direction of the SOC field given by the vector $\boldsymbol{n}$.

In contrast to the 2DEG, the Luttinger model does not allow such direct interpretation since the $4 \times 4$ basis of the $j = 3/2$ spin matrices has 16 (15 plus unit matrix) independent basis matrices. We show in this section, that a combination of parity and spin allows to seperate the $4 \times 4$ basis into a tensor product of two $2 \times 2$ matrices, which we define as two sets of Pauli matrices $\tilde{\kappa}_i$ and $\tilde{\sigma}_i$. Afterwards, we can compare the $\tilde{\sigma}_i$ terms in the $j = 3/2$ basis with the $\hat{\sigma}_i$ terms in the $j = 1/2$ basis to get an effective SOC field in the Luttinger model. Following Ref. [158], we use the isoparity operator

$$\tilde{\mathcal{P}}_z = \hat{\mathcal{P}}_z \hat{Q}, \tag{4.32}$$

where the parity operator $\hat{\mathcal{P}}_z : z \mapsto -z, p_z \mapsto -p_z$ acts on the spatial coordinates, and $-i\hat{Q}$ is the diagonal representation matrix of the parity operator on the space of $j = 3/2$ states. The eigenvalues of $\hat{Q}$ come in pairs of $\pm 1$, with opposite signs for opposite $j_z$ values. We demand that $\tilde{\mathcal{P}}_z$ is a conserved quantity $[\hat{H}(\boldsymbol{p}), \tilde{\mathcal{P}}_z] = 0$. In the usual basis of the Luttinger model $[(c_{\frac{3}{2}}, c_{\frac{1}{2}}, c_{-\frac{1}{2}}, c_{-\frac{3}{2}})^T]$, one finds

$$\hat{Q} = \begin{pmatrix} +1 & 0 & 0 & 0 \\ 0 & -1 & 0 & 0 \\ 0 & 0 & +1 & 0 \\ 0 & 0 & 0 & -1 \end{pmatrix}. \tag{4.33}$$

It is convenient to rewrite the Luttinger Hamiltonian $\hat{H}^{\mathbf{O}_h}(\mathbf{p})$ [Eq.(3.7)] in a basis ordered by the eigenvalues of $\hat{Q}$ $[(c_{\frac{3}{2}}, c_{-\frac{1}{2}}, c_{-\frac{3}{2}}, c_{\frac{1}{2}})^T]$

$$\tilde{H}_L(\boldsymbol{p}) = \Big\{\alpha_0 \boldsymbol{p}^2 \tilde{\kappa}_0 + \tilde{\alpha}_z \Big[\big(p_\perp^2 - 2p_z^2\big)\tilde{\kappa}_z - \sqrt{3}\big(p_x^2 - p_y^2\big)\tilde{\kappa}_x)\Big]\Big\}\tilde{\sigma}_0 + \boldsymbol{n}_L \cdot \tilde{\boldsymbol{\sigma}},$$

$$\text{with} \quad \boldsymbol{n}_L = -2\sqrt{3}\Big(\alpha_z + \frac{1}{5}\alpha_\Box\Big)\tilde{\kappa}_y \begin{pmatrix} p_y p_z \\ -p_x p_z \\ p_x p_y \end{pmatrix}. \tag{4.34}$$

Here, $\tilde{\alpha}_z = \alpha_z - \frac{3}{10}\alpha_\Box$, $p_\perp^2 = p_x^2 + p_z^2$, $\tilde{\boldsymbol{\sigma}} = (\tilde{\sigma}_x, \tilde{\sigma}_y, \tilde{\sigma}_z)^T$ acts on the isoparity as pseudospin and $\tilde{\kappa}_i$ acts on the LH and HH states $|j_z| \in \big\{\frac{3}{2}, \frac{1}{2}\big\}$. From the shape of $\tilde{H}_L(\mathbf{p})$, we can identify $\boldsymbol{n}_L$ as the effective intrinsic SOC field of the Luttinger model. Since $\boldsymbol{n}_L$ vanishes if two momentum components are zero (i.e. $p_y = p_z = 0$), Eq. (4.34) shows that the $\mathbf{O}_h$ symmetric 1D Luttinger Hamiltonian is pseudospinless.

In Sec. 4.5, we study the effect of the 1D inversion symmetry breaking SOC terms given by linear BIA from Eq. (3.15). In the basis of Eq. (4.34), it takes the form

$$\hat{H}_{\text{BIA}}(p_x) = \boldsymbol{n}_{\text{BIA}} \cdot \tilde{\boldsymbol{\sigma}}, \quad \text{with} \quad \boldsymbol{n}_{\text{BIA}} = -\frac{\sqrt{3}}{2}\beta(\tilde{\kappa}_x + \sqrt{3}\tilde{\kappa}_z)\begin{pmatrix} p_x \\ 0 \\ 0 \end{pmatrix}. \tag{4.35}$$

Therefore, a 1D superconducting Luttinger wire with $\mathbf{T}_d$ symmetry has an intrinsic effective SOC field parallel to the wire. Since the BIA breaks $\hat{\mathcal{P}}_z$ symmetry, it is off-diagonal and couples the blocks of $\tilde{H}_L(p_x, p_y, p_z = 0)$, even for $p_z = 0$.

The $j = 1/2$ superconducting models, discussed in Secs. 2.3.4 and 2.3.5, show that a topological phase requires a perpendicular Zeeman and SOC field. We write the Zeeman term from Eq. (3.27) in the pseudospin basis and find

$$\hat{H}_Z = \boldsymbol{n}_Z \cdot \tilde{\boldsymbol{\sigma}}, \quad \text{with} \quad \boldsymbol{n}_Z = \frac{1}{2}\begin{pmatrix} B_x\big(\sqrt{3}\tilde{\kappa}_x + \tilde{\kappa}_0 - \tilde{\kappa}_z\big) \\ B_y\big(\sqrt{3}\tilde{\kappa}_x - \tilde{\kappa}_0 + \tilde{\kappa}_z\big) \\ B_z(\tilde{\kappa}_0 + 2\tilde{\kappa}_z) \end{pmatrix}, \tag{4.36}$$

where $\mathbf{n}_Z || \mathbf{B}$.

Considering the direction of $\mathbf{n}_{\text{BIA}}$ relative to the system, we predict that the 1D superconducting Luttinger wire hosts a topological phase if a magnetic field is applied perpendicular to the wire. Since $\mathbf{n}_L$ points out-of-plane for $p_z = 0$, any in-plane magnetic field in the 2D Josephson junction setup without BIA is sufficient for a topological phase transition.

## 4.5 One dimensional superconducting Luttinger wire

In this Section, we discuss the emergence of topological superconductivity in 1D Luttinger wires. Here, we assume a setup shown in Fig. 4.1(a), where the proximity of the yellow SC induces $s$-wave superconductivity. The Luttinger model generally describes a wide variety of metals and semimetals, where the Fermi energy is close to the $\Gamma_8$ bands [159, 116]. We choose three materials as examples to show the effect of these phases under inversion symmetry breaking.

For the general analysis of a 1D SC without SOC, we present calculations for $\alpha$-Sn parameters, shown in Tab. A.2 with $\mathbf{O}(3)$ symmetry without BIA. The emergence of a topological phase with MBSs is shown for HgTe as a semimetal and p-doped GaAs as a metal, with $\mathbf{T}_d$ symmetry, due to an intrinsic lack of inversion symmetry.

Our study shows that the coexistence of HH and LH states introduces new features to the topological behavior, which were not present in the $j = 1/2$ Rashba wire [Eq. (2.65)] [109, 110]. We show that the extra band is responsible for a second phase transition, leading to an upper boundary in the magnetic field for the existence of MBSs. This can be used as an additional knob in future experiments.

### 4.5.1 Inversion symmetric phase

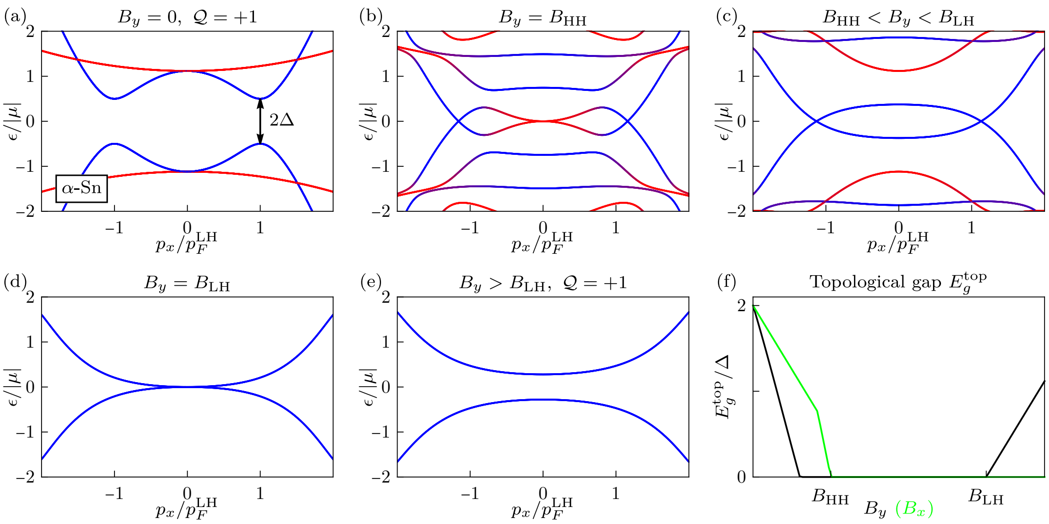

Figure 4.4: (a) - (e) Bulk band structure of the Luttinger semimetal without spin-orbit coupling. We apply a magnetic field $B_y$ in the $y$-direction, using the parameters for $\alpha$-Sn (see Tab. A.2), $\Delta = 0.56$meV and $\mu = 2\Delta$. The color indicates the band to have either heavy-hole (red) or light-hole (blue) character. The critical magnetic fields $B_{\mathrm{HH}}$ and $B_{\mathrm{LH}}$ are defined in Eq. (4.40). If the band structure has a finite topological gap $\epsilon_g^{\mathrm{top}} = \min_{p_x} \epsilon_g(p_x)$, one can calculate the topological invariant $\mathcal{Q}$ from Eq. (4.20). (f) Topological gap $\epsilon_g^{\mathrm{top}}$ as a function of a magnetic field in $y$-direction (black) and $x$-direction (green).

We take the cubic symmetric Luttinger Hamiltonian in 1D $\hat{H}^{\boldsymbol{O}_h}(p_x, 0, 0)$ [Eq. (3.7)] and apply a general Zeeman field $\boldsymbol{B} = (B_x, B_y, B_z)$. In the Nambu basis $\Psi_N$ [Eq. (4.10)] it takes the form

$$\hat{H}_W^{\boldsymbol{O}_h}(p_x) = \hat{\tau}_z \left[\hat{H}^{\boldsymbol{O}_h}(p_x, 0, 0) - \mu \hat{1}_4\right] + \hat{\tau}_x \Delta + \boldsymbol{B} \cdot \hat{\boldsymbol{J}}. \tag{4.37}$$

First, we consider a wire with infinite length ($L \to \infty$) [see Fig. 4.1(a)], where $p_x$ is a good quantum number. Therefore, one cas study the bulk properties of the system. One must find the gap closings at zero momentum for the topological phase transition. Taking a general magnetic field orientation, we find the energy

$$\varepsilon^{W,\boldsymbol{O}_h}_{|j_z|=\frac{3}{2}}(p_x=0)=\pm\left(\frac{3}{2}|\boldsymbol{B}|-2\sqrt{\Delta^2+\mu^2}\right), \tag{4.38}$$

$$\varepsilon^{W,\boldsymbol{O}_h}_{|j_z|=\frac{1}{2}}(p_x=0)=\pm\left(\frac{1}{2}|\boldsymbol{B}|-2\sqrt{\Delta^2+\mu^2}\right), \tag{4.39}$$

with $|\boldsymbol{B}|=\sqrt{B_x^2+B_y^2+B_z^2}$. One can see that the HH and the LH states behave differently under magnetic fields due to the different magnitudes of $j_z$. The critical field, where the bulk gap closes [see Fig. 4.4 (b) and (d)], is given by:

$$B_{\mathrm{HH}}=\frac{2}{3}\sqrt{\Delta^2+\mu^2}\quad\text{and}\quad B_{\mathrm{LH}}=2\sqrt{\Delta^2+\mu^2}. \tag{4.40}$$

It is important to emphasize that these critical fields do not depend on the effective masses of the Luttinger model ($\alpha_0$, $\alpha_z$, $\alpha_\square$). Therefore, our findings apply to semimetals and metals, as long as the Luttinger model describes the band structure around the chemical potential.

It is convenient to perform a unitary basis rotation

$$\hat{\mathcal{R}}_y^\dagger(\frac{\pi}{2})\hat{H}_W^{\boldsymbol{O}_h}(p_x)\hat{\mathcal{R}}_y(\frac{\pi}{2}),\ \text{where}\quad \hat{\mathcal{R}}_y(\theta)=e^{-i\theta J_y} \tag{4.41}$$

is the unitary rotation operator around the $y$-axis by an angle $\theta$. For a magnetic field in $x$-direction, the Hamiltonian decouples into four $2\times 2$ blocks

$$\hat{h}_{|j_z|=\frac{3}{2},\sigma}(p_x)=\left(\tilde{\alpha}_-p_x^2-\mu\right)\hat{\tau}_z+\Delta\hat{\tau}_x+\sigma\frac{3}{2}B_x\hat{\tau}_0, \tag{4.42}$$

$$\hat{h}_{|j_z|=\frac{1}{2},\sigma}(p_x)=\left(\tilde{\alpha}_+p_x^2-\mu\right)\hat{\tau}_z+\Delta\hat{\tau}_x+\sigma\frac{1}{2}B_x\hat{\tau}_0. \tag{4.43}$$

Here, $\sigma=\pm1$ indicates the $\mathrm{sgn}(j_z)$ and $\tilde{\alpha}_\pm=\alpha_0\pm2\tilde{\alpha}_z$. In this basis, we can interpret the $\alpha_z$ and $\alpha_\square$ terms as different effective masses for the HH and LH states and do not act as symmetric SOC in 1D. For a wire with infinite length $L$ [Fig. 4.1(a)], where $p_x$ is a good quantum number, we can solve the Bogoliubov-de Gennes (BdG) equation to get the bulk dispersion

$$\varepsilon^{W,\boldsymbol{O}_h}_{|j_z|=\frac{3}{2}}(p_x, B_y = B_z = 0) = \sigma\frac{3}{2}B_x + \tau\sqrt{\left(\tilde{\alpha}_- p_x^2 - \mu\right)^2 + \Delta^2}, \tag{4.44}$$

$$\varepsilon^{W,\boldsymbol{O}_h}_{|j_z|=\frac{1}{2}}(p_x, B_y = B_z = 0) = \sigma\frac{1}{2}B_x + \tau\sqrt{\left(\tilde{\alpha}_+ p_x^2 - \mu\right)^2 + \Delta^2}, \tag{4.45}$$

where $\tau = \pm 1$ gives the particle-hole degree of freedom. Taking zero energy, we can find the momentum solution for a gap-closing analytically to be

$$p^2_{|j_z|=\frac{3}{2}} = \frac{\mu \pm \sqrt{\left(\frac{3}{2}B_x\right)^2 - \Delta^2}}{\tilde{\alpha}_-} \quad \text{and} \quad p^2_{|j_z|=\frac{1}{2}} = \frac{\mu \pm \sqrt{\left(\frac{1}{2}B_x\right)^2 - \Delta^2}}{\tilde{\alpha}_+}. \tag{4.46}$$

If at least one of these solutions is real, one can always find a critical momentum where two bulk states cross at zero energy. The gap of the HH and LH states is closed for

$$|j_z| = \frac{3}{2} \Rightarrow \begin{cases} B_x \geq \frac{2}{3}\Delta & \text{if} \quad \mu\tilde{\alpha}_- > 0 \\ B_x \geq B_{\text{HH}} & \text{if} \quad \mu\tilde{\alpha}_- < 0 \end{cases} \tag{4.47}$$

$$|j_z| = \frac{1}{2} \Rightarrow \begin{cases} B_x \geq 2\Delta & \text{if} \quad \mu\tilde{\alpha}_+ > 0 \\ B_x \geq B_{\text{LH}} & \text{if} \quad \mu\tilde{\alpha}_+ < 0. \end{cases} \tag{4.48}$$

The $\text{sgn}(\tilde{\alpha}_\mp)$ determines if the HH and LH states are n or p-type. Therefore, the conditions of Eqs. (4.47) and (4.48) describe if the chemical potential lies in the corresponding band $[\mu\tilde{\alpha}_\mp > 0]$ or not $[\mu\tilde{\alpha}_\mp < 0]$. Since the Luttinger model for $\mathbf{O}_h$ symmetric materials has no SOC in 1D [see Eq. (4.34)], there is no topological gap opening beyond the critical magnetic field. The green line in Fig. 4.4 (f) shows the topological gap $\epsilon_g^{\text{top}} = \min_{p_x} \epsilon_g(p_x)$, which is the smallest gap for all momenta as a function of $B_x$.

Since a magnetic field $B_y$, perpendicular to the wire, mixes the HH and LH states at finite momentum, the BdG equation cannot be solved analytically. Fig. 4.4 shows the bulk band structure of a wire of $\alpha$-Sn for different $B_y$. Without magnetic field [$B_y = 0$, see Fig. 4.4 (a)], the bulk bands are double degenerate with a gap in the LH states due to the superconducting coupling $\Delta$. Since the chemical potential does not intersect the HH states, their quasi-particle and hole spectrum forms a trivial gap unaffected by superconductivity. Here, we can calculate the topological invariant $\mathcal{Q} = +1$ using the method discussed in Sec. 4.2. At a finite magnetic field, the degeneracy of the bands is lifted, and the size of the topological gap is decreased until it is closed [see black line in Fig. 4.4 (f)]. The topological gap between the two critical magnetic fields is fully closed for a magnetic field perpendicular to the wire. It reopens for $B_y > B_{\mathrm{LH}}$, with a trivial topological invariant $\mathcal{Q} = +1$. Therefore, one cannot find a non-trivial topological phase in the 1D Luttinger materials without external SOC, like a Dresselhaus term from inversion symmetry breaking.

From Eqs. (4.47) and (4.48), one can see that the value of the critical magnetic field behaves similarly as in the $j = 1/2$ model of Eq. (2.65). In both models, the critical fields depend only on the superconducting coupling and the chemical potential. The only difference is the $|j_z|$ dependent prefactor in the Zeeman term of the corresponding state.

### 4.5.2 Intrinsic inversion symmetry breaking by BIA

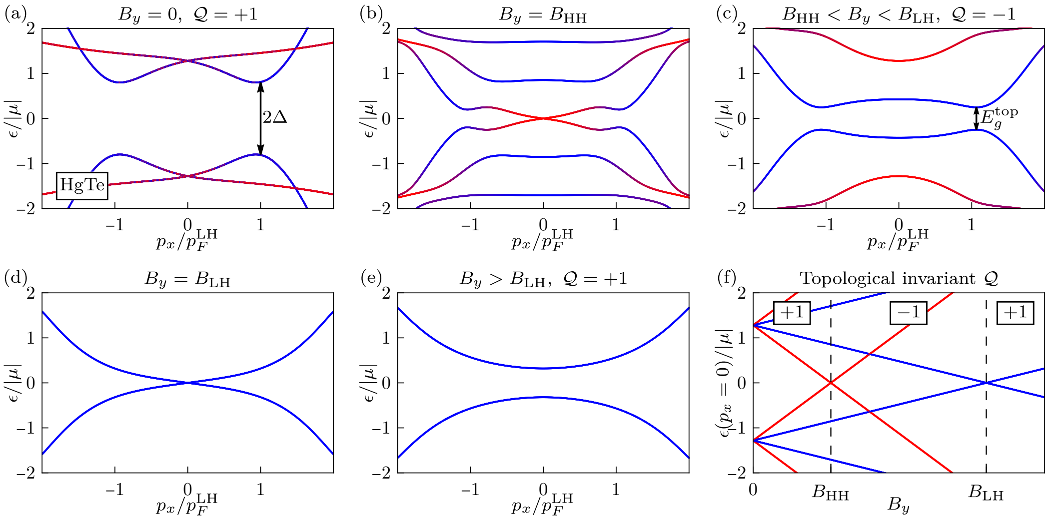

Figure 4.5: (a-e) Bulk band structure for a Luttinger semimetal with bulk inversion asymmetry. We apply magnetic field $B_y$ in $y$-direction, using the parameters for HgTe (see Tab. A.2), $\Delta = 0.2$meV and $\mu = 0.25$meV. The color code corresponds to Fig. 4.4, and the topological invariant is calculated using Eq. (4.20). Without magnetic field (a), the band structure is double degenerate with $\mathcal{Q} = +1$. At the critical magnetic fields $B_{\mathrm{HH}}$ (b) and $B_{\mathrm{LH}}$ (d) [Eq. (4.40)] the corresponding bands cross at $p_x = 0$, inducing a gap inversion with a change in $\mathcal{Q}$. (c) The bulk inversion asymmetry term opens the gap at finite momentum $E_g^{\mathrm{top}}$. (f) Energy at $p_x = 0$ as a function of $B_y$. The framed insets correspond to $\mathcal{Q}$ in the regions between the critical magnetic fields indicated by the dashed lines.

This section discusses the effect of an intrinsic SOC given by the BIA. We focus on the linear BIA term, added to the cubic symmetric Hamiltonian $\hat{H}_W^{\mathbf{O}_h}(p_x)$ from Eq. (4.37). This leads to a tetrahedral symmetric Hamiltonian, which has the shape of

$$\hat{H}_W^{\mathbf{T}_d}(p_x) = \hat{H}_W^{\mathbf{O}_h}(p_x) + \hat{\tau}_z \beta_1 p_x \Big\{ \hat{J}_x, \hat{J}_y^2 - \hat{J}_z^2 \Big\}, \tag{4.49}$$

in the previously used Nambu basis $\Psi_N$ [Eq. (4.10)].

As discussed in Sec. 4.4, the effective SOC field of the BIA is parallel to a Zeeman field in the $x$-direction and perpendicular to a field in the $y$ or $z$-direction. The evolution of the bulk band structure of a semimetal with $\mathbf{T}_d$ symmetry under increasing magnetic field $B_y$ is shown in Fig. 4.5. Here, we use the material-specific parameters of HgTe (see Tab. A.2). To study the effect of the BIA term, we can compare Fig. 4.4 with Fig. 4.5.

In Fig. 4.5(a), one can see that the quadratic nodal point around zero momentum and $\epsilon = \pm\mu$ gets a linear character due to the linear BIA term. As discussed in Ref. 3.1.2, the dispersion in a small momentum scale is dominated by the BIA term. In addition, a small hybridization between the HH and LH states exists, even without a magnetic field. Since the BIA term vanishes at zero momentum, the critical magnetic fields $B_{\mathrm{HH}}$ [Eq. (4.47)] and $B_{\mathrm{LH}}$ [Eq. (4.48)] are still valid, which can be seen in the gap closings in Figs. 4.5(b) and (d).

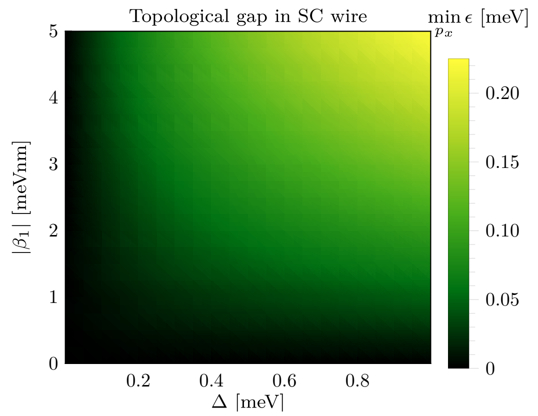

Figure 4.6: Topological gap $\min_{p_x} \epsilon$ in a superconducting Luttinger wire [Eq. (4.49)] at finite magnetic field $B_y = (B_{\mathrm{HH}} + B_{\mathrm{LH}})/2$ as a function of bulk inversion asymmetry strength $\beta_1$ and induced $s$-wave superconducting coupling $\Delta$. One can see that there is no topological gap in inversion symmetric crystals ($\beta_1 = 0$).

The most important effect of the BIA is shown in Fig. 4.5(c). Here, one can see a gap opening between the two critical magnetic fields ($B_{\mathrm{HH}} < B_y < B_{\mathrm{LH}}$) around the Fermi vector of the LH states $p_F^{\mathrm{LH}}$. Therefore, the band structure has a finite gap at all momentum, giving the topological gap size $\epsilon_g^{top}$. We can determine that the topological gap size is directly proportional to the strength of the BIA term $\beta_1$ (see Fig. 4.6).

Due to the existence of a topological gap, we can assign a topological invariant to the system, given by the determinant of the reflection matrix at the interface of the wire, as explained in Sec. 4.2. Analog to the $\mathbf{O}_h$ symmetric phase, we find that the system is topologically trivial for $B_y < B_{\mathrm{HH}}$ and $B_y > B_{\mathrm{LH}}$ with $\mathcal{Q} = +1$ [see Fig. 4.5(a,e)]. More strikingly, one finds a non-trivial regime in between the two critical magnetic fields ($B_{\mathrm{HH}} < B_y < B_{\mathrm{LH}}$) with $\mathcal{Q} = -1$ [Fig. 4.5(c)]. Considering the bulk-boundary correspondence, we expect the formation of topologically protected MBSs at the ends of the wire in this regime.

Compared to the $j = 1/2$ model with a Rashba SOC [Eq. (2.65)], the coexistence of the HH and LH bands leads to a second topological phase transition. Therefore the topological region does not extend to infinite magnetic fields but has an upper limit [see Fig. 4.5(f)]. This can be used as an additional knob to identify topological features in future experiments, such as in Ref. [160].

Since the critical magnetic fields are independent of the effective masses of the bands, one can raise the question if these features are also applicable to the metallic phase of the Luttinger model. For this reason, we use the parameters of GaAs (see Tab. A.2) with a negative chemical potential, which models its p-doped regime. This material is generally also $\mathbf{T}_d$ symmetric, where the BIA is present, though one entire order of magnitude smaller than HgTe [161, 116]. The band structure of a 1D wire of p-doped GaAs with a proximitized $s$-wave superconducting coupling and magnetic field in the $y$-direction is presented in Fig. 4.7.

The striking difference in the metallic regime is that the chemical potential lies simultaneously in both HH and LH states. Therefore, the superconducting potential opens a gap for red and blue states around their corresponding Fermi vector $p_F^{\mathrm{HH/LH}}$ in Fig. 4.7(a). Under magnetic field, both bands hybridize at finite momentum, showing the same band inversions at the critical magnetic fields as in the semimetal regime [see Fig. 4.7(b,d)].

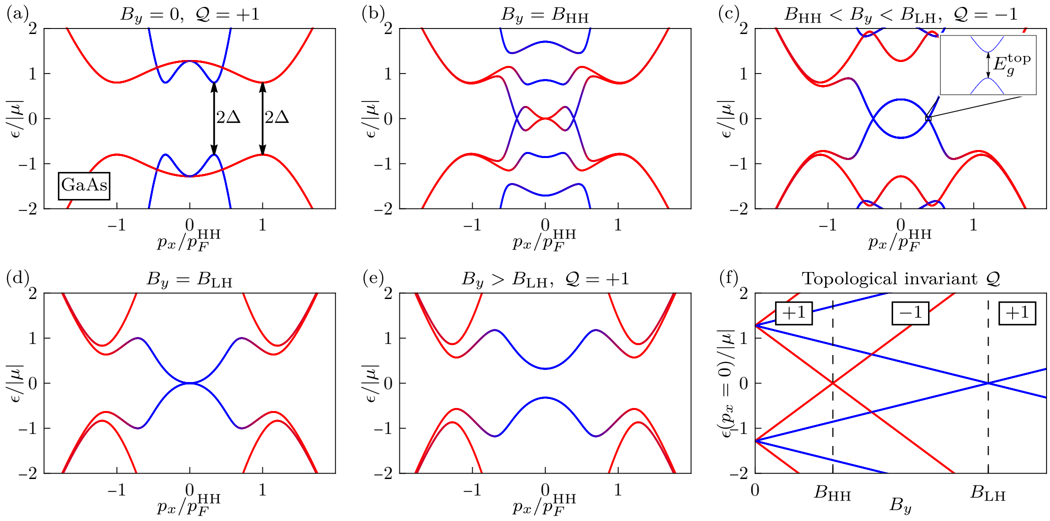

Figure 4.7: (a-e) Bulk band structure analog to Fig. 4.5 for a Luttinger metal with weak bulk inversion asymmetry, using the parameters for GaAs (see Tab. A.2), $\Delta = 0.2$meV and $\mu = -0.25$meV. The inset in (c) shows a zoom-in around the gap opening $E_g^{\rm top}$ at finite $p_x$. (f) Energy at $p_x = 0$ as a function of $B_y$. The framed insets correspond to $\mathcal{Q}$ in the regions between the critical magnetic fields indicated by the dashed lines.

For p-doped GaAs, the topological gap in the topological regime [Fig. 4.7(c)] is tiny due to its small BIA parameter $\beta_1$. Therefore, we provide an inset with a zoom around the framed region in Fig. 4.7(c). We expect that such a small gap leads to weaker topological protection for any bound states, which will come with a substantial localization length. Interestingly, the topological phase diagram, indicated by the gaps at $p_x = 0$, is identical for the metal and semimetal regime [compare Figs. 4.5(f) and 4.7(f)] since the Luttinger parameters ($\alpha_0$, $\alpha_z$, and $\alpha_\square$) do not contribute at zero momentum.

Following the discussion about the effective SOC field directions of the BIA [Sec. 4.4], our results can also be achieved with magnetic fields in any direction perpendicular to the $x$-axis. A magnetic field in the $x$-direction, parallel to the effective SOC field of the BIA, will not induce a topological gap between the two critical fields. Therefore, we do not expect the formation of MBSs if the material has an inversion symmetric crystal or if the magnetic field is parallel to the wire. On the other hand, our calculations predict the existence of MBSs in any 1D Luttinger wire made from a $\mathbf{T}_d$ symmetric material, disregarding its metallic or semimetallic nature, in the proximity of an $s$-wave SC with a perpendicular applied magnetic field.

### 4.5.3 Emergence of Majorana bound states in a finite wire

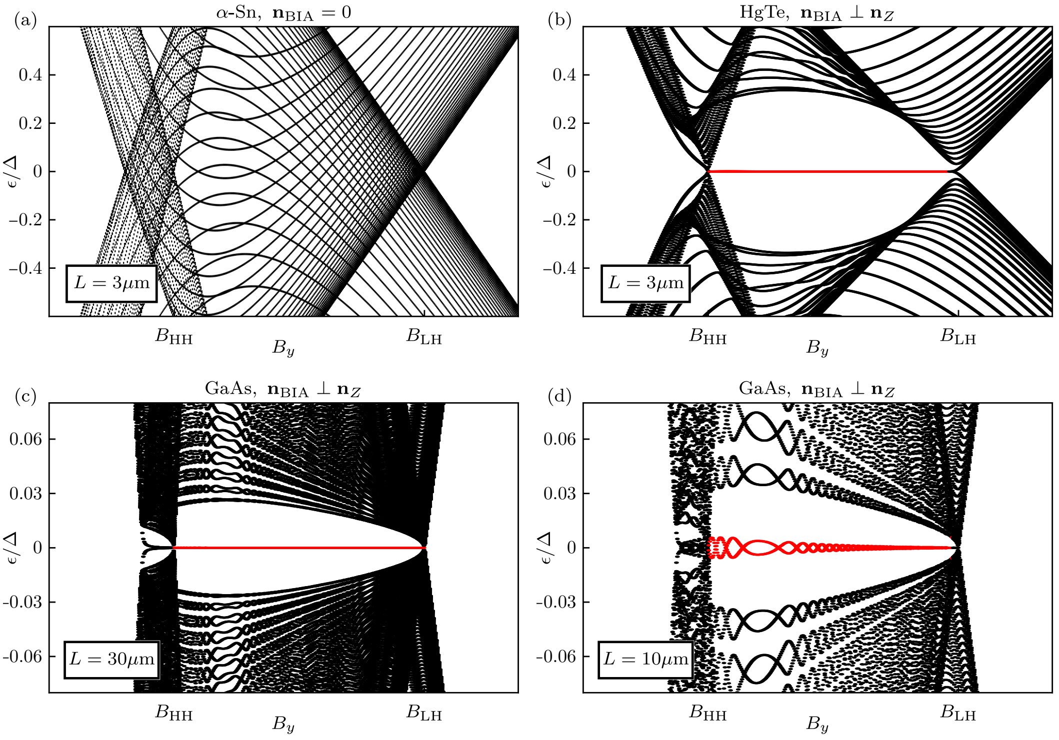

Figure 4.8: Energy dispersion of a 1D Luttinger superconducting wire with finite length $L$ as a function of magnetic field $B_y$, perpendicular to the spin-orbit coupling field of the bulk inversion asymmetry term $n_{\mathrm{BIA}}$ [Eq. (4.35)]. (a) $\alpha$-Sn [$\mathbf{O}(3)$ symmetry] with inversion symmetry. (b) HgTe [$\mathbf{T}_d$ symmetry] without inversion symmetry. (c,d) GaAs [$\mathbf{T}_d$ symmetry] with weak inversion breaking for two different wire lengths. In the topological non-trivial regions $B_{\mathrm{HH}} < B_y < B_{\mathrm{LH}}$, where a topological gap exists, a localized state forms at the wire's ends (red).

In the previous sections, we analyzed the existence of a topological phase in the 1D superconducting Luttinger wire between the two critical magnetic fields, $B_{\mathrm{HH}}$ and $B_{\mathrm{LH}}$, if the magnetic field is perpendicular to the effective SOC field $\boldsymbol{n}_{\mathrm{BIA}} \perp \boldsymbol{n}_Z$ [Eqs. (4.35) and (4.36)]. Due to the bulk-boundary correspondence, one expects topologically protected states localized at the ends of the wire, which are MBSs. Therefore we apply the finite-difference method via the Kwant code [157], introduced in Sec. 4.3, to put the Luttinger model of Eq. (4.49) on a finite lattice. Fig. 4.8 shows the results of the calculations.

As mentioned in Sec. 4.5.1 and 4.5.2, no topological gap opens at finite magnetic fields if the effective SOC field is parallel to the magnetic field or absent. In Fig. 4.8(a), we show the band structure of the inversion symmetric $\alpha$-Sn, without any SOC field. One can see that the finite length of the wire introduces discrete subbands in the dispersion due to the confinement in space. As expected, there is no gap opening for $B_{\mathrm{HH}} < B_y < B_{\mathrm{LH}}$, and therefore, no localized states at the boundaries of the wire.

A topological gap with a non-trivial topological invariant opens as soon as an effective SOC is present. In Fig. 4.8(b), we analyze HgTe with a tetrahedral $\mathbf{T}_d$ symmetric crystal, including BIA, which acts as SOC in the system. Since $\boldsymbol{n}_{\mathrm{BIA}} \perp \boldsymbol{n}_Z$, a topological gap exists between the critical fields with a topological invariant $\mathcal{Q} = -1$ [see Fig. 4.5(f)].

This topological region hosts a double degenerate flat state at zero energy [red state in Fig. 4.5(b)]. From the wavefunction of a single state, we can determine its expectation value of the position. We identify the zero energy states as MBSs, which are localized at the ends of the wire if the wire is much longer than the localization length ($L \gg \lambda$).

The MBSs also exist in the metallic phase of the Luttinger model. Following the calculations of the previous section, we show the band structure of p-doped GaAs in Figs. 4.8(c,d). Since the strength of the BIA term in GaAs is approximately one order of magnitude smaller than in HgTe (see Tab. A.2), the topological gap is also one order of magnitude smaller (see Fig. 4.6).

In general, the localization length $\lambda$ of the MBSs is proportional to the inverse of the topological gap size. We present the dispersion for two different lengths in Figs. 4.8(c,d). For $L = 30\mu$m, the condition $L \gg \lambda$ is satisfied, and the MBSs are completely flat. For a shorter wire [$L = 10\mu$m Fig. 4.8(d)], the wavefunction of the MBSs at the opposite ends overlap. Therefore, the states hybridize, which pushes their energy to finite values. This gives the so-called Majorana oscillation around zero energy, as conceptional shown in Fig. 2.3.

We emphasize that these results apply to systems with Rashba SOC instead of BIA. Here, the magnetic field needs to be applied perpendicular to the $y$-direction, which is the direction of the effective Rashba SOC field.

## 4.6 Emergence of intrinsic Majorana bound states in 2D Luttinger Josephson junctions

This section dedicates to the analysis of 2D Luttinger Josephson junctions. We sketch the setup in Fig. 4.1(b), showing a 2D Luttinger material between two $s$-wave SCs with the length $W_S$, the distance $W$, and the superconducting phase difference $\phi$. A magnetic field $B_x$ is applied along the $x$-direction in the normal region only, indicated by the red arrow.

From previous discussions on the 2D Rashba Josephson junction system for $j = 1/2$ electrons, we expect the existence of a topological phase with a combination of magnetic and SOC fields [23, 24, 25, 98]. We discuss this system in more detail in Sec. 2.3.5. In Sec. 4.4, we show that the 2D Luttinger model has an intrinsic symmetric SOC, given by the $\alpha_z$ and $\alpha_\square$ terms, even with conserved inversion symmetry.

Therefore, we focus in this section on $\alpha$-Sn as a semimetal without BIA and p-doped GaAs as a metal with very small BIA. The Hamiltonian

$$\hat{H}_{\mathrm{JJ}}(x, p_y) = \hat{\tau}_z \left[\hat{H}^{\mathbf{O}_h}(\hat{p}_x, p_y, 0) - \mu \hat{1}_4\right] + \hat{H}^{\mathrm{JJ}}_{\Delta}(x)\hat{1}_4 + \left(V_0 \hat{\tau}_z \hat{1}_4 + B_x \hat{\tau}_0 \hat{J}_x\right) h(x) \tag{4.50}$$

describes this, where $\hat{p}_x = -i\partial_x$, $\hat{H}^{\mathbf{O}_h}(\boldsymbol{p})$ is the cubic symmetric Luttinger Hamiltonian from Eq. (3.7), and $V_0$ is the chemical potential mismatch between the SCs and the normal region. The superconducting coupling term is given by

$$\hat{H}_{\Delta}^{\mathrm{JJ}}(x) = \Delta(x)[e^{i\mathrm{sgn}(x)\phi/2}\hat{\tau}_+ + e^{-i\mathrm{sgn}(x)\phi/2}\hat{\tau}_-]. \tag{4.51}$$

Throughout this work, we model the Josephson junction with a finite normal region in numerical calculations, with $h(x) = \theta(W/2 - |x|)$ and $\Delta(x) = \Delta\theta(|x| - W/2)$. For analytical calculations, we apply the short-junction limit using a $\delta$-barrier junction with $h(x) = W\delta(x)$ and $\Delta(x) = \Delta$.

This section shows that the coupling between the two coexisting HH and LH states is sufficient to induce a topological phase in the Josephson junction. In addition, we find that the chemical potential can be used to tune the system into different topological phases, given by either the HH or LH states or both simultaneously. Our findings of the semimetallic phase are also published in Ref. [28].

### 4.6.1 Andreev bound states in one dimensional Josephson junctions

In this section, we calculate the ABSs for $p_y = 0$ in the short-junction limit, where the normal conducting region of the Josephson junction is modeled with a $\delta$-barrier. The SCs are considered to be semi-infinite leads. On the one hand, this method allows us to get analytical results for the ABS spectrum, which is crucial to understanding the topological behavior in the Josephson junction. On the other hand, the barriers in real Josephson junctions are often significantly wide. The short-junction approximation only captures the effect of varying barrier widths to the lowest order.

Similar to Sec. 4.5.1, we can again use the basis rotation $\hat{\mathcal{R}}_y^{\dagger}(\pi/2)\hat{H}_{\mathrm{JJ}}(x,0)\hat{\mathcal{R}}_y(\pi/2)$ [Eq. (4.41)] to decouple the Hamiltonian into four blocks given by

$$\hat{h}^{\mathrm{JJ}}_{|j_z|=\frac{3}{2},\sigma}(x) = \left[\tilde{\alpha}_-\hat{p}_x^2 - \mu\right]\hat{\tau}_z + \hat{H}_{\Delta}^{\mathrm{JJ}}(x) + \left(V_0\hat{\tau}_z + \sigma\frac{3}{2}B_x\hat{\tau}_0\right)W\delta(x), \tag{4.52}$$

$$\hat{h}^{\mathrm{JJ}}_{|j_z|=\frac{1}{2},\sigma}(x) = \left[\tilde{\alpha}_+\hat{p}_x^2 - \mu\right]\hat{\tau}_z + \hat{H}_{\Delta}^{\mathrm{JJ}}(x) + \left(V_0\hat{\tau}_z + \sigma\frac{1}{2}B_x\hat{\tau}_0\right)W\delta(x), \tag{4.53}$$

where $\sigma = \mathrm{sgn}(j_z)$. We can determine the ABSs analytically for each block. To solve the BdG equation, we first need to derive the effective boundary conditions for each block. Foremost, the wavefunction $\Psi(x)$ must be continuous at the barrier, giving

$$\Psi(0^+) = \Psi(0^-). \tag{4.54}$$

The $\delta$ barrier will modify the condition for the derivative of the wavefunction. We integrate the BdG equation around $x = 0$ and get the boundary conditions

$$\partial_x \Psi(x)\bigg|_{x=0^+} - \partial_x \Psi(x)\bigg|_{x=0^-} = \frac{1}{\tilde{\alpha}_s}(Z_0\hat{\tau}_0 + \sigma Z_s \hat{\tau}_z)\Psi(0), \tag{4.55}$$

with $Z_0 = V_0 W$. Here, $s = +1$ indicates the $|j_z| = 1/2$ LH states with $Z_+ = B_x W/2$ and $s = -1$ the $|j_z| = 3/2$ HH states with $Z_- = 3B_x W/2$.

First, we need to find the wavefunctions in the superconducting leads, which need to decay for $x \to \pm\infty$. Using the identities $\arccos(z) = -i\ln[i\sqrt{1-z^2} + z]$ and $\arccos(-z) = \pi - \arccos(z)$, we get

$$\Psi_l(x<0) = \frac{A_l}{\sqrt{2}}\begin{pmatrix} e^{-i\phi/2} \\ e^{i\eta} \end{pmatrix} e^{i\mathrm{sgn}(\tilde{\alpha}_s)\sqrt{\frac{\mu - i\Omega}{\tilde{\alpha}_s}}x} + \frac{B_l}{\sqrt{2}}\begin{pmatrix} e^{i\eta} \\ e^{i\phi/2} \end{pmatrix} e^{-i\mathrm{sgn}(\tilde{\alpha}_s)\sqrt{\frac{\mu + i\Omega}{\tilde{\alpha}_s}}x}, \tag{4.56}$$

$$\Psi_r(x>0) = \frac{A_r}{\sqrt{2}}\begin{pmatrix} e^{i\phi/2} \\ e^{i\eta} \end{pmatrix} e^{-i\mathrm{sgn}(\tilde{\alpha}_s)\sqrt{\frac{\mu - i\Omega}{\tilde{\alpha}_s}}x} + \frac{B_r}{\sqrt{2}}\begin{pmatrix} e^{i\eta} \\ e^{-i\phi/2} \end{pmatrix} e^{i\mathrm{sgn}(\tilde{\alpha}_s)\sqrt{\frac{\mu + i\Omega}{\tilde{\alpha}_s}}x}, \tag{4.57}$$

where $A_{l,r}$ and $B_{l,r}$ are arbitrary coefficients, $\eta = \arccos(\epsilon/\Delta)$, and $\Omega = \sqrt{\Delta^2 - \epsilon^2}$. Solving the boundary conditions for a zero-energy solution, gives the condition

$$\cos(\phi) = \frac{k_0^2 - 3\sqrt{k_0^4 + \kappa^4}}{k_0^2 + \sqrt{k_0^4 + \kappa^4}} + \frac{Z_s^2 - Z_0^2 - 4\tilde{\alpha}_s Z_0 \,\mathrm{Im}(\sqrt{k_0^2 + i|\kappa^2|})}{\tilde{\alpha}_s^2\left(k_0^2 + \sqrt{k_0^4 + \kappa^4}\right)}, \tag{4.58}$$

with $k_0^2 = \mu/\tilde{\alpha}_s$ and $\kappa^2 = \Delta/\tilde{\alpha}_s$. Eq. (4.58) is similar to the predictions of Ref. [25] in the $j = 1/2$ Rashba Josephson junction, where the Luttinger parameters renormalize the effective mass. We present the diagram of the critical superconducting phase against the magnetic field with the solid lines in Fig. 4.9 (c,f). Eq.(4.58) does not have a solution for finite $\Delta$ in the absence of a potential barrier and magnetic field

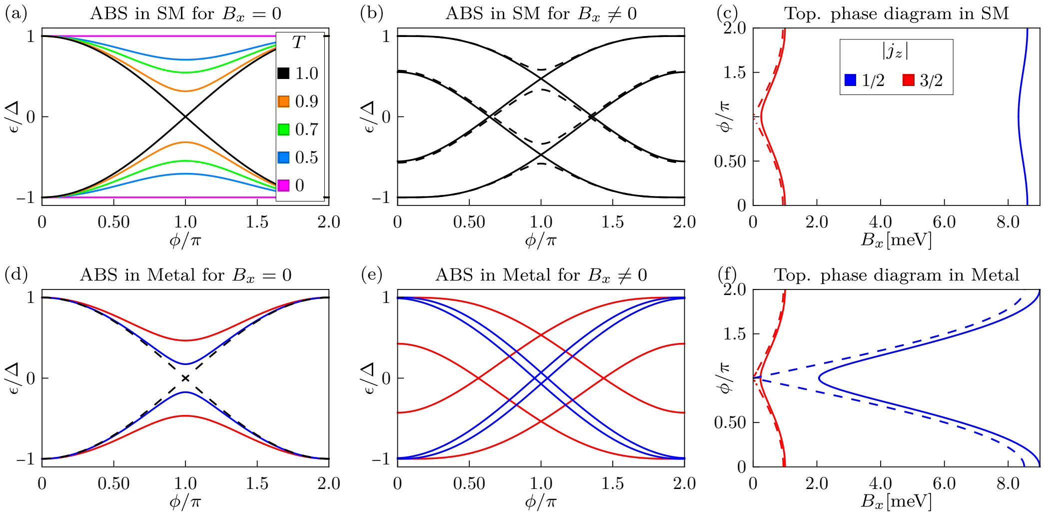

Figure 4.9: Andreev bound state (ABS) spectrum in the short junction limit using a $\delta$-barrier approach as a function of superconducting phase difference $\phi$. (a) Effect of a finite potential on a single ABS [Eq. (4.60)] without magnetic field. (b) Single ABS state under finite magnetic field $B_y$ [Eq. (4.61)] with (dashed line) and without (solid line) potential barrier. (c,f) Zero energy ABSs, without [Eq. (4.58), solid] and with Andreev approximation ($\mu \gg \Delta$) [Eq. (4.61), dashed], as a function of $B_y$. (d) Metal regime, where the ABSs of the heavy-hole and light-hole states are degenerate without potential (black dashed line) and evolve differently under a finite potential barrier (solid colored lines). (e) Difference of the spin- splitting of magnetic field in the different states without potential. (a-c) Semimetal regime, using the parameters of $\alpha$-Sn, with $\mu = -1.0$meV and $\Delta = 0.56$meV. (d-f) Metal regime, using the parameters of GaAs, with $\mu = -2.0$meV and $\Delta = 1.0$meV.

$(Z_x = Z_0 = 0)$ since

$$\frac{k_0^2 - 3\sqrt{k_0^4 + \kappa^4}}{k_0^2 + \sqrt{k_0^4 + \kappa^4}} < -1 \quad \text{for} \quad \kappa \neq 0. \tag{4.59}$$

To get the total energy dispersion of the ABSs, we use the Andreev approximation, which assumes an immense chemical potential ($|\mu| \gg |\Delta|$). We apply this limit to the wavenumbers in the exponentials of the wavefunctions and get without magnetic field ($Z_x = 0$)

$$\varepsilon_s(\phi) = \pm\Delta\sqrt{1 - T_s \sin^2\left(\frac{\phi}{2}\right)} \quad \text{with} \quad T_s = \begin{cases} \frac{1}{1+\frac{Z_0^2}{4\tilde{\alpha}_s\mu}} & \text{if } \tilde{\alpha}_s\mu > 0 \\ 0 & \text{if } \tilde{\alpha}_s\mu < 0 \end{cases} . \tag{4.60}$$

Here, we defined the transparency of the junction $T_s$, which determines the superconducting phase dependence of the ABSs. From this, we can see that all ABSs are flat if the chemical potential does not lie in the corresponding bulk band. Fig. 4.9 (a) shows the effect of a mismatch of chemical potential in the N and SC regions. Without a potential barrier ($T = 1$), the ABS spectrum is proportional to $\pm\Delta\cos(\phi/2)$, indicating a crossing at $\phi = \pi$ and a $4\pi$ periodicity, similar to the $j = 1/2$ Josephson junction model. A finite potential barrier ($0 < T < 1$) lifts this degeneracy and opens a gap leading to a $2\pi$ periodicity in the states. This means that the zero energy state in the Josephson junction for $p_y = 0$ is not topologically protected. A band that is not crossed by the chemical potential ($\tilde{\alpha}_s\mu < 0$) gives vanishing transparency ($T = 0$). One can only find the flat bulk energy solutions outside the superconducting gap.

In the metallic regime, the chemical potential can simultaneously lie in both HH and LH states. Therefore, two sets of ABSs are generated by the corresponding bands. This coexistence is a new feature of the Luttinger model, which the simpler $j = 1/2$ models do not capture. One can see in Fig. 4.9 (d) that the ABSs from the HH bands react differently to a potential barrier than the LH states. This comes from the fact that transparency is a function of the effective mass [see Eq. (4.60)]. Without a potential, the ABSs are double degenerate.

With the application of a magnetic field, one gets

$$\varepsilon_s(\phi) = \pm\Delta\sqrt{1 - 4\tilde{\alpha}_s\mu f_s^{\pm}(\phi)}, \tag{4.61}$$

$$f_s^{\pm}(\phi) = \begin{cases} \frac{4\tilde{\alpha}_s\mu\sin^4(\frac{\phi}{2})+\left(\sqrt{Z_s^2\cos^2(\frac{\phi}{2})+Z_0^2\sin^2(\frac{\phi}{2})+\tilde{\alpha}_s\mu\sin^2(\phi)}\pm Z_s\right)^2}{\left[4\tilde{\alpha}_s\mu+(Z_0-Z_s)^2\right]\left[4\tilde{\alpha}_s\mu+(Z_0+Z_s)^2\right]} & \text{if } \tilde{\alpha}_s\mu > 0 \\ 0 & \text{if } \tilde{\alpha}_s\mu < 0 \end{cases} .$$

We see that the ABS dispersion is flat if the chemical potential does not lie in the corresponding bulk band ($\tilde{\alpha}_s \mu < 0$).

The effect of the magnetic field is presented in Figs. 4.9(b) and (e). Focusing on a single ABS, one can see that the degeneracy is lifted due to the TRS breaking of the magnetic field $B_y$. Since the ABSs split into two spin-resolved states, one finds two gap closing points at finite $\phi$. This preserves the $4\pi$ periodicity in the dispersion. In contrast to the degenerate case without a magnetic field, the zero-energy crossings under a magnetic field are stable under the application of a finite potential in the barrier [see dashed line in Fig. 4.9(b)].

Interestingly, the intersection of the opposite spin ABSs at finite energy and $\phi = \pi$ is not protected from the potential barrier. This leads to a $2\pi$ periodicity in the ABS spectrum. Therefore, the potential is coupling the two effective spin ABSs, leading to the anti-crossing, shown by the dashed line in Fig. 4.9(b).

The structure of the ABSs in constant magnetic fields indicates that the gap between the crossings is inverted. Therefore, the topological invariant at the gap inversion points needs to change. Similar to $j = 1/2$ Rashba Josephson junctions, the system is topologically non-trivial ($\mathcal{Q} = -1$) in between the crossings and trivial ($\mathcal{Q} = +1$) outside.

Analyzing the gap closings of the ABSs as a function of magnetic field and superconducting phase difference gives a topological phase diagram, shown in Figs. 4.9(c) and (f). Here, we offer the difference between calculations in (dashed lines) and outside (solid lines) of the Andreev approximation. The Andreev approximation always leads to a gap closing at $\phi = \pi$ and $B_x = 0$ in the states around the chemical potential. Additionally, no subgap ABSs are generated from bands not crossed by the chemical potential. Without the Andreev approximation, both HH and LH states form an ABS.

A new consequence of the additional state in the Luttinger model is the superposition of two sets of ABSs, which is most striking in the metallic regime. Since these states have different spins, they are affected differently by a magnetic field. This can be seen in Fig. 4.9(e), where the splitting of the zero-energy crossings is more significant for the HH states (red) in comparison to the LH states (blue). Here, we expect a different behavior of the topological invariant since the spectrum has four gap closings with effective gap inversions. Consequently, one finds unique features in the system's topology, which is discussed in detail in Sec. 4.6.2.

### 4.6.2 Topological phase diagram

In this section, we apply the analysis of the ABSs at zero momentum to a full Josephson junction with finite widths of the normal ($W_N$) and superconducting regions ($W_S$), as shown in Fig. 4.1(b). We discretize $\hat{H}_{\mathrm{JJ}}(x, p_y)$ on a square lattice with infinite length in the $y$-direction ($L \to \infty$) to have $p_y$ as a good quantum number. To analyze the topological phase diagram, we focus on $p_y = 0$, similar to Refs. [23, 24, 25, 98]. Here, we use the finite-difference method introduced in Sec. 4.3 through the Kwant code [157].

Similar to the $j = 1/2$ Rashba Josephson junction, discussed in Sec. 2.3.5, the zero-energy ABSs form a diamond shape as a function of magnetic field $B_x$ and superconducting phase difference $\phi$. One can understand this by looking at the ABS dispersion $\epsilon(\phi)$ at a constant $B_x$. We show this dispersion for a Josephson junction built from the semimetal $\alpha$-Sn in Fig. 4.10(a). We put the chemical potential into the HH states ($\mu < 0$) to avoid any additional effects from the edge states of the LSM discussed in Sec. 3.5. At a finite magnetic field, the ABSs have crossings at zero energy, which indicates a gap inversion at finite $\phi = \phi_{\mathrm{crit}}$ [see dashed lines in Fig. 4.10(a)]. This gap inversion induces a topological phase transition, where the topological invariant from Eq. (4.20) is $\mathcal{Q} = +1$ outside the crossings and $\mathcal{Q} = -1$ in between.

We can draw the topological phase diagram by calculating the gap of the lowest energy ABS as a function of magnetic field and phase $\epsilon_g(B_x, \phi)$ [Fig. 4.10(b)]. Here, the black lines correspond to gap closings in the ABS spectrum, which indicate the topological phase transitions. The gap closings form the characteristic diamond shape, centered around the Thouless energy $\epsilon_T = (\pi/2)\hbar v_F / W_N$ [23], similar to the $j = 1/2$ model. For the used parameters for $\alpha$-Sn, we get $\epsilon_T^{\alpha\text{-Sn, HH}} = 2.2\mathrm{meV}$. We find that the topological invariant is trivial outside the diamond and non-trivial inside, as indicated by the framed insets in Fig. 4.10(b).

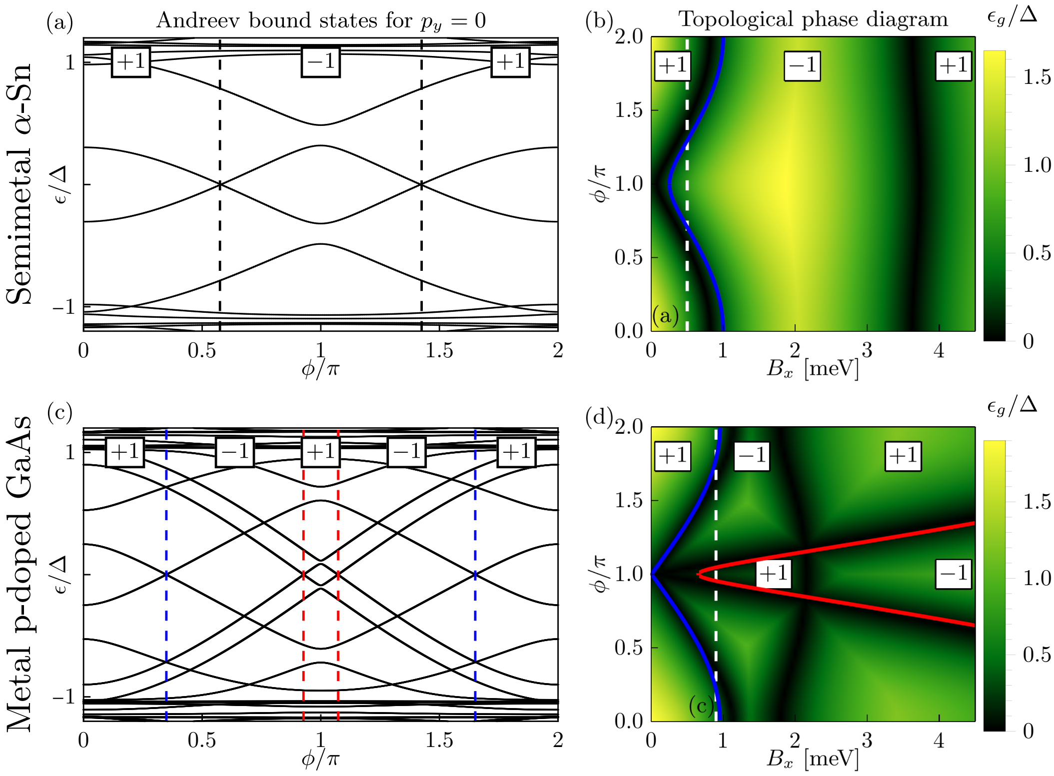

Figure 4.10: Andreev bound state spectrum in the Luttinger Joesphson junction for (a,b) $\alpha$-Sn as a semimetal [$\Delta = 0.56$meV, $\mu = -1.0$meV, $V_0 = 0$, $W_N = 20$nm, and $W_S = 150$nm] and (c,d) p-doped GaAs for the metallic phase [$\Delta = 0.5$meV, $\mu = -2.0$meV, $V_0 = 0.2$meV, $W_N = 20$nm, and $W_S = 300$nm] (see Tab. A.2 for material-specific parameters). The framed insets indicate the calculated topological invariant from Eq. (4.20). (a, c) Spectrum as a function of superconducting phase difference $\phi$ for constant magnetic field (a) $B_x = 0.5$meV and (c) $B_x = 0.9$meV, indicated by the dashed line in (b, d). (b, d) Gap of the Andreev bound states as a function of $\phi$ and $B_x$. The green to black color code indicates the gap of the numerical calculations. For comparison, we show the topological phase boundaries, given by the analytical calculations in the short-junction limit [Eq. (4.58)].

As discussed in Sec. 4.6.1, the different states of the Luttinger model can only form relevant ABSs, if the chemical potential lies inside the corresponding band. Therefore, we expect a combination of multiple ABSs in the metallic regime. In Fig. 4.10(c,d), we show the corresponding calculations for p-doped GaAs. Here, we can see the coexistence of two distinct topological phase diagrams, depicted by two diamond-shaped ABS gap closings. Each topological transition line is centered around the Thouless energy of the corresponding band [$\epsilon_T^{\text{GaAs, HH}} = 2.2\text{meV}$ and $\epsilon_T^{\text{GaAs, LH}} = 6.7\text{meV}$]. Since the $v_F$ of the LH states is much larger than for the HH states, their topological region is stretched strongly along the magnetic field.

To compare the numerical calculations on a finite lattice with the analytical results of the $\delta$-barrier approach, we additionally show the solutions of Eq. (4.58) in Fig. 4.10(b,d). Here, the HH states are shown in red, and the LH states are in blue. The main difference between the analytical and numerical results come from the assumption of infinite superconducting leads ($W_S \to \infty$). In the numerical calculations, the SCs are finite, leading to backscattering effects of the states at the boundary of the SCs with the vacuum. To reduce this effect, we take $W_S$ to be larger than the coherence length in the SCs $\xi = \hbar v_F/\Delta$. For $\alpha$-Sn, only the $\xi$ of the HH states is essential, with $\xi^{\alpha\text{-Sn, HH}} = 50\text{nm}$. In the metallic regime, both states are relevant, where the LH states have a more considerable coherence length ($\xi^{\text{GaAs, LH}} = 170\text{nm}$) than the HH states ($\xi^{\text{GaAs, HH}} = 57\text{nm}$). Therefore, we take $W_S$ as large as possibly allowed by our computational resources.

### 4.6.3 Opening of a topological gap

Previous research showed that the opening of a topological gap in the ABSs depends on the relative alignment between the Zeeman and SOC fields [25]. A unique feature of the Luttinger model is the existence of an intrinsic SOC in at least two dimensions. Therefore, the 2D Josephson junction setup does not require the presence of an external Rashba or Dresselhaus (BIA) term. We show in Sec. 4.4 that the SOC field of the $\alpha_z$ and $\alpha_\square$ terms points out of plane. This implies that any in-plane Zeeman field will lead to a topological gap opening in the ABSs.

First, we analyze the simple case of the semimetallic phase, using the parameters

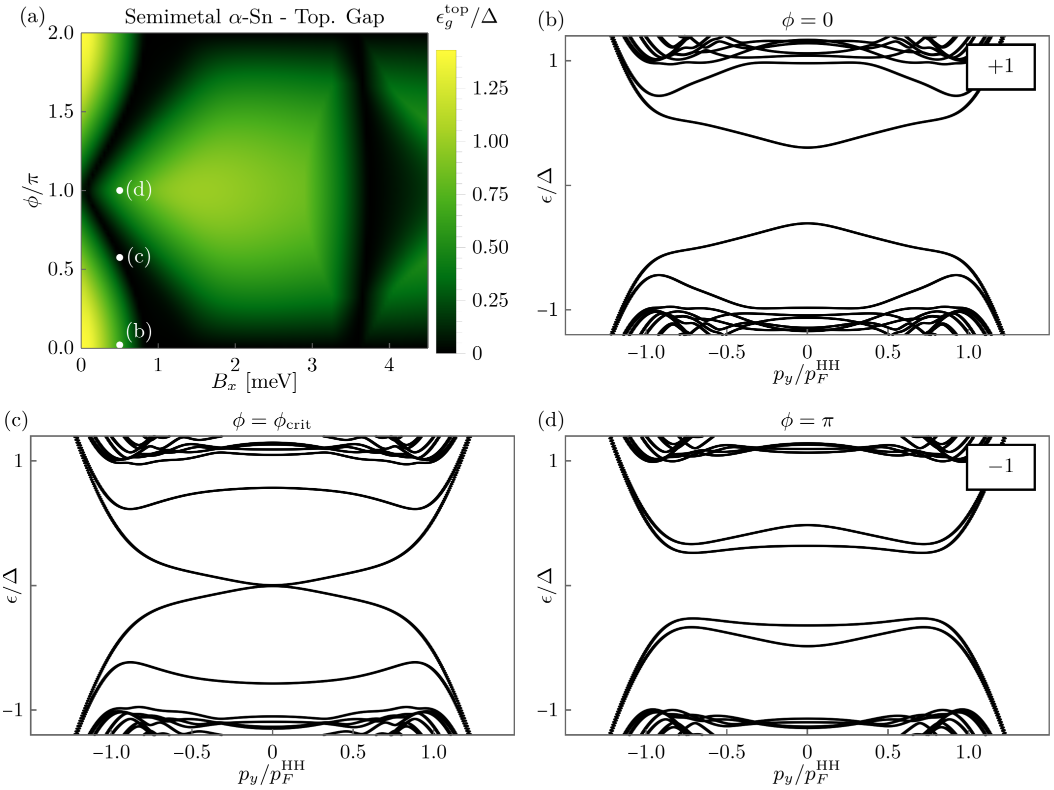

Figure 4.11: (a) Topological gap $\epsilon_g^{\mathrm{top}} = \min_{p_y} \epsilon_g(p_y)$ of the Andreev bound states in a Josephson junction of $\alpha$-Sn. (b-d) Energy dispersion as a function of momentum $p_y$ at $B_x = 0.5$meV for (b) $\phi = 0$, (c) $\phi = \phi_{\mathrm{crit}}$, and (d) $\phi = \pi$. This shows the topological phase transition with the topological invariant $\mathcal{Q} = \det(\hat{r})$ [Eq. (4.20)] indicated by the framed insets.

of $\alpha$-Sn (see Tab. A.2), where only one species of ABSs exists in the subgap region. Fig. 4.11(a) shows the topological gap as a function of the Zeeman field and superconducting phase. These calculations use the finite-difference method from Sec. 4.3 for a system with infinite length $L$ in $y$-direction [see Fig. 4.1(b)], where $p_y$ is still a good quantum number. One can still see the boundaries of the topological phase diagram of Fig. 4.10(b) due to the gap closings at $p_y = 0$. Around these lines, the topological gap is small, but in the center of the non-trivial region away from $\phi = \{0, 2\pi\}$, it takes values in the order of $\epsilon_g^{\mathrm{top}} \approx \Delta$. This shows that an in-plane Zeeman field, combined with a finite superconducting phase, is sufficient to open a topological gap in the system. Bulk-boundary correspondence suggests that a non-trivial topological invariant $\mathcal{Q} = -1$ in combination with a topological gap induces topologically protected states localized at the system's boundary. These are the MBSs, which are analyzed in the following section.

The topological transition is presented with the dispersion of the ABSs as a function of momentum $p_y$ in Figs. 4.11(b-d). These calculations are along a constant $B_x = 0.5\text{meV}$ with varying $\phi$. Outside of the topological region [Fig. 4.11(b)], the spectrum has a gap with a trivial band ordering ($\mathcal{Q} = +1$). The gap slowly closes for increasing $\phi$ until $\phi_{\text{crit}}$, indicated by the dashed line in Fig. 4.10(a), is reached. Here, the bands cross at $p_y = 0$, and the system undergoes a topological transition [see Fig. 4.11(c)]. In the topological region $\phi_{\text{crit}} < \phi < 2\pi - \phi_{\text{crit}}$, the gap reopens with an inverted band structure, giving rise to a non-trivial topological invariant ($\mathcal{Q} = -1$), shown in Fig. 4.11(d).

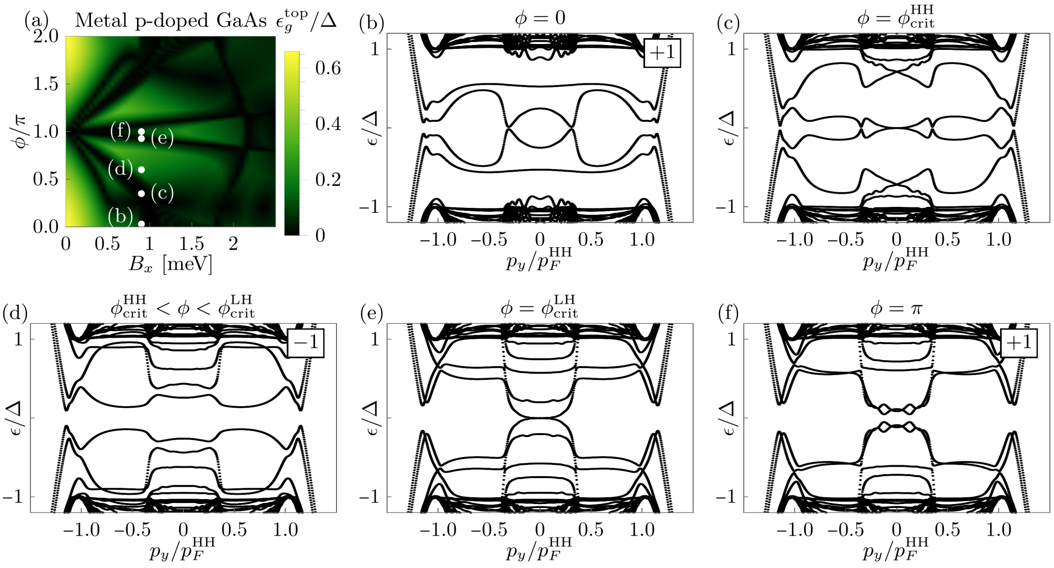

Figure 4.12: (a) Topological gap $\epsilon_g^{\text{top}} = \min_{p_y} \epsilon_g(p_y)$ of the Andreev bound states in a Josephson junction of GaAs. (b-f) Energy dispersion as a function of $p_y$ at $B_x = 0.9\text{meV}$ for (b) $\phi = 0$, (c) $\phi = \phi_{\text{crit}}^{\text{HH}}$, (d) $\phi = 0.6\pi$, (e) $\phi = \phi_{\text{crit}}^{\text{LH}}$, and (f) $\phi = \pi$. This shows the topological phase transition with the topological invariant $\mathcal{Q} = \det(\hat{r})$ [Eq. (4.20)] indicated in the framed insets.

The previous section showed that the metallic region hosts two sets of ABSs from the HH and LH states. The topological phase diagram in Fig. 4.10(d) shows that both groups of states undergo their specific topological phase transition. In Figs. 4.12(b-f), we illustrate the existence of two critical superconducting phases $\phi_{\text{crit}}^{\text{HH}}$ and $\phi_{\text{crit}}^{\text{LH}}$, where the ABSs cross at $p_y = 0$ and perform a gap inversion with a change in $\mathcal{Q}$.

The effective topological gaps are summarized in Fig. 4.12(a). Here, one can see the topological phase diagram of Fig. 4.10(d) in combination with the gap size, which protects the boundary states in the topological regions.

From the dispersions of the ABSs, one can see that the gap is smallest around the Fermi momentum $p_F$ of the relevant state (HH or LH). This corresponds to the expectations from the simpler 2DEG Josephson junction, where the crossing at $p_F$ is opened by a finite SOC field, which needs to be perpendicular to the magnetic field. In Sec. 4.4, we showed that the effective intrinsic SOC field of the Luttinger model $\boldsymbol{n}_L$ has an out-of-plane orientation, which is only present for $p_x p_y \neq 0$. From this, one can see that the topological gap opens for any in-plane magnetic field, and the topological phase transition can only happen at $p_y = 0$, where $\boldsymbol{n}_L = 0$.

### 4.6.4 Majorana bound states

This chapter showed that Luttinger materials in a 2D Josephson junction host ABSs. Even without external SOC, a topological gap opens under the application of a magnetic field. In addition, we can link a topological invariant $\mathcal{Q}$ [Eq. (4.20)] to specific magnetic fields and topological phase differences, leading to a topological phase diagram, shown in Fig. 4.10. With the combination of a topological gap and a non-trivial topological invariant, one expects the existence of topologically protected states at the edges of the system due to bulk boundary correspondence.

Our numerical finite-difference approach (see Sec. 4.3) allows us to define a finite 2D system and solve for the lowest energy wavefunctions from the BdG equation. The results for an $\alpha$-Sn Josephson junction with $L = 2000$nm are shown in Fig. 4.13.

Since we expect the MBSs to exist around zero energy, we show the energy of the lowest state in the finite system as a function of magnetic field and superconducting phase difference in Fig. 4.13(a). One can see that areas exist in the topological region of the phase diagram, where the energy of the lowest states is close to zero,

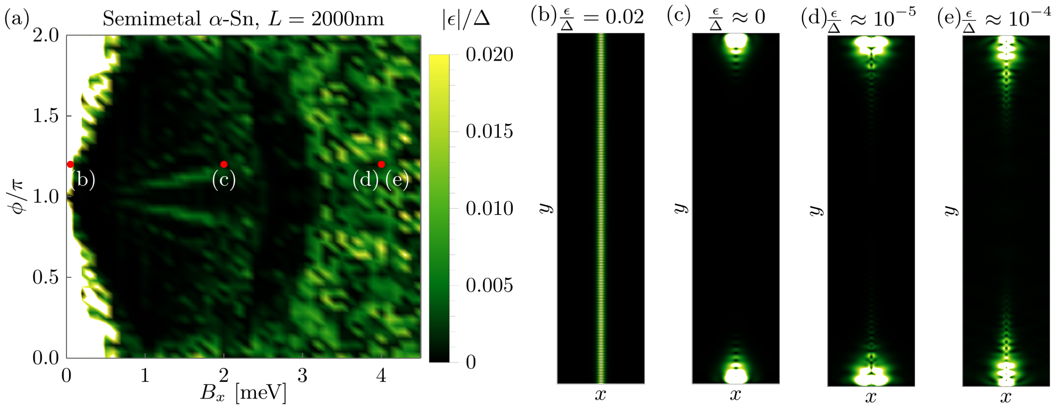

Figure 4.13: (a) Lowest energy states in a finite Josephson junction with the semimetal $\alpha$-Sn. (b-e) Wavefunctions of the lowest energy sates at $\phi = 1.2\pi$ and (b) $B_x = 0.05$meV, (c) $B_x = 2.0$meV, and (d,e) $B_x = 4.0$meV. The positions of (b-e) in the $(B_x, \phi)$ space are indicated by the red points in (a). We used the material specific parameters of $\alpha$-Sn (see Tab. A.2), with $\mu = -1.0$meV and $\Delta = 0.56$meV. The dimensions of the junction are $W = 20$nm, $W_S = 150$nm, and $L = 2000$nm.

indicated by the black color. In theory, one would expect the formation of MBSs in the entire topological region, but the finite $L$ leads to Majorana oscillations, similar to the 2D Rashba Josephson junction (see Fig. 2.4).

The difference between the lowest energy state in the topological and trivial regions can be seen in Fig. 4.13(b-e). For small magnetic fields outside of the topological diamond [Fig. 4.13(b)] one can find an ABS localized in the N region along the full sample length in the $y$-direction. These are considered to be the quasi-1D bulk states, similar to the superconducting wires.

As shown conceptionally in Fig. 2.2, we expect the formation of MBSs at the ends of the N region around $x \in [-W/2, W/2]$ and $y \approx \pm L/2$. Inside the topological region [Fig. 4.13(c)], we find a zero energy state, perfectly localized in the expected region. We identify these states as MBSs. If the magnetic field is sufficient to be in the second trivial regime, one finds two localized states [Fig. 4.13(d,e)], due to the second gap inversion in the ABS spectrum. These states hybridize, which moves them to higher energies. This leads to a fermionic system of an even number of MBSs, which is topologically trivial.

These calculations are done in the semimetallic regime with negative chemical potential. Therefore, we find that the wavefunctions of all lowest ABSs and MBSs have mainly HH character with $|j_z| = 3/2$.

We show the coexistence of two topological phases from the HH and LH states in the metallic regime. As indicated in Fig. 4.10(d), we expect a region around $\phi = \pi$, where both states are topological simultaneously. This leads to an even number of MBSs and a trivial topological invariant ($\mathcal{Q} = +1$). Our numerical calculations confirm that in this region, two MBSs exist, where one has mainly HH character and the other mostly LH character. The coexistence of multiple MBSs from different topological origins makes studying Luttinger Josephson junctions a rich field to investigate in future experiments.

We emphasize that the formation of MBSs in the 2D Luttinger Josephson junctions without the direct application of a Rashba or Dresselhaus SOC is a novel conclusion of this thesis. We have checked that the presence of a Dresselhaus SOC in the form of a BIA term does not change these results, as long as the BIA terms are small compared to the Luttinger parameters.

### 4.6.5 Zero-bias peak in the edge conductance

In this chapter, we discuss the calculation of the edge conductance of the Josephson junction setup. This provides a concrete prediction for possible future experiments.

We are using the numerical approach from Sec. 4.3 requires additional leads to compute the conductance. Therefore, we use the method of Ren et al. [136] and attach a probe on top of the edge of the N region, where the MBSs form [see Fig. 4.14(a)]. This extends the general 2D model to 3D, where the $z$-direction consists of two layers. The finite Josephson junction forms the bottom layer, where leads are attached to the two SCs, which extend $y \to \infty$ [grey area in Fig. 4.14(a)]. The conductance probe [red in Fig. 4.14(a)] is localized on the top layer and is modeled with the normal Luttinger Hamiltonian [Eq.(3.7)]. It is connected to the Josephson junction via vertical tunnel coupling. The corresponding coupling term

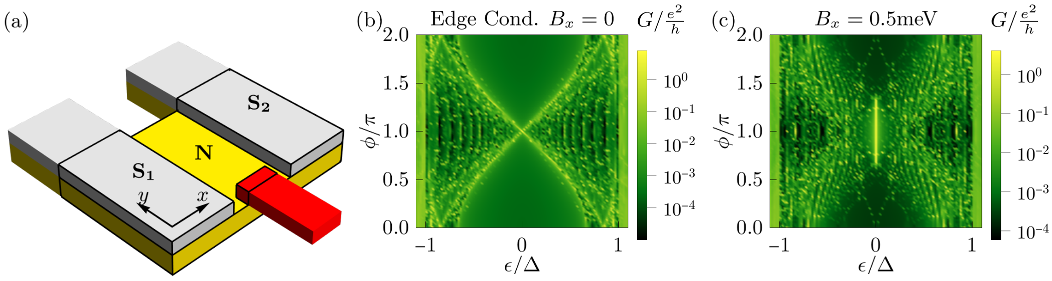

Figure 4.14: (a) Setup for the edge conductance calculations in the Luttinger Josephson junction motivated by Ref. [136]. The normal N region (yellow) lies between two $s$-wave superconductors $S_{1,2}$ (grey). Two leads are attached to the superconducting regions extending to $y \to \infty$. The Josephson junction is a 2D object where a normal conductance probe (red) is put on a second layer in $z$ on the top of a small area around the edge of the N region. A lead is attached to this probe extending it to $y \to -\infty$. (b,c) Calculated edge conductance $G(\epsilon)$ [Eq. (4.63)] as a function of energy and superconducting phase difference for the semimetal $\alpha$-Sn. (b) Without a magnetic field ($B_x = 0$), one can see the signal of the Andreev bound statesm and (c) at $B_x = 0.5$meV, the edge conductance shows the zero-bias peak of the Majorana bound state in the topological region.

in the tight-binding Hamiltonian has the shape

$$\mathcal{H}^{\mathrm{TB}}_{\mathrm{coupling}} = t_p \sum_{i=i_1}^{i_2} \sum_{j=j_1}^{j_2} \hat{d}^\dagger_{i,j} \hat{\tau}_z \hat{1}_4 \hat{c}_{i,j} + \mathrm{h.c.} \tag{4.62}$$

Here, $i_1 \leq i \leq i_2$ and $j_1 \leq j \leq j_2$ indicate the $x$ and $y$ coordinates in the square lattice. For our calculations, we used a contact area of $(10 \times 25)$nm, which is motivated by the localization length of the MBS. The creation (annihilation) operators $c^\dagger_{i,j}$ $(c_{i,j})$ act on the Josephson junction in the bottom layer, and $d^\dagger_{i,j}$ $(d_{i,j})$ act on the normal probe in the top layer. For the presented calculations, we use the coupling strength $t_p = 0.5$meV.

We can use the Kwant code [157] to calculate the scattering matrix of the system numerically. This way, one can determine the conductance between the normal probe and the superconducting leads at given energy with

$$G(\epsilon) = \frac{e^2}{h}[N - R_{ee}(\epsilon) + R_{eh}(\epsilon)], \tag{4.63}$$

where $N$ is the number of channels in the lead, and the reflection probabilities $R_{ee}(\epsilon)$ and $R_{eh}(\epsilon)$ correspond to normal and Andreev reflection in the normal lead.

The results of the conductance calculations as a function of energy and superconducting phase difference are shown in Fig. 4.14(b,c). Without a magnetic field [Fig. 4.14(b)], one can see the signatures of the ABSs. This is highlighted by the zero energy crossing at $\phi = \pi$ and the $\cos(2\phi)$ dependence. Applying a finite magnetic field leads to splitting the $\phi = \pi$ crossing towards finite $\phi$. This can be seen in Fig. 4.14(c), where the two crossings are in good agreement with the ABS dispersion in Fig. 4.10(a). As discussed in the previous sections, one can find a non-trivial topological phase between the two ABS crossings with $\mathcal{Q} = -1$. The zero-bias peak in Fig. 4.14(c) is a solid indicator of the existence of an MBS in the topological regime.

We predict that this conductance peak in the topological regime can be observed in future experiments. Our parameters for the superconducting coupling are motivated to form a Josephson junction, where the normal region is built from $\alpha$-Sn and $\beta$-Sn acts as the SCs. One can expect this to be interesting for $\alpha$-Sn samples, where local $\beta$-Sn defects can form on the surface.

# 5 Conclusion and Outlook

In this thesis, we provided a detailed analysis of a wide array of topological phases arising in the 4-band Luttinger model. We showed that this model is a low-energy description of the hole states with total angular momentum $j = 3/2$ states in many materials, as long as the characteristic gap with the $j = 1/2$ states is significantly larger than the relevant energy scale. The most significant topological properties arise in crystals with an inverted band structure between the $s$ and $p$-orbitals and strong intrinsic spin-orbit coupling (SOC). Therefore, the Luttinger model is relevant for describing Luttinger semimetals, which host a quadratic node in the dispersion. Examples are HgTe, $\alpha$-Sn, or iridate compounds, like $\mathrm{Pr_2Ir_2O_7}$.

To study the topological behavior in the Luttinger semimetal, we analyzed the surface states of a half-infinite system with a single surface in Ch. 3. Here, we found that the number of surface states is related to the difference between the effective masses of the light-hole (LH) and heavy-hole (HH) states $\bar{\alpha}$ from Eq. (3.34). For $\bar{\alpha} = 0$, the system has two particle-hole symmetric surface states with quadratic dispersion originating from the quadratic bulk node. For $0 \leq |\bar{\alpha}| < 1$, one surface state flattens while the other state moves closer to the bulk boundary. We found a critical transition point at $|\bar{\alpha}| = 1$, where one surface state has zero curvature and the second state merges entirely with the bulk and vanishes. In the remaining range of the semimetal phase $1 \leq |\bar{\alpha}| \leq 2$, the Luttinger semimetal hosts a single surface state. For $|\bar{\alpha}| > 2$, the effective masses of the HH and LH states have the same sign, giving a metallic regime where no surface states exist.

We could explain the existence of the surface states from two different points of view. Considering the higher-order 6-band Kane model from Eq. (3.65) with the additional $j = 1/2$ states, we can relate the existence of surface states to the inverted band structure. Utilizing the folding procedure performed in Sec. 3.2.3, we found that the required $\bar{\alpha}$ values of the Luttinger model can never be achieved with a trivial band ordering in the Kane model. Hence, the inverted gap is necessary for the existence of surface states in the Luttinger model. In Sec. 3.5.1, we summarized the results presented in Ref. [26], which considers the most general Hamiltonian of a chiral symmetric node. In the reference, we showed that flat surface states exist, as long as chiral symmetry is only partially broken, which holds true for the Luttinger semimetal. Therefore, the chiral symmetric quadratic node is the high-symmetry parent model of the Luttinger model. Overall, we can relate the existence of surface states in the Luttinger semimetal to the inverted band structure of the higher order Kane model and the chiral symmetry of the lower order quadratic node.

Strain engineering is often used to modify the band structure of Luttinger semimetals by growing the sample on a substrate with a different lattice constant. As discussed in Sec. 3.1.2, tensile strain leads to a topological insulator phase, and compressive strain gives a topological semimetal phase with linear nodes in the dispersion discussed in this work. We distinguish between the Dirac semimetal (DSM) phase, where inversion and time-reversal symmetry (TRS) is conserved, and the Weyl semimetal (WSM) phase, with either of these symmetries broken.

In Sec. 3.6, we analyzed the evolution of the surface states under compressive strain, where the quadratic node of the Luttinger semimetal splits into two linear Dirac nodes. We showed that one can choose the surface orientation to project the Dirac points onto each other or separate, illustrated in Fig. 3.1. Using a semi-analytical approach (see Sec. 3.4), we provide the surface states of the DSM phase for both surface orientation cases numerically in the full range of effective masses $\bar{\alpha}$. Additionally, we discussed the surface states analytically in the proximity of the Dirac nodes, using the linearized Hamiltonian described by Eq. (3.52). In general, the curvature of the surface states behaves similarly to the Luttinger semimetal phase as a function of $\bar{\alpha}$. If the surface is chosen perpendicular to the strain, where the Dirac nodes are separated (see Sec. 3.6.1), the surface states exist only for a finite range of angles in momentum space, which also depends on $\bar{\alpha}$. This leads to the existence of double Fermi arcs, connecting the Dirac points in the surface Brillouin zone for $1 < \bar{\alpha} \leq 2$. Suppose both Dirac points are projected onto each other in the surface Brillouin zone. In the case, where both Dirac points are projected onto each other, the surface states are flat in the vicinity of the nodes. This can also be related to the chiral symmetric linear node, discussed in Ref. [26].

We break inversion symmetry with the linear and cubic bulk inversion asymmetry (BIA) terms from Eq. (3.14) to achieve a WSM phase. For instructive reasons, we analyzed the effect of the linear BIA terms first in Sec. 3.7. We discussed that under this condition, the Dirac points split into ring-shaped line nodes, giving the line-node semimetal phase. Additional cubic BIA terms lift the line-node degeneracy for $p_{x,y} \neq 0$, providing eight Weyl points with a finite chirality. Again, the surface orientation is essential since Weyl points that project onto each other modify the total chirality of the nodes. We showed that the surface states form Fermi arcs, which connect Weyl points with positive chirality to Weyl points with negative chirality. As discussed in Sec. 2.2.1, 2D momentum planes can be considered effective 2D Chern insulators, where the Chern number is given by the chiralities of the surrounding Weyl points. We confirmed this property of the WSM phase with the presence or absence of chiral surface states along these momentum planes using the bulk-boundary correspondence.

Since the compressive strain and the BIA terms are considered small perturbations, we could define a hierarchy of momentum and energy scales corresponding to the specific semimetal phases (see Sec. 3.3). The smallest regime considered in this thesis is determined by the cubic BIA terms, where the Weyl physics is most relevant. Here, one can approximate the system with the well-known low-energy Weyl Hamiltonian from Eq. (2.17), originating from high-energy physics. Outside the vicinity of the Weyl points, the cubic BIA terms get dominated by the linear ones, leading to a line-node semimetal phase. Increasing the momentum and energy range further gives more significance to the compressive strain. The system can be approximated in this scale by a DSM, even if inversion symmetry is broken. Away from the linear nodes, the dispersion becomes quadratic in momentum and takes the shape of the Luttinger semimetal phase. We showed in Sec. 3.5.3 that the Luttinger model has a validity limit at energies in the order of the characteristic gap related to the $j = 1/2$ electron states. Here, the hybridization of the $s$ and $p$-orbitals becomes relevant, and one has to consider the multiband Kane model.

The research of superconductivity in Luttinger materials is of high interest in the scientific community since the $j = 3/2$ states open the possibility of $s$, $p$, $d$, and $f$-wave Cooper pairing. In Ch. 4, we studied the topological superconductor (SC) phase of the Luttinger model with spin-singlet Cooper pairing. It was previously shown in ordinary $j = 1/2$ models that specific combinations of SOC and magnetic fields drive the system into a non-trivial phase with Majorana bound states (MBSs) forming at the boundary of the system, as discussed in Sec. 2.3. We illustrated that Luttinger materials could be topological SCs without needing an external SOC application. While our findings of Luttinger semimetals are published in Ref. [28], this thesis extends the study to the metallic phase of the Luttinger model, relevant to materials like p-doped GaAs.

In a 1D superconducting wire, we showed that inversion asymmetric materials could be driven into a non-trivial topological phase by gap inversion under a magnetic field (see Sec. 4.5). Here, the $j = 1/2$ model gives only a single topological transition point, where the MBS survives for infinitely large magnetic fields. Interestingly, we found that the heavy-hole (HH) and light-hole (LH) states of the Luttinger model are affected differently by a Zeeman field due to their difference in $j_z$. Hence, the system is topologically trivial for small magnetic fields until the HH states cross at zero momentum. Using the topological invariant given by the reflection matrix of the wire, we proved that the gap inversion of the HH states leads to a topologically non-trivial phase with MBSs forming at the ends of the wire. A new feature of the Luttinger model is the existence of a second phase transition, where the superconducting gap of the LH states is closed. Under this condition, our system aquired two band inversions, giving a trivial topological invariant, and destroying the MBSs. For even higher magnetic fields, the system stays in a trivial regime.

The critical magnetic fields from Eq. (4.40) are independent of the effective masses of the bands. Therefore, our findings apply to both the semimetallic and metallic phases of the Luttinger model. Using our numerical calculations, we showed that the localization length of the MBSs is related to the strength of the BIA terms. This dictates the required minimum length of the wire to avoid Majorana oscillations coming from the hybridization of the wavefunctions from both ends.

In Sec. 4.6, we considered the Josephson junction setup, where a normal conducting region separates two $s$-wave Luttinger SCs with a finite phase difference. We showed that the Luttinger model in 2D includes an intrinsic SOC, which is sufficient to open a topological gap in the Andreev bound states (ABSs), even if inversion symmetry is preserved. The gap closing of the ABSs as a function of the Zeeman field and superconducting phase difference gives a topological phase diagram, where the non-trivial region lies in the resulting diamond shape depicted in Fig. 4.10.

Using a $\delta$-barrier approach, we could derive an analytical expression for the ABS dispersion. Here, we found that both HH and LH states can form subgap ABSs if the chemical potential lies in the corresponding bands. Similar to the superconducting wire, the ABSs of the HH states behave differently under magnetic fields than the LH states due to the individual $j_z$ values. Therefore, the topological phase diagram in the semimetal regime changes significantly by inverting the sign of the chemical potential. For the metal regime, we find a coexistence of two independent diamond shapes, where the gap closings of both types of ABSs lead to a topological transition.

Our numerical calculations on a finite junction in Sec. 4.6.4 showed the formation of zero-energy MBSs at the boundary of the normal region (see Fig. 2.2). The number of Majorana modes is odd inside the diamond shape of the ABS gap-closings, which corresponds to a non-trivial topological invariant computed via the reflection matrix (see Sec. 4.2). In the metallic regime, the diamonds overlap in the phase diagram, where two types of MBSs exist with HH and LH characters. This results in an even number of MBSs, where the topological invariant is trivial. By calculating the conductance at the edge of the normal region, we could confirm the existence of MBSs with a well-resolved zero-bias peak in the topological regime.

Throughout our study of the Luttinger SC, we focused on Cooper pairs from the HH and LH bulk states. Hence, we considered only chemical potentials away from the surface states. It was shown that induced superconductivity in surface states of topological insulators provides a wide array of exciting properties. We believe that induced superconductivity in a Luttinger semimetal, where the chemical potential lies in both surface and bulk states, will provide a combination of the physical features discussed in Ch. 4 and the ones found in topological insulators. The relation between both topological systems and their potential hybridization is an exciting topic for future research.

# A Appendix

## Contents

## A.1 Matrices

$$\hat{\sigma}_x = \begin{pmatrix} 0 & 1 \\ 1 & 0 \end{pmatrix} \qquad \hat{\sigma}_y = \begin{pmatrix} 0 & -i \\ i & 0 \end{pmatrix} \qquad \hat{\sigma}_z = \begin{pmatrix} 1 & 0 \\ 0 & -1 \end{pmatrix} \qquad \hat{1}_2 = \begin{pmatrix} 1 & 0 \\ 0 & 1 \end{pmatrix} \tag{A.1}$$

$$\hat{J}_x = \frac{1}{2}\begin{pmatrix} 0 & \sqrt{3} & 0 & 0 \\ \sqrt{3} & 0 & 2 & 0 \\ 0 & 2 & 0 & \sqrt{3} \\ 0 & 0 & \sqrt{3} & 0 \end{pmatrix} \qquad \hat{J}_y = \frac{i}{2}\begin{pmatrix} 0 & -\sqrt{3} & 0 & 0 \\ \sqrt{3} & 0 & -2 & 0 \\ 0 & 2 & 0 & -\sqrt{3} \\ 0 & 0 & \sqrt{3} & 0 \end{pmatrix} \tag{A.2}$$

$$\hat{J}_z = \frac{1}{2}\begin{pmatrix} 3 & 0 & 0 & 0 \\ 0 & 1 & 0 & 0 \\ 0 & 0 & -1 & 0 \\ 0 & 0 & 0 & -3 \end{pmatrix} \qquad \hat{1}_4 = \begin{pmatrix} 1 & 0 & 0 & 0 \\ 0 & 1 & 0 & 0 \\ 0 & 0 & 1 & 0 \\ 0 & 0 & 0 & 1 \end{pmatrix} \tag{A.3}$$

$$\hat{T}_x = \frac{1}{3\sqrt{2}}\begin{pmatrix} -\sqrt{3} & 0 & 1 & 0 \\ 0 & -1 & 0 & \sqrt{3} \end{pmatrix} \qquad \hat{T}_y = \frac{-i}{3\sqrt{2}}\begin{pmatrix} \sqrt{3} & 0 & 1 & 0 \\ 0 & 1 & 0 & \sqrt{3} \end{pmatrix} \tag{A.4}$$

$$\hat{T}_z = \frac{\sqrt{2}}{3}\begin{pmatrix} 0 & 1 & 0 & 0 \\ 0 & 0 & 1 & 0 \end{pmatrix} \tag{A.5}$$

$$\hat{T}_{xx} = \frac{1}{3\sqrt{2}}\begin{pmatrix} 0 & -1 & 0 & \sqrt{3} \\ -\sqrt{3} & 0 & 1 & 0 \end{pmatrix} \qquad \hat{T}_{yy} = \frac{3}{\sqrt{2}}\begin{pmatrix} 0 & -1 & 0 & -\sqrt{3} \\ \sqrt{3} & 0 & 1 & 0 \end{pmatrix} \tag{A.6}$$

$$\hat{T}_{zz} = \frac{\sqrt{2}}{3}\begin{pmatrix} 0 & 1 & 0 & 0 \\ 0 & 0 & -1 & 0 \end{pmatrix} \tag{A.7}$$

$$\hat{T}_{yz} = \frac{i}{2\sqrt{6}} \begin{pmatrix} -1 & 0 & -\sqrt{3} & 0 \\ 0 & \sqrt{3} & 0 & -1 \end{pmatrix} \qquad \hat{T}_{zx} = \frac{1}{2\sqrt{6}} \begin{pmatrix} -1 & 0 & \sqrt{3} & 0 \\ 0 & \sqrt{3} & 0 & -1 \end{pmatrix} \tag{A.8}$$

$$\hat{T}_{xy} = \frac{i}{\sqrt{6}} \begin{pmatrix} 0 & 0 & 0 & -1 \\ -1 & 0 & 0 & 0 \end{pmatrix} \tag{A.9}$$

$$\hat{\boldsymbol{\sigma}} = (\hat{\sigma}_x, \hat{\sigma}_y, \hat{\sigma}_z)^T \qquad \hat{\boldsymbol{J}} = \left(\hat{J}_x, \hat{J}_y, \hat{J}_z\right)^T \qquad \hat{\boldsymbol{T}} = \left(\hat{T}_x, \hat{T}_y, \hat{T}_z\right)^T \tag{A.10}$$

## A.2 Material specific parameters

| | $E_g$ | $\gamma_{\frac{1}{2}}$ | $\gamma_0$ | $\gamma_z$ | $\gamma_\Box$ |
|---|---|---|---|---|---|
| HgTe | $-303$ meV | $\frac{\hbar^2}{2m_0}$ | $-4.1\frac{\hbar^2}{2m_0}$ | $-0.98\frac{\hbar^2}{2m_0}$ | $-1.6\frac{\hbar^2}{2m_0}$ |
| GaAs | 1519 meV | $\frac{\hbar^2}{2m_0}$ | $-6.85\frac{\hbar^2}{2m_0}$ | $-2.58\frac{\hbar^2}{2m_0}$ | $-1.6\frac{\hbar^2}{2m_0}$ |

| | $v^2$ | $\beta_1^K$ | $B_+$ | $B_-$ | |
|---|---|---|---|---|---|
| HgTe | $12.53\frac{\hbar^2}{2m_0}$eV | $-4.31$ meVnm | $-75.48$ meVnm$^2$ | 0 | |
| GaAs | $19.27\frac{\hbar^2}{2m_0}$eV | $-0.20$meVnm | | | |

Table A.1: Material-specific parameters for the 6-band Kane model $\hat{H}^K(\mathbf{p})$ [Eq. (3.65)] for HgTe and GaAs [161, 116, 129], where $\hbar$ is the reduced Planck constant and $m_0$ is the electron mass. The quadratic bulk inversion asymmetry constants $B_\pm$ were fitted to DFT calculations.

| | $\alpha_0$ | $\alpha_z$ | $\alpha_\Box$ | $\beta_1$ |
|---|---|---|---|---|
| HgTe | $16.58\frac{\hbar^2}{2m_0}$ | $9.36\frac{\hbar^2}{2m_0}$ | $-1.6\frac{\hbar^2}{2m_0}$ | $-4.31$ meVnm |
| $\alpha$-Sn | $18.62\frac{\hbar^2}{2m_0}$ | $11.88\frac{\hbar^2}{2m_0}$ | | |
| GaAs | $-13.19\frac{\hbar^2}{2m_0}$ | $-5.75\frac{\hbar^2}{2m_0}$ | $-1.6\frac{\hbar^2}{2m_0}$ | $-0.20$meVnm |

| | $\beta_{31}$ | $\beta_{32}$ | $\beta_{33}$ | $\beta_{34}$ |
|---|---|---|---|---|
| HgTe | 140.36 meVnm$^3$ | 25.6 meVnm$^3$ | 4.3 meVnm$^3$ | $-8.5$ meVnm$^3$ |

Table A.2: Material-specific parameters for the 4-band Luttinger model $\hat{H}^{\mathbf{T}_d}(\mathbf{p})$ [Eq. (3.8)] and the bulk inversion asymmetry term $\hat{H}^{\mathrm{BIA}}(\mathbf{p})$ [Eq. (3.14)] for HgTe, GaAs, and $\alpha$-Sn, where $\hbar$ is the reduced Planck constant and $m_0$ is the electron mass. The HgTe and GaAs parameters are calculated by the folding procedure from Sec. 3.2.3 using the parameters from Table A.1 and the $\alpha$-Sn parameters are taken from Ref. [128].

## A.3 Character table of the tetrahedral double group $\mathbf{T}_d$

| $\mathbf{T}_d$ | $E$ | $\bar{E}$ | $8C_3$ | $8\bar{C}_3$ | $3C_2$, $3\bar{C}_2$ | $6S_4$ | $6\bar{S}_4$ | $6\sigma_d$, $6\bar{\sigma}_d$ |
|---|---|---|---|---|---|---|---|---|
| $\Gamma_1$ | 1 | 1 | 1 | 1 | 1 | 1 | 1 | 1 |
| $\Gamma_2$ | 1 | 1 | 1 | 1 | 1 | $-1$ | $-1$ | $-1$ |
| $\Gamma_3$ | 2 | 2 | $-1$ | $-1$ | 2 | 0 | 0 | 0 |
| $\Gamma_4$ | 3 | 3 | 0 | 0 | $-1$ | 1 | 1 | $-1$ |
| $\Gamma_5$ | 3 | 3 | 0 | 0 | $-1$ | $-1$ | $-1$ | 1 |
| $\Gamma_6$ | 2 | $-2$ | 1 | $-1$ | 0 | $\sqrt{2}$ | $-\sqrt{2}$ | 0 |
| $\Gamma_7$ | 2 | $-2$ | 1 | $-1$ | 0 | $-\sqrt{2}$ | $\sqrt{2}$ | 0 |
| $\Gamma_8$ | 4 | $-4$ | $-1$ | 1 | 0 | 0 | 0 | 0 |

Table A.3: Character table for the tetrahedral double group $\mathbf{T}_d$. The conserved symmetry operations of the group are shown in the top row, where $E$ is the identity, $C_n$ is a rotation by $2\pi/n$, $S_n$ represents a rotation by $2\pi/n$, followed by a reflection in a plane perpendicular to the rotation axis, and $\sigma$ denotes a reflection [118].

The character table A.3 describes the tetrahedral double group $\mathbf{T}_d$. The irreducible representations $\Gamma_1$ to $\Gamma_5$ form the single group $\mathbf{T}_d$ for integer angular momentum states without spin. The tetrahedral group contains the following symmetry operations: (1) The identity $E$. (2) Threefold ($2\pi/3$) rotational symmetry with respect to eight different axis ($8C_3$). (3) Twofold ($2\pi/2$) rotational symmetry with respect to three seperate axis ($3C_2$). (4) Six axis with a fourfold rotational symmetry ($2\pi/4$), followed by a reflection in a perpendicular plane to the rotation ($6S_4$). (5) Reflection symmetry with respect to six diagonal planes ($6\sigma_d$) [117, 118].

With spin, the group is expanded to the $\mathbf{T}_d$ double group, containing the additional irreducible representations $\Gamma_6$, $\Gamma_7$, and $\Gamma_8$. Here, one must include the additional $2\pi$ rotation $\mathcal{R}$, since only a $4\pi$ rotation restores a half-integer angular momentum state. In Tab. A.3, we use the notation from Koster et al. [162], where the barred symmetry operations include an additional $2\pi$ rotation (e.g. $\bar{E} = \mathcal{R}E$, with $\bar{E}^2 = E$).

In the Kane model, discussed in Sec. 3.2.1, the $j = 1/2$ states transform according to the $\Gamma_6$ and the $j = 3/2$ states transform according to the $\Gamma_8$ irreducible representation of the $\mathbf{T}_d$ double group. The blocks of the Kane Hamiltonian $\hat{H}^K(\mathbf{p})$ from Eq. (3.65) can be found with the direct product of the corresponding irreducibe representation. These direct products can be expanded as a linear combination of the single group irreducibe representations. Therefore, the blocks of $\hat{H}^K(\mathbf{p})$ have the representations

$$\hat{H}_{\frac{1}{2}\frac{1}{2}}(\mathbf{p}) \rightarrow \Gamma_6 \otimes \Gamma_6^* = \Gamma_1 + \Gamma_4, \tag{A.11}$$

$$\hat{H}_{\frac{3}{2}\frac{3}{2}}(\mathbf{p}) \rightarrow \Gamma_8 \otimes \Gamma_8^* = \Gamma_1 + \Gamma_2 + \Gamma_3 + 2\Gamma_4 + 2\Gamma_5, \tag{A.12}$$

$$\hat{H}_{\frac{1}{2}\frac{3}{2}}(\mathbf{p}) \rightarrow \Gamma_6 \otimes \Gamma_8^* = \Gamma_3 + \Gamma_4 + \Gamma_5. \tag{A.13}$$

With the help of these representations, we can use the symmetrized matrices and irreducible tensor products, shown in Tabs. 3.1 and 3.2, to write the most general form of the Kane Hamiltonian.

## A.4 Bulk dispersion of the Weyl semimetal phase

We provide the details of the bulk analysis of the Weyl semimetal (WSM) phase, discussed in Sec. 3.1.2. In the transformed basis of Eq. (3.37), the WSM Hamiltonian $\hat{H}^W(\boldsymbol{p})$ from Eq. (3.26) decouples into two blocks for $\varphi = \pi/4$

$$\tilde{H}^W(p_\perp, \varphi = \frac{\pi}{4}, p_z) = \hat{U}^\dagger_{\frac{\pi}{4}} \hat{H}^W(p_\perp, \varphi = \frac{\pi}{4}, p_z) \hat{U}_{\frac{\pi}{4}} \tag{A.14}$$

$$= \begin{pmatrix} \hat{h}_+(p_\perp, p_z) & 0 \\ 0 & \hat{h}_-(p_\perp, p_z) \end{pmatrix} \tag{A.15}$$

with

$$\hat{h}_\pm(p_\perp, p_z) = \left[d_0^\pm(p_\perp, p_z) + \delta_0^\pm(p_\perp, p_z)\right] \hat{1}_2 + \left[\boldsymbol{d}^\pm(p_\perp, p_z) + \boldsymbol{\delta}^\pm(p_\perp, p_z)\right] \cdot \hat{\boldsymbol{\sigma}}. \tag{A.16}$$

The components of the blocks without cubic bulk inversion asymmetry (BIA) terms are given by

$$d_0^\pm(p_\perp, p_z) = \alpha_0(p_\perp^2 + p_z^2) \pm \frac{3}{2}\beta_1 p_\perp, \tag{A.17}$$

$$d_x^\pm(p_\perp, p_z) = \sqrt{3}\left[\frac{|\beta_1|}{p_{\beta_1}} p_\perp \mp \beta_1\right] p_z, \tag{A.18}$$

$$d_y^\pm(p_\perp, p_z) = \frac{\sqrt{3}}{2}\left[\mp\frac{|\beta_1|}{p_{\beta_1}} p_\perp + \beta_1\right] p_\perp, \tag{A.19}$$

$$d_z^\pm(p_\perp, p_z) = 2\tilde{\alpha}_z\left(p_z^2 - \frac{1}{2}p_\perp^2 - p_u^2\right). \tag{A.20}$$

And the cubic BIA terms take the form

$$\delta_0^\pm(p_\perp, p_z) = \pm\frac{1}{2}p_\perp\left[\frac{1}{2}p_\perp^2\left(\beta_{31} + \frac{7}{4}\beta_{32} + 3\beta_{33} + 3\beta_{34}\right) - p_z^2\left(\beta_{31} + \frac{7}{4}\beta_{32} - 3\beta_{33}\right)\right], \tag{A.21}$$

$$\delta_x^\pm(p_\perp, p_z) = \mp\sqrt{3}p_z\left(\beta_{33}p_\perp^2 + \beta_{34}p_z^2\right), \tag{A.22}$$

$$\delta_y^\pm(p_\perp, p_z) = \frac{\sqrt{3}}{2}p_\perp\left[p_z^2(\beta_{31} + \frac{7}{4}\beta_{32} + \beta_{33}) - \frac{1}{2}p_\perp^2(\beta_{31} + \frac{7}{4}\beta_{32} - \beta_{33} - \beta_{34})\right], \tag{A.23}$$

$$\delta_z^\pm(p_\perp, p_z) = \pm\frac{1}{2}p_\perp\left(\frac{1}{2}p_\perp^2 - p_z^2\right)\left(\beta_{31} + \frac{13}{4}\beta_{32}\right). \tag{A.24}$$

We take the crossing point from the line node phase of the Luttinger Hamiltonian $\hat{H}^{LN}(\boldsymbol{p})$, $\boldsymbol{p}_0 = (p_{\perp 0}, p_{z0})$ with $p_{\perp 0} = p_{\beta_1}$ and $p_{z0}^2 = p_u^2 + p_{\beta_1}^2/2$ [Eq. (3.45)], and expand the Hamiltonian to linear order in momentum. From $d^{\pm}_{x,y}(p_\perp, p_z)$, one can see that the Hamiltonian is separated into a low and a high energy block, depending on the sign of $\beta_1$. We only focus on the low energy block $\hat{h}_{\mathrm{sgn}(\beta_1)}(p_\perp, p_z)$ and expand the cubic BIA terms to zeroth order and the other terms to first order in momentum. It is convenient to use the new basis

$$\hat{\sigma}_1 = \frac{v_{x,\perp}\hat{\sigma}_x + v_{y,\perp}\hat{\sigma}_y}{v_{1,\perp}}, \qquad \hat{\sigma}_2 = \frac{v_{x,\perp}\hat{\sigma}_x - v_{y,\perp}\hat{\sigma}_y}{v_{1,\perp}}, \tag{A.25}$$

$$v_{x,\perp} = \sqrt{3}\frac{p_{z0}}{p_{\perp 0}}|\beta_1|, \qquad v_{y,\perp} = -\frac{\sqrt{3}}{2}|\beta_1|, \qquad v_{1,\perp} = \sqrt{v_{x,\perp}^2 + v_{y,\perp}^2}. \tag{A.26}$$

This simplifies the expanded term $d_x(p_\perp, p_z)\hat{\sigma}_x + d_y(p_\perp, p_z)\hat{\sigma}_y \approx v_{1,\perp}\hat{\sigma}_1 q_\perp$, with $\boldsymbol{q} = (q_\perp, q_z) = (p_\perp - p_{\perp 0}, p_z - p_{z0})$. We get the effective low energy Hamiltonian

$$\tilde{h}(\boldsymbol{q}) = (\epsilon_0 + v_{0,\perp}q_\perp + v_{0,z}q_z)\hat{1}_2 + (v_{1,\perp} + \epsilon_1)\hat{\sigma}_1 + \epsilon_2\hat{\sigma}_2 + [v_{z,\perp}q_\perp + v_{z,z}q_z + \epsilon_z]\hat{\sigma}_z, \tag{A.27}$$

with the effective parameters from the Luttinger model

$$v_{0,\perp} = 2\alpha_0 p_{\perp 0} + \frac{3}{2}|\beta_1|, \qquad v_{0,z} = 2\alpha_z p_{z0}, \tag{A.28}$$

$$v_{z,\perp} = -2\tilde{\alpha}_z p_{\perp 0}, \qquad v_{z,z} = 4\tilde{\alpha}_z p_{z0}, \tag{A.29}$$

coming from the partial derivatives of $d_{0,z}(p_\perp, p_z)$. The constant terms are given by

$$\epsilon_0 = d_0(\boldsymbol{p}_0) + \delta_0(\boldsymbol{p}_0) \tag{A.30}$$

$$\epsilon_1 = \frac{\delta_x(\boldsymbol{p}_0)v_{x,\perp} + \delta_y(\boldsymbol{p}_0)v_{y,\perp}}{v_{1,\perp}} \tag{A.31}$$

$$\begin{aligned}\epsilon_2 &= \frac{\delta_y(\boldsymbol{p}_0)v_{x,\perp} - \delta_x(\boldsymbol{p}_0)v_{y,\perp}}{v_{1,\perp}} \\ &= \sqrt{3}\left(\beta_{31} + \frac{7}{4}\beta_{32} + \beta_{33} - \beta_{34}\right)\frac{p_{\perp 0}p_{z0}p_u^2}{\sqrt{p_{\perp 0}^2 + 4p_{z0}^2}}\end{aligned} \tag{A.32}$$

$$\epsilon_z = \delta_z(\boldsymbol{p}_0). \tag{A.33}$$

Utilizing the shape of $\tilde{h}(\mathbf{q})$, we can easily diagonalize the Hamiltonian to find the energy dispersion

$$\varepsilon(q_\perp, q_z) = \epsilon_0 + v_{0,\perp} q_\perp + v_{0,z} q_z \pm \sqrt{\left(v_{1,\perp} q_\perp + \epsilon_1\right)^2 + \epsilon_2^2 + \left(v_{z,\perp} q_\perp + v_{z,z} q_z + \epsilon_z\right)^2}. \tag{A.34}$$

The analysis of this equation is provided in Sec. 3.1.2 of the main text.

# Bibliography

[1] B. Volkov and O. Pankratov. "Two-dimensional massless electrons in an inverted contact". *Soviet Journal of Experimental and Theoretical Physics Letters*, **42**, 178 (1985).

[2] C. L. Kane and E. J. Mele. "Quantum spin hall effect in graphene". *Phys. Rev. Lett.*, **95**, 226801 (2005).

[3] C. L. Kane and E. J. Mele. "$Z_2$ topological order and the quantum spin Hall effect". *Phys. Rev. Lett.*, **95**, 146802 (2005).

[4] B. A. Bernevig and S.-C. Zhang. "Quantum spin Hall effect". *Phys. Rev. Lett.*, **96**, 106802 (2006).

[5] M. König, S. Wiedmann, C. Brüne, A. Roth, H. Buhmann, L. W. Molenkamp, X.-L. Qi, and S.-C. Zhang. "Quantum spin Hall insulator state in HgTe quantum wells". *Science*, **318**, 766–770 (2007).

[6] R. Parr, W. Yang, and Y. Y. Weitao. *Density-Functional Theory of Atoms and Molecules*. Density-functional Theory of Atoms and Molecules. Oxford University Press, USA (1994). ISBN 9780195092769. `https://books.google.de/books?id=8XQ8DwAAQBAJ`.

[7] B. A. Bernevig, T. L. Hughes, and S.-C. Zhang. "Quantum spin Hall effect and topological phase transition in HgTe quantum wells". *science*, **314**, 1757–1761 (2006).

[8] J. M. Luttinger. “Quantum theory of cyclotron resonance in semiconductors: General theory”. *Phys. Rev.*, **102**, 1030–1041 (1956).

[9] B. Büttner, C. Liu, G. Tkachov, E. Novik, C. Brüne, H. Buhmann, E. Hankiewicz, P. Recher, B. Trauzettel, S. Zhang, et al. “Single valley Dirac fermions in zero-gap HgTe uantum wells”. *Nature Physics*, **7**, 418–422 (2011).

[10] L. Fu and C. L. Kane. “Topological insulators with inversion symmetry”. *Phys. Rev. B*, **76**, 045302 (2007).

[11] S. M. Young, S. Zaheer, J. C. Y. Teo, C. L. Kane, E. J. Mele, and A. M. Rappe. “Dirac semimetal in three dimensions”. *Phys. Rev. Lett.*, **108**, 140405 (2012).

[12] Z. Wang, Y. Sun, X.-Q. Chen, C. Franchini, G. Xu, H. Weng, X. Dai, and Z. Fang. “Dirac semimetal and topological phase transitions in $A_3$Bi ($a =$ Na, K, Rb)”. *Phys. Rev. B*, **85**, 195320 (2012).

[13] A. Burkov. “Topological semimetals”. *Nature materials*, **15**, 1145–1148 (2016).

[14] H. Weyl. “Gravitation and the electron”. *Proceedings of the National Academy of Sciences*, **15**, 323–334 (1929).

[15] N. P. Armitage, E. J. Mele, and A. Vishwanath. “Weyl and Dirac semimetals in three-dimensional solids”. *Rev. Mod. Phys.*, **90**, 015001 (2018).

[16] X. Wan, A. M. Turner, A. Vishwanath, and S. Y. Savrasov. “Topological semimetal and Fermi-arc surface states in the electronic structure of pyrochlore iridates”. *Phys. Rev. B*, **83**, 205101 (2011).

[17] S. L. Adler. “Axial-vector vertex in spinor electrodynamics”. *Physical Review*, **177**, 2426 (1969).

[18] D. E. Kharzeev. “The chiral magnetic effect and anomaly-induced transport”. *Progress in Particle and Nuclear Physics*, **75**, 133–151 (2014).

[19] D. M. Mahler, J.-B. Mayer, P. Leubner, L. Lunczer, D. Di Sante, G. Sangiovanni, R. Thomale, E. M. Hankiewicz, H. Buhmann, C. Gould, and L. W. Molenkamp. "Interplay of Dirac nodes and Volkov-Pankratov surface states in compressively strained HgTe". *Phys. Rev. X*, **9**, 031034 (2019).

[20] E. Majorana. "Teoria simmetrica dell'elettrone e del positrone". *Il Nuovo Cimento (1924-1942)*, **14**, 171–184 (1937).

[21] M. Sato, Y. Takahashi, and S. Fujimoto. "Non-abelian topological order in s-wave superfluids of ultracold fermionic atoms". *Physical review letters*, **103**, 020401 (2009).

[22] A. Kitaev. "Fault-tolerant quantum computation by anyons". *Annals of Physics*, **303**, 2–30 (2003).

[23] F. Pientka, A. Keselman, E. Berg, A. Yacoby, A. Stern, and B. I. Halperin. "Topological superconductivity in a planar Josephson junction". *Phys. Rev. X*, **7**, 021032 (2017).

[24] A. Fornieri, A. M. Whiticar, F. Setiawan, E. Portolés, A. C. Drachmann, A. Keselman, S. Gronin, C. Thomas, T. Wang, R. Kallaher, et al. "Evidence of topological superconductivity in planar Josephson junctions". *Nature*, **569**, 89–92 (2019).

[25] B. Scharf, F. Pientka, H. Ren, A. Yacoby, and E. M. Hankiewicz. "Tuning topological superconductivity in phase-controlled Josephson junctions with Rashba and Dresselhaus spin-orbit coupling". *Phys. Rev. B*, **99**, 214503 (2019).

[26] M. Kharitonov, J.-B. Mayer, and E. M. Hankiewicz. "Universality and stability of the edge states of chiral-symmetric topological semimetals and surface states of the Luttinger semimetal". *Phys. Rev. Lett.*, **119**, 266402 (2017).

[27] M. Kharitonov, J.-B. Mayer, and E. M. Hankiewicz. "Evolution of the surface states of the Luttinger semimetal under strain and inversion-symmetry breaking: Dirac, line-node, and Weyl semimetals". *submitted to Physical Review B* (2022).

[28] J. B. Mayer, M. A. Sierra, and E. M. Hankiewicz. "Intrinsic emergence of Majorana modes in Luttinger $j = \frac{3}{2}$ systems". *Phys. Rev. B*, **105**, 224513 (2022).

[29] A. P. Schnyder, S. Ryu, A. Furusaki, and A. W. W. Ludwig. "Classification of topological insulators and superconductors in three spatial dimensions". *Phys. Rev. B*, **78**, 195125 (2008).

[30] A. Kitaev. "Periodic table for topological insulators and superconductors". *AIP Conference Proceedings*, **1134**, 22–30 (2009).

[31] A. P. Schnyder, S. Ryu, A. Furusaki, and A. W. W. Ludwig. "Classification of topological insulators and superconductors". *AIP Conference Proceedings*, **1134**, 10–21 (2009).

[32] S. Ryu, A. P. Schnyder, A. Furusaki, and A. W. W. Ludwig. "Topological insulators and superconductors: tenfold way and dimensional hierarchy". *New Journal of Physics*, **12**, 065010 (2010).

[33] M. Z. Hasan and C. L. Kane. "Colloquium: Topological insulators". *Rev. Mod. Phys.*, **82**, 3045–3067 (2010).

[34] A. Altland and M. R. Zirnbauer. "Nonstandard symmetry classes in mesoscopic normal-superconducting hybrid structures". *Phys. Rev. B*, **55**, 1142–1161 (1997).

[35] M. Sato and Y. Ando. "Topological superconductors: a review". *Reports on Progress in Physics*, **80**, 076501 (2017).

[36] A. N. Redlich. "Parity violation and gauge noninvariance of the effective gauge field action in three dimensions". *Physical Review D*, **29**, 2366 (1984).

[37] A. N. Redlich. "Gauge noninvariance and parity nonconservation of three-dimensional fermions". *Physical Review Letters*, **52**, 18 (1984).

[38] G. W. Semenoff. “Condensed-matter simulation of a three-dimensional anomaly”. *Physical Review Letters*, **53**, 2449 (1984).

[39] E. Fradkin, E. Dagotto, and D. Boyanovsky. “Physical realization of the parity anomaly in condensed matter physics”. *Physical review letters*, **57**, 2967 (1986).

[40] F. D. M. Haldane. “Model for a quantum hall effect without Landau levels: Condensed-matter realization of the ”parity anomaly””. *Phys. Rev. Lett.*, **61**, 2015–2018 (1988).

[41] J. Böttcher, C. Tutschku, L. W. Molenkamp, and E. Hankiewicz. “Survival of the quantum anomalous hall effect in orbital magnetic fields as a consequence of the parity anomaly”. *Physical Review Letters*, **123**, 226602 (2019).

[42] L.-X. Wang, F. Schmitt, V. L. Müller, D. M. Mahler, L. Lunczer, J.-B. Mayer, W. Beugeling, H. Buhmann, E. M. Hankiewicz, and L. W. Molenkamp. “Parity anomaly, spectral asymmetry, and a re-entrant quantum hall effect in a single topological surface state”. *in preparation* (2023).

[43] D. J. Thouless, M. Kohmoto, M. P. Nightingale, and M. den Nijs. “Quantized hall conductance in a two-dimensional periodic potential”. *Phys. Rev. Lett.*, **49**, 405–408 (1982).

[44] O. Pankratov. “Supersymmetric inhomogeneous semiconductor structures and the nature of a parity anomaly in (2+ 1) electrodynamics”. *Physics letters A*, **121**, 360–366 (1987).

[45] M. Z. Hasan and J. E. Moore. “Three-dimensional topological insulators”. *Annu. Rev. Condensed Matter*, **1**, 00 (2010).

[46] Y. Hatsugai. “Chern number and edge states in the integer quantum Hall effect”. *Phys. Rev. Lett.*, **71**, 3697–3700 (1993).

[47] J. C. Y. Teo and C. L. Kane. “Topological defects and gapless modes in insulators and superconductors”. *Phys. Rev. B*, **82**, 115120 (2010).

[48] M. Sato, Y. Tanaka, K. Yada, and T. Yokoyama. “Topology of Andreev bound states with flat dispersion”. *Phys. Rev. B*, **83**, 224511 (2011).

[49] A. M. Essin and V. Gurarie. “Bulk-boundary correspondence of topological insulators from their respective Green’s functions”. *Phys. Rev. B*, **84**, 125132 (2011).

[50] X.-L. Qi and S.-C. Zhang. “Topological insulators and superconductors”. *Rev. Mod. Phys.*, **83**, 1057–1110 (2011).

[51] K. S. Novoselov, A. K. Geim, S. V. Morozov, D. Jiang, M. I. Katsnelson, I. Grigorieva, S. Dubonos, and a. Firsov. “Two-dimensional gas of massless Dirac fermions in graphene”. *nature*, **438**, 197–200 (2005).

[52] Y. Zhang, Y.-W. Tan, H. L. Stormer, and P. Kim. “Experimental observation of the quantum Hall effect and Berry’s phase in graphene”. *nature*, **438**, 201–204 (2005).

[53] P. A. M. Dirac. “The quantum theory of the electron”. *Proceedings of the Royal Society of London. Series A, Containing Papers of a Mathematical and Physical Character*, **117**, 610–624 (1928).

[54] B. A. Bernevig. “Topological insulators and topological superconductors”. In *Topological Insulators and Topological Superconductors.* Princeton university press (2013).

[55] H. B. Nielsen and M. Ninomiya. “Absence of neutrinos on a lattice:(i). proof by homotopy theory”. *Nuclear Physics B*, **185**, 20–40 (1981).

[56] H. B. Nielsen and M. Ninomiya. “Absence of neutrinos on a lattice:(ii). intuitive topological proof”. *Nuclear Physics B*, **193**, 173–194 (1981).

[57] G. B. Halász and L. Balents. “Time-reversal invariant realization of the Weyl semimetal phase”. *Phys. Rev. B*, **85**, 035103 (2012).

[58] K.-Y. Yang, Y.-M. Lu, and Y. Ran. “Quantum hall effects in a Weyl semimetal: Possible application in pyrochlore iridates”. *Phys. Rev. B*, **84**, 075129 (2011).

[59] C.-Z. Chang, J. Zhang, X. Feng, J. Shen, Z. Zhang, M. Guo, K. Li, Y. Ou, P. Wei, L.-L. Wang, et al. “Experimental observation of the quantum anomalous hall effect in a magnetic topological insulator”. *Science*, **340**, 167–170 (2013).

[60] C.-X. Liu, S.-C. Zhang, and X.-L. Qi. “The quantum anomalous Hall effect: theory and experiment”. *Annual Review of Condensed Matter Physics*, **7**, 301–321 (2016).

[61] H. B. Nielsen and M. Ninomiya. “The Adler-Bell-Jackiw anomaly and Weyl fermions in a crystal”. *Physics Letters B*, **130**, 389–396 (1983).

[62] D. Son and B. Spivak. “Chiral anomaly and classical negative magnetoresistance of Weyl metals”. *Physical Review B*, **88**, 104412 (2013).

[63] J. Ruan, S.-K. Jian, H. Yao, H. Zhang, S.-C. Zhang, and D. Xing. “Symmetry-protected ideal Weyl semimetal in HgTe-class materials”. *Nature communications*, **7**, 1–6 (2016).

[64] C.-Z. Xu, Y.-H. Chan, Y. Chen, P. Chen, X. Wang, C. Dejoie, M.-H. Wong, J. A. Hlevyack, H. Ryu, H.-Y. Kee, N. Tamura, M.-Y. Chou, Z. Hussain, S.-K. Mo, and T.-C. Chiang. “Elemental topological Dirac semimetal: $\alpha$-Sn on InSb(111)”. *Phys. Rev. Lett.*, **118**, 146402 (2017).

[65] L. Michel and J. Zak. “Connectivity of energy bands in crystals”. *Physical Review B*, **59**, 5998 (1999).

[66] J. L. Manes. “Existence of bulk chiral fermions and crystal symmetry”. *Physical Review B*, **85**, 155118 (2012).

[67] J. A. Steinberg, S. M. Young, S. Zaheer, C. Kane, E. Mele, and A. M. Rappe. “Bulk Dirac points in distorted spinels”. *Physical review letters*, **112**, 036403 (2014).

[68] Z. Wang, H. Weng, Q. Wu, X. Dai, and Z. Fang. "Three-dimensional Dirac semimetal and quantum transport in Cd 3 As 2". *Physical Review B*, **88**, 125427 (2013).

[69] B.-J. Yang and N. Nagaosa. "Classification of stable three-dimensional Dirac semimetals with nontrivial topology". *Nature communications*, **5**, 1–10 (2014).

[70] M. Kargarian, M. Randeria, and Y.-M. Lu. "Are the surface Fermi arcs in Dirac semimetals topologically protected?" *Proceedings of the National Academy of Sciences*, **113**, 8648–8652 (2016).

[71] C. Fang, L. Lu, J. Liu, and L. Fu. "Topological semimetals with helicoid surface states". *Nature Physics*, **12**, 936–941 (2016).

[72] D. Zhang, H. Wang, J. Ruan, G. Yao, and H. Zhang. "Engineering topological phases in the Luttinger semimetal $\alpha$-sn". *Phys. Rev. B*, **97**, 195139 (2018).

[73] Z. Liu, B. Zhou, Y. Zhang, Z. Wang, H. Weng, D. Prabhakaran, S.-K. Mo, Z. Shen, Z. Fang, X. Dai, et al. "Discovery of a three-dimensional topological Dirac semimetal, Na3Bi". *Science*, **343**, 864–867 (2014).

[74] S.-Y. Xu, C. Liu, S. K. Kushwaha, R. Sankar, J. W. Krizan, I. Belopolski, M. Neupane, G. Bian, N. Alidoust, T.-R. Chang, et al. "Observation of Fermi arc surface states in a topological metal". *Science*, **347**, 294–298 (2015).

[75] S. Borisenko, Q. Gibson, D. Evtushinsky, V. Zabolotnyy, B. Büchner, and R. J. Cava. "Experimental realization of a three-dimensional Dirac semimetal". *Physical review letters*, **113**, 027603 (2014).

[76] Z. Liu, J. Jiang, B. Zhou, Z. Wang, Y. Zhang, H. Weng, D. Prabhakaran, S. K. Mo, H. Peng, P. Dudin, et al. "A stable three-dimensional topological Dirac semimetal Cd3As2". *Nature materials*, **13**, 677–681 (2014).

[77] M. Neupane, S.-Y. Xu, R. Sankar, N. Alidoust, G. Bian, C. Liu, I. Belopolski, T.-R. Chang, H.-T. Jeng, H. Lin, et al. "Observation of a three-dimensional

topological Dirac semimetal phase in high-mobility Cd3As2". *Nature communications*, **5**, 1–8 (2014).

[78] N. Read and D. Green. "Paired states of fermions in two dimensions with breaking of parity and time-reversal symmetries and the fractional quantum Hall effect". *Phys. Rev. B*, **61**, 10267–10297 (2000).

[79] A. Y. Kitaev. "Unpaired Majorana fermions in quantum wires". *Physics-Uspekhi*, **44**, 131–136 (2001).

[80] N. Bogoljubov, V. V. Tolmachov, and D. Širkov. "A new method in the theory of superconductivity". *Fortschritte der physik*, **6**, 605–682 (1958).

[81] M. Tinkham. *Introduction to Superconductivity*. Dover Books on Physics Series. Dover Publications (2004). ISBN 9780486134727. `https://books.google.de/books?id=VpUk3NfwDIkC`.

[82] J. Bardeen, L. N. Cooper, and J. R. Schrieffer. "Theory of superconductivity". *Phys. Rev.*, **108**, 1175–1204 (1957).

[83] R. Holm and W. Meissner. "Messungen mit hilfe von flüssigem helium. xiii". *Zeitschrift für Physik*, **74**, 715–735 (1932).

[84] H. Meissner. "Superconductivity of contacts with interposed barriers". *Phys. Rev.*, **117**, 672–680 (1960).

[85] P. A. M. Dirac et al. *The principles of quantum mechanics*. 27. Oxford university press (1981).

[86] F. Wilczek. "Majorana returns". *Nature Physics*, **5**, 614–618 (2009).

[87] D. A. Ivanov. "Non-abelian statistics of half-quantum vortices in $p$-wave superconductors". *Phys. Rev. Lett.*, **86**, 268–271 (2001).

[88] S.-Q. SHEN. *Topological Insulators: Dirac Equation in Condensed Matter*. Springer (2018).

[89] L. H. Kauffman. "Knots and physics world scientific publishing co". *Pte. Ltd* (1993).

[90] M. Leijnse and K. Flensberg. "Introduction to topological superconductivity and Majorana fermions". *Semiconductor Science and Technology*, **27**, 124003 (2012).

[91] C. Nayak, S. H. Simon, A. Stern, M. Freedman, and S. Das Sarma. "Non-abelian anyons and topological quantum computation". *Rev. Mod. Phys.*, **80**, 1083–1159 (2008).

[92] J. Alicea. "New directions in the pursuit of Majorana fermions in solid state systems". *Reports on Progress in Physics*, **75**, 076501 (2012).

[93] C. Beenakker. "Search for Majorana fermions in superconductors". *Annual Review of Condensed Matter Physics*, **4**, 113–136 (2013).

[94] T. D. Stanescu and S. Tewari. "Majorana fermions in semiconductor nanowires: fundamentals, modeling, and experiment". *Journal of Physics: Condensed Matter*, **25**, 233201 (2013).

[95] C. Tutschku, R. W. Reinthaler, C. Lei, A. H. MacDonald, and E. M. Hankiewicz. "Majorana-based quantum computing in nanowire devices". *Phys. Rev. B*, **102**, 125407 (2020).

[96] J. A. Sauls. "Andreev bound states and their signatures". *Philosophical Transactions of the Royal Society A: Mathematical, Physical and Engineering Sciences*, **376**, 20180140 (2018).

[97] A. Andreev. "The thermal conductivity of the intermediate state in superconductors". *JETP*, **19**, 1228 (1964).

[98] E. Prada, P. San-Jose, M. W. A. de Moor, A. Geresdi, E. J. H. Lee, J. Klinovaja, D. Loss, J. Nygård, R. Aguado, and L. P. Kouwenhoven. "From Andreev to Majorana bound states in hybrid superconductor–semiconductor nanowires". *Nature Reviews Physics*, **2**, 575–594 (2020).

[99] L. Fu and C. L. Kane. “Superconducting proximity effect and Majorana fermions at the surface of a topological insulator”. *Phys. Rev. Lett.*, **100**, 096407 (2008).

[100] L. Hao and T. Lee. “Surface spectral function in the superconducting state of a topological insulator”. *Physical Review B*, **83**, 134516 (2011).

[101] T. H. Hsieh and L. Fu. “Majorana fermions and exotic surface Andreev bound states in topological superconductors: application to Cu x Bi 2 Se 3”. *Physical review letters*, **108**, 107005 (2012).

[102] T. Hashimoto, K. Yada, A. Yamakage, M. Sato, and Y. Tanaka. “Bulk electronic state of superconducting topological insulator”. *Journal of the Physical Society of Japan*, **82**, 044704 (2013).

[103] T. Hashimoto, K. Yada, A. Yamakage, M. Sato, and Y. Tanaka. “Effect of Fermi surface evolution on superconducting gap in superconducting topological insulator”. *Superconductor Science and Technology*, **27**, 104002 (2014).

[104] G. Y. Cho, J. H. Bardarson, Y.-M. Lu, and J. E. Moore. “Superconductivity of doped Weyl semimetals: Finite-momentum pairing and electronic analog of the 3 He-A phase”. *Physical Review B*, **86**, 214514 (2012).

[105] G. Bednik, A. Zyuzin, and A. Burkov. “Superconductivity in Weyl metals”. *Physical Review B*, **92**, 035153 (2015).

[106] T. Zhou, Y. Gao, and Z. Wang. “Superconductivity in doped inversion-symmetric Weyl semimetals”. *Physical Review B*, **93**, 094517 (2016).

[107] S. Kobayashi and M. Sato. “Topological superconductivity in Dirac semimetals”. *Physical Review Letters*, **115**, 187001 (2015).

[108] T. Hashimoto, S. Kobayashi, Y. Tanaka, and M. Sato. “Superconductivity in doped Dirac semimetals”. *Physical Review B*, **94**, 014510 (2016).

[109] R. M. Lutchyn, J. D. Sau, and S. D. Sarma. “Majorana fermions and a topo-

logical phase transition in semiconductor-superconductor heterostructures". *Physical review letters*, **105**, 077001 (2010).

[110] Y. Oreg, G. Refael, and F. Von Oppen. "Helical liquids and Majorana bound states in quantum wires". *Physical review letters*, **105**, 177002 (2010).

[111] B. D. Josephson. "Possible new effects in superconductive tunnelling". *Physics letters*, **1**, 251–253 (1962).

[112] G. Tkachov and E. M. Hankiewicz. "Helical andreev bound states and superconducting klein tunneling in topological insulator josephson junctions". *Physical Review B*, **88** (2013).

[113] M. König, H. Buhmann, L. W. Molenkamp, T. Hughes, C.-X. Liu, X.-L. Qi, and S.-C. Zhang. "The quantum spin Hall effect: Theory and experiment". *Journal of the Physical Society of Japan*, **77**, 031007 (2008).

[114] C. Brüne, C. X. Liu, E. G. Novik, E. M. Hankiewicz, H. Buhmann, Y. L. Chen, X. L. Qi, Z. X. Shen, S. C. Zhang, and L. W. Molenkamp. "Quantum hall effect from the topological surface states of strained bulk HgTe". *Phys. Rev. Lett.*, **106**, 126803 (2011).

[115] S. Shamim, W. Beugeling, J. Böttcher, P. Shekhar, A. Budewitz, P. Leubner, L. Lunczer, E. M. Hankiewicz, H. Buhmann, and L. W. Molenkamp. "Emergent quantum Hall effects below 50 mT in a two-dimensional topological insulator". *Science Advances*, **6** (2020).

[116] R. Winkler. *Spin–Orbit Coupling Effects in Two-Dimensional Electron and Hole Systems*, volume 191 of *Springer Tracts in Modern Physics*. Springer Berlin Heidelberg, Berlin, Heidelberg (2003). ISBN 978-3-540-01187-3. `http://link.springer.com/10.1007/b13586`.

[117] M. Tinkham. *Group theory and quantum mechanics*. Courier Corporation (2003).

[118] M. S. Dresselhaus, G. Dresselhaus, and A. Jorio. *Group theory: application to the physics of condensed matter.* Springer Science & Business Media (2007).

[119] G. Bir and G. Pikus. *Symmetry and Strain-induced Effects in Semiconductors*. A Halsted Press book. Wiley (1974). ISBN 9780470073216. `https://books.google.de/books?id=38m2QgAACAAJ`.

[120] S. Chuang. *Physics of Optoelectronic Devices*. Wiley Series in Pure and Applied Optics. Wiley (1995). ISBN 9780471109396. `https://books.google.de/books?id=ect6QgAACAAJ`.

[121] U. Rössler. "Nonparabolicity and warping in the conduction band of GaAs". *Solid state communications*, **49**, 943–947 (1984).

[122] P. Pfeffer and W. Zawadzki. "Conduction electrons in GaAs: Five-level $k \cdot p$ theory and polaron effects". *Physical Review B*, **41**, 1561 (1990).

[123] H. Mayer and U. Rössler. "Spin splitting and anisotropy of cyclotron resonance in the conduction band of GaAs". *Phys. Rev. B*, **44**, 9048–9051 (1991).

[124] D. M. Mahler, V. L. Müller, C. Thienel, J. Wiedenmann, W. Beugeling, H. Buhmann, and L. W. Molenkamp. "Massive and topological surface states in tensile-strained HgTe". *Nano Letters*, **21**, 9869–9874 (2021).

[125] S. Shamim, P. Shekhar, W. Beugeling, J. Böttcher, A. Budewitz, J.-B. Mayer, L. Lunczer, E. M. Hankiewicz, H. Buhmann, and L. W. Molenkamp. "Counterpropagating topological and quantum Hall edge channels". *Nature Communications*, **13**, 1–7 (2022).

[126] P.-O. Löwdin. "A note on the quantum-mechanical perturbation theory". *The Journal of Chemical Physics*, **19**, 1396–1401 (1951).

[127] C.-K. Chiu, J. C. Y. Teo, A. P. Schnyder, and S. Ryu. "Classification of topological quantum matter with symmetries". *Rev. Mod. Phys.*, **88**, 035005 (2016).

[128] O. Madelung. “Elements of the IVth group and IV-IV compounds”. In *Semiconductors: Data Handbook*, pages 7–70. Springer (2004).

[129] E. G. Novik, A. Pfeuffer-Jeschke, T. Jungwirth, V. Latussek, C. R. Becker, G. Landwehr, H. Buhmann, and L. W. Molenkamp. “Band structure of semimagnetic $\mathrm{hg}_{1-y}\mathrm{mn}_y\mathrm{Te}$ quantum wells”. *Phys. Rev. B*, **72**, 035321 (2005).

[130] S. Tchoumakov, V. Jouffrey, A. Inhofer, E. Bocquillon, B. Plaçais, D. Carpentier, and M. Goerbig. “Volkov-Pankratov states in topological heterojunctions”. *Physical Review B*, **96**, 201302 (2017).

[131] R. M. Lutchyn, E. P. Bakkers, L. P. Kouwenhoven, P. Krogstrup, C. M. Marcus, and Y. Oreg. “Majorana zero modes in superconductor–semiconductor heterostructures”. *Nature Reviews Materials*, **3**, 52–68 (2018).

[132] R. Aguado and L. P. Kouwenhoven. “Majorana qubits for topological quantum computing”. *Physics Today*, **73**, 44–50 (2020).

[133] G. Goldstein and C. Chamon. “Decay rates for topological memories encoded with Majorana fermions”. *Phys. Rev. B*, **84**, 205109 (2011).

[134] V. Mourik, K. Zuo, S. M. Frolov, S. R. Plissard, E. P. A. M. Bakkers, and L. P. Kouwenhoven. “Signatures of Majorana fermions in hybrid superconductor-semiconductor nanowire devices”. *Science*, **336**, 1003–1007 (2012).

[135] M.-T. Deng, S. Vaitiekėnas, E. Prada, P. San-Jose, J. Nygård, P. Krogstrup, R. Aguado, and C. M. Marcus. “Nonlocality of Majorana modes in hybrid nanowires”. *Phys. Rev. B*, **98**, 085125 (2018).

[136] H. Ren, F. Pientka, S. Hart, A. T. Pierce, M. Kosowsky, L. Lunczer, R. Schlereth, B. Scharf, E. M. Hankiewicz, L. W. Molenkamp, et al. “Topological superconductivity in a phase-controlled Josephson junction”. *Nature*, **569**, 93–98 (2019).

[137] R. Wakatsuki, M. Ezawa, and N. Nagaosa. “Majorana fermions and multiple

topological phase transition in Kitaev ladder topological superconductors". *Phys. Rev. B*, **89**, 174514 (2014).

[138] P. Szumniak, D. Chevallier, D. Loss, and J. Klinovaja. "Spin and charge signatures of topological superconductivity in Rashba nanowires". *Phys. Rev. B*, **96**, 041401 (2017).

[139] M. Kharitonov, E. M. Hankiewicz, B. Trauzettel, and F. S. Bergeret. "Ever-present Majorana bound state in a generic one-dimensional superconductor with odd number of Fermi surfaces". *Phys. Rev. B*, **104**, 134516 (2021).

[140] Y. Peng, F. Pientka, E. Berg, Y. Oreg, and F. von Oppen. "Signatures of topological Josephson junctions". *Phys. Rev. B*, **94**, 085409 (2016).

[141] P. M. R. Brydon, L. Wang, M. Weinert, and D. F. Agterberg. "Pairing of $j = 3/2$ fermions in Half-Heusler superconductors". *Phys. Rev. Lett.*, **116**, 177001 (2016).

[142] H. Kim, K. Wang, Y. Nakajima, R. Hu, S. Ziemak, P. Syers, L. Wang, H. Hodovanets, J. D. Denlinger, P. M. R. Brydon, D. F. Agterberg, M. A. Tanatar, R. Prozorov, and J. Paglione. "Beyond triplet: Unconventional superconductivity in a spin-3/2 topological semimetal". *Science Advances*, **4**, eaao4513 (2018).

[143] B. Roy, S. A. A. Ghorashi, M. S. Foster, and A. H. Nevidomskyy. "Topological superconductivity of spin-3/2 carriers in a three-dimensional doped Luttinger semimetal". *Phys. Rev. B*, **99**, 054505 (2019).

[144] H. Kim, J. Lee, H. Hodovanets, K. Wang, J. D. Sau, and J. Paglione. "Anomalous quantum oscillations in spin-3/2 topological semimetal YPtBi" (2020). `https://arxiv.org/abs/2010.12085`.

[145] P. Dutta, F. Parhizgar, and A. M. Black-Schaffer. "Superconductivity in spin-3/2 systems: Symmetry classification, odd-frequency pairs, and Bogoliubov Fermi surfaces". *Phys. Rev. Research*, **3**, 033255 (2021).

[146] C. Timm and A. Bhattacharya. “Symmetry, nodal structure, and Bogoliubov fermi surfaces for nonlocal pairing”. *Phys. Rev. B*, **104**, 094529 (2021).

[147] M. Bahari, S.-B. Zhang, and B. Trauzettel. “Intrinsic finite-energy Cooper pairing in $j = 3/2$ superconductors”. *Phys. Rev. Research*, **4**, L012017 (2022).

[148] D. F. Agterberg, P. M. R. Brydon, and C. Timm. “Bogoliubov Fermi surfaces in superconductors with broken time-reversal symmetry”. *Phys. Rev. Lett.*, **118**, 127001 (2017).

[149] J. W. F. Venderbos, L. Savary, J. Ruhman, P. A. Lee, and L. Fu. “Pairing states of spin-$\frac{3}{2}$ fermions: Symmetry-enforced topological gap functions”. *Phys. Rev. X*, **8**, 011029 (2018).

[150] J. Yu and C.-X. Liu. “Singlet-quintet mixing in spin-orbit coupled superconductors with $j = \frac{3}{2}$ fermions”. *Phys. Rev. B*, **98**, 104514 (2018).

[151] P. M. R. Brydon, D. F. Agterberg, H. Menke, and C. Timm. “Bogoliubov Fermi surfaces: General theory, magnetic order, and topology”. *Phys. Rev. B*, **98**, 224509 (2018).

[152] D. Griffiths. *Introduction to Quantum Mechanics*. Cambridge University Press (2017). ISBN 9781107179868. `https://books.google.de/books?id=0h-nDAAAQBAJ`.

[153] A. R. Akhmerov, J. P. Dahlhaus, F. Hassler, M. Wimmer, and C. W. J. Beenakker. “Quantized conductance at the Majorana phase transition in a disordered superconducting wire”. *Phys. Rev. Lett.*, **106**, 057001 (2011).

[154] I. C. Fulga, F. Hassler, A. R. Akhmerov, and C. W. J. Beenakker. “Scattering formula for the topological quantum number of a disordered multimode wire”. *Phys. Rev. B*, **83**, 155429 (2011).

[155] I. C. Fulga, F. Hassler, and A. R. Akhmerov. “Scattering theory of topological insulators and superconductors”. *Phys. Rev. B*, **85**, 165409 (2012).

[156] C. W. J. Beenakker. “Three “universal” mesoscopic Josephson effects”. *Transport Phenomena in Mesoscopic Systems*, page 235–253 (1992).

[157] C. W. Groth, M. Wimmer, A. R. Akhmerov, and X. Waintal. “Kwant: a software package for quantum transport”. *New Journal of Physics*, **16**, 063065 (2014).

[158] W. Beugeling. “Parity symmetry as the origin of ‘spin’ in the quantum spin hall effect”. *Phys. Rev. B*, **104**, 115428 (2021).

[159] W. Kohn and J. M. Luttinger. “Quantum theory of cyclotron resonance in semiconductors”. *Phys. Rev.*, **96**, 529–530 (1954).

[160] J. Hajer, M. Kessel, C. Brüne, M. P. Stehno, H. Buhmann, and L. W. Molenkamp. “Proximity-induced superconductivity in CdTe–HgTe core–shell nanowires”. *Nano Letters*, **19**, 4078–4082 (2019).

[161] M. Cardona, N. E. Christensen, and G. Fasol. “Terms linear in k in the band structure of zinc-blende-type semiconductors”. *Phys. Rev. Lett.*, **56**, 2831–2833 (1986).

[162] G. Koster, J. Dimmock, R. Wheeler, and H. Statz. *Properties of the Thirty-two Point Groups*. M.I.T. Press research monographs. M.I.T. Press (1963). ISBN 9780262110105. `https://books.google.de/books?id=iMTQAAAAMAAJ`.

# Acknowledgements

> “I feel I learned as much from fellow students as from the professors.“
>
> Jack Steinberger

Undoubtedly, a significant part of someone’s personality is shaped by the people in his social environment. Throughout my eleven-year journey into the depths of physics, I was lucky to meet a broad spectrum of extraordinary characters. Every one of them is reflected in the scientist I am today.

First and foremost, I express my deepest gratitude to Prof. Dr. Ewelina Hankiewicz. As a member of her group, I matured during my time as a master’s and Ph.D. student. Her guidance showed me what it really means to be a physicist. I am more than grateful for our extraordinary working relationship and personal support, which made this thesis possible in the first place.

Additionally, I am incredibly grateful for my close colleagues Dr. Jan Böttcher, Dr. Christian Tutschku, Dr. Daniel Hetterich, Dr. Benedikt Scharf, and Philipp Heilmann. They demonstrated that a heated discussion over a cup of coffee can be more enlightening than an entire lecture. I could not have wished for a better group who understood to put delight into everyday work. A special mention goes to Dr. Daniel Gresta and Dr. Raffael Klees, who recently joined the group and were so kind to proofread this thesis. Moreover, I would like to thank Prof. Dr. Björn Trauzettel, who was always available for advice, and Nelly Meyer for being the heart and soul of our group.

Throughout my time, I had the honor to collaborate with many people outside of

my group. First, I thank Prof. Dr. Giorgio Sangiovanni and Prof. Dr. Domenico Di Sante for providing the DFT calculations, which were used to determine the parameters of HgTe used in this thesis. Moreover, many thanks to my collaborators from experimental physics: Prof. Dr. Laurens Molenkamp, Prof. Dr. Hartmut Buhmann, Dr. Wouter Beugeling, Dr. Saquib Shamim, and Dr. Lixian Wang.

Last but not least, let me thank my family. The emotional support I received from my mother, Birgit Mayer, could not have been surpassed. Foremost, this work would not have been possible without my wife, Daniela Eckardt, and our beloved children. Words can not express how grateful I am for their unreserved support and love.